Constraints on Askja Volcano, Iceland, from Surface Deformation and Gravity Change

Jeanne Marie Giniaux

Submitted in accordance with the requirements for the degree of
Doctor of Philosophy

The University of Leeds
School of Earth and Environment

November 2019

The candidate confirms that the work submitted is her own, except where work which has formed part of jointly authored publications has been included. The contribution of the candidate and the other authors to this work has been explicitly indicated below. The candidate confirms that appropriate credit has been given within the thesis where reference has been made to the work of others.

Acknowledgements

This PhD has been a long journey, hard, often frustrating and rarely fun, but studying volcanoes has also been very fascinating! I gained a lot from this tough experience, regarding science but also personally, and I could never have finished this thesis without the support of many people, whom I would like to thank here.

First of all, I would like to express my gratitude to my supervisor, Andy Hooper, who guided me to achieve a piece of work that I am proud of today. Thank you for all what you thought me during these few years and for your open-mindedness, especially in difficult moments.

The overall project was supported by the University of Leeds 110 Anniversary Research Scholarship. In addition, I received external support for fieldwork campaigns from the European Community's Seventh Framework Programme Grant No. 308377 (Project FUTUREVOLC), the Geological and Remote Sensing Group (GRSG), the Royal Astronomical Society (RAS) and the Centre for Observation and Modelling of Earthquakes, volcanoes and Tectonics (COMET). I also acknowledge the Icelandic Volcanoes Supersite project supported by the Committee on Earth Observing Satellites (CEOS) for providing access to COSMO-SkyMed data over Askja, via FUTUREVOLC.

Many thanks to the Icelandic colleagues, especially Freysteinn Sigmundsson and Magnús Tumi Guđmudsson. The free rein and support that you provided me to carry on my gravity surveys at Askja has been wonderful, as well as the constant warm welcome at the University of Iceland. I also would like to thank Vincent Drouin, for his collaboration with the GPS measurements, and big thanks go to Stephanie Dumont and again to Andy Hooper, for their committed and fun assistance in the field, without forgetting Ben Hooper, who impressed me every morning, with his unlimited enthusiasm.

I also would like to thank my colleagues at the University of Leeds. Special thanks go to my office mates, in particular Matt Gaddes, Lin Shen, Huw Goodall and Ita Alvarez, for their friendly, supportive and generous company. To Ruth Amey and Tom Ingleby, who have been available for any questions from the beginning until the end, have been highly supportive and for their availability in proofreading some of my thesis chapters. To Locko (Jurgen Neuberg) for great gravity discussions every September in Lanzarote and for having allowed me to expand my teaching skills during this undergraduate fieldtrip. To Richard Rigby for his availability in fixing computer issues so quickly and

so generously. To Tim Wright who provided me useful feedback. To Karsten Spaans, Ekbal Hussain and David Bekaert for sharing their InSAR skills.

Additionally, many thanks to Philippe Jousset (GFZ Potsdam, Germany) for providing local free-air gradient measurements from Merapi volcano, Thomas Jacob (University of Colorado, U.S.A.) for providing information about calibration and Karina Nielsen (National Space Institute of Denmark) for providing the lake-level time-series over Öskjuvatn, from satellite altimetry. To Maurizio Battaglia and Mike Poland for their advice and support regarding some of my work. Again to Stephanie Dumont for reviewing some parts of my Introduction. To Rachel Holley, my future colleague, for her great support and generosity in offering help and for having proofread one of my thesis chapters.

Regarding assistance in managing stress and emotions, I would like to especially warmly thank the yoga teacher, Lara Hepell, the osteopaths, Ami Sevi and Frederic Holmann, as well as some authors, such as Laurent Gounelle, Jonathan Lemman and Hal Elrod, with his wonderful miracle morning routine.

I also would like to thank families and friends from Leeds, Iceland and France, who supported me directly or indirectly. Special thanks go to Drífa and Pedro, who warmly welcomed me in their home, in Reykjavik, for several weeks every summer. To Jean-Damien Sebastian for all the great moments spent in Leeds before he moved back to France. Helping around at his French cafe was a great way to cut off from PhD. Many thanks also to my close friend, Thomas Guermont, who always had the right word at the right time.

Finally, I cannot thank my partner, Jérémie, my sister, Juliette and my mother, Bénédicte, enough for their unlimited support and love, throughout this long journey. You have been amazing in guiding me to move forward in a healthy way.

I dedicate this thesis to my father, Dominique Giniaux.

Abstract

Moving towards detecting and understanding volcanic unrest prior to eruptions, there has been significant improvements in understanding the structure and dynamics of magma plumbing systems. However, deciphering subsurface processes during inter-eruptive periods often remains challenging, and whether magma is involved or not is an essential question to be able to assess the degree of activity of a volcano. In this thesis, I explore the integration of surface deformation and temporal gravity, using the Askja volcano (Iceland) as a case study.

Magmatic processes are usually closely linked to pressurization-depressurization mechanisms, which can translate into subsurface volume changes and lead to surface deformation responses. Because magmatic processes are diverse, integrating temporal gravity can help narrowing down the list of possible on-going processes. Indeed, temporal gravity is related to subsurface mass change, and for example, a surface uplift associated with a gravity increase could be caused by a magma intrusion, whereas an uplift with no mass change could be caused by gas pressurization resulting from temperature increase. Additionally, comparing both signals can help evaluating the contributions of external processes, such as of hydrothermal or tectonic origin.

The Askja volcano, which is one of the most active volcanoes in Iceland, has erupted at least 40 times in the last 1,100 years. Some events were very powerful, such as the 1875 VEI-5 caldera-forming Plinian event and the most recent event was a basaltic fissure eruption, which occurred in 1961. Since at least 1983, the main caldera has been subsiding and all the previous studies that applied analytical modelling to surface deformation records at Askja agree that the subsidence can be best explained over periods of $\leq$10 years, by a deflating source, located at 3-3.5 km depth beneath the caldera centre. The constrained linear volume changes have diminished from about -0.002 km^3 yr^{-1} near 2000 to about -0.001 km^3 yr^{-1} near 2010.

In parallel, gravity measurements, which were recorded between 1988 and 2010, highlighted a gradual gravity decrease of about 140 microgal up to 2007, centred on the main caldera, and a gravity increase of about 60 microgal was observed between 2007 and 2009, while the subsidence continued. Due to the lack of spatial coverage, no analytical model could be performed using the gravity results, hence there were no constraints on the depth and magnitude of mass changes. Due to the correlation in

locations, previous studies assumed that mass and volume changes were related to the same process, occurring at 3-3.5 km depth. Based on this assumption it was suggested that the main process causing the subsidence was a magma drainage down to deeper levels with possible additional effects from magma crystallisation. A magma intrusion at the shallow reservoir and/or mass variations in the hydrothermal system were proposed to explain the temporary gravity increase. Finally, the likely high contribution of plate spreading as a cause of subsidence was demonstrated using finite-element modelling, considering the caldera and shallow chamber as zones of weak materials, embedded in a two-layer crust model with a visco-elastic lower crust.

In this thesis, I take the analyses of both surface deformation and temporal gravity at Askja a step further, to clarify the causes of subsidence. I use the Interferometric Synthetic Aperture Radar (InSAR) technique to investigate the spatial and temporal signature of the long-term subsidence, considering a 15-year-long time period. This technique, which was used at Askja in two previous studies, can measure surface deformation at the centimetre scale over large areas with spatial resolution of tens to hundreds of meters. My results show that the caldera is steadily subsiding as a whole, and can be fitted by an exponential decay with relaxation time of about 42 years. Using the Bayesian inversion modelling approach paired with the Markov chain Monte Carlo sampling, and incorporating the exponential behaviour of the subsidence, I refine the depth of the shallow reservoir with narrower bounds compared with previous studies: when assuming a point pressure source, which can reproduce well the circular spatial deformation pattern observed in the caldera, there is 95% chance that the reservoir is located at 3±0.1 km beneath the caldera centre and the exponential volume decrease has total amplitude of 0.07±0.01 km^3.

In parallel, I investigate the spatial and temporal evolution of gravity changes over 2015-2017, from a larger gravity network and using improved methodologies compared with previous studies. My results show a spatial-bowl shape signature over 2015-2016, with maximum decrease of about 100±30 microgal at the caldera centre. Although this annual change is spatially correlated with the synchronous subsidence, the following annual gravity change, showing negligible variations across the caldera, is not. This suggests that both signals do not relate to the same processes, and the difference in magnitude of gravity changes compared with previous studies is due to the choice of reference station. I then further investigate the link between gravity changes and deformation, by performing the first gravity inversion at Askja, and using the Bayesian inversion modelling approach paired with the Markov chain Monte Carlo sampling. Even though poorly constrained, the inversion suggests that, when assuming a spherical source, the gravity changes over 2015-2016 have 95% chance to be due to a mass decrease within 1.5×10^{12}-7.5×10^{10} kg and located within 2.7-9.9 km. These large confidence intervals are due to the large uncertainties of the gravity results. Assuming magma drainage, the mass change derived from the volume decrease constrained from the exponential defor-

mation is outside the 95% confidence interval of mass change constrained from gravity. The uncorrelated temporal variations and discrepancy in magnitude between both types of signals therefore suggest that magma drainage is unlikely to be responsible for the subsidence at Askja. Alternatively, the steady and gradually decaying subsidence could be driven by extension due to plate spreading, which would induce pressure decrease at the shallow reservoir, and crystallisation processes could also participate. On the other hand, the gravity changes could be due to mass fluctuations in a hydrothermal system just above the shallow magma reservoir.

To precisely extract gravity changes related to magma movements and/or hydrothermal mass variations and fully integrate errors in my gravity analysis, I have developed a statistical approach that estimates the total error budget associated with temporal gravity, when using spring relative gravimeters. In this thesis, I present the method in detail, providing equations for users to estimate case-by-case error budgets, and I also provide ranges of best-to-worst case scenarios, to guide users on where to focus effort to minimizing errors, depending on the magnitude of the signal of interest. My results show that the choice of gravimeter is essential to minimize vibration noise and errors due to imprecise levelling, which can both reach hundreds of microgals. Similarly, monitoring the temporal evolution of calibration factor should be usual practice, especially when studying gravity time-series spanning several years. Finally, I demonstrate that a bulk estimate of errors due to unknown meterological effects, which can reach a few tens of microgals, can be derived from base station measurements spanning at least a few days.

Table of Contents

List of Figures

List of Tables

List of Abbreviations

List of acronyms

AML	Axial Melt Lens
ASTER	Advanced Spaceborne Thermal Emission and Reflection Radiometer DEM
COMET	Centre for the Observation and Modelling of Earthquakes, volcanoes and Tectonics
CSK	COSMO-SkyMed satellite
DEM	Digital Elevation Model
DORIS	Delft Object-oriented Radar Interferometric Software
Envisat	Environmental satellite
ERS	European Remote-sensing Satellite
FAG	Free-Air gravity Gradient
FIR	Fast-to-Intermediate spreading Ridge
GBIS	Geodetic Bayesian Inversion Software
GIA	Glacial Isostatic Adjustment
GNSS	Global Navigation Satellite System
GPS	Global Positioning System
GRSG	Geological Remote Sensing Group
InSAR	Interferometric Synthetic Aperture Radar
ITRF14	International Terrestrial Reference Frame 2014
LCR	LaCoste & Romberg gravimeter

LOS	satellite Line-Of-Sight
LS,boot	Least-Squares percentile bootstrap approach
MCMC	Markov chain Monte Carlo
MOR	Mid-Oceanic Ridge
MSR	Magma-dominated Slow-spreading Ridge
OTM	Ocean Tide Model
OTP	Ocean Tide Program
PS	Persistent Scatterer
Radar	RAdio Detection And Ranging
RAS	Royal Astronomical Society
RMSE	Root Mean Square Error
ROI_PAC	Repeat Orbit Interferometry PACkage
S1	Sentinel-1 satellite
SAML	Sub-Axial Melt Lens
SAR	Synthetic Aperture Radar
SB	Small Baseline
SCG	SCintrex Gravimeter
SDFP	Slowly-Decorrelating Filtered Phase
StaMPS	Stanford Method for Persistent Scatterers
VGG	Vertical Gravity Gradient
WLS	Weighted-Least Squares
WRSS	Weighted Residual Sum of Squares

List of symbols

α	Satellite heading angle	[°]
β	Coefficient of isothermal compressibility	[Pa^{-1}]
$\boldsymbol{d}$	Displacement unit vector	[-]

$\boldsymbol{los}$	LOS unit vector	[-]
$\Delta\rho$	Temporal density change	[kg m^{-3}]
$\Delta\varphi$	Interferometric phase difference along LOS	[rad]
δf	Calibration scale factor difference between surveys	[-]
Δg	Temporal gravity change	[m s^{-2},μGal]
Δh	Surface elevation between two gravity surveys	[-]
ΔL	Vertical separation between gravity measurements	[m]
ΔM	Temporal mass change	[kg]
ΔV	Temporal volume change	[m^{-3}]
ΔV_∞	Exponential amplitude of temporal volume change	[m^{-3}]
Δz	Groundwater level variations	[m]
γ	Semi-variance in semi-variogram	[unit^2]
ι	Coefficient of isobaric thermal expansion	[°C^{-1}]
λ	Radar wavelength	[m]
μ	Shear modulus	[Pa]
ν	Degree of freedom	[-]
ϕ	Open porosity	[-]
ρ	Density	[kg m^3]
σ	Standard deviation	
τ	Relaxation time	[years]
Θ	Satellite incidence angle	[°]
θ	Gravimeter instrumental tilt	[°]
ε	Residual error at any time	
ϱ	Gravity reading before conversion	[volt,counter units]
ξ	Residual error between two different times	
A	Radar amplitude	[m]

a	Radius	[m]
C	Covariance	[unit^2]
D	Displacement	[m]
E	Young's modulus	[Pa]
f	Calibration scale factor for spring gravimeters	[-]
f_D	Drift function	[-]
G	Universal gravitational constant	[m^3 kg^{-1} s^{-2}]
g	Gravity signal	[m s^{-2},μGal]
K	Bulk modulus	[Pa]
k	Calibration factor for spring gravimeters	[-]
M	Mass	[kg]
o	Displacement offset	[m]
P	Pressure	[Pa]
R	Range for semi-variogram	[m]
r	Distance	[m]
T	Temperature	[°C]
t	Time	[year,day,hour,min,s]
u	Dot product between unit vectors	[-]
V	Volume	[m^3]
y	Poisson's ratio	[-]
z	Depth	[m]

Chapter 1

Introduction

1.1 Overview

One of the biggest challenges in volcanology is to forecast eruptions as precisely as possible, in order to reduce the impact on local communities. Moving towards this goal, there has been some significant improvements during the last few decades, in detecting and understanding volcanic unrest, and consequently, better understanding the subsurface structure and dynamics of active volcanoes (e.g. Dzurisin, 2007d, Moran et al., 2011, Sparks et al., 2012, Acocella et al., 2015, Burchardt, 2018).

The extensive development of the Interferometric Synthetic Aperture Radar (InSAR) technique, which can monitor surface deformation from space over km-scale areas, has contributed to better understanding subsurface magmatic processes, especially before, during and after eruptive events. Indeed, magma movements are usually closely linked to pressurization-depressurization mechanisms, which commonly lead to measurable upwards-downwards ground movements, often referred to as inflation-deflation phases (e.g. Dzurisin, 2007c, Biggs et al., 2014). However, apart from the scenario of a very likely up-coming eruption, where magma is clearly propagating at shallow levels (e.g Grandin et al., 2010, Sigmundsson et al., 2014), it is often challenging to discriminate between processes causing deformation. For example, a surface uplift, which is very likely the response of a subsurface volume increase, can be caused by a magma flow replenishing a reservoir, but also by the degassing of volatile species contained in

a closed magma reservoir or even water vaporisation in a closed hydrothermal system (e.g. Dzurisin, 2007c).

In addition to possibly produce surface deformation signatures related to volume changes, magmatic processes are also likely to produce gravity change signatures, related to the addition or removal of mass from the reservoir. On the basis that magmatic processes have specific signatures of mass, density and volume changes, closely monitoring temporal variations in surface gravity should contribute to narrow down the list of possible mechanisms involved at a deforming volcano, and especially, prior to observing clear signs of upcoming eruption (e.g. Battaglia et al., 2008, Carbone et al., 2017). Indeed, a surface uplift without any observed gravity change suggests that the pressurized reservoir is a closed thermodynamic system, and a magma intrusion is therefore unlikely.

An interesting example to study is the gradual subsidence that has been on-going for at least 35 years at the Askja volcano in central Iceland. Despite extensive analysis of surface deformation, using analytical and finite-element modelling techniques, as well as the regular record of gravity changes, the causes of this uniquely long subsidence are still unclear: magma and/or hydrothermal fluids could be involved, with or without transport (e.g. de Zeeuw-van Dalfsen et al., 2012, 2013), and, because Askja is located on a segment of the mid-Atlantic ridge, regional tectonic processes could also participate (e.g. Pedersen et al., 2009). Due to insufficient coverage of gravity data, it has never been demonstrated that surface deformation and gravity variations come from the same source, and this missing information should be a key element in better understanding the causes of subsidence at Askja.

This thesis provides a fresh perspective on the puzzling Askja subsidence, by exploiting surface deformation records more deeply from a 15-year InSAR time-series, and improving the integration of gravity changes, by enlarging the network and refining methodologies.

In this first chapter, I provide background information on magmatic systems lying along mid-oceanic ridges, such as does the magmatic system of Askja. I then summarize the volume-mass-density signatures of common magmatic processes, before presenting

an overview of the Askja volcano case study, stating my aims and objectives, and introducing the thesis structure.

1.2 Magmatic systems and processes beneath mid-oceanic ridges

A mid-oceanic ridge (MOR) consists of a segmented oceanic mountain range, at the boundary of diverging plates, where new oceanic crust is being produced along a central rift valley. This accretion process concentrates ∼90% of the magmatic activity on Earth, into a succession of magma plumbing systems, which are discrete networks of interconnected magma pockets, having various sizes and shapes (e.g. Galland et al., 2018, van Wyk de Vries and van Wyk de Vries, 2018). Depending on the storage duration and local conditions of pressure and temperature, these magma pockets can have different proportions of melt and crystals, as well as dissolved and exsolved (bubbles) volatiles (e.g. Francis and Oppenheimer, 2004). When containing at least 55-65% of crystals, magma can be referred to as mush (e.g. Cashman et al., 2017, Sparks and Cashman, 2017).

1.2.1 Structure of magma plumbing systems beneath MORs

Magma plumbing systems commonly develop beneath fast (>9 cm/yr) to intermediate (4-9 cm/yr) spreading ridge (FIR) segments, such as beneath the East Pacific rise (e.g. Tan et al., 2016), but also beneath slow (<4 cm/yr) spreading ridge segments, when underlain by an upwelling of abnormally hot melt in the upper mantle, so-called mantle plume (e.g. Sigmundsson, 2006a, Wright et al., 2012). In such anomalous contexts, as observed in central Iceland (and therefore at Askja) where the mid-Atlantic ridge emerges, but also in Afar (Ethiopia) where the main Ethiopian rift emerges, the unusually thick crust (∼35-40 km) provides suitable pressure and temperature conditions to preserve molten rock (e.g. Darbyshire et al., 1998, Corti, 2009, van Wyk de Vries and van Wyk de Vries, 2018). However, especially due to the difference in tectonic settings, which controls the spreading rate and crustal thickness, these magma-dominated slow-

spreading ridge (MSR) segments produce magma plumbing systems that have a slightly different bulk structure than the ones produced by FIR segments (Figure 1.1).

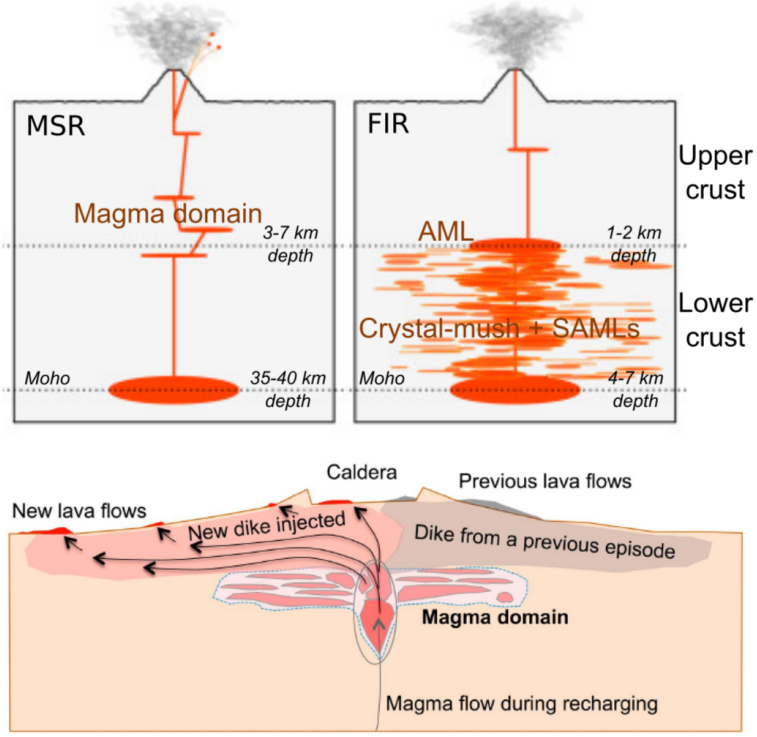

Figure 1.1: Top: Crustal structures beneath magma-dominated slow spreading oceanic ridges (MSR, left) and fast-to-intermediate oceanic ridges (FIR, right). AML: axial melt lens, SAMLs: sub-axial melt lenses (Not to scale - adapted from Galland et al. (2018)). Bottom: More detailed structure of a "magma domain", commonly encountered in the upper crust beneath MSR ridges (Not to scale - adopted from Sigmundsson (2016)). In Iceland, magma plumbing systems are referred to as volcanic systems, the main edifice centred above the magma domain is the "central volcano", and "fissure swarms" usually extend along the rift axis, as illustrated here, in the bottom figure (e.g. Sigmundsson, 2006a).

Even though each system is unique, MSR magma plumbing systems usually contain an isolated shallow reservoir, located in the upper crust at ∼3-7 km depth, and often referred to as a magma chamber, but likely to rather be a concentration of interconnected magma pockets (e.g. Sigmundsson, 2006a, Wright et al., 2012, Sigmundsson, 2016, Sigmundsson et al., 2018). These shallow "magma domains" (Sigmundsson, 2016), tend to act as main storage regions between the surface and deeper mushy reservoirs, having unclear structures, but usually located near the Moho, which defines the boundary between the upper mantle and the lower ductile crust (Figure 1.1).

On the other hand, FIR magma plumbing systems usually contain an axial melt lens,

lying at the lower-to-upper crustal boundary (∼1-2 km depth) and overlying a mush zone, which extends down to the Moho (Figure 1.1). This lower crystal-rich domain usually contains a series of intrusive horizontal sheets of magma, so-called sills, which are specifically called sub-axial lenses in these environments (e.g. Dunn et al., 2000, Marjanović et al., 2014, 2018, Galland et al., 2018).

1.2.2 Accretion and magma transport meachnisms beneath MORs

Accretion and magma transport mechanisms have been mainly studied beneath FIR segments, from offshore seismic imaging, but it is very likely that similar processes occur beneath onshore MSR segments, which have been studied mainly using surface deformation and seismicity (e.g. Wright et al., 2012, Sigmundsson, 2016).

Due to the correlation of pressure-temperature conditions with depth, magma is generally transported by porous flow, from the upper mantle to the ductile lower crust (e.g. Wright et al., 2012, Marjanović et al., 2014, Lissenberg et al., 2019, van Wyk de Vries and van Wyk de Vries, 2018), and by upward focussed channelisation, i.e. dyke intrusion or rifting episode, from the lower crust to the more brittle upper crust (e.g. Maclennan et al., 2001, Grandin et al., 2010, Lissenberg et al., 2019, Marjanović et al., 2014, van Wyk de Vries and van Wyk de Vries, 2018, Sigmundsson et al., 2014).

Porous flow is mostly controlled by (1) lithostatic load on porosity (and permeability), i.e. compaction, which increases crustal density with depth, and (2) buoyancy, which triggers the rise of less dense and more viscous materials, such as magma (Figure 1.2). But it can also be controlled by plate spreading decompression, which triggers the injection of pressurized magma towards the newly created low pressure zones. During porous flow motion, chemical reactions are likely to occur with other magma bodies and/or with surrounding mushy crustal materials (Figure 1.2).

Dyke intrusions into the upper crust can be triggered by chemical destabilisation resulting from such mixing. Alternatively, they can also be triggered by overpressurization of a magma pocket being replenished or heated up, and by shallower decompression due to plate-spreading or, more occasionally, extensive ice sheet mass removal (e.g. Sigmundsson et al., 2010). Once the intrusion has started, the dyke prop-

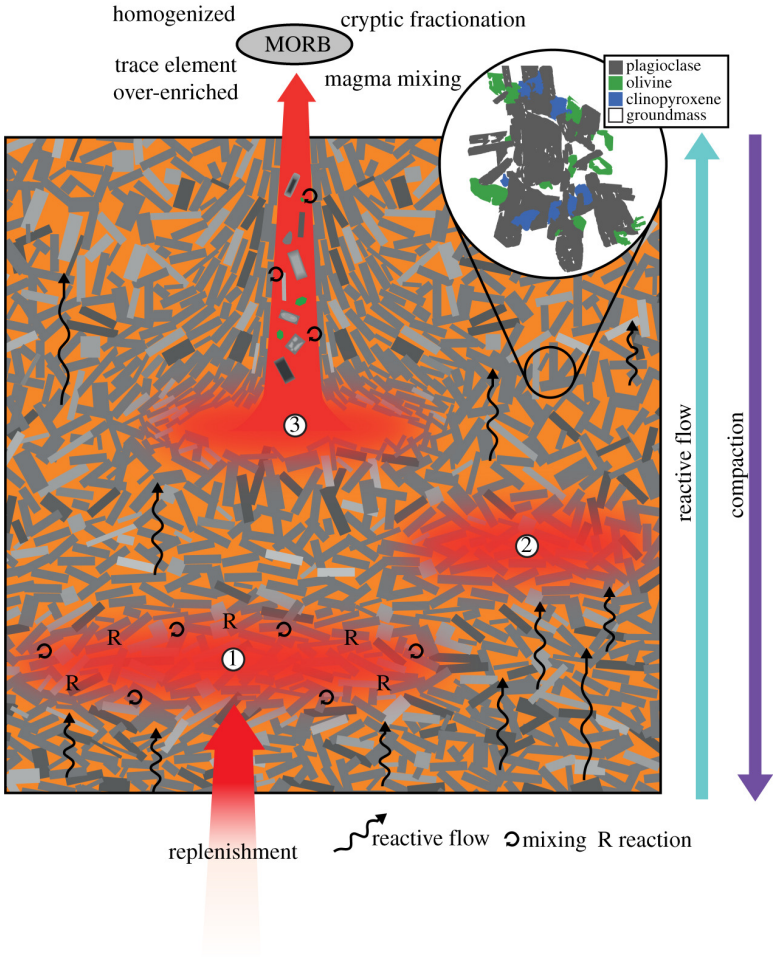

Figure 1.2: Sketch showing transport mechanisms that are occurring in the lower crust beneath FIR segments, and are very likely to occur, beneath MSR segments (Lissenberg et al., 2019, Wright et al., 2012). The melt lens (or sill) 1 is being replenished by primitive melt coming up from the upper mantle. The melt from the crystal-rich crust segregates to form sill 2. Mixing occurs at the boundaries of sills, by chemical reactions. Transport mechanisms in crystal-rich zones, are mainly porous flows, facilitated by compaction and buoyancy, whereas more focussed channelisation is likely to drain sill (3) to the upper-crust, to possibly feed eruptions.

agation, mainly controlled by the regional stress field and local topography, can either stop or lead to an eruption (e.g. Grandin et al., 2010, Sigmundsson et al., 2014). In the former case, a shallow magma pocket or a set of interconnected pockets could form where the state of neutral buoyancy is reached, and in MSR settings, this could contribute to the development of the "magma domain" (Figure 1.1 and e.g. Sparks and Cashman (2017)). In the second case, the onset of the eruption could drain even more magma from the plumbing system, leading to more mixing.

Even though magma intrusions tend to go upwards and/or laterally (e.g. Grandin

et al., 2010, Sigmundsson et al., 2014), downwards or "drain-back" movements have sometimes been proposed as mechanisms occurring to re-equilibrate pressure and buoyancy (e.g. de Zeeuw-van Dalfsen et al., 2005, Soriano et al., 2008).

1.3 Magmatic processes translated into mass, volume and density changes

Because magmatic processes are mainly controlled by pressure and buoyancy, as well as temperature (Section 1.2), they can be classified by specific signatures of mass, volume and density changes, which might be detected at the Earth's surface, from surface deformation and gravity changes. Monitoring these surface parameters can therefore help to better understand subsurface processes related to volcanic unrest.

Considering magma as a thermodynamic fluid, the ratio between the mass, M, of a magma body contained in a pressurized pocket, and the volume, V, of the pocket, provides the bulk density, ρ, of the system, at any time t (e.g. Sigmundsson, 2006b, Segall, 2010c):

$$\rho(t) = \frac{M(t)}{V(t)} \tag{1.1}$$

It is worth noting that, regarding pressure conditions, a set of interconnected pockets can be assimilated to a single larger pocket, and I use the term reservoir to define a thermodynamic system of any size, containing magma and being surrounded by crustal materials.

Taken independently, each of these parameters can be expressed as proportions of changes, k, from an initial state, described by M_0, V_0 and ρ_0:

$$M(t) = M_0 + \Delta M = M_0(1 + k_M) \tag{1.2}$$

$$V(t) = V_0 + \Delta V = V_0(1 + k_V) \tag{1.3}$$

$$\rho(\mathrm{t}) = \rho_0 + \Delta\rho = \rho_0(1 + \mathrm{k}_\rho) \tag{1.4}$$

By substituting equations 1.2-1.4 into Equation 1.1, the proportion of density change

can be expressed depending on the proportions of mass and volume changes:

$$k_\rho = \frac{k_M - k_V}{1 + k_V} \tag{1.5}$$

This relationship illustrates the link between the three parameters, which is mainly controlled by three factors (Figure 1.3 and e.g. Francis and Oppenheimer (2004)):

1. The type of system (open or closed reservoir), which initially depends on the degree of permeability of the surrounding host rock but can be controlled, in a latter stage, by internal pressure changes,

2. The degree of compressibility of the system, which depends on the proportion of exsolved volatiles in the melt, but also on the compressibility of the host rock,

3. The degree of internal pressure equilibrium, which can be destabilised by external pressure and temperature variations.

Based on these factors, magmatic processes occurring in closed systems should not generate any mass changes because by definitions, these systems cannot transfer any matter with the exterior; magmatic processes occurring under pressure equilibrium should not generate any volume changes; and no density change is expected when the system is incompressible (Figure 1.3).

As the Earth's surface is a free surface, a volume change at depth, resulting from a pressure variation, is likely to generate some ground deformation, which can therefore be used to constrain the location, depth and magnitude of the subsurface volume change (e.g. Sigmundsson, 2006b, Segall, 2010c). However, the relationship between the amount of volume change at depth and the surface deformation response highly depends on the reservoir geometry, crustal properties and compressibility. Following the same reasoning, a subsurface mass change can trigger a variation in the gravitational acceleration at the Earth's surface, and which can then be used to constrain the location, depth and magnitude of the subsurface mass change (e.g. Kearey et al., 2002, Battaglia et al., 2008). However, if the reservoir deforms simultaneously as experiencing a mass change, the gravity change response might be altered by the redistribution of density

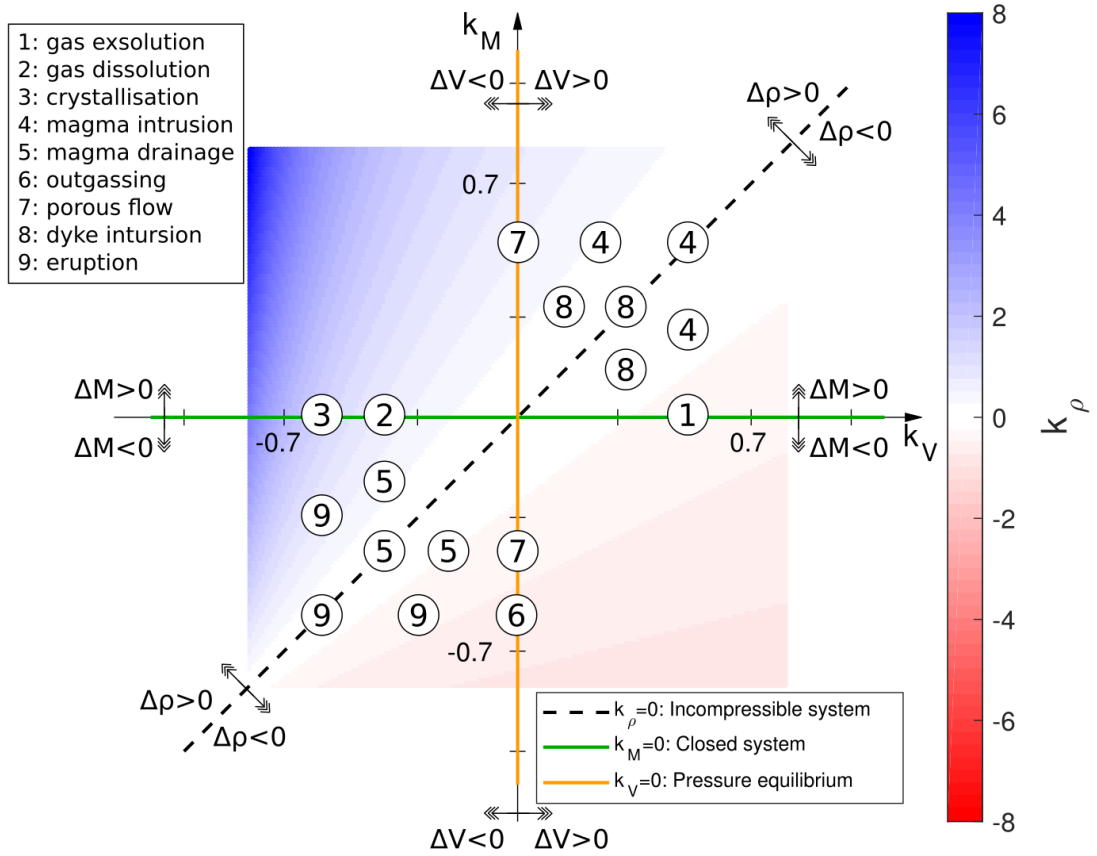

Figure 1.3: Relationship between mass, volume and density variations, quantified as proportions of changes from initial conditions (Equations 1.2-1.4). The dashed line highlights the scenario of incompressible system (no density change), the green horizontal axis highlights the scenario of closed system (no mass change) and the orange vertical axis highlights the scenarios of pressure equilibrium (no volume change). Circled numbers indicate the expected signs of mass-volume-density change signatures for common magmatic processes (See Sections 1.3.2-1.3.4 for more details). The placement of these circled numbers is not precise, but the zones where they have been placed matter. Number 7 appears in to regions as it is a transport process inducing mass loss to mass gain variations.

field in the crust, resulting from the reservoir volume change, and this effect depends on the geometry of the reservoir (e.g. Eggers, 1987, Walsh and Rice, 1979, Segall, 2010b).

After providing a clear definition of the compressibility of the system, I translate the most common magmatic processes, expected beneath MORs (Section 1.2), into signatures of mass-volume-density changes.

1.3.1 Compressibility of a magmatic reservoir embedded in the crust

By definition, any compressible material can undergo a volume change and an opposite density change, as a response to pressure, temperature and/or composition variations,

whereas an incompressible material requires the addition or removal of mass to undergo a volume change in same proportions, while density remains constant (Figure 1.3).

Due to the principle of mass conservation, any infinitesimal pressure and temperature variations (δP and δT) imposed on a closed system with constant composition, triggers infinitesimal volume and density responses (δV and $\delta \rho$), which depend on the coefficients of isothermal compressibility, β, and isobaric thermal expansion, ι:

$$\delta V = \Big[\beta V_0 \delta P\Big]_T + \Big[\iota V_0 \delta T\Big]_P \tag{1.6}$$

$$\delta \rho = \Big[\beta \rho_0 \delta P\Big]_T + \Big[-\iota \rho_0 \delta T\Big]_P \tag{1.7}$$

where β and ι, characterise together the degree of compressibility of the material, during pressure and temperature variations:

$$\beta = \frac{-1}{\mathrm{V}_0}\Big(\frac{\delta \mathrm{V}}{\delta \mathrm{P}}\Big)_{\mathrm{T}} = \frac{1}{\rho_0}\Big(\frac{\delta \rho}{\delta \mathrm{P}}\Big)_{\mathrm{T}} \tag{1.8}$$

$$\iota = \frac{1}{\mathrm{V}_0}\Big(\frac{\delta \mathrm{V}}{\delta \mathrm{T}}\Big)_{\mathrm{P}} = \frac{-1}{\rho_0}\Big(\frac{\delta \rho}{\delta \mathrm{T}}\Big)_{\mathrm{P}} \tag{1.9}$$

Magma is likely to have a certain level of compressibility, defined by β_m and ι_m, as it usually contains some proportion of exsolved volatiles. However, because magma reservoirs are embedded in the crust, they interact with the surrounding host rock, itself having a certain degree of compressibility, defined by β_c and ι_c. Consequently, whether a subsurface magma volume change can produce a surface deformation signature not only depends on the magma compressibility, but it rather depends on the ratio of the magma to host rock compressibilities (e.g Rivalta and Segall, 2008, Segall, 2010c).

This can be demonstrated assuming a reservoir with compressible magma, being replenished (or drained). The infinitesimal mass change, δM, caused by any δP and/or δT, can be expressed as the total differential of Equation 1.1 (e.g. Rivalta and Segall, 2008, Segall, 2010c):

$$\delta M = \rho_0 \delta V + V_0 \delta \rho \tag{1.10}$$

where $\rho_0 \delta V$ is the incompressible component with constant density, and $V_0 \delta \rho$ the compressible component with varying density.

At constant temperature, this density change initially depends on β_m (Equation 1.7):

$$\delta M = \rho_0 \delta V + V_0(\beta_m \rho_0 \delta P) \tag{1.11}$$

and the δP, which is generated by the replenishment (or drainage), then interacts with the host rock as the volume of the reservoir varies. Substituting δP as a function of δV from Equation 1.6 into Equation 1.11, provides a measure of the resulting density change between t_0, when the density equals ρ_0, and any time t, when the density equals $\rho(t)$:

$$\rho(\mathrm{t}) = \rho_0(1 + \frac{\beta_\mathrm{m}}{\beta_\mathrm{c}}) \tag{1.12}$$

Following the same reasoning, the density change obtained during replenishment (or drainage) at constant pressure but with a temperature variation is:

$$\rho(t) = \rho_0(1 + \frac{\iota_m}{\iota_c}) \tag{1.13}$$

A compressible magma body can therefore be treated as incompressible when β_c and ι_c largely exceed β_m and ι_m. However, when ignoring a non-negligible degree of compressibility, the mass change resulting for a replenishment (or drainage) will be underestimated by a factor of $(1 + \beta_m/\beta_c)$ at constant temperature and by a factor of $(1 + \iota_m/\iota_c)$ at constant pressure (e.g. Rivalta and Segall, 2008, Segall, 2010c). Based on this overall definition, I use the term "compressibility of the system" to refer to both the ratios of magma to host rock isothermal compressibilities and isobaric thermal expansions.

1.3.2 Magmatic processes in a closed system, initially in equilibrium

Some reservoirs contained in a magma plumbing system (Figures 1.1 and 1.2) can be analogous to closed systems when the surrounding host rock has a degree of permeability that is low enough to prevent any addition or removal of mass. When in place, these systems should initially be under pressure and buoyancy equilibrium, and temperature variations can cause pressure changes, which induce some degree of volume changes

depending on the compressibility of the system (Section 1.3.1).

When subjected to a temperature increase, the vapor pressure of the volatiles, dissolved in the melt, increases because their solubility decreases (e.g. Francis and Oppenheimer, 2004, Wallace et al., 2015, Burgisser and Degruyter, 2015). When the vapor pressure of a given volatile species equals the pressure of the host rock acting on the reservoir, so-called lithostatic pressure, saturation is reached and bubbles start nucleating, leading to the formation of bubbles in the melt. This degassing process, often referred to as ***(first boiling) gas exsolution***, or vesiculation, leads to increasing the volume and decreasing the density of the overall pressurized system (Figure 1.3).

Conversely, when a closed magma reservoir is subjected to a temperature decrease, the volume of the system decreases while its density increases, due to ***gas dissolution***, (so-called devesiculation), as volatiles become more and more soluble (Figure 1.3 and e.g. Francis and Oppenheimer (2004), Wallace et al. (2015), Burgisser and Degruyter (2015)).

If the temperature decrease persists, ***crystallisation*** can start, leading to further volume decrease (or thermal contraction) and density increase (Figure 1.3). However, despite the temperature decrease, a ***(second boiling) gas exsolution*** can ensue, as the crystal-melt separation process increases the saturation of the volatiles dissolved in the melt (e.g. Francis and Oppenheimer, 2004, Wallace et al., 2015, Burgisser and Degruyter, 2015). Consequently, the volume of a cooling gas-rich and crystallising magma reservoir is likely to increase, when embedded in a compressible system, leading to a density decrease (Section 1.3.2); but if the system is incompressible, pressure will increase without any volume nor density change.

During any type of gas exsolution, a critical state of rock wall failure can be reached when the sum of the vapor pressures of the exsolved volatiles largely exceeds the lithostatic pressure, leading to the sudden opening of the system (e.g. Francis and Oppenheimer, 2004, Wallace et al., 2015, Burgisser and Degruyter, 2015).

1.3.3 Magmatic processes in a open system, initially in equilibrium

An open magma reservoir in equilibrium, lies at neutral buoyancy and is surrounded by a host material, permeable enough to allow addition/removal of material to/from the system (Figures 1.1 and 1.2). Unlike closed systems, open systems are therefore subjected to mass changes, but the surface gravity change signature of a deforming reservoir can be contaminated with the effect of density field variations as the crust is being displaced (e.g. Eggers, 1987, Walsh and Rice, 1979, Segall, 2010b).

When new magma mixes within an existing open reservoir (Section 1.2.2), more mass is added to the system and volume increases simultaneously. This process, often referred to as a ***magma intrusion***, can lead to a density change, depending on the degree of compressibility of the system (Figure 1.3 and Section 1.3.1). Similarly as for long-lasting gas exsolution undergoing within gas-rich closed systems (Section 1.3.2), the pressure of an open system being replenished can exceed the lithostatic pressure, up to a critical failure stage.

Contrary to magma instrusions, a ***magma drainage*** consists of partially or fully emptying an open system, leading to a mass and volume decrease, and possibly, a density change depending on the compressibility of the sytem (Figure 1.3 and Section 1.3.1).

An open reservoir can also undergo temperature changes, which can initiate gas exsolution and crystallisation processes, such as in closed systems (Section 1.3.2). However, because the system is open, the exsolved volatiles can freely escape from the melt (e.g. Francis and Oppenheimer, 2004, Wallace et al., 2015, Burgisser and Degruyter, 2015). This process, called ***outgassing***, generates a mass loss but it is unlikely to produce a volume change as the volume increase caused by gas exsolution should be compensated by the volume decrease from outgassing. Consequently, the density of the reservoir should decrease (Figure 1.3). If the reservoir is vertically elongated, outgassing can trigger a convection process where the gas-rich buoyant portions of the magma rise up, while the denser degassed portions sink, leading to density homogenisation (e.g. Shinohara, 2008, Bagnardi et al., 2014). These systems sometimes emerge at the surface as lava lakes (e.g. Shinohara, 2008, Bagnardi et al., 2014), but when buried, the volatiles can either be trapped at shallower levels or reach the surface as hot springs

and fumaroles, depending on the permeability of the crust and nature of the released volatile species (e.g. Francis and Oppenheimer, 2004).

1.3.4 Magmatic processes during transport

Even though not analogous to a static open or closed system, a moving magma body generates a surface deformation response to pressure changes, depending on the crustal properties, which usually vary with depth. Indeed, ***porous flows*** (Section 1.2.2) are unlikely to produce a deformation signal, because the induced pressure variations accompanying the movement should be accommodated within the viscous and mushy lower crust. On the other hand, ***dyke intrusions*** (Section 1.2.2), which can follow a sudden decompression, e.g. ensuing gas exsolution or magma intrusion (Sections 1.3.2 and 1.3.3), are more likely to generate some ground deformation while the dyke makes its way through the brittle upper crust (e.g. Grandin et al., 2010, Sigmundsson et al., 2014).

Both types of magma transport should generate a traceable mass loss to mass gain variation when the propagation is lateral and over at least a few kilometers. However, in practice, this implies that the discrete gravity measurements are recorded at the right times, and along the right path, and that the possible gravity response of crustal density field variations is removed (e.g. Eggers, 1987, Walsh and Rice, 1979, Segall, 2010b). At the end of propagation, a porous flow is likely to become a magma intrusion, whereas a dyke intrusion can either become a magma intrusion, or the transporting process can lead to an ***eruption***, which usually has a clear signature of deflation and mass loss, as a subsequent amount of material leaves the crust (e.g. Dzurisin, 2007d).

Finally, the processes of "magma filling void spaces" and "drain-back movements" sometimes mentioned in the literature to explain a measured gravity change with little or no observed deformation (Section 1.2.2 and e.g. Johnson et al. (2010), Vajda et al. (2012)) are likely due to porous flows, triggered by e.g. tectonic processes such as plate spreading or earthquakes, inducing high-to-low pressure magma movements.

It is worth noting that even though all these magmatic processes can be classified based on their expected mass-volume-density signatures, complex responses of surface

deformation and gravity changes are usually generated, as magma plumbing systems can be analogous to a set of open and closed reservoirs, between which magma propagates (Section 1.3). Moreover, external processes of hydrothermal or tectonic origin can further complicate the interpretation, by contaminating the magma-related gravity and deformation signals (e.g. Hautmann et al., 2010), and alternatively, an assumed volcanic unrest might not have any direct magmatic origin (e.g. Gottsmann et al., 2006). Despite these complexities, simple analytical models are widely used to predict the gravity and deformation responses of magmatic processes, and results have been especially successful when one process dominates among the others (e.g. Grandin et al., 2010, Bagnardi et al., 2014, Sigmundsson et al., 2014).

1.4 Analytical models to constrain magmatic processes

Analytical equations have been derived to calculate the observed surface displacement or gravity change that would be produced by a magmatic reservoir, given e.g. its location, depth and magnitude of volume or mass change, and assuming simple reservoir geometries as well as some basic crustal and magmatic properties (e.g. Sigmundsson, 2006b, Lisowski, 2007, Segall, 2010c, Battaglia et al., 2008; and references therein). Based on these non-linear forward problems, statistical approaches, such as simulated annealing or the Bayesian inversion (e.g. Tarantola, 2005), have been used to invert for the most probable set of parameters that would best describe the observations, assuming a reservoir geometry. Even though a model fitting the data does not necessarily represent the reality, there is 95% chance that they reproduce well the distribution of pressure and mass changes at depth, and results can be compared with other disciplines, such as seismic tomography, which can indicate, to some extent, the position of large magma bodies in the subsurface. Once satisfied with the deformation and gravity models, hypotheses on the most probable on-going processes can be suggested based on Figure 1.3.

1.4.1 Conceptual representation of the Earth's crust

Analytical models commonly consider the Earth's crust as a homogeneous elastic half-space medium (e.g. Lisowski, 2007, Segall, 2010c). In other words, beneath the bounding Earth's surface, which is not subjected to any stress (free-surface), the crust is a solid, extending to infinity in all directions (half-space), having uniform composition and properties throughout (homogeneous), and its mechanical properties are constant in all directions (elastic). The crust elasticity (and isotropy) can therefore be defined by several moduli, which are linked to the isothermal compressibility coefficient (β_c, Section 1.3.1):

$$E = 2\mu(1+y) = 3K(1-2y) = \frac{3(1-2y)}{2\beta_c} \tag{1.14}$$

where E is the Young's modulus, describing the material's response to linear stress, μ is the shear modulus, describing the material's response to shear stress, K is the bulk modulus, which is a measure of resistance to compression, and y is the Poisson's ratio, describing the lateral expansion versus longitudinal contraction of a material under stress (Table 1.1). The common symbol for the Poisson's ratio is ν, but in this thesis, this symbol is used for the degree of freedom.

	Somewhat fractured to Intact crust	Typical value
μ	10-30 $\times 10^{10}$ Pa	20 $\times 10^{10}$
y	0.15-0.3	0.25

Table 1.1: Typical shear modulus (μ) and Poisson's ratio (y) ranges and values used to describe the elasticity of the oceanic crust (e.g. Rivalta and Segall, 2008, Lisowski, 2007). From these two moduli, the rest of the other moduli can be derived (Equation 1.14).

Based on this overall definition of the crust, a pressure change applied anywhere deforms the material linearly, and this very simplistic conceptual model usually approximates well the conditions of deformation undergone in the shallow brittle crust.

To reproduce the effect of any embedded deforming magma body, the magma is usually assumed to be an incompressible fluid. This suggests that the crust is more compliant than the magma (Section 1.3.1), and it also implies that the reservoir can only deform when mass is added to or removed from the system (Figure 1.3). In these conditions, the surface deformation and gravity change signatures vary depending on

the reservoir geometry, and analytical solutions have been derived for e.g. spheroids, sills and dykes, but I only present here the simplest and most widely used model (e.g. Sigmundsson, 2006b, Lisowski, 2007, Battaglia et al., 2008, Segall, 2010c)

1.4.2 The "Mogi" reservoir or point pressure source model

The simplest and routinely used magma reservoir model is the so-called "Mogi" model (Mogi, 1958, McTigue, 1987), which assumes an incompressible magma stored within a spherical reservoir embedded in a homogeneous elastic half-space medium (Section 1.4.1), and of which the uniform internal pressure can be concentrated into a central point (Figure 1.4).

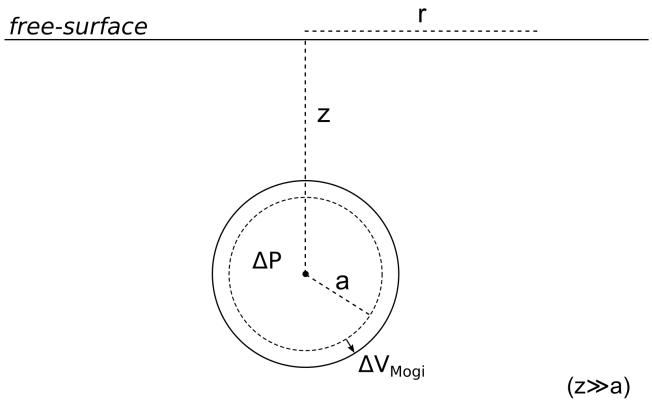

Figure 1.4: Geometry of the conceptual Mogi model, where a pressurized spherical source of initial radius, a, centered at the depth, z, and embedded in an elastic-half-space medium, undergoes a volume change, ΔV (positive in this example), induced by an mass change, as the system is incompressible (Figure 1.3 and Section 1.3.1). The reservoir's pressure is isotropic and its depth is much larger than its radius. See Section 1.4.2 for more details on the conceptual model and related analytical solutions.

When a pressurized magma reservoir, which can be a set of interconnected pockets (Section 1.2), can be approximated by the Mogi model, its volume change, ΔV, which results from the addition or removal of mass from the system, translates into horizontal and vertical displacements, D_h and D_v, at any site on the free-surface, as follows:

$$D_h = \frac{(1-y)\Delta V}{\pi} \frac{r}{(z^2+r^2)^{3/2}} \tag{1.15}$$

$$D_v = \frac{(1-y)\Delta V}{\pi} \frac{z}{(z^2+r^2)^{3/2}} \tag{1.16}$$

where z is the depth to the centre of the Mogi reservoir, r is the horizontal distance from the top of the source to the site, and y is usually assumed to equal 0.25, implying that the crust is compressible to some degree (Table 1.1 and Section 1.3.1). Figure 1.5 simulates gravity changes and surface deformation expected from a magma intrusion, depending on z and r.

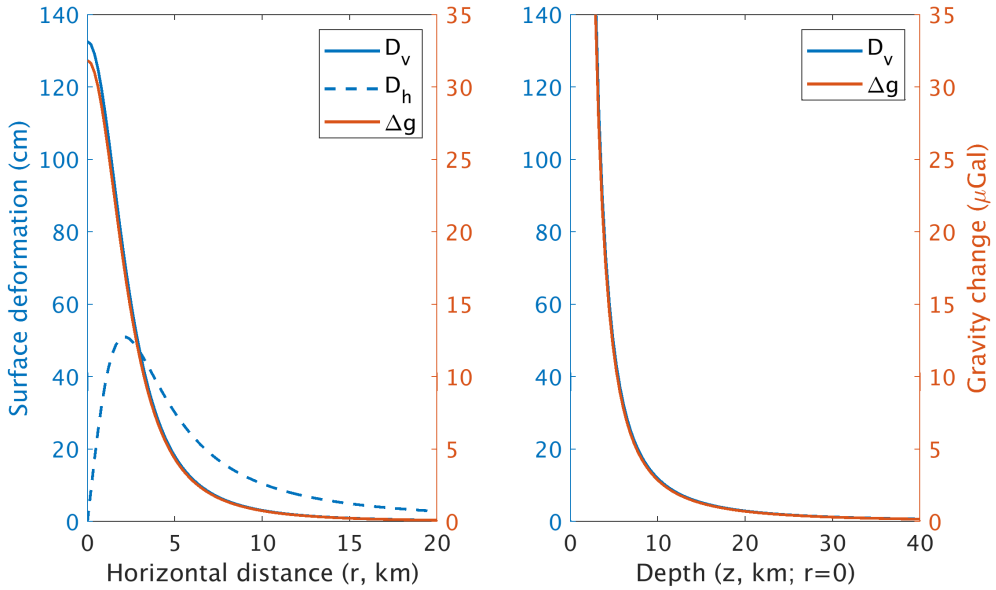

Figure 1.5: Vertical (solid blue) and horizontal (dashed blue) deformation signal, as well as gravity change signature (solid orange), produced by a Mogi reservoir undergoing a volume increase of 0.05 km^3, which is the order of magnitude expected (Sigmundsson (2006b) and is equivalent to 20,000 times an Olympic swimming pool). Left: Signals varying with horizontal distance (r, Figure 1.4) when the reservoir is at 3 km depth, i.e. within the "magma domain" (Figure 1.1). Right: Signals expected at the top of the reservoir (r=0), depending on depth, which ranges from the surface to the Moho (Figure 1.1). This example highlights the order of magnitudes of expected surface deformation and gravity changes induced by a Mogi reservoir (1 μGal = 10^{-8} m s^{-2}).

Because ΔV is the integral of radial displacements at the wall of the reservoir, from initial conditions (Figure 1.4), it correlates with the inner pressure change, ΔP:

$$\Delta V = \frac{\pi a^3 \Delta P}{\mu} \tag{1.17}$$

where μ is the shear modulus of the host rock (Table 1.1). This relationship highlights the non-uniqueness of the model where ΔP cannot be separated from the radius: a small ΔP in a large reservoir produces the same surface deformation as a large ΔP in

a small reservoir. For this reason, the Mogi model applies only when $z \gg a$ (Figure 1.4 and e.g. Sigmundsson (2006b), Lisowski (2007), Segall (2010c)).

As the pressure change linearly propagates through the crust (Section 1.4.1), ΔV also correlates with the volume of surface deformation, $[\Delta V]_{\text{surface}}$, which is the integral of surface vertical displacements:

$$[\Delta V]_{\text{surface}} = 2(1-y)\Delta V \tag{1.18}$$

In the presence of an incompressible crust ($y = 0.5$), $[\Delta V]_{surface}$ equals ΔV at the Mogi reservoir, but considering a usual y of 0.25, $[\Delta V]_{surface}$ is 1.5 times greater than ΔV, due to the crust dilation response (e.g. Sigmundsson, 2006b, Segall, 2010c; and references therein). It is worth noting that Equation 1.18 relates to a Mogi geometry only.

Based on the Newton's law, the mass change, ΔM, caused by the incompressible magma, replenishing the deforming Mogi reservoir, equals $\rho_0 \Delta V$ (Section 1.3.1), with ΔV being radial. The spatial dependence of ΔM with the gravity change recorded at the surface, Δg, is therefore the same as the one between ΔV and D_h (e.g. Battaglia et al., 2008, Lisowski, 2007, Segall, 2010b):

$$\Delta g - \Delta g_{\text{elev}} = \frac{G\Delta M z}{(z^2+r^2)^{3/2}} = \frac{G\rho_0 \Delta V z}{(z^2+r^2)^{3/2}} \tag{1.19}$$

where G is the universal gravitational constant, ρ_0 is the magma density in the spherical reservoir, and Δg_{elev}, is the so-called free-air effect, i.e the gravity change induced by the deforming surface, which varies the distance to the Earth's gravitational centre. This analytical solution is also non-unique as it also depends on the inseparable radius and pressure change (Equation 1.17). Moreover, it is worth noting that, in this special case of spherical geometry, the variations in crustal density field induced by the deforming reservoir acting on the surrounding crustal material cancel, whereas a non-negligible effect becomes involved for other geometries (e.g. Eggers, 1987, Walsh and Rice, 1979, Segall, 2010b).

Only when the geometry of the reservoir and compressibility of the system approx-

imate the bulk magmatic and crustal properties well, the constant magma density is proportional to the ratio of gravity change, corrected for the free-air effects, to vertical deformation (Equations 1.16 and 1.20):

$$\rho_0 = \frac{\Delta g - \Delta g_{\text{elev}}}{D_v} \frac{(1-y)}{\pi G} \tag{1.20}$$

However, if the magma has a non-negligible degree of compressibility, ρ_0 cannot be constrained, and Δg is underestimated (Section 1.3.1).

1.5 Case study: Askja volcano, central Iceland

As briefly mentioned in Section 1.1, the physical processes responsible for the subsidence at Askja are still unclear. Being aware of the processes likely to occur in such magma-dominated slow-spreading ridge context (Section 1.2), and knowing how their mass-volume-density signatures (Section 1.3) can relate to surface deformation and gravity changes (Section 1.4), I aim to exploit more deeply the potential of integrating these two types of measurable parameters at Askja. Here, I present an overview of the Askja case study.

The Askja volcanic system, located in central Iceland, to the North of the Vatnajökull icecap, lies in a segment of the mid-Atlantic ridge, near the centre of the Icelandic mantle plume (e.g. Sigmundsson, 2006a). It is the longest volcanic system on the island, with its ∼190-km-long set of fissure swarms, extending from Vatnajökull up to the North coast of Iceland (Figure 1.6). Its central volcano is composed of at least three nested calderas, of which the largest one, called Askja and measuring ∼8 km in diameter, has given its name to both the central volcano and the overall volcanic system (Figure 1.1).

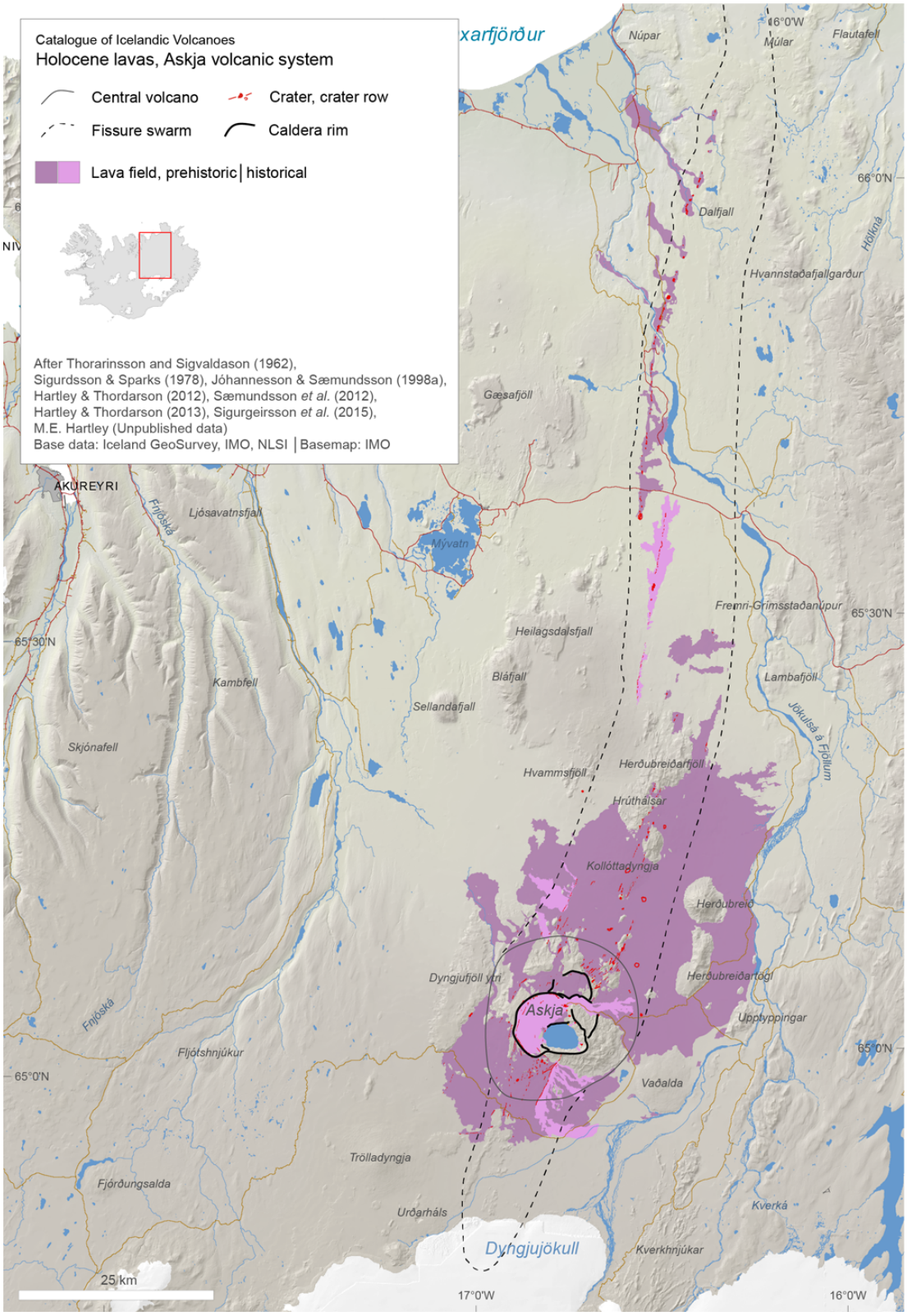

Figure 1.6: Map of the Askja volcanic system, located to the North of the Vatnajökull icecap (Dyngjujökull is an outlet glacier of Vatnajökull). The central volcano (thin plain line) is composed of a least three nested calderas (thick black lines), and the set of fissure swarms (dashed line) extends over ∼190 km. The eruptive products resulting from effusive activity are classified into prehistorical (>1,000 years, purple) and historical (<1,000 years, pink) lavas (Thordarson and Hartley, 2016).

This largest Askja caldera as well as the northernmost ∼4-km-across caldera, named Kollur, were both created more than 10,000 years ago, during large silicic eruptions (e.g. Sigvaldason, 2002, Thordarson and Hartley, 2016; and references therein). On the other hand, the youngest caldera, measuring ∼5 km in diameter and named after its hosted >260-m-deep Öskjuvatn lake, was formed after the most recent subplininan silicic eruption, which occurred in 1875 (e.g. Hartley and Thordarson, 2012). In addition to these large silicic eruptive events, some minor basaltic eruptions occurred in the last 10,000 years along the fissure swarms, and the most recent was in 1961, on the north-east flank of the Askja caldera (Figure 1.6).

Shortly after this last event, the Askja volcano deformation was monitored using levelling, and more extensive geodetic measurements were then progressively implemented from GPS and InSAR, but also from temporal gravity, as a subsidence had been detected in the main Askja caldera. Currently, the subsurface processes responsible for this still on-going subsidence remain unclear, but a recent microseismic tomography, brought new information on the bulk morphology of the magma plumbing system of Askja. Here, I summarize the results from all these previous studies.

1.5.1 Surface deformation at Askja

Tryggvason (1989) presented the first optical tilt and levelling results, which had been planned initially to monitor the post-eruptive behaviour of the 1961 lava flows in the north-east of the Askja caldera (Table 1.2). The study revealed a subsidence pattern likely to affect the entire caldera, and unlikely to be linked to the 1875 explosive event, neither to the 1961 effusive event. Sturkell et al. (2006) then highlighted the exponentially decaying long-term evolution of this subsidence, characterized by a relaxation time of ∼39 years from 1973 to 2003 (Table 1.2). This overall pattern is still on-going, and the updated relaxation time is now ∼42 years (Figure 1.7A).

In parallel, GPS (1987-2014) and InSAR (1992-2010) studies highlighted the approximately concentric shape of the subsidence, and confirmed its center in the middle of the Askja caldera (Figure 1.7 and Table 1.2). Even though the circular morphology of the caldera itself does not clearly show that the volcano is affected by the diverg-

Period	Technique	Modelling method, Best-fit geometry	Best-fit parameters	Ref.
1966-1987	Optical tilt, Levelling	Forward modelling 1 Mogi reservoir	16.83-16.75°W 65.07-65.04°N	[1]
1988-1991	Optical tilt, Levelling	Forward modelling 1 Mogi reservoir	16.77°W,65.05°N Depth: 3 km	[2]
1992-1993	Static GPS	Forward modelling 1 Mogi reservoir	Rift: 2.5 cm yr^{-1} towards N100°E Fixed location and depth from [2]	[3]
1993-1998	Optical tilt, Levelling, Static GPS	Forward modelling, 1 Mogi source	16.78°W, 65.04°N Depth: 3 km ΔV = -0.0017 km^3 yr^{-1}	[4]
1992-2000	InSAR	Simulated annealing, Ellipsoidal reservoir, Elastic half-space	16.771°W, 65.045°N (fixed) Depth: 3.5 km ΔV = -0.0021 km^3 yr^{-1}	[5]
1993-2003	Static GPS, Levelling	Forward modelling*, 2 Mogi reservoirs	16.780°W, 65.045°N Depths: 3 and 16 km $[\Delta V]_{3km}$ = -0.0021 km^3 yr^{-1} $[\Delta V]_{16km}$ = -0.0137 km^3 yr^{-1}	[6]
2000-2009	InSAR	Bayesian inversion**, 1 Mogi reservoir	16.778°W, 65.050°N Depth: 3.5 km ΔV = -0.0014 km^3 yr^{-1}	[7]
2003-2010	InSAR	No modelling	Comparison of the subsidence rate with the gravity change rate	[8]
2008-2014	Static GPS	Simulated annealing, 1 Mogi reservoir	Fixed location and depth from [7] ΔV = -0.0010 km^3 yr^{-1}	[9]

Table 1.2: Summary of previous geodetic studies performed at Askja. (*) Plate spreading incorporated in the modelling; (**) additional used of finite-element models to demonstrate the very likely impact of plate spreading on the subsidence; [1]: Tryggvason (1989); [2]: Rymer and Tryggvason (1993); [3]: Camitz et al. (1995); [4]: Sturkell and Sigmundsson (2000); [5]: Pagli et al. (2006); [6]: Sturkell et al. (2006); [7]: de Zeeuw-van Dalfsen et al. (2012); [8]: de Zeeuw-van Dalfsen et al. (2013); [9]: Drouin et al. (2017).

ing plates, such as does e.g. the elongated Erta Ale volcano in Afar, Pedersen et al. (2009) highlighted some regional subsidence pattern, approximately aligned with the plate spreading axis.

Using levelling and/or GPS and/or InSAR data, forward and subsequent inversion models provided the most probable location, depth and magnitude of volume decrease that could explain the subsidence (Table 1.2). Assuming a homogeneous elastic half-space medium (Section 1.4.1), all these models suggest that the subsidence can mainly be explained by a deflating isotropic pressurized reservoir, spherical (Mogi) or ellipsoidal, located at ∼3-3.5 km depth, in the centre of the Askja caldera (Figure 1.7B). The constrained volume change rates have decreased from -2 km^3 yr^{-1}, before 2000, to -1 km^3 yr^{-1}, more recently (Table 1.2). Even though an additional deeper reservoir

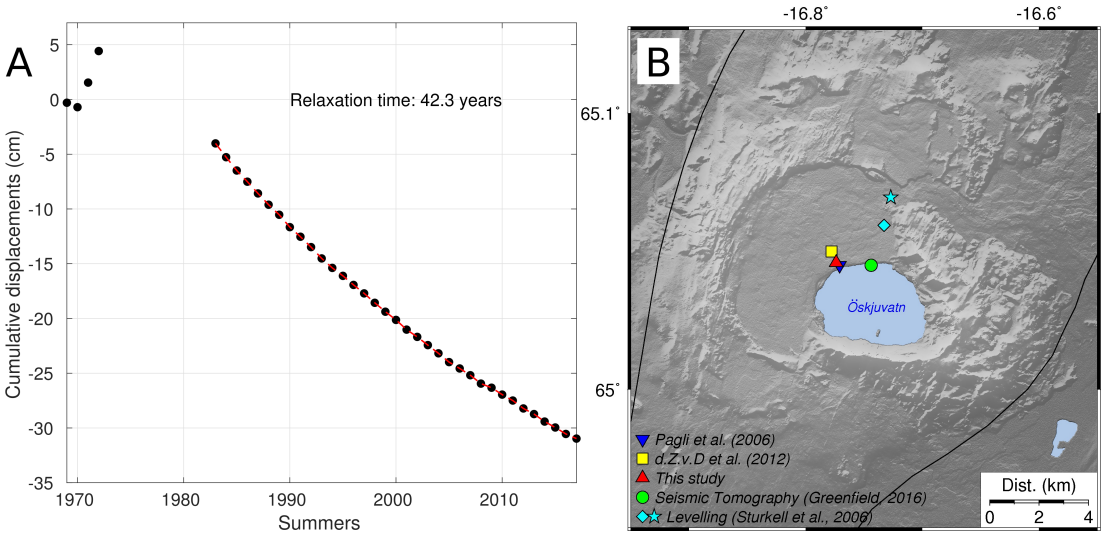

Figure 1.7: A: Cumulative vertical displacements recorded using precise levelling, at the A406 levelling site (cyan diamond in B) relative to the A429 station (cyan star in B). Erik Sturkell, from the University of Gothenburg (Sweden) provided the data (Sturkell et al., 2006, de Zeeuw-van Dalfsen et al., 2013). B: Map of the Askja volcano, locating the levelling stations used in A, the centre of the spheroid reservoirs constrained in previous studies from surface deformation data (yellow square and blue triangle, Table 1.2) versus the one I constrained in this thesis (red triangle), and the approximate location of the primary melt storage reservoir (green circle), recently imaged from seismic tomography (Section 1.5.4).

was constrained by Sturkell et al. (2006) to account for some contracting horizontal deformation, outside the caldera, there is a lot of uncertainty is this deeper source, especially because the horizontal deformation pattern relied on the 2-source model itself. From now on, I refer to the 3-km-deep reservoir as the "geodetic reservoir".

1.5.2 Temporal gravity changes at Askja

In parallel with deformation records, regular gravity surveys have been carried out within the Askja caldera, from 1988 to 2010, by Hazel Rymer *et al.* (Open University, UK). The first results were published by Rymer and Tryggvason (1993), but de Zeeuw-van Dalfsen et al. (2005) presented a revised study of the gravity change evolution from 1988 to 2003, with results averaged over three main zones, called the "centre", "northern" and "south-eastern" parts of the Askja caldera. The time-series were then extended to 2010 by Rymer et al. (2010) and de Zeeuw-van Dalfsen et al. (2013) (Figure 1.8A).

Overall, a gradual gravity decrease of ∼140 μGal was observed from 1988 to 2007, in the same central area of maximum subsidence, and it was followed by an increase

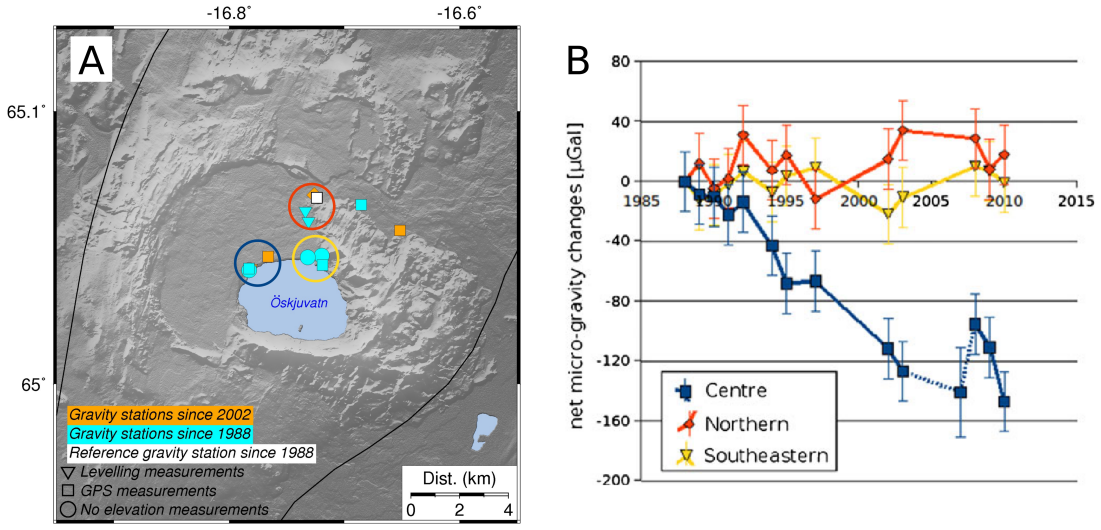

Figure 1.8: A: Map of the gravity network within the Askja caldera, from 1988 to 2010, highlighting the extension performed in 2002 (symbol colors), mentioning the method of elevation measurement, if any (symbol shapes), and delineating the centre, northern and south-eastern groups of gravity stations (blue, red and yellow circles) (de Zeeuw-van Dalfsen, 2004, Rymer et al., 2010). B: Time-series of the gravity changes, from 1988 to 2010, after free-air correction, at each of the three gravity groups, and relative to the station shown on the map with the white square (de Zeeuw-van Dalfsen et al., 2013).

of ∼60 μGal, from 2007 to 2009 (Figure 1.8B). Because the data were reduced as much as possible for unwanted signals, including the free-air effect (Section 1.4.2), these variations were assumed to be the response of mass changes occurring in a buried pressurized reservoir, but due to the lack of spatial coverage, inversion modelling could not be performed. It was rather assumed that these mass changes were occurring at the geodetic reservoir (Rymer and Tryggvason, 1993, de Zeeuw-van Dalfsen et al., 2005, 2013).

It is worth noting that when looking at Figure 1.8B, the centre gravity increase, which did not perturb the subsidence, could also be just noise. Moreover, because standard LaCoste & Romberg gravimeters (i.e. not upgraded with any automated recording systems, neither electronic tilt sensors) were used to record all these gravity measurements, the error budget associated to each measurement may have been underestimated. Indeed, despite the high-precision of these instruments, the error budget associated to magma-related micro-scale gravity changes (Figure 1.5), not only depends on the extreme meticulousness of the operator but also on the unknown level of noise in the area. The "extreme" meticulousness, because LaCoste & Romberg gravimeters are analog in-

struments, which need to be levelled using spirit bubble levels and taking a reading consists of turning a dial to visually fit a beam to a reading line (LaCoste & Romberg, 2004); and the "unknown" noise, because, without any upgrade, these standard instruments are only able to record readings one by one, preventing statistically estimating the noise (Chapter 4). To optimise the results, two gravimeters were usually used simultaneously at Askja, and measurements were usually repeated three times (de Zeeuw-van Dalfsen, 2004), but this procedure still does not allow statistically estimating the noise.

1.5.3 Previous interpretations for the Askja subsidence

Because the onset of the Askja subsidence (Figure 1.7A) coincided with the start of the last fissure eruption at the Krafla volcanic system (1975-1984, e.g. Björnsson et al. (1977)), which is also located along the mid-Atlantic ridge, at ∼70 km North of Askja, Tryggvason (1989) suggested some pressure links between the two volcanic systems to explain the Askja subsidence: magma could have been drained from Askja to Krafla by travelling along the Mid-Atlantic ridge. However, the end of the Krafla fissure eruption did not affect the subsidence.

Based on the correlation in location between the negative peak values of deformation and gravity changes (Sections 1.5.1 and 1.5.2), Rymer and Tryggvason (1993) suggested that the Askja subsidence could be the response of some continuous magma drainage from the geodetic reservoir (Figure 1.3). But because no deformation signal typical for vertically upward nor lateral dyke intrusion was detected, they proposed a "drain-back" magma movement to deeper levels. While supporting this hypothesis as a likely cause, Sturkell and Sigmundsson (2000) suggested that the main process could rather be some magma crystallization at the geodetic reservoir (Figure 1.3).

These two main ideas were supported as possible causes of subsidence by the subsequent studies (Table 1.2 and de Zeeuw-van Dalfsen et al. (2005)), which also suggested that the plate spreading could have a non-negligible impact. This additional hypothesis was first proposed by Sturkell et al. (2006), and then highly supported by Pedersen et al. (2009) and de Zeeuw-van Dalfsen et al. (2012), who both used finite element modelling to implement a 2-layer crust model with a visco-elastic lower crust.

Finally, the "magma intrusion filling void spaces", initially proposed by Rymer et al. (2010) to explain the gravity increase recorded over 2007-2009 (Figure 1.8B), was revisited by de Zeeuw-van Dalfsen et al. (2013), who suggested a more likely magma intrusion at the geodetic reservoir and/or some condensation processes within a shallower hydrothermal system.

1.5.4 Local earthquake tomography at Askja

Some recent microseismicity analysis provided a tomography of the magma plumbing system, beneath the Askja central volcano (Mitchell et al., 2013, Greenfield et al., 2016, Greenfield, 2016). These studies highlighted a low-velocity zone, which can be approximated as a 3-km thick cylinder of $\sim$100 km^3, located at the upper-to-lower crust transition (6-10 km depth below the surface), and likely to have been the primary mushy-magma reservoir for the large caldera-forming eruptions (Figure 1.9).

As shown on Figure 1.7B, the centre of this large body is slightly offset from the centre of the geodetic reservoir constrained in previous studies, and of which the size is unlikely to exceed 15 km^3, as it could not be imaged (Figure 1.9). However, beyond the resolution of the tomography, some velocity attenuation still suggest the presence of a magma reservoir in this area (Personal communication, T. Greenfield, 2018).

Additionally, the tomography highlighted a high-velocity zone, at $\sim$3 km depth, but located on a ring, along the eastern side of the Askja caldera and Öskjuvatn lake (Figure 1.9). Greenfield et al. (2016) suggested that this area, likely to be made of intrusive gabbros, hosts an active hydrothermal system, maintained by some residual local heat and producing some seismicity, possibly due to high pore fluid pressure. However, as offset from the centre of the Askja caldera, Greenfield et al. (2016) do not think that the physical processes occurring in this hydrothermal system are related to the Askja subsidence, but they rather suggest that the hydrothermal system could be a cooling source for the geodetic reservoir.

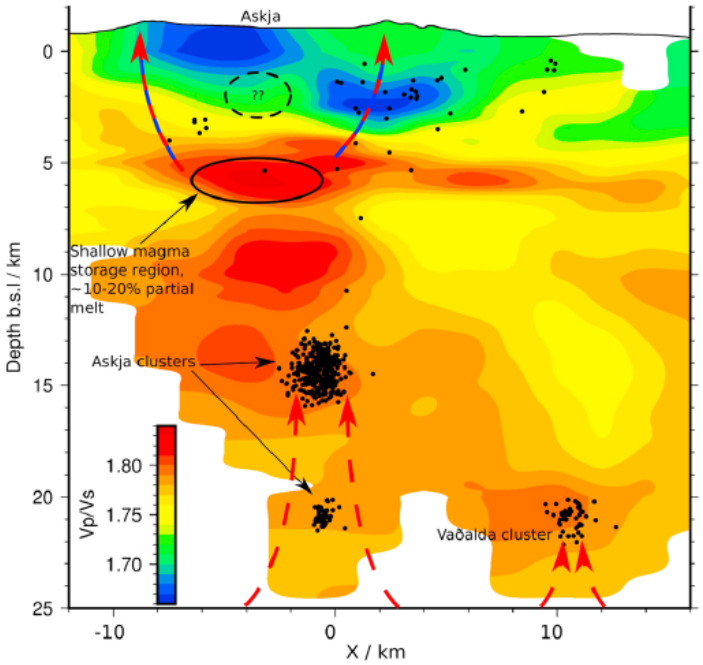

Figure 1.9: Velocity structure of the magma plumbing system beneath the Askja central volcano, perpendicular to the axis ridge (i.e. along an approximate east-west profile from left to right). The black circles show the local seismicity within 2 km of the cross-section, the solid black line highlights the possible primary shallow magma reservoir of the Askja volcanic system, the dashed line outlines the maximum possible size of the geodetic reservoir, if it exists, and the red arrows show the likely magma flow between some discrete mushy magma reservoirs (Greenfield et al., 2016, Greenfield, 2016).

1.6 Aims and objectives

The aim of this thesis is to take the integration of surface deformation with temporal gravity a step further, and contribute to the clarification of the causes of subsidence at Askja. More broadly, I aim to shed light on physical processes operating at shallow volcanic systems located along mid-oceanic ridges, and I also aim to present some new methodologies, which can be equally applicable to other studies, in order to help the scientific community to decipher subsurface physical processes.

My objectives are as follows:

1. Explore whether the long-term subsidence of the entire Askja caldera evolves similarly as locally highlighted from levelling data, and investigate whether unknown deformation signals can be extracted from the removal of the long-term subsidence trend.

2. Use inversion modelling to solve for the most probable location, depth and magnitude of the volume change associated to each extracted deformation pattern, including the long-term subsidence.

3. Develop a method to precisely estimate the error budget associated to micro-scale gravity changes.

4. Record new gravity surveys at Askja, improving methodologies and enlarging the gravity network to capture a precise gravity change signature across the caldera.

5. Use inversion modelling to solve for the most probable location, depth and magnitude of the mass changes, and compare results with the ones obtained from my second objective.

1.7 Thesis structure

In **Chapter 2**, I provide some background information on the InSAR technique, which I used to measure surface deformation at Askja, and on temporal gravity surveying.

In **Chapter 3**, I address my first and second objectives by presenting a detailed analysis of the Askja caldera surface deformation, comparing a 15-year time-series of new InSAR data (2002-2017) with existing GPS records.

In **Chapter 4**, I address my third objective by presenting a statistical approach for estimating the full error budget associated with micro-scale temporal gravity changes, taking into account the uncertainty associated to the reduction of the usual unwanted signals.

In **Chapters 5**, I address my fourth and fifth objectives by presenting a 3-year (2015-2017) study of new gravity changes, which I have recorded over a larger network in the Askja caldera, and for which I have estimated the full error budget. In this chapter, I also discuss the likely causes of subsidence, comparing the surface deformation and gravity results.

In **Chapter 6**, I summarize the key findings of this thesis, and I discuss their contributions and limitations, providing suggestions for future work.

Chapter 2

Methods

In order to measure surface deformation over Askja, I used the Interferometric Synthetic Aperture Radar (InSAR) technique, which can generate deformation maps at the centimeter scale, with a spatial resolution of tens of meters. In parallel, I carried out yearly gravity surveys during my PhD to measure temporal gravity changes at Askja.

Here, I provide a brief summary of these two methods, focusing on the key processing steps and discussing the benefits and limitations in each case. I recommend the reader to consult e.g. Massonnet and Feigl (1998), Bürgmann et al. (2000), Hanssen (2001), Ferretti et al. (2007), Hooper et al. (2007) and Dzurisin and Lu (2007), to get an exhaustive description of the InSAR technique, and e.g. Eggers (1987), Rymer (1996), Dzurisin (2007a), Battaglia et al. (2008), Williams-Jones et al. (2008), Crossley et al. (2013), Carbone et al. (2017) and Van Camp et al. (2017), to find more details on the temporal gravity method.

2.1 Interferometric Synthetic Aperture Radar (InSAR)

The RAdio Detection And Ranging (Radar) technique can be used to determine (1) the distance to a target, from the time duration needed for the pulsed electromagnetic microwave, or absolute phase, to be reflected back to the sensor, and (2) the amplitude (or brightness) of the target, from the strength of reflection (e.g. Curlander and McDonough, 1991, Bürgmann et al., 2000, Dzurisin and Lu, 2007).

When orientated obliquely downward, satellite-mounted side-looking radar systems can cover larger regions than conventional radar, with a resolution of ten meters or less along range, i.e. in the radar beam direction (Figure 2.1A). The moving radar sensor enables the construction of a larger, synthetic aperture (Figure 2.1B). This technique, referred to as Synthetic Aperture Radar (SAR), can provide a resolution of a few tens of meters along the satellite track direction, or azimuth, and therefore improves the distinction between targets with same range coordinate. Such a side-looking SAR geometry can measure satellite-to-ground distances (or ranges) with higher resolution than conventional radar techniques. However, it is highly reliant on the presence of numerous stable features, or scatterers, which are able to backscatter the radar wave with high-amplitude (e.g. Ferretti et al., 2001, Hooper et al., 2007).

Rather than measuring distances from the absolute phase of the reflected radar waves, the InSAR technique can measure deformation at the centimeter-scale, from the temporal phase shift, between any two SAR acquisitions (e.g. Bürgmann et al., 2000, Hanssen, 2001, Ferretti et al., 2007).

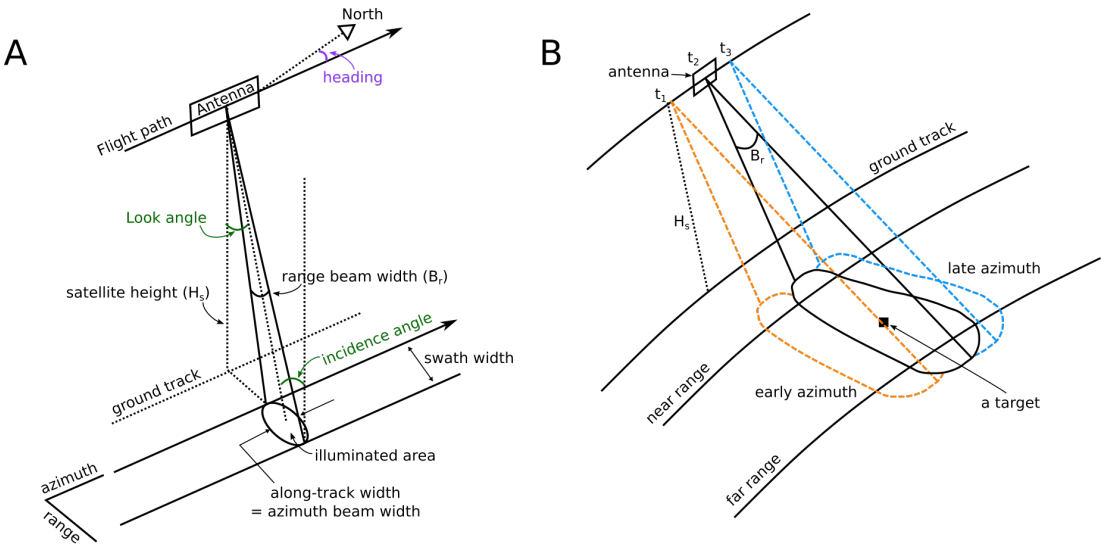

Figure 2.1: A: Configuration of a right-looking radar. B: Illustration of the Synthetic Aperture Radar (SAR) technique, where a target can be illuminated continuously from time t_1 to t_3, despite the much smaller real length of the antenna aperture. By improving the azimuth resolution, this technique improves the distinction between targets located at the same range, as the slight variations in look angle from t_1 to t_3, causes a frequency shift, so-called Doppler effect, unique per azimuth position. Both sketches are adapted from Dzurisin and Lu (2007).

2.1.1 Basic principles of InSAR

In a SAR acquisition, each pixel is defined by a complex number, Z, containing information on the amplitude, A, and phase, φ, of the returned radar wave (e.g. Massonnet and Feigl, 1998, Hanssen, 2001, Ferretti et al., 2007):

$$Z = Ae^{i\varphi} \tag{2.1}$$

When two SAR images have been acquired at different times and over the same region, the phase difference ($\Delta\varphi$), so-called interferometric phase, can be determined between both SAR acquisitions, per pixel, by multiplying Z_1 from the first SAR image, or master, with the complex conjugate of Z_2 from the second SAR image, or slave:

$$Z_1\bar{Z}_2 = A_2\, e^{i\varphi_2} A_1\, e^{-i\varphi_1} = A_2\, A_1\, e^{i(\varphi_2-\varphi_1)} = A_2\, A_1\, e^{i\Delta\varphi} \tag{2.2}$$

A wrapped interferogram plots a map of $\Delta\varphi$, wrapped within [-π;π] and commonly displayed as color fringe cycles (Figures 2.2 and 2.3), with a full color fringe cycle corresponding to a ground movement of half the satellite wavelength along the line-of-site (LOS) direction. The interferometric phase can be integrated between any two points of the scene, providing an unwrapped interferogram, i.e. a map showing the continuous unwrapped phase, $(\Delta\varphi)_{\text{unw}}$, given relative to a reference point (Figures 2.2 and 2.3). LOS deformation can be converted from radians into meters using:

$$\varphi_{\text{meters}} = \varphi_{\text{radians}} \frac{\lambda}{4\pi} \tag{2.3}$$

where λ is the wavelength of the satellite radar sensor.

Satellite-mounted InSAR can provide data from unreachable remote places with significantly better spatial resolution than, for example, any discrete network of the Global Navigation Satellite System (GNSS), of which the most famous is the U.S. Global Positioning System (GPS). Even though the technique mainly relies on the temporal stability of bright scatterers between SAR acquisitions and on the stability of the satellite acquisition geometry, statistical approaches have been developed in the

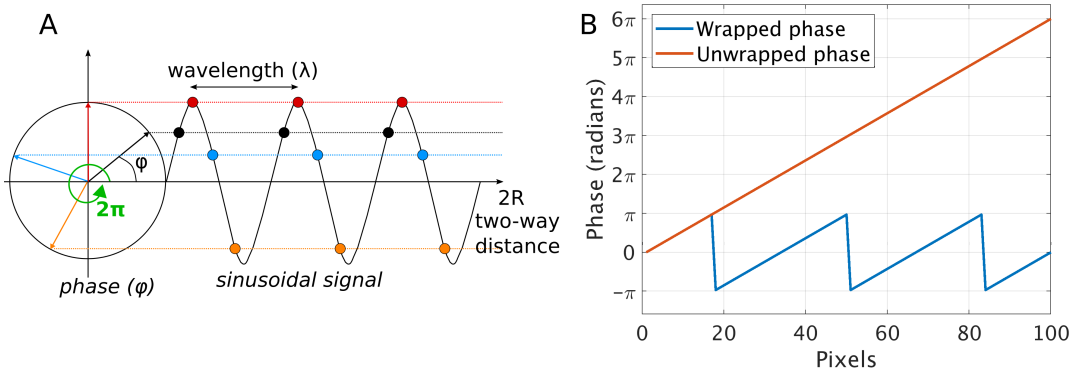

Figure 2.2: A: Sketch showing how the phase of a sinusoidal radar microwave is wrapped modulo 2π radians (adapted from Ferretti et al. (2007)). B: Simulation of phase unwrapping along a profile, where multiples of 2π are added to the wrapped phase to reproduce the continuous unwrapped phase.

last few decades to optimize results and provide high-resolution deformation time-series, by lessening areas with no pixel information, i.e. increasing the spatial coherence and therefore minimizing decorrelation.

2.1.2 From raw data to generating unwrapped time-series

The flow diagram in Figure 2.4 illustrates the main processing steps that I have carried out to generate the time-series of unwrapped phase over Askja, using several SAR images, provided at different times, by a given satellite sensor (e.g. Massonnet and Feigl, 1998, Hanssen, 2001, Ferretti et al., 2007).

First of all, the raw data (Section 2.1.1) are focused into Single Look Complex (SLC) images using precise orbital information, to extract A and φ at each pixel of every SAR acquisition (Section 2.1.1). The geometric differences between the master, and all the slaves, are then determined during the co-registration step. Once the slaves have been resampled to the master geometry, neighbouring pixels are averaged in range and azimuth (Figure 2.1A), using given multiples, so-called looks. This multi-looking step usually improves the signal-to-noise ratio of each SAR image, and provides approximately square pixel shapes.

Using the principle of Equation 2.2, a wrapped interferogram can then be generated, either between the master image and any slave (single master approach) or, as I did, between any pair of images (small baseline approach), to have more chances to form

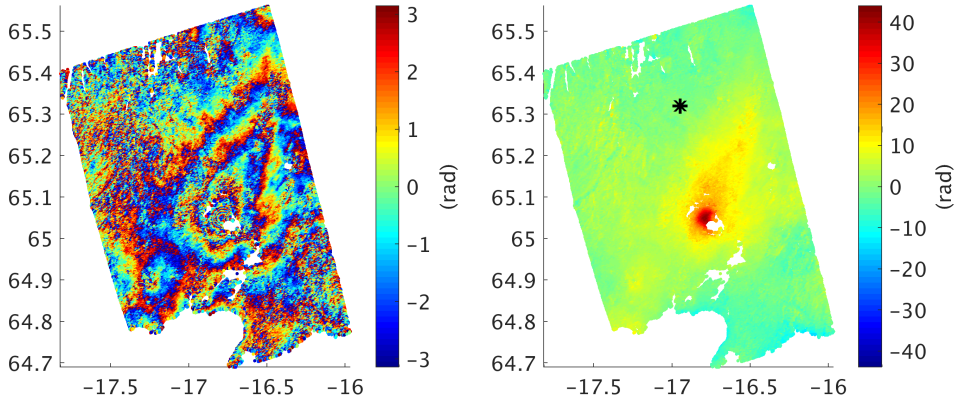

Figure 2.3: Interferogram obtained from the Envisat satellite sensor (wavelength = 5.6 cm), showing the surface deformation at Askja (red region on the right figure), between the 10th of July 2004 and 24th of July 2010. The deformation is displayed as wrapped within [-π;π] (left), versus unwrapped with respect to the star (right, positive = ground moving away from the satellite).

coherent interferograms. At this stage, $\Delta\varphi$, provided along LOS, is the sum of several contributions:

$$\Delta\varphi = \mathrm{W}\{\Delta\varphi_{\mathrm{def}} + \Delta\varphi_{\mathrm{atm}} + \Delta\varphi_{\mathrm{ref}} + \Delta\varphi_{\mathrm{topo}} + \Delta\varphi_{\mathrm{orb}} + \Delta\varphi_{\mathrm{noise}}\}, \tag{2.4}$$

where $\Delta\varphi_{\mathrm{def}}$ is the phase contribution caused by surface displacements, $\Delta\varphi_{\mathrm{atm}}$ is the phase delay caused by atmospheric property variations, $\Delta\varphi_{\mathrm{ref}}$ and $\Delta\varphi_{\mathrm{topo}}$ are the reference (or flat-Earth) and topographic phase components, which are both caused by the difference in the satellite position between acquisitions, $\Delta\varphi_{\mathrm{orb}}$ is the phase component due to any orbital residual error, $\Delta\varphi_{\mathrm{noise}}$ comprises all remaining errors, and W{} is the wrapping operator. Once $\Delta\varphi_{\mathrm{ref}}$ and $\Delta\varphi_{\mathrm{topo}}$ have been reduced, respectively using orbital information and a Digital Elevation Model (DEM), each wrapped interferogram is then flattened and topographically-corrected (Figure 2.4).

Among the various processors available to generate wrapped interferograms, I either used GAMMA (Werner et al., 2000), ROI_PAC (Rosen et al., 2004) and DORIS (Kampes and Usai, 1999), or LiCSAR (which uses GAMMA functions, González et al. (2016)), depending on the satellite sensor and number of SAR images with suitable coherence at Askja.

These flattened and topographically-corrected interferograms are then unwrapped,

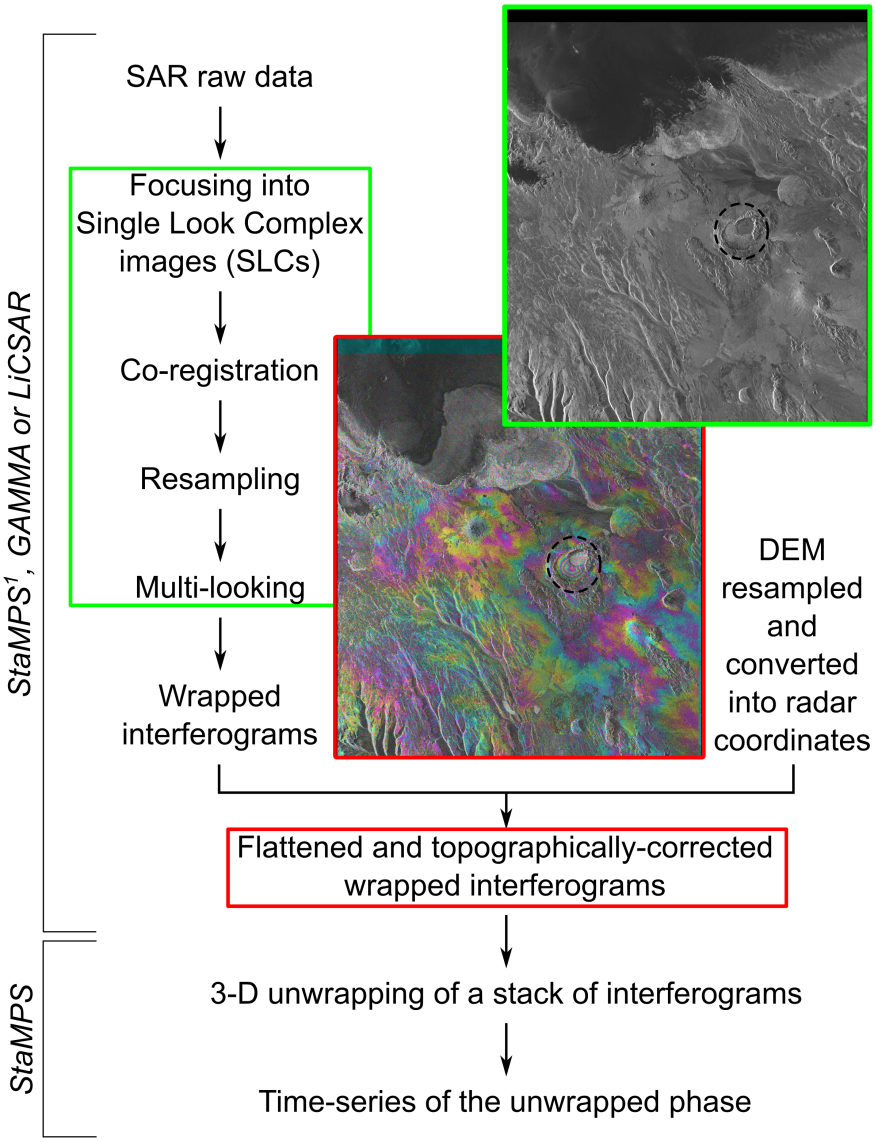

Figure 2.4: Flow diagram illustrating the key processing steps to generate a time-series of unwrapped interferometric phase (e.g. Massonnet and Feigl, 1998, Hanssen, 2001, Ferretti et al., 2007). On the left side of the figure, I have mentioned the names of the numerous software that I have used (Kampes and Usai, 1999, Werner et al., 2000, Rosen et al., 2004, Hooper et al., 2010, González et al., 2016). Two examples are shown here: a multi-looked amplitude image (framed in green), generated using the SAR acquisition of the 6^{th} of July 2002, from the ERS-2 ascending track 273, and a flattened and topographically-corrected wrapped interferogram (framed in red), generated using the SAR acquisition framed in green with another from the 15^{th} of July 2006. In these two examples, the black dashed circle locates the Askja volcano. See Section 2.1.2 for more details on the procedure.

providing $\Delta\varphi_{\text{unw}}$ (Section 2.1.1) as the sum of the following contributions:

$$\Delta\varphi_{\text{unw}} = \Delta\varphi_{\text{def}} + \Delta\varphi_{\text{atm}} + \Delta\varphi_{\text{DEM}} + \Delta\varphi_{\text{orb}} + \Delta\varphi_{\text{noise}} + \xi_{\text{unw}} \tag{2.5}$$

where $\Delta\varphi_{\mathrm{DEM}}$, often called the look angle error (or DEM error), is the phase component remaining after correcting for $\Delta\varphi_{\mathrm{ref}}$ and $\Delta\varphi_{\mathrm{topo}}$, i.e. due to DEM residual errors and any uncertainties in the position of the scatterers within each pixel, and ξ_{unw} is the residual error resulting from the unwrapping (e.g. Hooper et al., 2007).

To achieve the unwrapping, I used StaMPS (e.g. Hooper et al., 2004, Hooper, 2008, Hooper et al., 2010), because it uses a 3-D unwrapping procedure (2-D in space and 1-D in time), which evaluates the temporal stability of each pixel in addition to the classic spatial unwrapping (2-D unwrapping). Moreover, this package selects the stable pixels to be used in the 3-D unwrapping, by combining an improved version of the Persistent Scatterer (PS) approach with a Small Baseline (SB) approach.

The improved PS approach qualifies a pixel as stable when the coherent sum of the interferometric phase of all scatterers within the pixel is likely to remain steady with a given probability, over long time periods (large temporal baselines) and for large variations in the satellite position between acquisitions (large perpendicular baselines). Such stable pixel, so-called PS pixel (Hooper, 2008), usually contains a dominant bright scatterer (Figure 2.5), and because its coherent phase summation might contribute to those of the neighbouring pixels, the spatially-correlated total phases of neighbouring pixels are filtered out.

The SB approach qualifies a pixel as stable when it contains numerous distributed stable scatterers (Figure 2.5). Such pixel, sometimes called as a Slowly-Decorrelating Filtered Phase (SDFP) pixel (Hooper, 2008), remains stable for smaller temporal and perpendicular baselines than a PS pixel. Each of the approaches has limitations, and the best pixel coverage is achieved by combining the two methods.

2.1.3 Phase contribution due to surface deformation

Once all the interferograms have been unwrapped, $\Delta\varphi_{\mathrm{def}}$, which is the parameter of interest in my case, can be derived by reducing the effect of all the other unwanted unwrapped phase contributions (Equation 2.5).

StaMPS can estimate and remove a linear ramp across each interferogram, to reduce the remaining spatially-correlated phase contributions, i.e. $\Delta\varphi_{\mathrm{orb}}$, a part of $\Delta\varphi_{\mathrm{DEM}}$ and

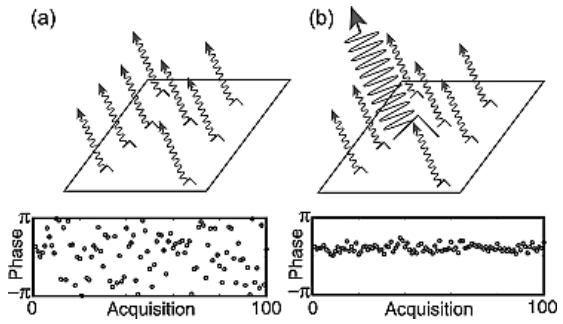

Figure 2.5: (a) Distribution of bright scatterers within an Slowly-Decorrelating Filtered Phase (SDFP) pixel, selected by the Small Baseline (SB) approach; (b) Distribution of bright scatterers within a Persistent Scatterer (PS) pixel, selected by the Persistent Scatterer (PS) approach (Adopted from Hooper et al., 2007).

a part of $\Delta\varphi_{\text{atm}}$ (Hooper, 2008). Any residual spatially-uncorrelated $\Delta\varphi_{\text{DEM}}$ is usually correlated with perpendicular baselines and can therefore also be filtered out, as well as the spatially-uncorrelated but topographically-correlated part of $\Delta\varphi_{\text{atm}}$ (e.g. Bekaert et al., 2015a).

The most challenging phase contribution to remove is usually the remaining part of $\Delta\varphi_{\text{atm}}$, which can mask small surface deformation signals. Various approaches have been developed to reduce such random and turbulent atmospheric phase component, using e.g. spectrometer data, weather models, or empirical methods. I refer to e.g. Bekaert et al. (2015b) for more details on this phase contribution because, in my case, removing the SAR images with strong random atmospheric signal turned out to be sufficient to extract the deformation at the Askja caldera.

2.2 Temporal gravity

Temporal gravity, also referred to as dynamic, time-lapse, time-variable or 4D gravimetry, is a geophysical technique used to monitor temporal surface variations in the Earth's gravitational acceleration (e.g. Dzurisin, 2007a, Battaglia et al., 2008, Williams-Jones et al., 2008, Van Camp et al., 2017). Gravity measurements are recorded using high-precision gravimeters, either set up in a continuous mode, with a common frequency of seconds-to-minutes, or by reiterating campaigns, usually every months-to-years.

2.2.1 Various types of instruments with benefits and limitations

Thanks to the high-precision gravimeters currently available, gravity changes can be detected at the microscale (1 μGal = 10^{-8} m s^{-2}), which is the minimum required to detect mass changes related to magmatic processes (e.g. Figure 1.5), or even at the nano-scale (10^{-11} m s^{-2}). However, the high-sensitivity of these instruments can also be a disadvantage as any other minute gravity change is captured along with the signal of interest (e.g. Carbone et al., 2017). In theory, the type of gravimeter should be chosen based on the magnitude of signal to be detected and on the noise conditions in the area of study, but the cost, transportation, and installation time are important criteria of selection, which often prevail.

For this reason, relative gravimeters, which measure gravity relative to a reference specific to each instrument, are usually preferred in remote volcanic environments, compared with absolute gravimeters, which directly provide a measure of the Earth's gravitational attraction (e.g. Crossley et al., 2013, Carbone et al., 2017, Van Camp et al., 2017). Indeed, relative gravimeters typically cost US$100,000-300,000, weigh up to a few tens of kilograms, and can be installed within minutes. On the other hand, absolute gravimeters typically cost US$500,000, can weight a few hundreds of kilograms and usually require a few hours of preparation before taking a measurement.

The two main types of relative gravimeters, are the spring-based and superconducting gravimeters (e.g. Crossley et al., 2013, Carbone et al., 2017, Van Camp et al., 2017). The former measures the relative gravitational attraction from the length difference between the reference and released positions of a spring-held proof mass, whereas the latter, based on the same principle, measures relative gravity by levitating a hollow of superconducting sphere (the test mass) in an extremely stable magnetic field. Superconducting gravimeters can reach the nano-scale precision, and due to their stability, they have the best quality/price ratio to perform continuous recording. However, because of their high electricity consumption, they are often replaced by a few spring-based relative instruments, which are less expensive, easier to handle and can work on direct current power. But in this case, more maintenance is required as spring gravimeters are affected by a drift of the reference, resulting from variations in the spring elastic properties.

Even though not ideal for continuous recording, these spring-based gravimeters are the best quality/price ratio for gravity surveying, which is the mode of measurement mostly used in remote volcanic environments, and significant progress has been made in detecting and quantifying unwanted effects (e.g. Carbone et al., 2017, Van Camp et al., 2017). At Askja, gravity surveying using spring gravimeters has always been preferred, especially because of the difficult access to the volcano, which is reached after ∼4 hours of driving on dirt-road, only between May to October each year. Moreover, no car is allowed in the caldera, and no continuous power supply is available in the area.

2.2.2 Temporal gravity using spring gravimeters

Among the few types of relative spring gravimeters, the analog LaCoste & Romberg G and D models (LCR, LaCoste & Romberg (2004)), which are not commercialised anymore, and the digital Scintrex CG-3/CG-3M and CG-5 models (SCG, Scintrex (1995, 2009)), have been widely used in volcanic environments, since the second half of the 21st century (e.g. Carbone et al., 2017). Figure 2.6 highlights the principle behind a spring gravimeter measurement.

While the reference position of the instrument slowly drifts through time, the released position of the proof mass mainly varies depending on the time of measurement, the latitude and altitude of the gravity station, the local subsurface structure and the local topography (e.g. Kearey et al., 2002). Taking the difference between two gravity measurements, recorded at the same gravity station, but at two different times, cancels the gravity effects due to latitude and local topography, as these two parameters do not vary through time, but new contributions must be taken into account, such as the gravity changes due to temporal variations in elevation and subsurface water-masses (e.g. Battaglia et al., 2008). In addition, the gravity effects due to large changes in e.g. air pressure, air temperature, and variations in the calibration factor, used to convert the record into milligal, can be of the same order of magnitude as or larger than the temporal signal of interest (e.g. Valliant, 1991, Merriam, 1992, Budetta and Carbone, 1997, El Wahabi et al., 2001). Precise estimation of each unwanted contribution is required to determine this signal of interest, often referred to as the residual gravity

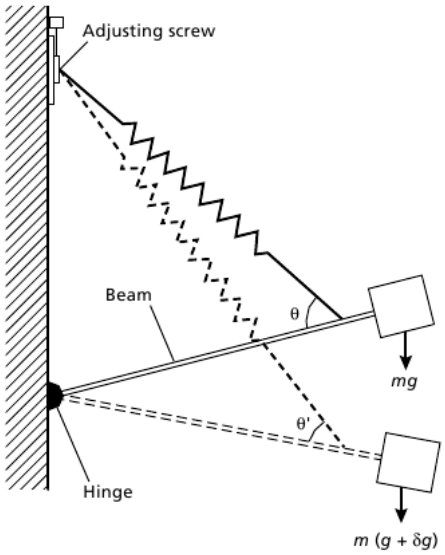

Figure 2.6: Sketch highlighting the principle of the standard LaCoste & Romberg (LCR) gravimeters, where the user turn a dial to bring the proof mass back to its reference position (taken from Kearey et al. (2002)). The spring is inclined to increase the sensitivity. Scintrex gravimeters are based on the same principle, but the spring is vertical as the mass is precisely brought back to its initial position by an automatic electronic feedback system. A similar electronic feedback system can be upgraded on any standard LCR gravimeters, but it needs to be regularly manually calibrated (LaCoste & Romberg, 2003).

change (e.g. Battaglia et al., 2008). Due to the lack of guidance in the quantification of uncertainties, I have developed a statistical approach that estimates the full error budget associated to any residual gravity change, recorded from spring gravimeters. This error analysis relies on estimating the error associated to each unwanted contributions, which are briefly explained below and presented in more details in the Chapter 4.

2.2.3 Residual gravity change from spring gravimeters

A gravity measurement, recorded, using a spring gravimeter, at any given site and any given time t, can be represented as follows (e.g. Battaglia et al., 2018; and references therein):

$$k(t)\Big[g_{\rm meas}(t) - g_{\rm ET}(t) - g_{\rm OL}(t) - g_{\rm P}(t) - g_{\rm T}(t)\Big] = g(t) + f_D(t) \tag{2.6}$$

where $k(t)$ is the calibration factor at t (i.e. GCAL2 in the Scintrex's manual, Scintrex (1995, 2009)), $g_{\rm meas}$ is the gravity measurement already converted in milligals using the

manufactured calibration factor (ie. GCAL1 in the Scintrex's manual, Scintrex (1995), LaCoste & Romberg (2004), Scintrex (2009)), g_{ET} and g_{OL} are caused by solid Earth tides and ocean loading, g_{P} and g_{T} are due to atmospheric pressure and temperature, g is the Earth-fixed gravitational acceleration, at the given station, but taken relative to the gravimeter's reference, which drifts through time, according to the function $f_D(t)$.

Consequently, when $k(t)$ is precise enough, reducing g_{meas} for estimates of each gravity effect external to the Earth body, provides an estimation, $\hat{g}$, of the relative gravitational attraction generated at t, by the local topography and subsurface crustal structures beneath the given site (Figure 2.7):

$$\hat{g}(t) = k(t)\Big[g_{\mathrm{meas}}(t) - \hat{g}_{\mathrm{ET}}(t) - \hat{g}_{\mathrm{OL}}(t) - \hat{g}_{\mathrm{P}}(t) - \hat{g}_{\mathrm{T}}(t)\Big] = g(t) + f_D(t) + \varepsilon_g \qquad (2.7)$$

where, ε_g is the residual error or deviation between g and its estimate $\hat{g}$. When $k(t)$ is imprecise, results can be recalibrated using an updated calibration factor.

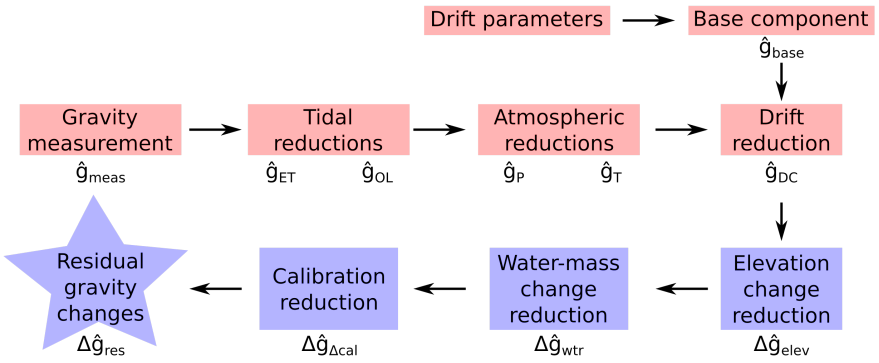

Figure 2.7: Flow diagram highlighting the key processing steps to determine the residual gravity change (star) at a given station, between any two surveys, from the record of a gravity measurement during each survey. The red steps are performed for each survey (Equation 2.8), whereas the blue steps relate to the temporal changes between the surveys (Equation 2.10). Refer to Section 2.2.3 for more details.

The parameters of the drift function, $f_D(t)$, are usually determined daily, from a series of tidally-corrected measurements ($g_{\mathrm{meas}}(t) - \hat{g}_{\mathrm{ET}}(t) - \hat{g}_{\mathrm{OL}}(t)$), reproduced at a station, often referred to as the base. From the estimated drift function, the tidally-corrected gravity signature at the base, $\hat{g}_{\mathrm{base}}$, can be predicted at the same time t of any given gravity measurement g_{meas} (e.g. Kearey et al., 2002, Battaglia et al., 2018). In Chapter 4, I demonstrate that it can be more suitable to estimate the drift parameters

over a few days, rather than over a single day, as any unknown variations, occurring simultaneously as the instrumental drift can then be estimated.

Taking the difference between $\hat{g}(t)$ and $\hat{g}_{\text{base}}(t)$, cancels the unknown drifting reference of the spring gravimeter, and therefore, provides a drift-corrected gravity estimate, $\hat{g}_{\text{DC}}$, at the given site:

$$\hat{g}_{\text{DC}}(t) = k(t)\Big[g_{\text{meas}}(t) - \hat{g}_{\text{ET}}(t) - \hat{g}_{\text{OL}}(t) - \hat{g}_{\text{P}}(t) - \hat{g}_{\text{T}}(t)\Big] - \hat{g}_{\text{base}}(t) = g_{\text{DC}}(t) + \varepsilon_{\text{DC}} \quad (2.8)$$

where ε_{DC} is the residual error or deviation between $g_{\text{DC}}(t)$ and its estimate $\hat{g}_{\text{DC}}(t)$. In the literature, $g_{\text{DC}}(t)$ is often referred to as the "observed gravity" (e.g. Battaglia et al., 2008), but, because an observation is synonym to a measurement, I prefer to use a clearer name to avoid any confusion. To estimate the drift-corrected gravity signature per station and for each survey that I carried out at Askja, I employed the GTOOLS software (Battaglia et al., 2012), which I improved to better constrain uncertainties.

Once the drift-corrected gravity signals have been computed at any station, an estimate of the temporal gravity change, Δg_{DC}, can be determined at any given site and between any two surveys, as follows:

$$\Delta\hat{g}_{\text{DC}} = \Big[\hat{g}_{\text{DC}}\Big]_{t_2} - \Big[\hat{g}_{\text{DC}}\Big]_{t_1} = \Delta g_{\text{DC}} + \xi_{\text{DC}}, \quad (2.9)$$

where t_1 and t_2 are the times of measurements recorded at a same site, during the first and second surveys, respectively, and ξ_{DC} is the residual error or deviation between the temporal variation Δg_{DC} and its estimate $\Delta\hat{g}_{\text{DC}}$.

Because Δg_{DC} is the sum of several contributions, the above equation can be decomposed as follows:

$$\Delta\hat{g}_{\text{DC}} = \Big[\hat{g}_{\text{DC}}\Big]_{t_2} - \Big[\hat{g}_{\text{DC}}\Big]_{t_1} = \Delta g_{\Delta\text{cal}} + \Delta g_{\text{elev}} + \Delta g_{\text{wtr}} + \Delta g_{\text{res}} + \xi_{\text{DC}}, \quad (2.10)$$

where $\Delta g_{\Delta\text{cal}}$ reflects the drift-corrected temporal gravity change caused by calibration variations between surveys, Δg_{elev} is the gravity change due to vertical surface deformation, Δg_{wtr}, reflects temporal variations in subsurface water-masses, and Δg_{res}, is

the residual gravity change or parameter of interest, in my case. In the literature, a component related to the redistribution of the crustal density layers, in response to a deforming source, is sometimes also taken into account (e.g. Battaglia et al., 2008); but because such gravity component depends on the geometry of the assumed reservoir, it is more appropriate to quantify it during the modelling, if necessary (Section 1.4.2).

Once all temporal unwanted effects have been estimated, $\Delta\hat{g}_{\text{res}}$, which relates to the mass variation of any magmatic and/or hydrothermal fluids, can be expressed as follows: (Figure 2.7):

$$\Delta\hat{g}_{\text{res}} = \Delta\hat{g}_{\text{DC}} - \Delta\hat{g}_{\Delta\text{cal}} - \Delta\hat{g}_{\text{elev}} - \Delta\hat{g}_{\text{wtr}} = \Delta g_{\text{res}} + \xi_{\text{res}}, \tag{2.11}$$

where ξ_{res} is the final residual error or deviation between Δg_{res} and its estimate $\Delta\hat{g}_{\text{res}}$. To determine the residual gravity changes between the three surveys that I carried out at Askja, I developed my own package, which estimates associated uncertainties.

In summary, spring gravimeters are the most practical types of gravimeters to be used in volcanic remote places (Section 2.2.1), but as illustrated from all these successive equations, precisely estimating the gravity signature of magma-related mass changes requires meticulous estimation of each of the unwanted contributions. Despite their similar precision, the SCG models are usually more reliable than the LCR models, as their automatic processing provides better constraints on measurement errors (Chapter 4).

Chapter 3

A 15-year Sample of Subsidence at the Askja Caldera (2002-2017)

This chapter addresses the first and second objectives of my thesis, by analysing the long-term subsidence over the entire Askja caldera as well as any possible distinct unknown deformation pattern. Results are jointly interpreted with gravity in Chapter 5.

3.1 Introduction

The main Askja caldera is likely to have been subsiding continuously since the early 1970s. As summarized in Section 1.5.1, this long-term deformation unrest, or restless phase (Acocella et al., 2015), has been closely monitored since 1983, using precise levelling, GPS and InSAR. Based on levelling, this subsidence has decayed exponentially between 1983 to 2006 with a relaxation time of ∼39 years (Sturkell et al., 2006), which can be updated to ∼42 years when considering the time-series up to 2017 (Figure 1.7). This overall levelling time-series has been based on the tilt of a 1.2-km-long baseline, in the north-east of the Askja caldera, ∼2.5 km from the centre of subsidence (Figure 1.7A).

Using InSAR and/or GPS time-series, spanning various periods of up to 10 years, between 1992 and 2014, parallel studies highlighted the overall bowl-shape spatial signature of the subsidence, with highest deflation constantly located in the centre of the

caldera (Table 1.2, Figure 1.7B and e.g. Sturkell and Sigmundsson (2000), Pagli et al. (2006), de Zeeuw-van Dalfsen et al. (2012, 2013)). Even though a decay in deformation rate was observed, it is not clear that the signals measured by GPS and InSAR also follow the exponential decay locally constrained from levelling. Using linear subsidence rates, all these deformation studies agreed that the subsidence can be best explained by a ∼3-3.5-km-deep deflating Mogi or ellipsoidal reservoir, when assuming an elastic half-space medium (Section 1.5.1 and Table 1.2). From these models, volume change rates have been gradually decreasing from about -0.002 to -0.001 km^3 yr^{-1} between 1993 and 2014.

Although this shallow reservoir would be consistent with the usual structure of magma plumbing systems expected beneath the magma-dominated slow-spreading mid-Atlantic ridge of Iceland (Section 1.2.1 and e.g. Sigmundsson (2006a)), its reliability can be questioned when comparing these geodetic results with the seismic tomography recently published by Greenfield et al. (2016) (Section 1.5.4). Indeed, the "magma domain" (Figure 1.1) of Askja seems to be located between 6-10 km depth, and even though a shallow reservoir might still be located at ∼3-3.5 km depth, it seems unlikely that the uniquely long and steady subsidence is mainly controlled by a relatively small and shallow magma reservoir. Alternatively, the observed surface deformation could be the cumulative result of several processes, having a combined centre of pressure change located at ∼3-3.5 km depth.

In this chapter, I test the hypothesis that one process is responsible for the long-term subsidence, locally constrained from levelling and which I estimate over the entire caldera, using an InSAR dataset spanning 15 years (2002-2017). Removing this long-term signal from the measured caldera subsidence might reveal unknown deformation signals, either due to any non-uniform evolution of the main source of subsidence, or to other distinct processes. The flow diagram in Figure 3.1 summarizes the overall procedure that I undertook to characterize the long-term subsidence over the entire caldera and extract any residual deformation signals. I explain each step in more detail below, before presenting and analysing results, using inversion modelling.

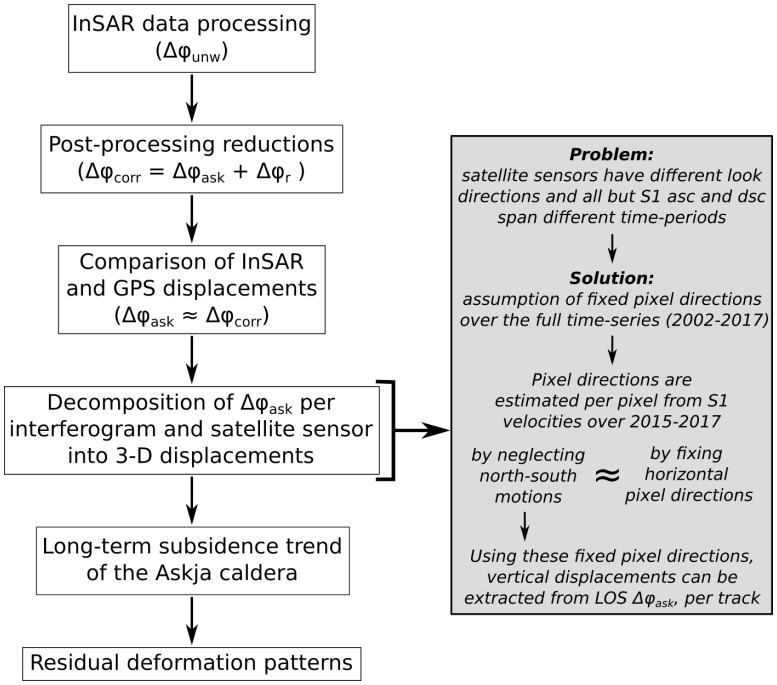

Figure 3.1: Flow diagram presenting the procedure that I undertook to estimate the long-term deformation over the Askja caldera, and extract any unknown residual deformation signals. Refer to Section 2.1 and 3.2 for symbols and abbreviations.

3.2 InSAR data processing

To capture the long-term caldera subsidence of Askja, I processed InSAR data over 15 years, from six tracks and four different satellites, as follows: an ERS ascending track covering 2002-2006, an Envisat ascending track covering 2004-2010, a COSMO-SkyMed (CSK) ascending track covering 2010-2012 and 2014-2015, a CSK descending track covering 2012-2015, and two Sentinel-1 (S1) tracks, one ascending and one descending, both covering 2015-2017 (Figure 3.2, Table 3.1 and Figure 3.3).

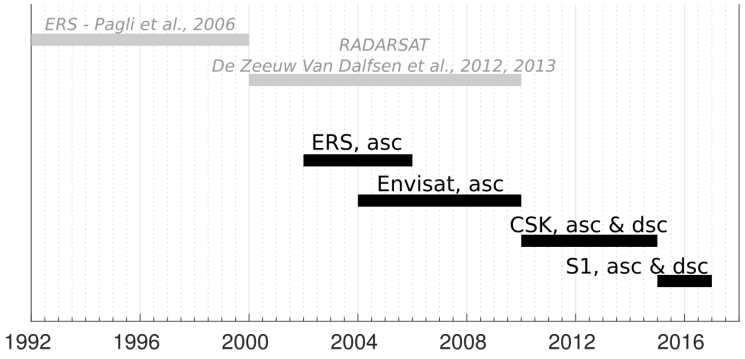

Figure 3.2: New InSAR dataset used in this thesis (black), in comparison with previous studies (grey). Refer to table 3.1 for more details on this new dataset.

Sensor	**ERS**	**Envisat**	**CSK**		**CSK**	**S1**	**S1**
Geometry	**A**	**A**	**A**		**D**	**A**	**D**
Track	273	273	26550		24670	147	111
Period start	Jul02	Jul04	Oct10	Jul14	Aug12	Sep15	Sep15
Period end	Jul06	Jul10	Aug12	Sep15	Sep15	Sep17	Sept17
Ifgs software	GAMMA[1]	StaMPS[2]	GAMMA[1]		GAMMA[1]	LiCSAR[3]	LiCSAR[3]
SAR images	13	19	15		14	55	48
Created ifgs	78	60	105		91	173	157
Used images	3	19	4	4	6	18	16
Used ifgs	3	37	4	3	11	41	42
Ifg pixel size (m)	100	200	100	100	100	100	100
unwTS software	StaMPS[2]	StaMPS[2]	StaMPS[2]	StaMPS[2]	StaMPS[2]	StaMPS[2]	StaMPS[2]
StaMPS reductions	None	$\Delta\varphi_{sc}$	$\Delta\varphi_{sc}$	None	None	$\Delta\varphi_{sc}$	$\Delta\varphi_{sc}$
Further reductions	$\Delta\varphi_{sc}$, $\Delta\varphi_{tc}$	$\Delta\varphi_{tc}$	$\Delta\varphi_{tc}$	$\Delta\varphi_{sc}$, $\Delta\varphi_{tc}$	$\Delta\varphi_{sc}$, $\Delta\varphi_{tc}$	$\Delta\varphi_{tc}$	$\Delta\varphi_{tc}$

Table 3.1: Summary of the InSAR data used to cover the period 2002-2017 at the Askja caldera (CSK: COSMO-SkyMed, S1: Sentinel-1, A: ascending, D: descending, ifgs: interferograms, SAR: Synthetic Aperture Radar, unwTS: unwrapped time-series, sc: spatially-correlated, tc: topographically-correlated). Refer to Section 2.1 for an overview on the InSAR technique, and to Sections 3.2 and 3.3 for more details on data processing and reductions. [1]Werner et al. (2000); [2]Hooper et al. (2010), which uses ROI_PAC (Rosen et al., 2004) to create the SLCs and DORIS (Kampes and Usai, 1999) to generate interferograms; [3]González et al. (2016), which uses GAMMA functions.

I created the wrapped interferograms, per satellite sensor, choosing the most appropriate software (StaMPS was not setup to process S1 interferograms and did not provide good intergerograms when too few images were available). I refer the reader to Section 2.1.2 and Figure 2.4 for a summary of the overall processing procedure. For consistency, I always used the same Digital Elevation Model (DEM), namely the Advanced Spaceborne Thermal Emission and Reflection Radiometer (ASTER) DEM, which has a resolution of 1 arcsecond, i.e. ∼30 m in latitude and ∼13 m in longitude at Askja; and I used the StaMPS package to generate the unwrapped time-series for all sensors (Hooper et al., 2010).

Even though I limited my selection of SAR images to dates between May and October to minimize incoherence due to snow, coherence was still very poor in the Askja caldera: when using my initial selection of images, no pixels were present in the Askja caldera. This is mainly because snowfalls can also happen even during the summertime. To maximize the number of stable pixels in the Askja caldera and to minimize strong random and turbulent atmospheric signals (Sections 2.1.2 and 2.1.3), I reduced even more the number of SAR images per sensor, using trial and error: I removed the images

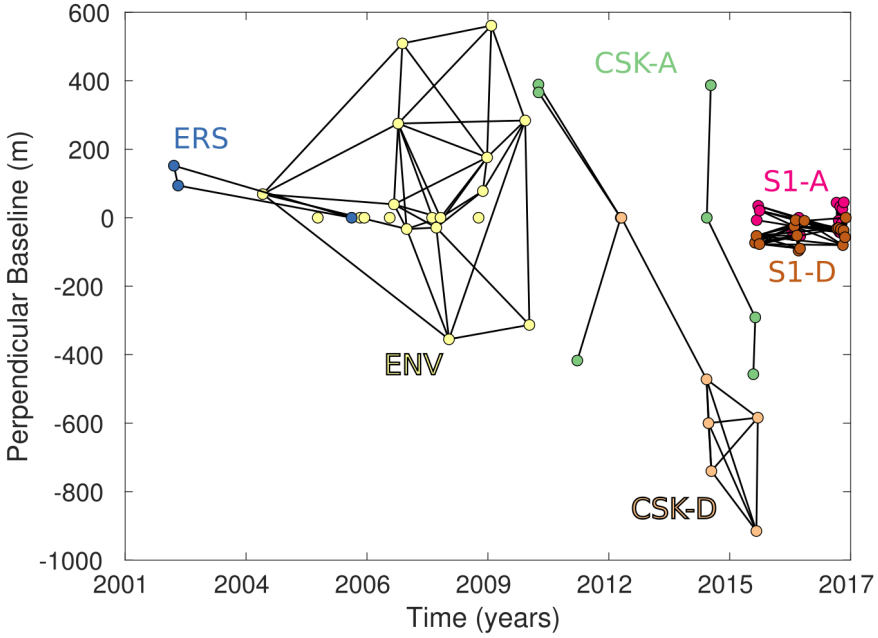

Figure 3.3: Network of used interferograms (black lines), where each dot corresponds to a SAR image, and each color to a satellite sensor. Refer to Table 3.1 for abbreviations and for more details on each dataset.

that seemed to repeatedly affect the coherence and/or show strong atmospheric signals, on by one. This approach increased the chances of obtaining a good quality unwrapping inversion in space, but it may have reduced the quality of unwrapping inversion in time. Even though I sometimes had a very low number of retained interferograms (Table 3.1), the StaMPS 3-D unwrapping inversion (Section 2.1.2) provided an unwrapped phase signal, $\Delta\varphi_{\text{unw}}$, at each pixel and per interferogram, with reasonably low residuals (ξ_{unw} in Equation 2.5) at Askja and surroundings (Appendix A.1). However, it is worth keeping in mind that the uncertainties of the ERS unwrapped phase might have been underestimated, as this dataset is composed of only three dates, of which two are separated by only one month.

This first step provided the time-series of $\Delta\varphi_{\text{unw}}$, per satellite sensor, but further reductions were necessary to isolate the phase component related to surface deformation only.

3.3 Post-processing reductions to extract $\Delta\varphi_{\text{ask}}$ from $\Delta\varphi_{\text{unw}}$

After unwrapping, I reduced the unwanted phase contributions to determine the component of interest, $\Delta\varphi_{\text{def}}$ (Equation 2.5 and Section 2.1.3), which I rename here $\Delta\varphi_{\text{ask}}$, as it represents the surface deformation related to the magma plumbing system of Askja. I re-write Equation 2.5, grouping the unwanted components depending on whether they are spatially-correlated ($\Delta\varphi_{\text{sc}}$), topographically-correlated ($\Delta\varphi_{\text{tc}}$), or neither, as detailed in Section 2.1.3:

$$\Delta\varphi_{\text{unw}} = \Delta\varphi_{\text{ask}} + \Delta\varphi_{\text{sc}} + \Delta\varphi_{\text{tc}} + \Delta\varphi_{\text{r}} \tag{3.1}$$

where $\Delta\varphi_{\text{r}}$ includes the remaining phase components, which are not correlated in space, nor with topography, but can either be correlated with perpendicular baseline (Hooper, 2008), or are just random, such as due to turbulent atmosphere. This component therefore also includes ξ_{unw} (Equation 2.5) and any other residual errors.

It is worth noting that, at Askja, $\Delta\varphi_{\text{sc}}$ is usually dominated by an additional local component, due to an ice-melting uplift response, so-called Glacial Isostatic Adjustment (GIA), from the nearby Vatnajökull icecap (e.g. Auriac, 2014, Drouin et al., 2017). However, for interferograms spanning 2014-2015, $\Delta\varphi_{\text{sc}}$ is dominated by a much more significant component, corresponding to the deformation induced by the Holuhraun dyke intrusion, which propagated south of Askja, along the mid-Atlantic ridge, up to ∼20 km south of the caldera (Sigmundsson et al., 2014, Spaans and Hooper, 2018).

As summarized in Table 3.1, I usually reduced $\Delta\varphi_{\text{sc}}$, via StaMPS, removing a ramp across each unwrapped interferogram. However, this approach produced suspiciously null results when applied to ERS data, and this is most likely due to the low coherence over the interferometric scene, which might have prevented a precise ramp estimation. Additionally, when applied to the two CSK datasets covering 2014-2015, the estimated ramp largely underestimated the Holuhraun dyke deformation signal.

To overcome these problems, I estimated $\Delta\varphi_{\text{sc}}$ for my ERS dataset, by interpolating the GIA model from Auriac (2014), who estimated velocities over all of Iceland between 2008 and 2010, and I assumed that the predicted uplift velocities over Askja were

applicable to and linear over 2002-2006 (Figure 3.4). Similarly, I estimated $\Delta\varphi_{\text{sc}}$ for the CSK interferograms covering 2014-2015 (ascending) and 2012-2015 (descending), using the Holuhraun dyke deformation model from Spaans and Hooper (2018). However, after removing this Holuhraun signal, the sign of deformation was flipped in the south-west of the scene, i.e. closest to the Holuhraun eruption site (Figure 3.4). This indicates that the dyke deformation model has likely overestimated the Holuhraun signal in this area, and some discrepancy might be observed at Askja.

Finally, although usually small, I estimated $\Delta\varphi_{\text{tc}}$ for all sensors, by quantifying the potential linear correlation between ($\Delta\varphi_{\text{unw}}$ - $\Delta\varphi_{\text{sc}}$) in a non-deforming zone, specific to each sensor scene, and each corresponding topographic pixel height, derived from the ASTER DEM (Figure 3.4).

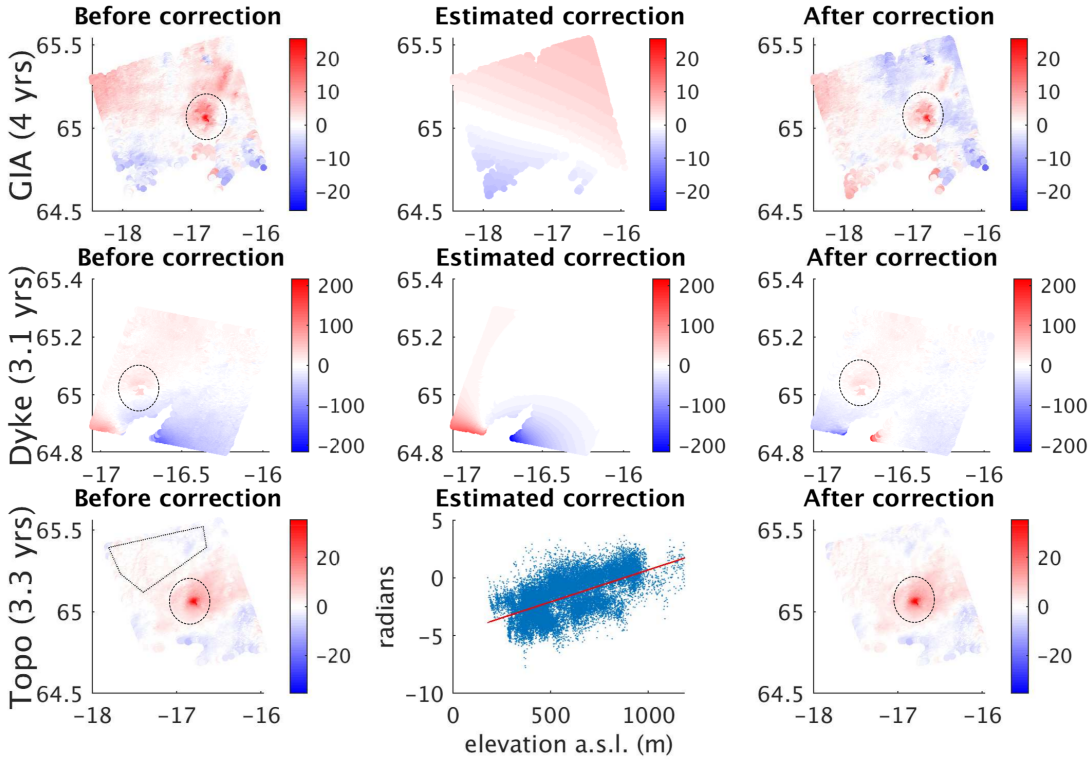

Figure 3.4: Top row: Example of GIA reduction on an ERS interferogram, spanning 4 years. Middle row: Example of Holuhraun dyke effect reduction on a CSK descending interferogram, spanning 3.1 years. Bottom row: Example of topographically-correlated signal reduction, estimated in the non-deforming zone highlighted on the bottom left graph, for an Envisat interferogram, spanning 3.3 years. Phases are given in radians, and the Askja central volcano is highlighted with the circles when appropriate.

At this stage, each interferogram shows the reduced unwrapped phase, $\Delta\varphi_{\text{corr}}$, com-

prising the surface deformation signal related to the Askja plumbing system, $\Delta\varphi_{\text{ask}}$, plus all remaining unknown signals contained in $\Delta\varphi_{\text{r}}$ (Figures 3.5 and 3.6). Equation 3.1 can therefore be re-written as follows:

$$\Delta\varphi_{\text{corr}} = \Delta\varphi_{\text{unw}} - \Delta\varphi_{\text{sc}} - \Delta\varphi_{\text{tc}} = \Delta\varphi_{\text{ask}} + \Delta\varphi_{\text{r}} \tag{3.2}$$

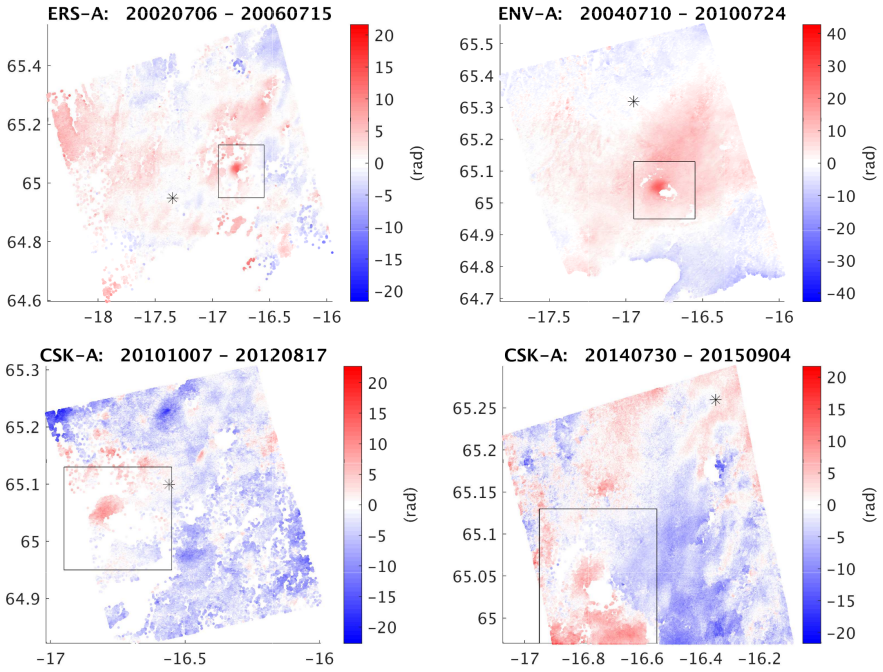

Figure 3.5: Reduced unwrapped phase for the longest interferogram of the ERS-A, Envisat-A and CSK-A datasets (Table 3.1). See Sections 3.2 and 3.3 for more details on data processing. Colorscales are independent (red = away from satellite), as well as the reference site (star), and because the sizes of interferometric scenes vary depending on the dataset, I have highlighted the area of study, shown e.g. on Figure 3.7. The full time-series are presented in Appendix A.2.

3.4 Robustness of $\Delta\varphi_{\text{corr}} \approx \Delta\varphi_{\text{ask}}$

As summarized in Figure 3.1, the next step was to compare the time-series of $\Delta\varphi_{\text{corr}}$, obtained after data processing and post-processing reductions, with 3-D GPS summer time-series, recorded at specific sites within the Askja caldera (Figure 3.7). This would confirm that $\Delta\varphi_{\text{r}}$ in Equation 3.2 is negligible, and hence, that I captured the deformation signal of interest ($\Delta\varphi_{\text{corr}} \approx \Delta\varphi_{\text{ask}}$).

For both types of data to be analogous while remaining independent, I reduced the

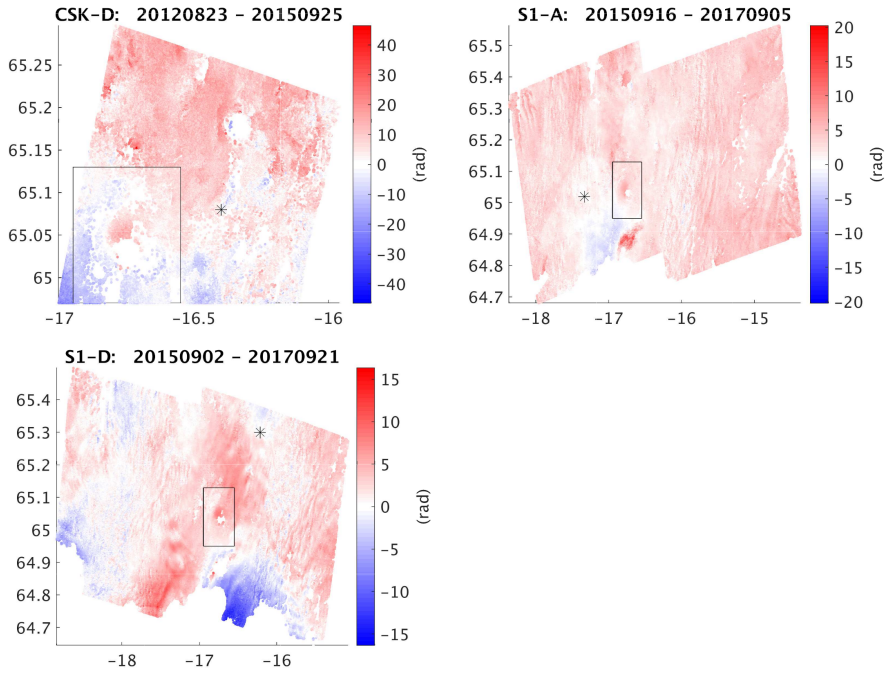

Figure 3.6: Same as Figure 3.5 but for the CSK-D, S1-A and S1-D interferograms.

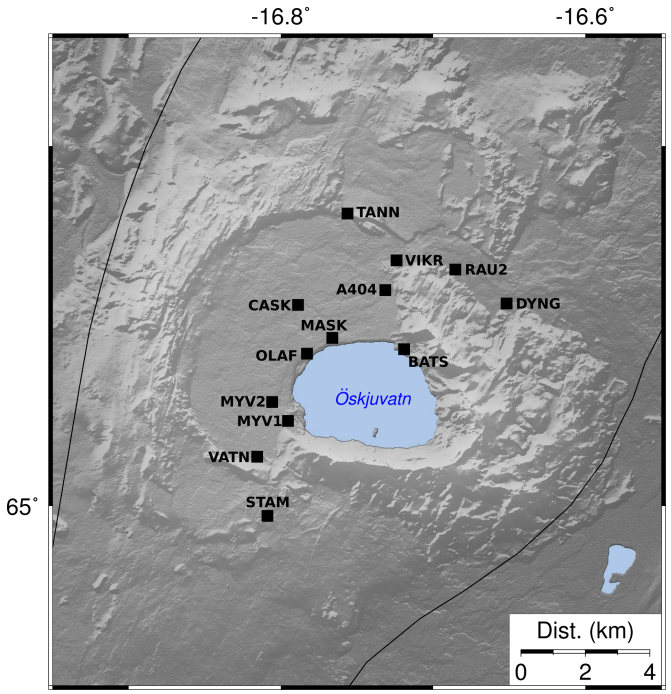

Figure 3.7: GPS network for summer campaigns at Askja. OLAF and MASK are the most frequently measured as they are closest to the centre of deflation (Figure 1.7B), while TANN has been measured only twice over 2002-2017 due to difficult access. DYNG is part of the continous GPS network of Iceland.

3-D GPS signals for unwanted effects caused by external magmatic intrusions, using an alternative approach than the one used to reduce similar effects from my InSAR

time-series (Section 3.3), and which I describe below, in Section 3.4.1. Additionally, I calibrated both types of signals independently from each other, by choosing a common reference site. I then projected the 3-D reduced GPS signals, into LOS, per satellite sensor, in order to obtain a time-series of $[\Delta\varphi_{\text{ask}}]_{\text{GPS}}$, comparable to $\Delta\varphi_{\text{corr}}$, extracted at each GPS station (See below Sections 3.4.1-3.4.4 for more details of the overall procedure).

Results show that both LOS time-series are in good agreement with each other, suggesting that $\Delta\varphi_{\text{corr}} \approx \Delta\varphi_{\text{ask}}$ (Figure 3.8). Indeed, the independent time-series usually overlap within two standard deviations, providing unweighted root-mean-square errors (RMSE) below 1.7 cm. The only time-period where a small discrepancy, inducing RMSEs between 1.7 and 3.2 cm, is sometimes observed is 2014-2015, which corresponds to the Holuhraun dike intrusion period. This inconsistency is therefore most likely due to errors in the dyke induced signal reduction (Section 3.3).

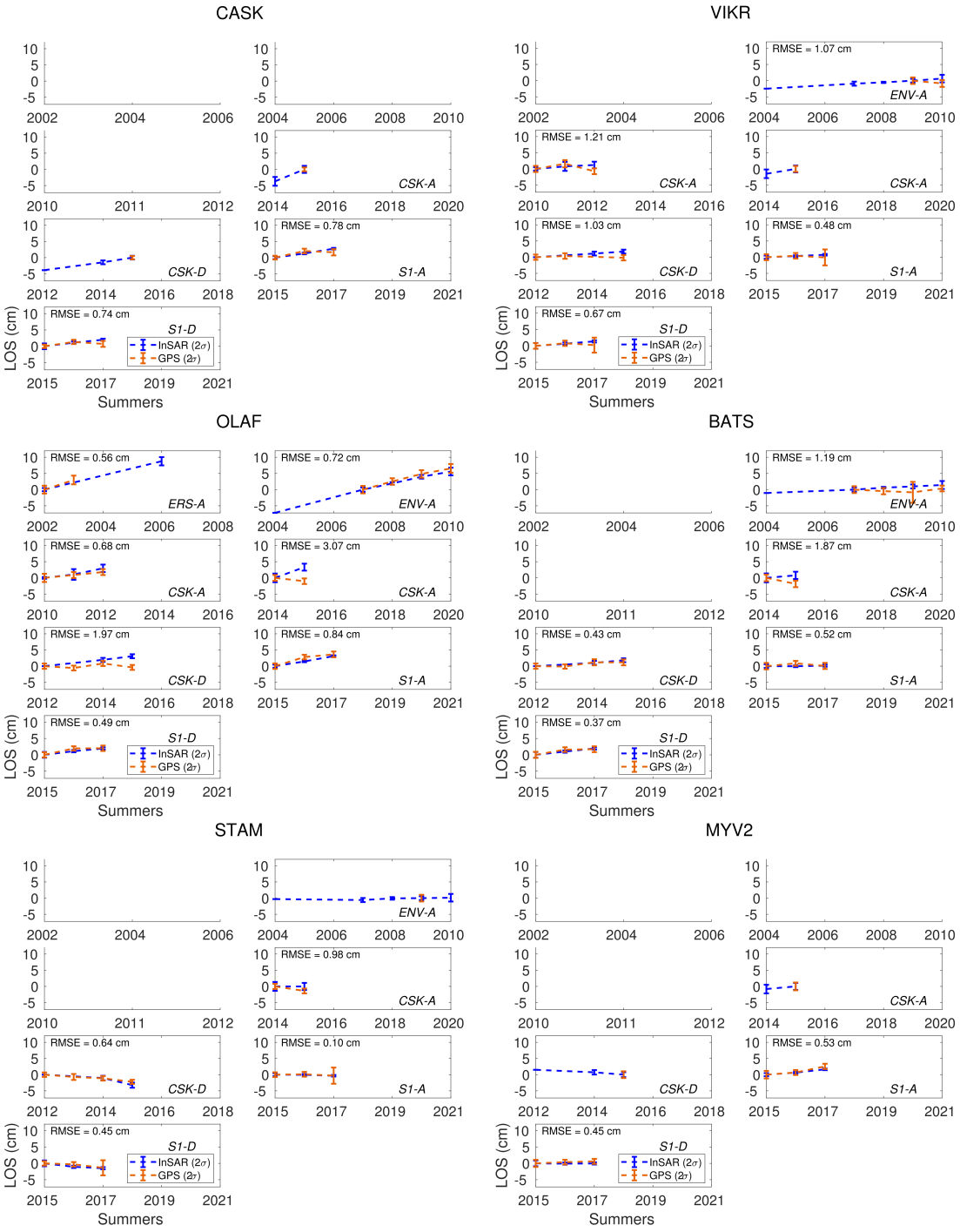

Figure 3.8: Example of InSAR and GPS LOS time-series (positive = away from satellite), at six stations within the Askja caldera. The InSAR data are the yearly reduced unwrapped phase, $\Delta\varphi_{\text{corr}}$, averaged at each GPS station, converted from radians to centimeters (Equation 2.3), and taken relative to DYNG (Figure 3.7). The GPS data are the line-of-sight (LOS) projections of the reduced 3-D GPS summer displacements, also taken relative to DYNG, and which can be expressed as $[\Delta\varphi_{\text{ask}}]_{\text{GPS}}$, as they are related to the magma plumbing system of Askja. Each graph refers to a satellite sensor, and results are shown only when GPS and InSAR data were both available. See Section 3.4 for more details on the procedure and Table 3.1 for satellite sensor abbreviations.

3.4.1 Reducing unwanted signals in GPS deformation time-series

Vincent Drouin (University of Iceland) provided the 3-D summer GPS displacements (east-west, north-south and vertical) at each GPS station within the Askja caldera (Figure 3.7) and spanning a maximum period between summer 2002 and summer 2017, which corresponds to my InSAR time-period. He estimated each summer site position using weighted-least-squares, from daily solutions evaluated in the ITRF14 reference frame, and reduced ocean loading effects (e.g. Drouin et al., 2017).

As expected from my InSAR results (Section 3.3), the deformation due the 2014-2015 Holuhraun dyke intrusion also contaminated the GPS time-series. Additionally, the 2007-2008 Upptyppingar intrusion, which occurred ∼25 km to the west of Askja (e.g. Hooper et al., 2011), affected the vertical deformation at DYNG. Because these two short-term contamination emerged as obvious shifts in the GPS time-series (Figure 3.9), I used weighted least-squares to quantify their effects as offsets, assuming a constant linear rate over each time-series, as illustrated by the following matrix system:

$$\begin{bmatrix} D_1 \\ D_2 \\ ... \\ D_{S-2} \\ D_{S-1} \\ D_S \end{bmatrix} = \begin{bmatrix} t_1 & 1 & 0 & 0 \\ t_2 & 1 & 1 & 0 \\ ... & ... & ... & ... \\ t_{S-2} & 1 & 1 & 0 \\ t_{S-1} & 1 & 1 & 1 \\ t_S & 1 & 1 & 1 \end{bmatrix} \begin{bmatrix} \hat{\dot{D}} \\ \hat{D}_0 \\ \hat{o}_{\text{upp}} \\ \hat{o}_{\text{hol}} \end{bmatrix} \tag{3.3}$$

where D_1 to D_S are the GPS displacements measured in a given direction and at a given station, between the times t_1 and t_S, and their variances, characterizing the uncertainties of the GPS measurements, are listed in the diagonal of the variance-covariance matrix; $\hat{\dot{D}}$ is the estimated constant linear deformation rate, $\hat{D}_0$ is the y-intercept, and $\hat{o}_{\text{upp}}$ and $\hat{o}_{\text{hol}}$ are the offsets due to the Upptyppingar and Holuhraun intrusions. The data that need to be corrected for each offset are indicated with 1 in the third and fourth columns of the forward matrix operator (Equation 3.3). In this example, the Upptyppingar offset happened between t_1 and t_2, and the Holuhraun offset occurred between t_{S-2} and t_{S-1}.

Even though these linear models did not always fit the 1-dimension GPS time-series with 95% confidence, this simple procedure is sufficiently reliable to estimate and reduce the offsets induced by the intrusions (Figure 3.9). Moreover, it is an alternative approach to using the Holuhraun dyke deformation model (Spaans and Hooper, 2018), which I applied to my InSAR time-series (Section 3.3); and as mentioned previously, treating the GPS and InSAR time-series independently from each other was necessary to make a reliable comparison.

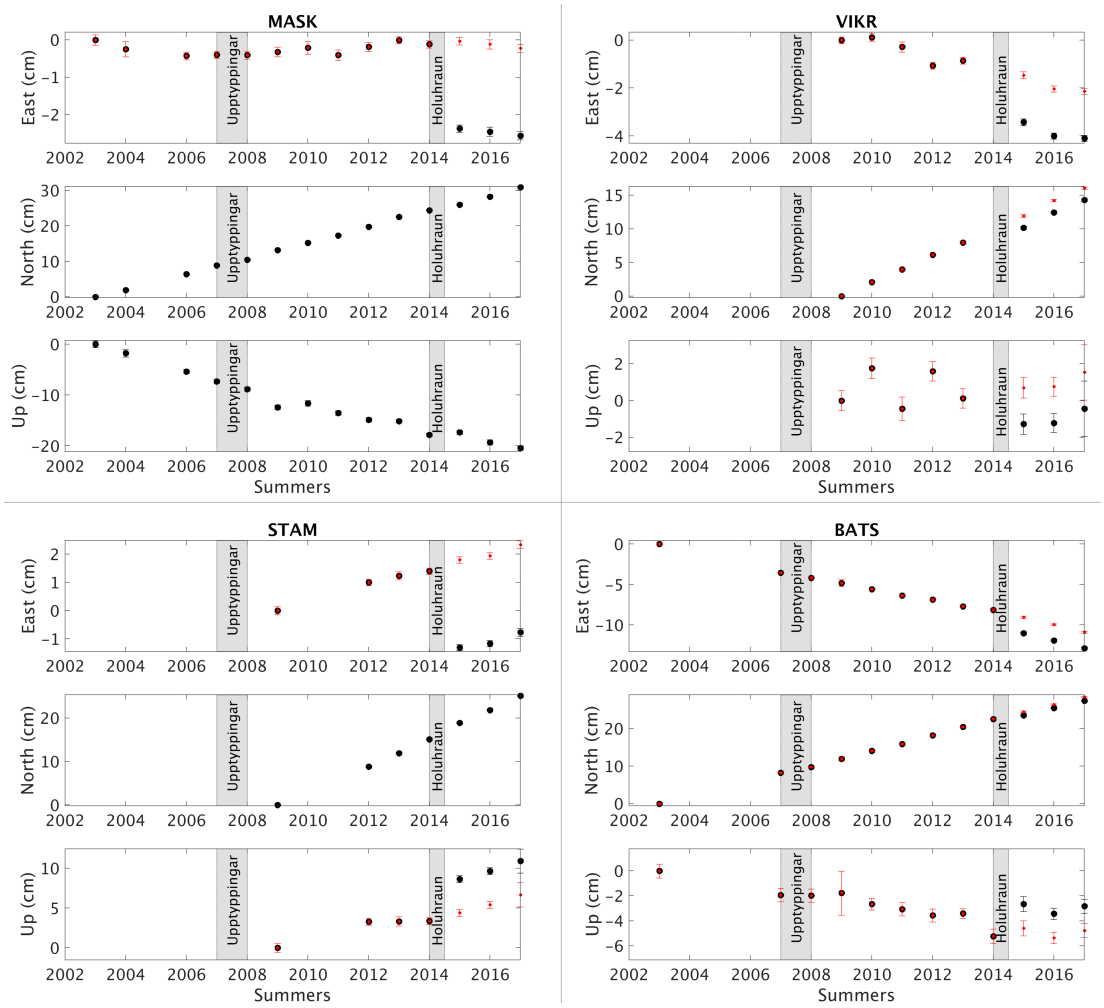

Figure 3.9: Example of deformation time-series, evaluated at four stations, in the ITRF14 reference frame, along the east-west (top graph), north-south (middle graph) and vertical (bottom graph) directions, before (black) and after (red) offset removal caused by external intrusions (Section 3.4.1). Eastward, Northward and upward displacements are positive.

3.4.2 Choice of reference station to compare InSAR and GPS time-series

To be comparable, the InSAR and GPS time-series needed to be calibrated to the same reference frame. It is common practice to transform the InSAR data into the GPS reference frame (e.g. Hussain et al., 2016), but to preserve the independence of both types of data, I instead estimated each deformation signals to a common reference site, while making sure that the signal of interest was well isolated and fully captured.

Because the whole Askja caldera is located on the American side of the rift segment (e.g. Drouin et al., 2017), choosing a reference station located on this tectonic plate should reduce the unwanted horizontal deformation effect due to plate-spreading. Even though close to the area of study, DYNG is an appropriate choice. Indeed, this station does not seem to be affected by the caldera subsidence because it shows negligible vertical deformation in the ITRF14 reference frame (Figure 3.10A). Moreover, when taking the caldera centre as the reference, rather than contracting towards the caldera, DYNG seems to be mostly affected by plate spreading as its residual horizontal deformation of $\sim$1.8 mm yr^{-1} is in azimuth direction of $\sim$280° (Figure 3.10B, e.g. Drouin et al. (2017)). Consequently, taking DYNG as the reference for deformation will imply assuming no deformation at this site, and this will reduce the plate spreading effect, while preserving the subsidence signal. I discarded the measurements from 2006 at DYNG, due to an anomalous vertical signal, which would have contaminated all other stations in the referencing procedure (Figure 3.10A).

3.4.3 Conversion of GPS data in LOS direction, per satellite sensor

The next step to reliably compare the GPS and InSAR time-series, was to project the reduced 3-D summer GPS displacements, taken relative to DYNG (Sections 3.4.1 and 3.4.2), into the LOS direction of each satellite sensor. I carried out the projection by multiplying the east-west, north-south and vertical reduced GPS components, $[D_E, D_N, D_V]^{\mathrm{T}}$, by the respective components of the LOS unit vectors (e.g. Wright

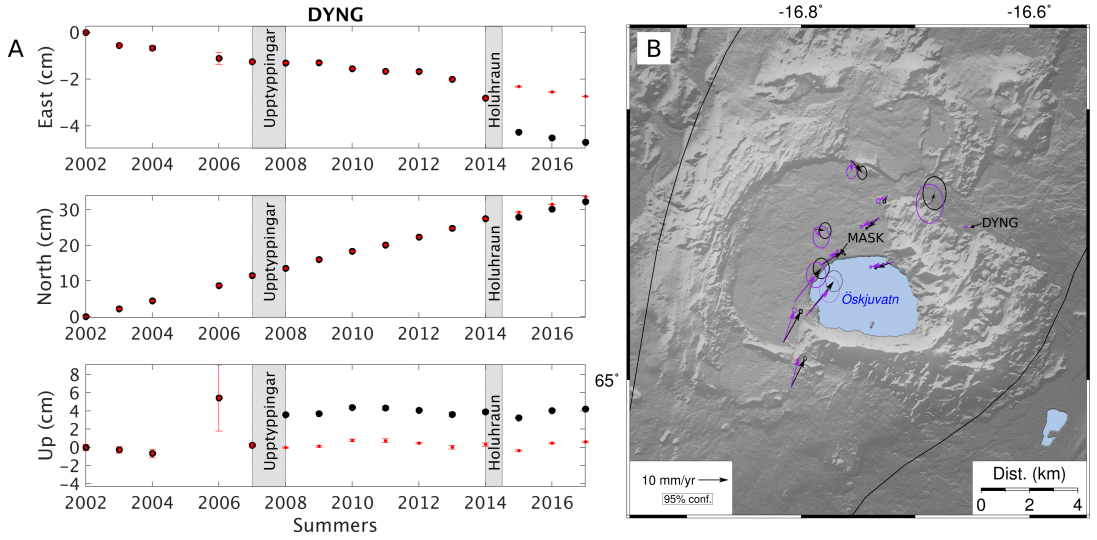

Figure 3.10: A: Deformation time-series, evaluated at DYNG, in the ITRF14 reference frame, along the east-west (top graph), north-south (middle graph) and vertical (bottom graph) directions, before (black) and after (red) offset removal caused by external intrusions (Section 3.4.1). East, North and uplift displacements are positive, and the 3-D measurements of 2006 were discarded, due to the suspicious vertical component. B: Horizontal linear deformation rates, relative to DYNG (black) and MASK (purple), after offset reductions. Ellipses show uncertainties within 95% confidence.

et al., 2004):

$$\begin{bmatrix} sin(\Theta)cos(\alpha) & -sin(\Theta)sin(\alpha) & -cos(\Theta) \end{bmatrix} \times \begin{bmatrix} D_E \\ D_N \\ D_V \end{bmatrix}_{\text{GPS}} = [\Delta\varphi_{\text{ask}}]_{\text{GPS}} \qquad (3.4)$$

where Θ and α are the incidence and heading angles of a given satellite sensor (Figure 2.1A). Because Θ is more likely to vary from pixel-to-pixel than α, I estimated Θ per GPS station, as the least-squares average of the incidence angles of all pixels located within a square box centered on each GPS station, whereas I estimated α per satellite sensor, as the least-squares average of the pixels located on a square box centered on CASK, i.e. in the middle of the area of interest (Figure 3.7). Depending on the satellite sensor and the number of pixels available, the side of the boxes varied between 400 and 1200 m.

3.4.4 Spatial and temporal averages of InSAR data at GPS stations

Because $[\Delta\varphi_{\text{ask}}]_{\text{GPS}}$ (Equation 3.4) reflects the LOS deformation related to the magma plumbing system of Askja, the last step before verifying that $[\Delta\varphi_{\text{ask}}]_{\text{GPS}} \approx \Delta\varphi_{\text{corr}}$ (Figure 3.8), was to extract $\Delta\varphi_{\text{corr}}$ at each GPS station, for each interferogram taken relative to DYNG.

I carried out this extraction by first, estimating the spatial average of $\Delta\varphi_{\text{corr}}$ combining all pixels located within a square box centred on each GPS station (see above), and I then combined results per summer, to obtain a single point per summer, and obtain a time-series analogous to the GPS time-series.

To perform the spatial average, I used weighted least-squares, with the variance-covariance matrix estimated using an exponential semi-variogram model with single nugget (e.g. Bagnardi and Hooper, 2018). This approach is based on the assumption that, in each interferogram, the errors of the LOS displacements covary with distance, and the covariance, C, between any pair of pixels, follows a negative exponential function depending on the pixels separating distance, r:

$$C = (C_s - C_n)\, e^{-r/R} \tag{3.5}$$

where C_n is the nugget variance, characterizing the constant error across each interferogram, analogous to a measurement error; C_s is the sill variance, characterizing the magnitude of error when r is null, i.e. mostly due to residual atmospheric signals; and R is the range or distance at which pixels do not covary anymore. Based on this function, the variance-covariance matrix lists constant variances equalling C_s in the diagonal, and lists the covariances C, depending on r, elsewhere. I estimated the nugget, sill and range parameters within a non-deforming zone of each interferogram, using the trial and error approach of the Geodetic Bayesian Inversion Software package (GBIS, Bagnardi and Hooper (2018)).

I verified the goodness-of-fit of each weighted spatial average by carrying out a χ^2 test, which consists of estimating the reduced Chi-Squared, χ^2_ν, equalling the weighted residual sum of squares divided by the degree of freedom ν (with ν equalling the number

of data, i.e. the number of pixels in each square box, minus the number of model parameters, i.e. 1). If χ^2_ν is smaller than or equal to the expected $\chi^2_{\nu,0.95}$ with given probability 0.95, χ^2_ν-$\chi^2_{\nu,0.95} \leq 0$, the model lies within the 95% confidence interval (e.g. Bevington and Robinson, 1992). Otherwise, the model is not representative of the data within errors, and this usually happens either when the model is wrong or when errors have been underestimated. Because deformation varies smoothly within the Askja caldera, estimating a spatial average across hundreds of meters should provide a reliable mean, and it is likely that a positive χ^2_ν-$\chi^2_{\nu,0.95}$ would be an indication of underestimated errors. In such situations, I used the percentile bootstrap method (Efron and Tibshirani, 1986) to re-estimate the spatial averages with more precise associated variances, taking into account the uncertainty of the model itself. Indeed, the spatial average estimation is iterated 10,000 times, from unique random selections of data, while preserving the total number of data considered, and the final spatial average and associated variance to retain are the mean and variance of the 10,000 iterations. To avoid any bias from the initial underestimated errors, weights are ignored and, instead, the normal least-squares approach is used.

To then perform the temporal average per summer, I used weighted least-squares with the variance-covariance matrix listing the variances resulting from the spatial average procedure, in the diagonal, and zeros elsewhere. All these estimated summer averages passed the χ^2 test with 95% probability, providing a time-series of $\Delta\varphi_{\text{corr}}$ analogous to $[\Delta\varphi_{\text{ask}}]_{\text{GPS}}$, per GPS station and satellite sensor. As already shown in Figure 3.8, $[\Delta\varphi_{\text{ask}}]_{\text{GPS}} \approx \Delta\varphi_{\text{corr}}$, meaning that my reduced InSAR time-series reasonably reflect the deformation associated to the magma plumbing system of Askja.

3.5 Vertical component of deformation at Askja

After verifying that my InSAR time-series were related to the deformation of Askja, the next step was to constrain the long-term subsidence signal over the entire caldera (Figure 3.1). When satellite sensors have different looking directions, they cannot be compared directly, and I therefore needed to decompose displacements from LOS to

3-D, to extract a component that I could assemble. To be able to compare my results with the levelling time-series (Figure 1.7), I focused on the vertical component.

As illustrated by Equation 3.4, decomposing LOS deformation into 3-D per satellite sensor is an ill-posed problem where three unknown parameters, $[D_E, D_N, D_V]^{\mathrm{T}}_{\mathrm{InSAR}}$, need to be constrained, per pixel, from a single LOS value, $[\Delta\varphi_{\mathrm{ask}}]_{\mathrm{InSAR}}$. Because satellite sensors lie in the same plane approximately, it is usually not possible to decompose LOS data with three tracks. Alternatively, two synchronous InSAR datasets with different viewing geometries are commonly used, while making an extra assumption (e.g. Wright et al., 2004, Fuhrmann and Garthwaite, 2019). I was not able to use this common approach as the first 13 years of my 15-year time-series are mainly covered by a succession of single tracks (Figure 3.2).

Alternatively, from the long-term GPS time-series (Figures 3.9 and 3.10), I assumed fixed directions of pixel motions, which I constrained from the two synchronous tracks spanning the last two years of my time-series (i.e. S1 ascending and S1 descending), and I extracted the component of interest, $\hat{D}_V$, per satellite sensor, by projecting $\Delta\varphi_{\mathrm{ask}}$ into a displacement, $\hat{D}_{\mathrm{ask}}$, along each pixel direction, in each interferogram:

$$\hat{D}_{\mathrm{ask}} = \frac{\Delta\varphi_{\mathrm{ask}}}{u} = \frac{\Delta\varphi_{\mathrm{ask}}}{\boldsymbol{los} \bullet \boldsymbol{d}} \tag{3.6}$$

$$\hat{D}_V = \hat{D}_{\mathrm{ask}} \boldsymbol{d_v} \tag{3.7}$$

where u is the length of the LOS unit vector, $\boldsymbol{los}$, when projected in the fixed pixel direction described by the unit vector $\boldsymbol{d}$, of which $\boldsymbol{d_v}$ is the vertical component. u can be therefore calculated as the dot product between $\boldsymbol{los}$ and $\boldsymbol{d}$.

3.5.1 Estimation of fixed pixel directions

I estimated the pixel directions $\boldsymbol{d}$ and $\boldsymbol{d_v}$ (Equations 3.6 and 3.7), using synchronous S1 LOS velocities, estimated from displacements, resampled onto a common 100-by-100-m ASTER grid. However, as mentioned above, this implied making an extra assumption, and to make sure my results were reliable, I tested two different approaches: on one hand, I assumed negligible north-south motions, and on the other hand, I assumed fixed

horizontal pixel directions contracting towards the caldera centre.

1. Neglecting north-south motions is a common decomposition approach as displacements along this direction, which is approximately perpendicular to the LOS direction, are usually poorly constrained by satellite sensors (Figure 2.1 and e.g. Wright et al. (2004), Fuhrmann and Garthwaite (2019)). In this case, the decomposition matrix system can be expressed as follows:

$$\begin{bmatrix} \left[\Delta\dot{\varphi}_{\text{ask}}\right]_{\text{A}} \\ \left[\Delta\dot{\varphi}_{\text{ask}}\right]_{\text{D}} \end{bmatrix} = \begin{bmatrix} sin(\Theta_{\text{A}})cos(\alpha_{\text{A}}) & -cos(\Theta_{\text{A}}) \\ sin(\Theta_{\text{D}})cos(\alpha_{\text{D}}) & -cos(\Theta_{\text{D}}) \end{bmatrix} \times \begin{bmatrix} \hat{\dot{D}}_E \\ \hat{\dot{D}}_V \end{bmatrix} \tag{3.8}$$

   where $\left[\Delta\dot{\varphi}_{\text{ask}}\right]_{\text{A}}$ and $\left[\Delta\dot{\varphi}_{\text{ask}}\right]_{\text{D}}$ are the ascending (A) and descending (D) S1 LOS velocities at any given grid node; Θ and α are the incidence and heading angles in each satellite viewing geometry (Figure 2.1A), and $\hat{\dot{D}}_E$ and $\hat{\dot{D}}_V$ are the velocities along east-west and vertical.

2. Assuming fixed horizontal pixel directions contracting towards the caldera centre, seemed to be a reasonable assumption at Askja due to the steady radial signal centered on the caldera (Figure 3.10B). In this case, horizontal, $\hat{\dot{D}}_H$, and vertical velocities, can be constrained per pixel, as follows:

$$\begin{bmatrix} \left[\Delta\dot{\varphi}_{\text{ask}}\right]_{\text{A}} \\ \left[\Delta\dot{\varphi}_{\text{ask}}\right]_{\text{D}} \end{bmatrix} = \begin{bmatrix} u_{\text{A}} & -cos(\Theta_{\text{A}}) \\ u_{\text{D}} & -cos(\Theta_{\text{D}}) \end{bmatrix} \times \begin{bmatrix} \hat{\dot{D}}_H \\ \hat{\dot{D}}_V \end{bmatrix} \tag{3.9}$$

   where $\hat{\dot{D}}_H$ is composed of the east-west, $\hat{\dot{D}}_E$, and north-south, $\hat{\dot{D}}_N$, velocity components, and, similarly as in Equation 3.6, u_{A} and u_{D} are the lengths of the S1 ascending and descending LOS unit vectors, when projected in each fixed horizontal pixel direction.

In Appendix A.3 I explain in more details how I carried out each of these two approaches, which provided similar results once velocities with largest errors, from the second approach, had been discarded. Indeed, assuming fixed horizontal pixel directions implied that radial signals were dominated by north-south motions along the central

north-south axis, whereas these motions are very poorly constrained by the LOS signals. Estimates of radial motion in this area were therefore dominated by the error in the InSAR, and corresponding pixels needed to be discarded (Appendix A.3).

Based on this analysis, I constrained the fixed pixel directions of motion using the decomposition approach that neglected north-south motions, as this provided a better spatial coverage than the other decomposition approach. To maximise even more the spatial coverage compared with when testing the decomposition approaches (Appendix A.3), I used the least-squares percentile bootstrap approach with 10,000 iterations (Section 3.4.4) to re-estimate the resampled LOS displacements and velocities that did not pass the χ^2 test. Moreover, I temporarily moved the reference from DYNG to an arbitrary site, located at ∼10 km south-west from the caldera centre, and which I referred to as SOUTH (Figure 3.11). This was to ensure that the S1 LOS velocities were non-negligible everywhere in the caldera and constrain non-negligible pixel directions in the zone of interest.

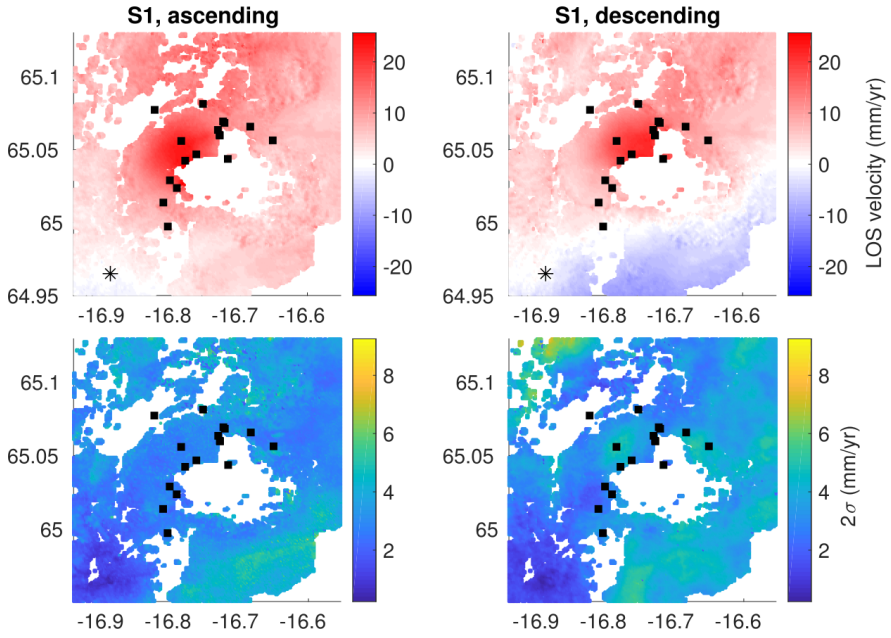

Figure 3.11: Top: Magnitudes of the resampled LOS velocities constrained from the S1 ascending (left) and descending (right) tracks, when taken relative to a SOUTH arbitrary location (star). Bottom: Associated standard deviations. Black squares are the GPS stations (Figure 3.7). See Section 3.5.1 for more details on the estimation of these velocities.

Indeed, once $\hat{\dot{D}}_E$ and $\hat{\dot{D}}_V$ had been constrained, I estimated $\boldsymbol{d}$ per pixel, with two

non-zero components, $\boldsymbol{d_e}$ (along east-west) and $\boldsymbol{d_v}$, as follows:

$$\hat{\dot{D}} = \sqrt{\hat{\dot{D}}_E^2 + \hat{\dot{D}}_V^2} \tag{3.10}$$

$$\boldsymbol{d_v} = \frac{\hat{\dot{D}}_V}{\hat{\dot{D}}} \tag{3.11}$$

$$\boldsymbol{d_e} = \frac{\hat{\dot{D}}_E}{\hat{\dot{D}}} \tag{3.12}$$

From these equations, any negligible $\hat{\dot{D}}_E$ and $\hat{\dot{D}}_V$ would generate a negligible direction of motion, which, when implemented in Equation 3.7, would generate negligible deformation, and this would be wrong in the caldera (Figure 3.12).

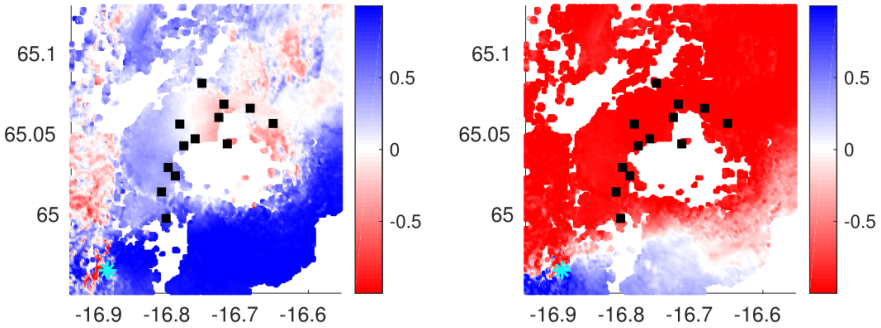

Figure 3.12: Map view of pixel directions along east-west (left, blue = towards east) and vertical (right, blue = upward motion), estimated using S1 velocities taken relative to SOUTH (cyan star) to constrain direction everywhere in the caldera, neglecting north-south motions to maximise spatial coverage (Figure 3.11). GPS stations are highlighted with the black squares (Figure 3.7).

3.5.2 Single-track LOS decomposition

After resampling the LOS displacements of each S1 interferogram onto the common ASTER grid, and moved the reference site from DYNG to SOUTH (Section 3.5.1), I used the east-west and vertical directions of motion, derived at each grid node (Figure 3.12), to constrain the vertical displacements, $\hat{D}_v$, per pixel, in each interferogram and for each satellite sensor (Equations 3.6 and 3.7).

As shown by Figures 3.13, 3.14 and 3.15, this approach seems to have well preserved the Askja subsidence signal, but as expected, the period 2014-2015 has been contaminated by the Holuhraun dyke intrusion reduction (Section 3.3).

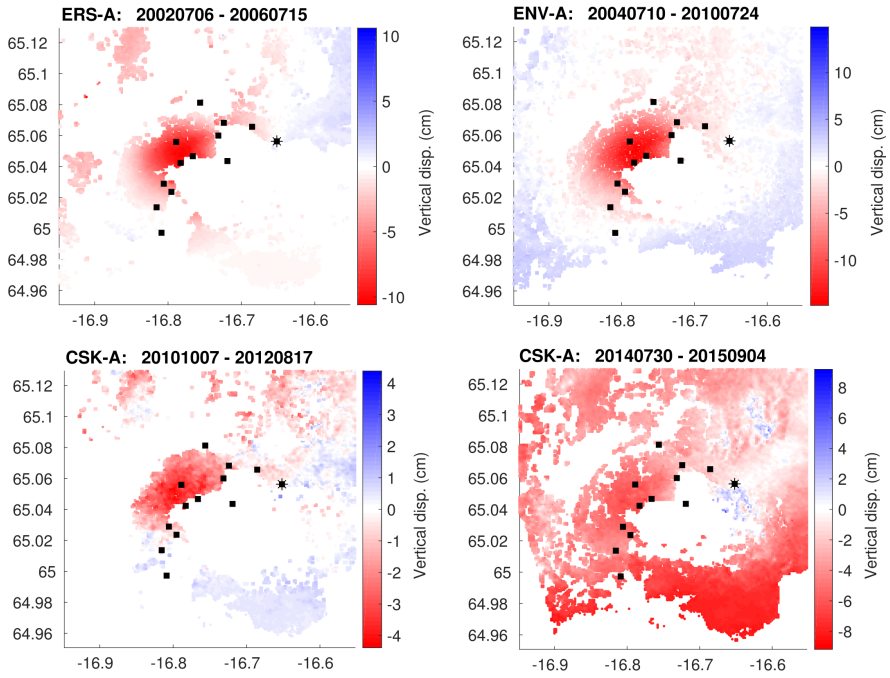

Figure 3.13: Vertical displacements decomposed for the longest interferograms of the ERS-A, Envisat-A and CSK-A datasets (Table 3.1), from the reduced unwrapped LOS phases per pixel (Section 3.5). Colorscales are independent (red = subsidence), while the reference site is DYNG for all datasets (star). Results are shown at grid nodes with non-negligible S1 velocities, non-negligible u, and non-negligible LOS displacement.

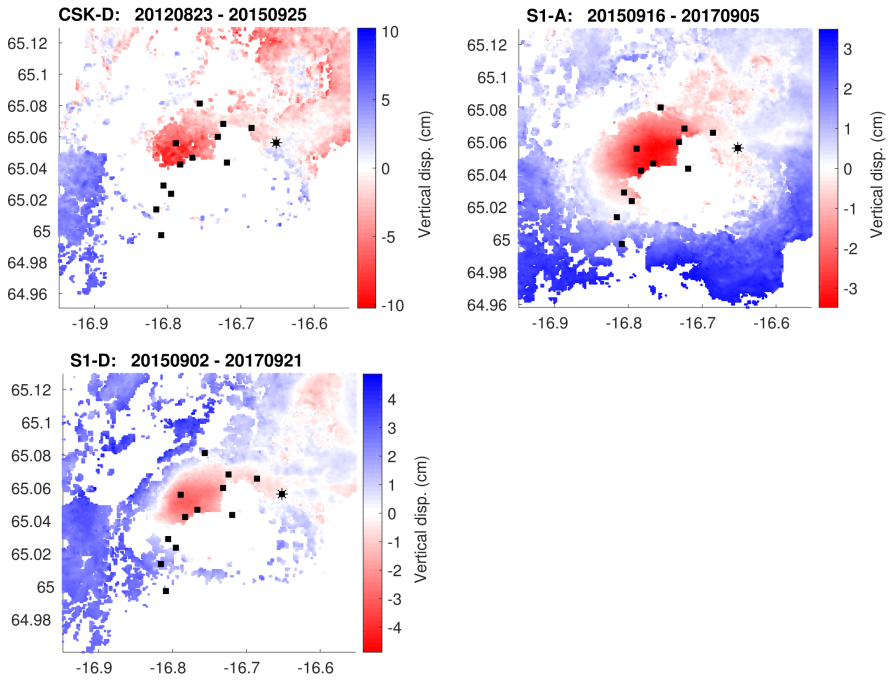

Figure 3.14: Same as Figure 3.13 but for the CSK-D, S1-A and S1-D longest interferograms.

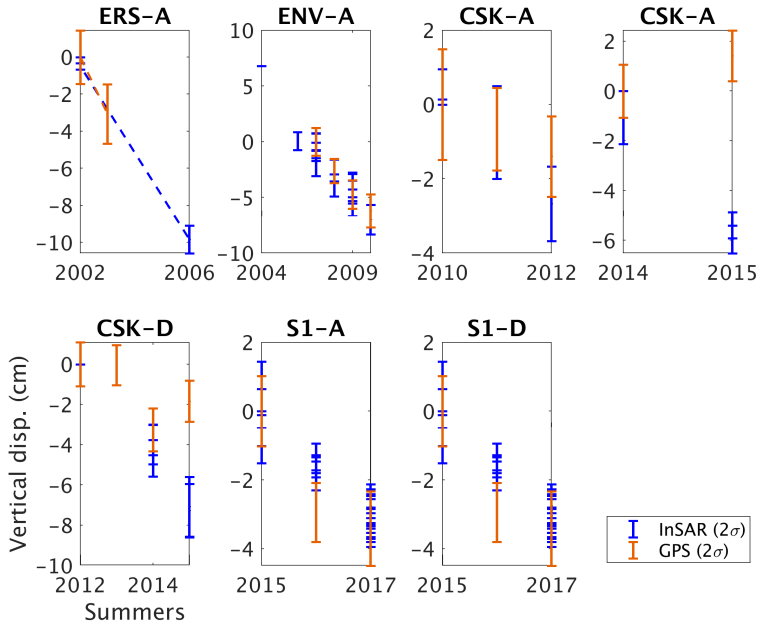

Figure 3.15: Example of vertical displacement time-series, comparing InSAR and GPS at OLAF. I chose this specific station because it is near the centre, and it is the GPS site with the longest time-series, i.e. spanning all InSAR time periods.

3.6 Long-term subsidence and residual signals at Askja

The main objective for this chapter is to test the hypothesis that the observed surface deformation could be the cumulative result of several processes. To test this, I needed to subtract the dominant long-term signal from the data and check the residuals for any signals that would be correlated spatially and temporally.

In Section 3.5, I have explained how I extracted the vertical displacements, $D_V(t)$, from my 15-year InSAR time-series, and I now present how I used these displacements to estimate a bulk vertical subsidence trend, which I then converted into LOS and removed from the full InSAR signal, to determine the residual deformation field over Askja (Figure 3.1).

3.6.1 Long-term subsidence

It is well-established that, for the last few decades, the deformation field at Askja, has been largely dominated by a subsidence signal, centered on the main caldera (Section 1.5.1). A relaxation time, τ, of ~42 years since 1983 was locally constrained from

levelling, in the north-east of the caldera (Section 1.5.1), but this exponential model has not been tested anywhere else in the caldera.

Assuming that a single process is responsible for the dominating long-term subsidence, all pixels should be subsiding exponentially according to the same relaxation time, which should then be very close to the one constrained from levelling. Any parts of the caldera having a different or null decaying time should stand out in the residuals. From this reasoning and considering the same reference time as taken for the levelling study, any deformation parameter, W, should evolve according to the following model:

$$W(t) = -c + W_{\infty}\, e^{-(t-1983)/\tau} \tag{3.13}$$

where $W(t)$ can be $D_V(t)$ at any given pixel, but it can also be the sum or mean of the $D_V(t)$ over a group of pixels or even over the entire Askja caldera, c is a constant and W_{∞} is the total amplitude of exponential decay for the parameter W, up to infinity.

To test whether the local exponential decay from levelling could be applicable to the entire caldera, I used a non-linear least-squares algorithm searching for the combination of model parameters that would best minimise the residual sum of squares between the observed and predicted $W(t)$ equalling the means of $D_V(t)$ per resampled interferogram and over the area of study (e.g. Figure 3.7). But to ensure to capture the long-term trend, I selected only the grid nodes with data available over the full 15-year InSAR time-series (i.e. >5,000 nodes over 50 dates spanning 2002-2017), and I did not use the CSK datasets, because they either had been contaminated by the Holuhraun dyke intrusion reduction (Section 3.3) and/or they would decrease the number of selected nodes in the caldera due to lower coherence (Figures 3.13 and 3.14). Moreover, in addition to solving for τ, c and W_{∞}, I simultaneously solved for offsets between the independent InSAR datasets, following the same approach as described in Equation 3.3.

As illustrated by Figure 3.16, this non-linear inversion approach could not converge towards a reasonable value for τ, and this is most likely because the InSAR data were too noisy. However, when solving for the rest of the parameters, while fixing τ to 42.3 years since 1983 (i.e. similarly as obtained from levelling), the best-fitting model seems to describe well the bulk subsidence trend. This observation supports the hypothesis

that a single process might be responsible for the long-term subsidence, characterized by the same relaxation time as constrained from levelling data.

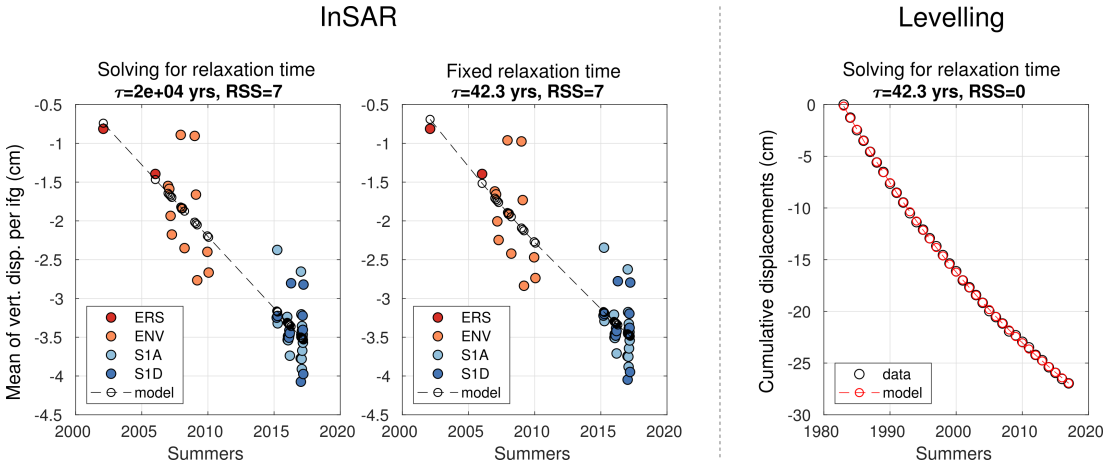

Figure 3.16: Left: Exponential decay model that best-fits the mean of InSAR vertical displacements over the area of study (e.g. Figure 3.7), decomposed from the ERS, Envisat (ENV) and Sentinel-1 (S1) datasets. RSS is the residual sum of squares between the data and the model. Middle: Same as left graph, but in this case, I fixed the relaxation time to equal the one constrained from levelling, i.e. 42.3 years since 1983, as shown to the right. See Section 3.6.1 for more details on calculations and Section 1.5.1 for more details on the levelling study).

Having determined an approximate τ for the entire Askja caldera, I then used normal least-squares to estimate the time-series of the bulk subsidence trend, per grid node, for each InSAR dataset. Indeed, when τ is known, Equation 3.13 becomes a linear problem where c and W_∞ can be constrained for each independent InSAR time-series (including the CSK ones), with the forward matrix operator listing a series of -1 in the first column, and $e^{-(t-1983)/\tau}$ relative to each date in the second column. Because I had used the resampled series of interferograms, I then projected the estimated vertical component of subsidence into LOS direction using Equations 3.6 and 3.7, to get a full constraint of the bulk subsidence field at Askja.

3.6.2 Residual deformation field

Removing this long-term LOS subsidence from the total deformation per resampled interferogram provided a time-series of residual deformation signals (Figures 3.17, 3.18 and Appendix A.4). Due to the rather low magnitudes of residual deformation, ranging within ±0 cm for ERS, ±3 cm for Envisat, ±1.5 cm for CSK and ±2 cm for S1, it is very likely that these time-series mainly reflect noise. The reason why ERS has very

smooth and negligible residuals is most likely because the data, or unwrapped LOS deformation, is almost an exact solution: the unwrapping inversion was performed in StaMPS from three images and three interferograms (Section 3.2).

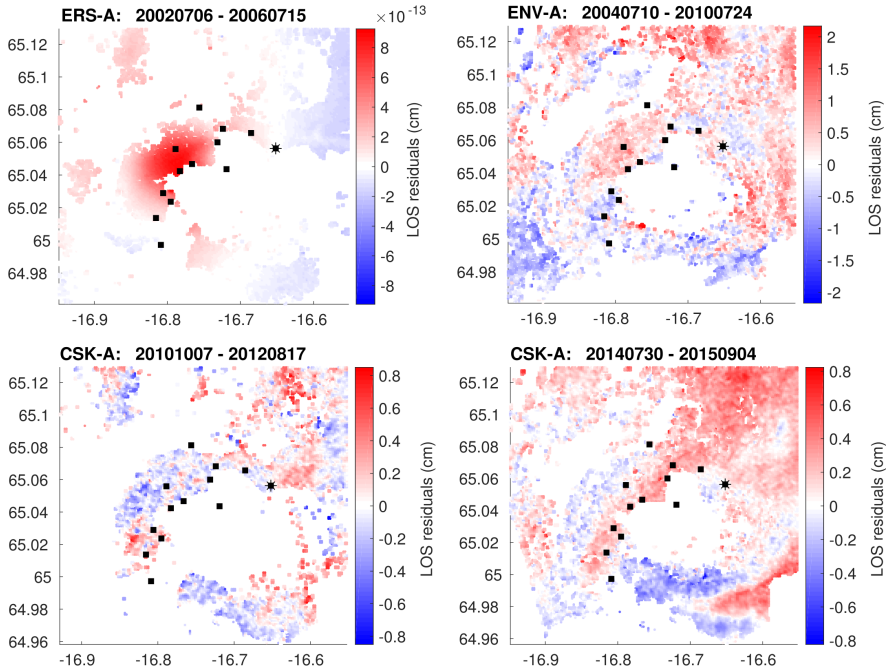

Figure 3.17: Residual LOS displacements shown for the longest interferograms of the ERS-A, Envisat-A and CSK-A datasets, after removal of the long-term exponential decaying subsidence trend. Colorscales are independent (red = away from satellite), while the reference site is DYNG for all datasets (star). See Figure 3.18 for the other sensors, and Appendix A.4 for the full time-series.

Even the small pattern that stands out near the GPS station CASK, in the longest S1-D interferogram (Figure 3.17) as well as in a few others from e.g. Envisat (Appendix A.4), is very likely to be just noise. Indeed, it correlates well with the atmospheric noise of the S1-D velocities (Figure 3.11), which I used to estimate the vertical displacements (Section 3.5.2), and therefore the bulk subsidence time-series.

To confirm these negligible residual results, I de-trended the LOS GPS time-series (Section 3.4) for the deformation modelled using Equation 3.13, estimated at each GPS station, using the same approach as for the InSAR (see above), and which I projected from vertical to LOS by extracting the required InSAR parameters around each station (Equations 3.6 and 3.7). Figure 3.19 shows the residual GPS LOS time-series at some key stations in comparison with the residual InSAR LOS time-series, extracted at each of these GPS stations.

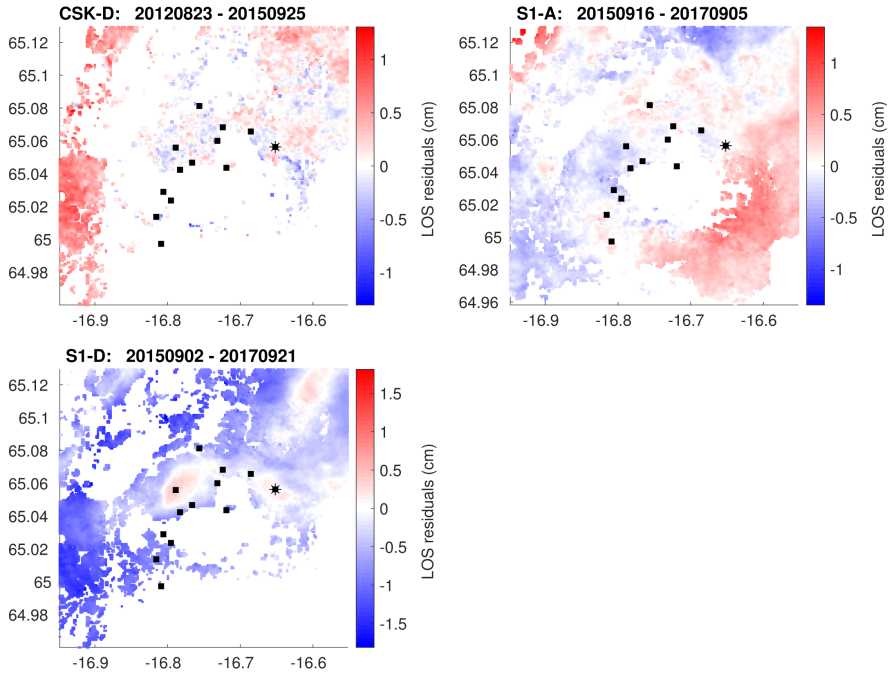

Figure 3.18: Same as Figure 3.17 but for the CSK-D, S1-A and S1-D longest interferograms.

As expected, the GPS and InSAR residual time-series usually agree with each other, and over 2014-2015, the discrepancy due to the Holuhraun dyke reduction is sometimes observed. The time-series at CASK fluctuating around zero confirm that the residual pattern observed in some interfrograms (see above) reflects noise. At OLAF and MASK, which are very near to the centre of deformation, the GPS residuals seem to show some signal correlated with time, between 2007 and 2010 (Envisat). However, as it is not observed in the InSAR residual time-series, this signal could either be noise, or it could reflect a very localised variation in the subsidence trend, but too small to be detectable at the InSAR spatial resolution of tens to hundreds of meters.

The absence of any clear residual signal suggests that no other deformation is superimposed on the subsidence, which has a steady temporal evolution. My hypothesis suggesting that the total deformation observed within the Askja caldera was the cumulative result of several processes, acting at different depths is therefore refuted, and it is likely that a single and steady process is causing the deformation at Askja.

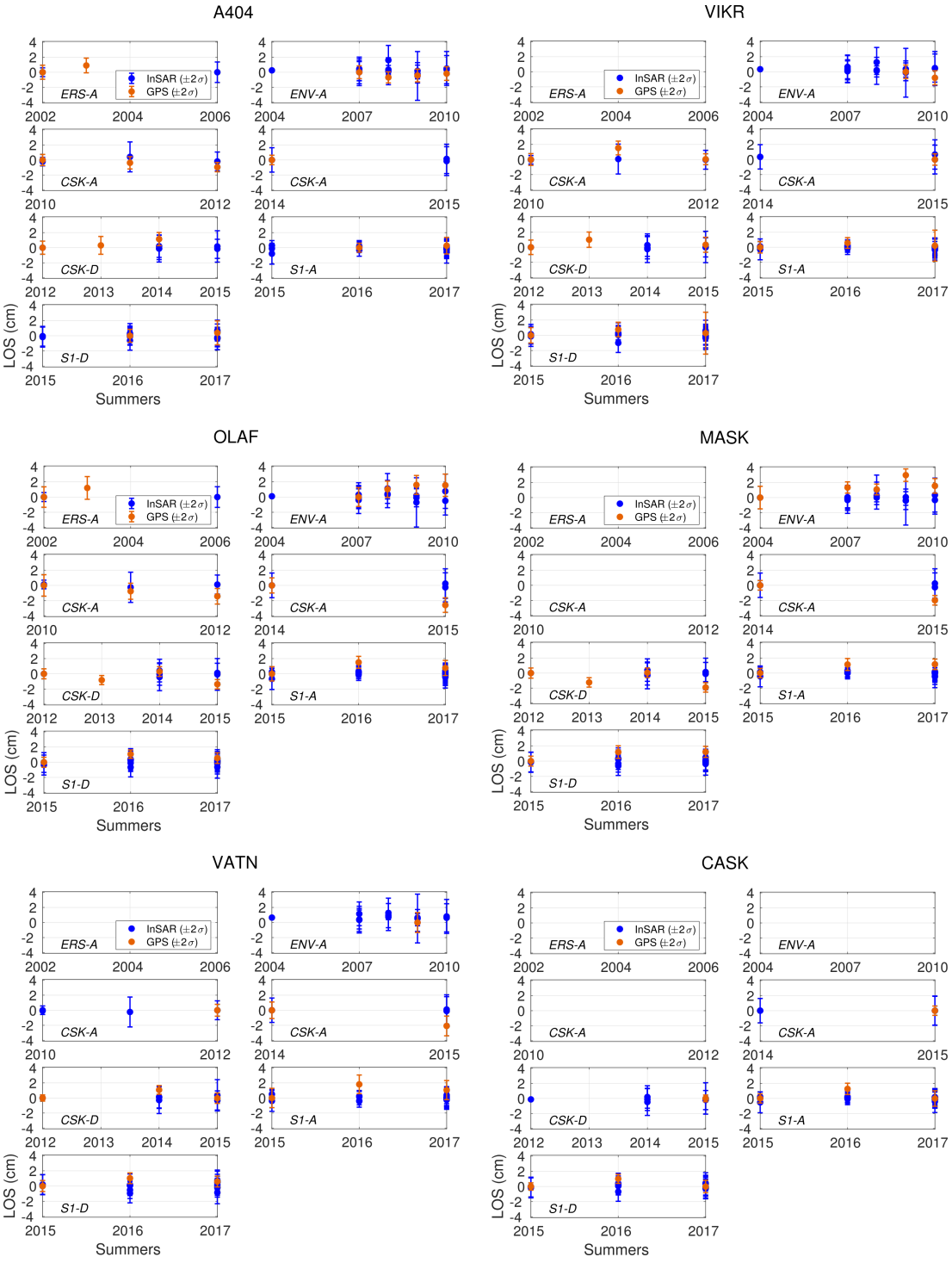

Figure 3.19: LOS GPS and InSAR time-series remaining after removal of the long-term subsidence trend (Section 3.6.1), and shown at key GPS stations, to cover the Askja caldera (positive = away from satellite). The uncertainties associated with the bulk subsidence time-series are not considered in the error bars, but the random variations in these residual time-series provide an estimation of these unknown uncertainties.

3.7 Modelling the exponential subsidence

As presented in Section 1.5.1 and recalled in the introduction of this chapter, several studies have explored the location, depth and magnitude of the most likely linear volume decrease that would be responsible for the Askja subsidence over periods of 10 years or less. Initially using forward models, but then improving results from statistical inversion approaches, these studies mainly agree that the subsidence is probably due to a deflating Mogi (or ellispoidal) reservoir, located at ∼3-3.5 km depth (Table 1.2, Section 1.4.2). Even though, I had questioned this depth, my analysis in Section 3.6 suggests that a single and steady process is likely causing the surface deformation at Askja.

In this section, I provide a redefined model for the Askja subsidence, by predicting the surface deformation, over 2002-2017, taking into account the exponentially decaying evolution. It is the first time that this many InSAR datasets are taken into account, and that such a 15-year-long time period is considered (Figure 3.2).

3.7.1 Bayesian approach with Markov Chain Monte Carlo sampling

In order to generate a fully integrated model, providing some constraints on uncertainties, I used the GBIS software package (Bagnardi and Hooper, 2018), which uses the Bayesian inversion modelling approach and pairs it with the Markov chain Monte Carlo (MCMC) sampling. Given a reservoir geometry chosen by the user and assuming uniform prior probability distributions for the model parameters, GBIS iteratively predicts the LOS surface displacements (or linear velocities) that would be produced by a given set of parameters (also called trial), at the data pixels, initially quadtree subsampled (Bagnardi and Hooper, 2018; and references therein).

The quadtree downsampling approach enables to significantly decrease the number of pixels, while preserving information in deforming areas, and it therefore improves the processing speed. The iteration process, controlled by the MCMC sampling approach, explores the parameter space, by accepting trials with a suitable probability, increasing the chances to converge around the optimal solution, i.e. the set of parameters with maximum probability, or in other words the solution at the peak bin of the N-D histogram (with N the number of parameters). Because all accepted trials are stored,

the posterior probability density function of each parameter can be drawn, and once convergence has been reached these distributions should be Gaussian with the optimal solution lying within the 95% confidence interval.

For each iteration the probability is computed using the residual sum of squares of all the provided downsampled interferograms (or velocity maps), which should be independent from each other and of which the variance-covariance matrices are generated using the semi-variogram approach, with sill, nugget and range provided by the user (Equation 3.5).

Although my InSAR datasets are independent from each other, the interferograms within any given dataset covary, and these covariances should be taken into account in the probability estimation. To avoid memory issues, I considered linear velocities rather than displacements, and this provided a single set of data per InSAR dataset and which do not covary. Because each of these datasets spans a relatively small time period, while they cover 2002-2017 between them all, such approach should not perturb the implementation of the exponentially decaying trend. Indeed, the estimated linear rates should give the tangents to the exponential subsidence trend at the mid-times of the datasets, and the gradual decrease should still be observed over the 15-year velocity time-series.

Using the total unwrapped phases, given in radians ($\Delta\varphi_{\text{corr}} \approx \Delta\varphi_{\text{ask}}$, Section 3.4), I estimated these LOS velocities per pixel, by applying weigthed least-squares, with variance-covariance matrix listing constant variances per interferogram in the diagonal (Equation 3.5 with r=0). I then re-computed a semi-variogram (Section 3.4.4) for each estimated velocity field, in order to provide a sill, nugget and range per satellite sensor for GBIS to estimate the variance-covariance matrix.

3.7.2 Implementation of the exponential decay using a Mogi model

As a first test, I assumed the point pressure source (Mogi, 1958), as it is the simplest approximation but also because, based on previous studies, this model seems to approximate well the deformation field at Askja (Table 1.2).

Because the Mogi model assumes a homogeneous and elastic crust (Section 1.4.2),

the volume change of the Mogi reservoir beneath Askja should evolve according to the same function as the displacements observed at the surface (Equation 3.13):

$$\Delta V(t) = -c + \Delta V_{\infty}\, e^{-(t-1983)/42.3} \tag{3.14}$$

where t is given in decimal years.

Incorporating this function into the default Mogi forward problem (Equations 1.15 and 1.16) can predict displacements. To predict velocities, I took the derivative of Equation 3.14 with respect to time. The forward problem used to estimate surface velocities caused by a Mogi reservoir experiencing an exponentially decaying volume change can therefore be expressed, at any pixel, as follows:

$$\dot{D}_H(t) = \frac{-(1-y)\Delta V_{\infty}\, e^{-(t-1983)/42.3}}{42.3\pi} \frac{r}{(z^2+r^2)^{3/2}} \tag{3.15}$$

$$\dot{D}_V(t) = \frac{-(1-y)\Delta V_{\infty}\, e^{-(t-1983)/42.3}}{42.3\pi} \frac{z}{(z^2+r^2)^{3/2}} \tag{3.16}$$

where y equals 0.25 (Poisson's ratio, Section 1.4.1), and $\dot{D}_H(t)$ and $\dot{D}_V(t)$ are the horizontal and vertical components of any LOS velocity, given at the time t, which is the mid-time of the related InSAR dataset (Section 3.7.1).

By implementing this forward model into GBIS, I solved for the longitude, latitude, depth and ΔV_{∞} related to an exponentially deflating Mogi reservoir. I also solved for a constant per dataset representing the velocity of the reference site, as well as for possible ramps affecting each velocity field, along longitude and latitude.

Because the CSK datasets spanning 2014-2015 were contaminated by unwanted deformation signals remaining after reduction of the Holuhraun dyke intrusion effect (Section 3.3), I performed the MCMC Bayesian inversion, with (Case A) and without (Case B) these two affected datasets, to check the influence of the imprecise reduction. I therefore solved for 25 model parameters in Case A and 19 in Case B.

3.7.3 Modelling results

In both cases, I ran two million iterations, and as shown in Appendix A.5, convergence was reached after <200,000 iterations. After convergence, the posterior probability density functions are, as expected, approximately Gaussian (Appendix A.5), and because the optimal solution lies within the 95% confidence interval, highlighted by the 2.5 and 97.5 percentiles, the inversion has worked well in both cases (Section 3.7.1). However, because the optimal solutions are not always centered on the Gaussian distributions, the median solutions provide a better fit (Appendix A.5). As summarized in Table 3.2, these medians are very close to each other when comparing the two cases, suggesting that the imprecise reduction of the Holuhraun dyke intrusion effect did not affect the inversion. Indeed, the ramp estimations have likely contributed to reducing this unwanted effect.

	Case A			Case B		
	2.5 perc.	**Median**	97.5 perc.	2.5 perc.	**Median**	97.5 perc.
Longitude (deg.)	-16.775	**-16.774**	-16.771	-16.775	**-16.774**	-16.772
Latitude (deg.)	65.045	**65.046**	65.047	65.045	**65.046**	65.047
Depth (km)	2.9	**3.0**	3.1	2.8	**3.0**	3.1
ΔV_∞ (km^3)	0.063	**0.070**	0.076	0.061	**0.067**	0.075

Table 3.2: Medians and 2.5-97.5 percentiles constrained when solving for an exponentially deflating Mogi reservoir beneath Askja, using the MCMC Bayesian approach provided by the GBIS software. In Case A, all InSAR datasets were considered, whereas in Case B, the two CSK datasets spanning the Holuhraun dyke intrusion period were not considered (Sections 3.7.1 and 3.7.2).

3.7.3.1 Models quality

To be able to compare the goodness-of-fit between Case A and Case B, I performed a χ^2 test (Section 3.4.4) with 95% probability and ν equalling the cumulative sum of quadtree pixels per satellite sensor minus 25 in Case A and minus 19 in Case B (See end of Section 3.7.2). Additionally, to evaluate the relative contribution of each dataset, I also performed a χ^2 test per satellite sensor, i.e. considering the number of subsampled pixels per sensor and 7 model parameters (4 Mogi parameters, 1 offset, and 2 ramps, Section 3.7.2).

As shown in Table 3.3, the reduced chi-squared, χ^2_ν, are very similar between the two

cases, and Case B fits the data sightly better with the ERS velocity field slightly better approximated (smaller χ^2_ν than in Case A). When looking at the difference between the observed and expected reduced chi-squared with 95% probability ($\chi^2_\nu - \chi^2_{\nu,0.95}$, Table 3.4), even though the Envisat and S1-A predicted maps are the only ones lying within the 95% confidence interval ($\chi^2_\nu - \chi^2_{\nu,0.95} \leq 0$), all the other predicted maps have acceptable near-zero differences, except the ERS one. This implies that a better fit to the ERS data is not necessarily representative of the Askja deformation, and Case A is therefore most likely the best-fitting model to predict the long-term deformation field of Askja (Figure 3.20).

χ^2_ν	**Total**	ERS	Envisat	CSK-A (10-12)	CSK-A (14-15)	CSK-D	S1-A	S1-D
Case A	**1.45**	7.73	0.59	1.77	1.76	2.40	1.28	0.44
Case B	**1.29**	7.71	0.59	1.77			1.28	0.44

Table 3.3: Reduced chi-squared, (χ^2_ν, Section 3.4.4), for the median solutions considering all satellite sensors (Case A) versus all but the ones affected by the imprecise reduction of the Holuhraun dyke intrusion effect (Case B). The first column provides the χ^2_ν of the full inversion, whereas the other columns provide the χ^2_ν per satellite sensor (Section 3.7.3.1).

χ^2_ν-$\chi^2_{\nu,0.95}$	**Total**	ERS	Envisat	CSK-A (10-12)	CSK-A (14-15)	CSK-D	S1-A	S1-D
Case A	**0.41**	6.53	-0.66	0.60	0.67	0.93	0.21	-0.64
Case B	**0.24**	6.51	-0.66	0.60			0.21	-0.64

Table 3.4: Same as Table 3.3 but here, the differences between the estimated and expected reduced chi-squared (χ^2_ν-$\chi^2_{\nu,0.95}$, Section 3.4.4) are provided.

Pagli et al. (2006) estimated their best solution as the mean of four independent simulated annealing inversions, each combining GPS displacements with a distinct interferogram of 2-6 years between 1992 and 2000 (Table 1.2). While fixing the reservoir location, they obtained a χ^2_ν of 0.77, 3.64, 4.03 and 7.99 per interfergoram. More recently, de Zeeuw-van Dalfsen et al. (2012) constrained their best-fit solution using an MCMC Bayesian algorithm, with ascending and descending velocity maps, both spanning 2000-2009, and respectively estimated from 4 and 5 interferograms (Table 3.5). If the residual standard deviation that they provide is the square root of the weighted residual sum of squares divided by the degree of freedom, they obtained a χ^2_ν of 1.15, when using only the descending velocity map, and a χ^2_ν of 15.62 when using both velocity

maps.

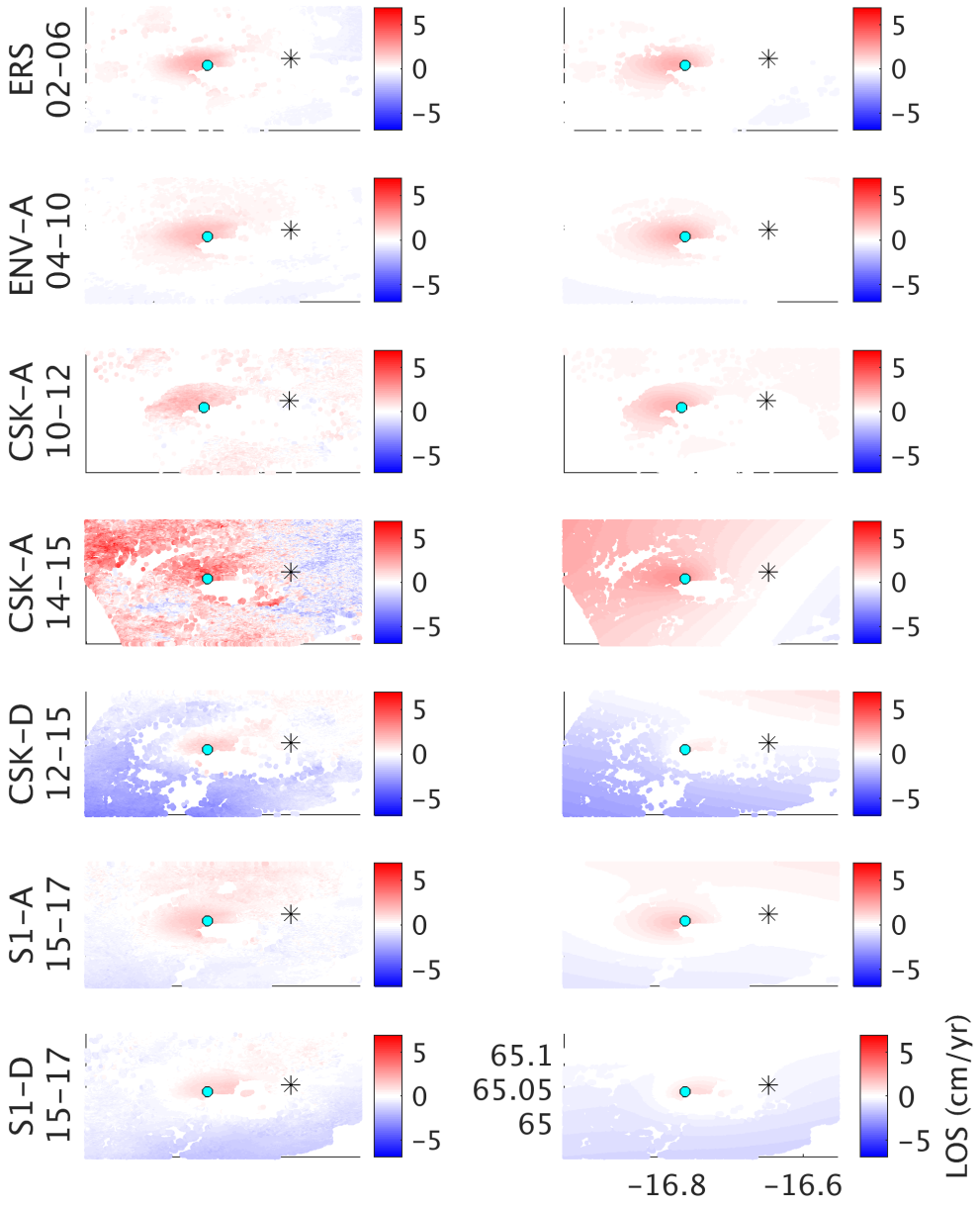

Figure 3.20: Observed (left) versus predicted (right) LOS velocity maps per satellite sensor (red = away from satellite). The predicted velocities were constrained using the median solutions, assuming an exponentially deflating Mogi reservoir beneath Askja (Case A, Table 3.2). The best-fit reservoir location is highlighted with the cyan circle, and the star is the reference for deformation (DYNG).

By comparison, the total χ^2_ν and χ^2_ν-$\chi^2_{\nu,0.95}$ obtained in this study and being respectively <1.5 and near zero, suggest that the inversion has well-constrained the long-term velocity time-series, especially because the larger the number of datasets used, the harder the fitting and therefore the more likely it is to get a high χ^2_ν.

95% confidence intervals	longitude	latitude	depth	ΔV_∞	ΔV
Case A (this study)	180 m	235 m	200 m	0.013 km^3	-
d.Z.v.D. et al. (2012)	400 m	400 m	600 m	-	-0.0005 km^3 yr^{-1}

Table 3.5: Comparison of the 95% confidence intervals constrained in this study (Case A) with the one provided by de Zeeuw-van Dalfsen et al. (2012). An MCMC Bayesian algorithm was used in both cases, assuming a Mogi model, but de Zeeuw-van Dalfsen et al. (2012) constrained a linear volume change, whereas I constrained the amplitude of an exponential decay (Section 3.7.2).

3.7.3.2 Comparison of the best solution with previous studies

In addition to having well-constrained the data, my long-term exponential inversion provided a best-fit solution with same order of magnitude as those estimated in previous studies (Table 1.2 and Figure 3.21). However, the redefined depth seems to be $3^{+0.1}_{-0.1}$ km rather than 3.5 km (Case A, Table 3.2), and the corresponding volume change rates are also lower (Figure 3.21). Assuming that the Mogi model is appropriate to approximate the pressure change distribution, which is linked to the bowl shape subsidence of the Askja caldera, these narrower error bounds are likely due to the length of time spanned in this study: it is the first time such a 15-year long deformation dataset is implemented in a inversion model at Askja.

Due to the non-uniqueness of deformation models, the depth and magnitude of volume changes are closely linked: for a given reservoir geometry, a deep and large volume change produces the same surface deformation as a smaller but shallower volume change (Section 1.4.2). The greater depths constrained from previous studies can therefore explain why the associated volume decreases have larger magnitudes. Indeed, the best-fit solution from de Zeeuw-van Dalfsen et al. (2012), who solved for all parameters using an MCMC Bayesian algorithm, was a 3.5-km deep Mogi reservoir, deflating at a linear rate of 0.0014 km^3 yr^{-1} over 2000-2009 (Section 3.7.3.1 and Figure 3.2). According to Equation 1.16, such scenario should produce a maximum vertical subsidence of ∼2.7

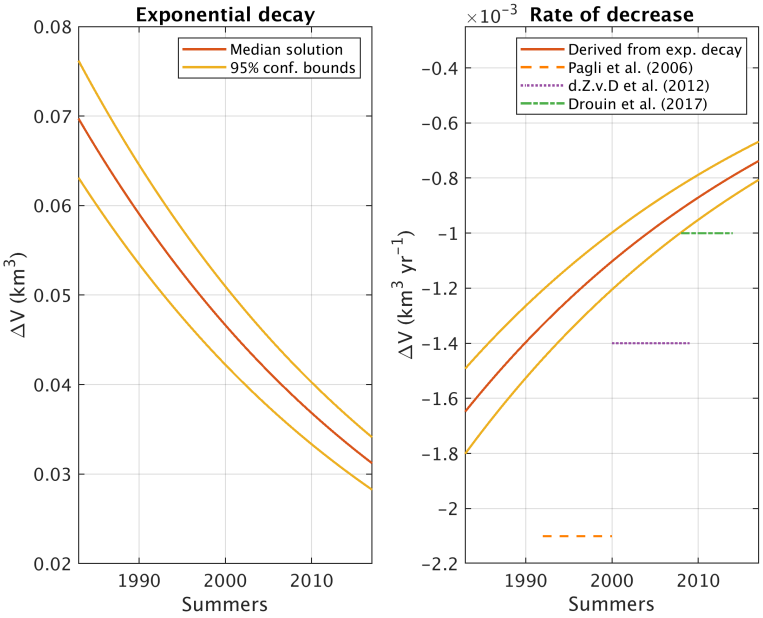

Figure 3.21: Left: Exponential decay expected at the Mogi source between 1983 and 2017 (Equation 3.14 with c=0), assuming a ΔV_∞ of 0.07 km^3 with a 95% confidence interval of 0.013 km^3 (Table 3.2). Right: Derivation of the rate of decrease at any time t, i.e. equalling $-\Delta V(t)/42.3$, and comparison with the linear volume rates that have been constrained in previous studies, using inversion modelling (Table 1.2). Note that the best-fit volume change from Pagli et al. (2006) is the average of several models, for which the average depth is 3.5 km.

cm yr^{-1}, which would also result from a 3-km deep Mogi reservoir, deflating at rate of ∼0.0010 km^3 yr^{-1}. Based on my exponential model, this is what we should expect in 2003, i.e. at the mid-time of 2000-2009 (Figure 3.21).

Similarly, among the various single-interferogram inversions tested by Pagli et al. (2006), the few solutions that provided a depth around 3 km were associated to volume changes of -0.0012 to 0.0014 km^3 yr^{-1}, and, based on my exponential model, this is approximately what should be expected at the time of their study (Figure 3.21). Because Pagli et al. (2006) solved for an ellipsoid reservoir, this either suggests that the constrained aspect ratio, orientation and depth of the ellipsoid produced similar surface deformation as a Mogi reservoir, or it is just a coincidence.

Finally, based on the results from de Zeeuw-van Dalfsen et al. (2012), Drouin et al. (2017) assumed a Mogi reservoir at 3.5 km depth and constrained a volume change of -0.0010±0.00001 km^3 yr^{-1}, from a simulated annealing inversion applied to GPS data over 2008-2014. This scenario should induce a maximum vertical deformation rate

between -1.94 and -1.96 cm yr^{-1} if the source would be at 3 rather than 3.5 km depth (Equation 1.16). From my exponential model, the maximum vertical deformation at this period should range between -1.98 and -2.52 cm yr^{-1}, which is very close to their result. In addition to using discrete GPS datapoints (Figure 3.7), the fact that they did not solve for all parameters simultaneously might the reason why a slight discrepancy still remains.

Overall, the quasi-systematic offset does not seem to be due to different observed deformation, neither to the assumed models, which are very similar: ellispoid or Mogi reservoir, embedded in an elastic half-space, having a Poisson's ratio of 0.25. It is therefore likely that the offsets comes from the different dataset sizes and the use of different temporal functions might also have induced some discrepancy. The good quality of my inversion (Section 3.7.3.1), which considers the exponential evolution of the subsidence using the longest dataset, suggests that the results presented in this study are more robust. To confirm this, other source geometries could be tested, and the GPS data could be jointly inverted with the InSAR.

3.7.3.3 Residual velocity maps

Using the median solution from Case A, which I think is the most appropriate to predict the long-term deformation at Askja (Section 3.7.3.1), I predicted the LOS velocity field that would be produced by such exponentially deflating Mogi reservoir, considering the initial pixel distribution of each velocity map.

After removing these predicted velocities from the observed ones, residuals seem to be mainly dominated by random noise, but two subsidence signals remain (Figure 3.22): one is approximately centred on the caldera, clearly observed in the CSK-D 2012-2015 map and has a magnitude of ∼1-1.5 cm yr^{-1} along LOS (away from the satellite), whereas the other one, observed at least in the ERS, Envisat and S1-A maps, is located in the north-east of the caldera, near station A404 (Figure 3.7) and has a magnitude of ∼0.5 cm yr^{-1} along LOS. de Zeeuw-van Dalfsen et al. (2012) did not detect this latter quasi-persistent anomaly, and it is not clear whether Pagli et al. (2006) detected it. Indeed, the only mentioned residual subsidence has a rate of ∼0.8 cm yr^{-1} and is

located to the west of the lake Öskjuvatn, while this anomaly is rather located to the north of the lake (incoherent area in Figure 3.22, see Figure 3.7).

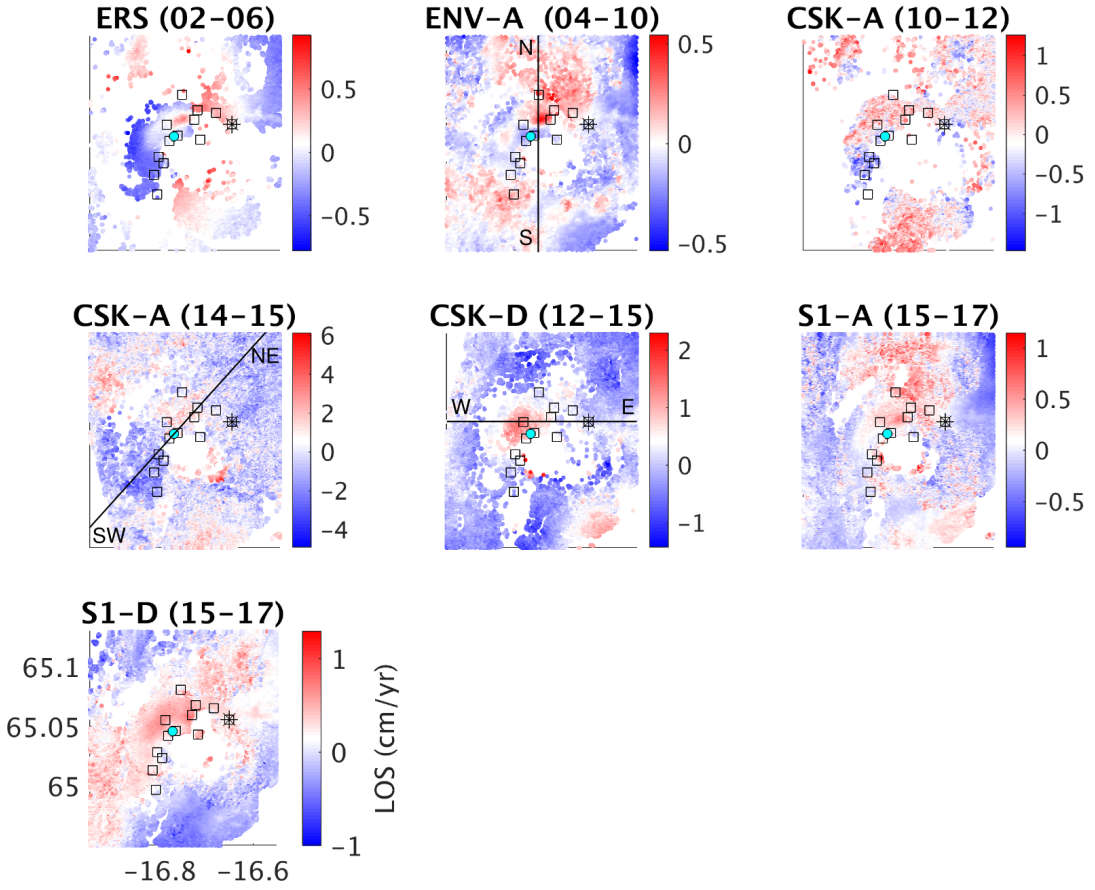

Figure 3.22: Residual LOS velocity maps per satellite sensor (red = away from satellite), after removing the predicted deformation caused by an exponentially deflating Mogi reservoir beneath Askja (Case A, Section 3.7). The best-fit reservoir location is highlighted with the cyan circle, GPS stations are shown with the black squares, DYNG (star) is the reference for deformation and the location of the profiles presented below are highlighted with the black lines. Note that scales are independent due to the large residuals in the CSK-A 2014-2015 maps.

When comparing the observed and predicted velocities along a SW-NE profile passing through the centre of the caldera (Figure 3.23), it is confirmed that the Mogi model (Case A in Table 3.2) seems to well predict the observed subsidence signature. Moreover, the overall shape of the CSK-D profile confirms that unwanted effect caused by the imprecise Holuhraun dyke reduction has mainly been reduced by the ramp estimation (See beginning of Section 3.7.3). Finally, as expected from Figure 3.22, residuals are mainly around zero, with a quasi-persistent anomaly on the NE side of the caldera centre, and the CSK-D anomaly seems to appear as an offset from the modeled subsidence.

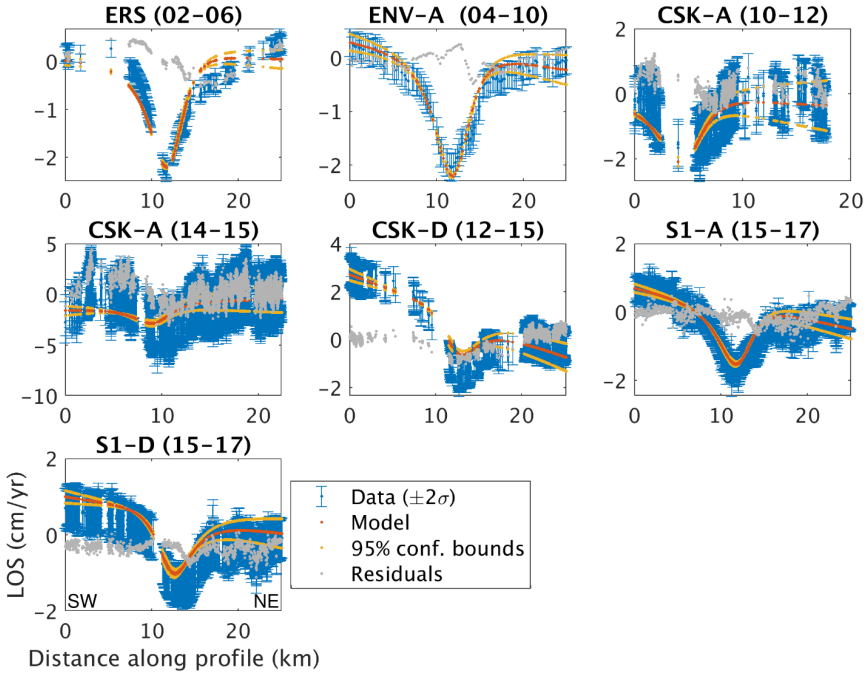

Figure 3.23: Comparison of the observed LOS velocities (blue) with the predicted ones (red, Case A in Table 3.2), along a SW-NE passing through the best-fit Mogi reservoir location (Figure 3.22). The 95% confidence interval (yellow) was computed using the 2.5 and 97.5 percentile median solutions, and residuals are shown in grey. Signs have been flipped to provide the subsidence (positive LOS) as a negative signature.

Based on Figure 3.24, which displays results along a north-south profile passing through the quasi-persistent residual signal, it seems that this anomaly is due to the geometry of the Mogi model, which cannot fully reproduce the surface deformation field, likely to be due to a single and steady process (Section 3.6). But it is worth noting that such inversion procedure does not primarily aim to determine the geometry of the magma reservoir, if any. The aim is rather to reproduce the conditions of pressure changes in the subsurface, likely to reproduce a surface deformation pattern (Section 1.4). The Mogi model assumes isotropic inner pressure distribution, surrounded by a homogeneous and elastic crust. The anomaly therefore suggests that, in this localised area, either the subsurface pressure cannot be approximated by an isotropic distribution and/or the property of the host-rock vary too much to be approximated by the homogeneous and elastic medium. Although it is challenging to determine the exact reason of such residual anomaly, this area has been overloaded by lavas from the most recent 1961 fissure eruption and such extra load could have modified the local crustal

properties enough to increase the subsidence locally, while having re-equilibrated to the same relaxation time as over the entire caldera (Figure 3.6.2).

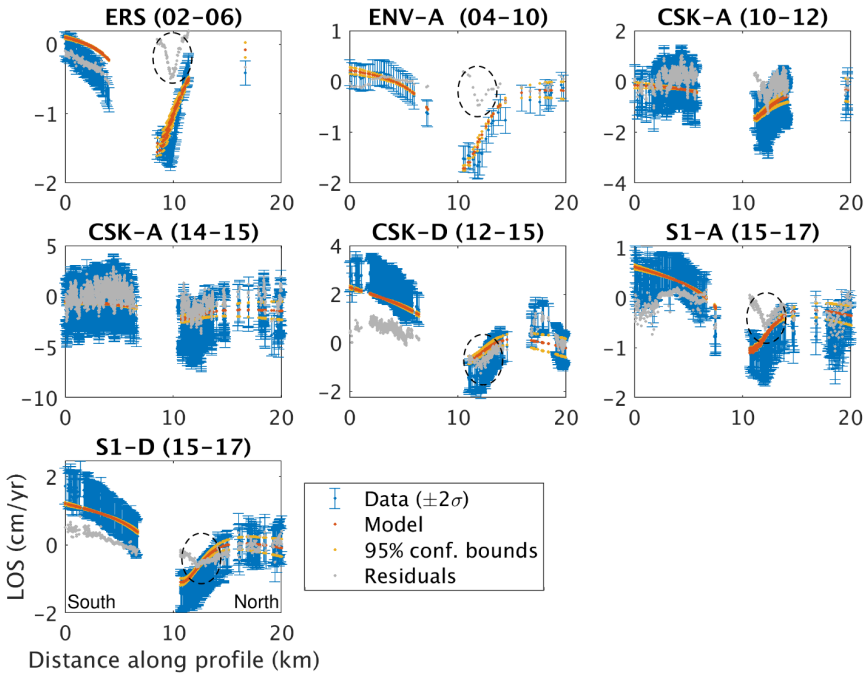

Figure 3.24: Same as Figure 3.23, but this profile is north-south orientated (Figure 3.22) and passes through the persisting residual anomaly observed near the GPS station A404, in the north-east of the caldera (dashed circle).

Finally, Figure 3.25, which shows results along an east-west profile passing through the residual subsidence detected in the centre of the caldera, confirms that this anomaly is only observed on the CSK-D map. Because the imprecise Holuhraun dyke reduction mostly affected the centre of the caldera (Figure 3.8), is it very likely that the anomaly results from this remaining deformation signal. Indeed, it seems that the observed subsidence has been shifted from the predicted one, and this pattern is also noticed when comparing the imprecisely reduced CSK-D InSAR signal with the more precisely reduced GPS signal (OLAF in Figure 3.8). Based on this reasoning, the CSK-A map should also show a similar pattern, but in this case, the ramp estimation might have reduced most of the unwanted effect.

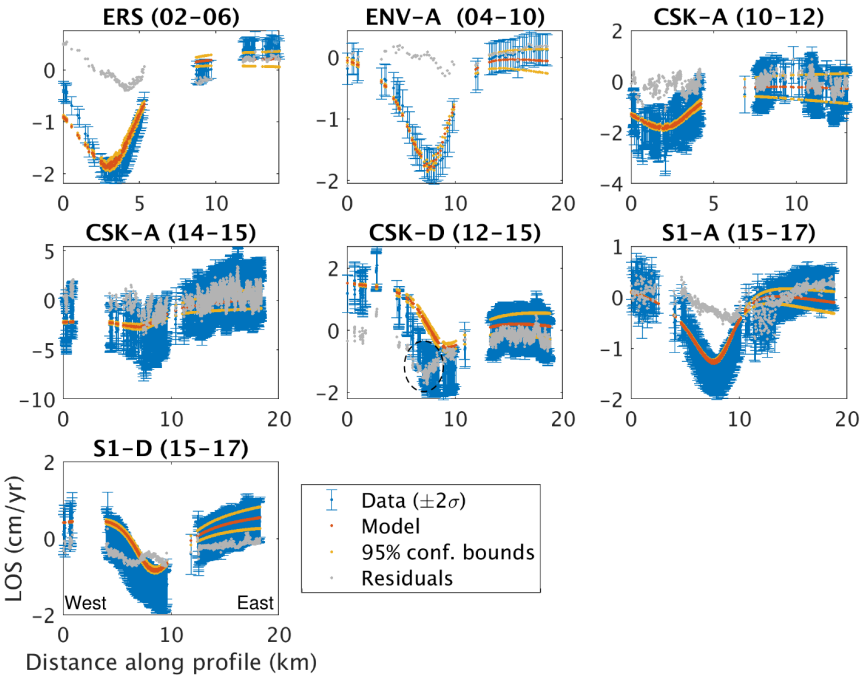

Figure 3.25: Same as Figure 3.23, but this profile is east-west orientated (Figure 3.22) and passes through the residual anomaly observed near the centre of deformation, in the CSK-D map (dashed circle).

3.8 Conclusions

In this Chapter, I demonstrated that the subsidence, which has been on-going within the Askja caldera between at least 1983 and 2017, can be modeled by an exponential decay with a relaxation of ∼42 years since 1983, i.e. similarly as locally constrained from levelling data. This steady subsidence seems to be the main deformation pattern affecting the caldera.

Using a 15-year sample of InSAR data spanning 2002-2017, I demonstrated that the long-term caldera deformation can be robustly predicted by a 3-km deep Mogi reservoir, centered on the Askja caldera and undergoing an exponential deflation with total volume change amplitude of 0.07 km^3. Based on this model, the rate of volume decrease has diminished from ∼0.0016 km^3 yr^{-1} in 1983 to ∼0.0008 km^3 yr^{-1} in 2017. A persisting residual subsidence signal of ∼0.5 cm yr^{-1} along LOS, remains in the north-east of the caldera, and it could be due to a wrong approximation of subsurface pressure distribution assumed by the Mogi model. Alternatively, it could also be due to some strong crustal heterogeneity, and the possible lava overloads from 1961 might

be something to explore.

Because I demonstrated several times that the GPS and InSAR data agreed well over 2002-2017, jointly inverting for these two types of data would very likely provide a similar solution, but it could still be interesting to verify this. Moreover, even though the Mogi reservoir provided very good results, testing this new exponential model with other source geometries may improve the results.

Even though the deformation can be explained by a Mogi model, which is often used for magma intrusion or magma drainage scenarios, this analysis does not imply that magma is involved. Moreover, a dominant magma contribution from a 3-km deep reservoir to produce such a long-term and steady subsidence can be questioned. Before testing the implication of magma by comparing this detailed deformation study to some new gravity measurements (Chapter 5), I present, in Chapter 4, an error analysis of temporal gravity changes.

Chapter 4

Error Budget Analysis for Residual Gravity Changes

This chapter addresses the third objective of my thesis, by presenting a statistical approach I have developed to better estimate uncertainties associated to residual gravity changes. In Chapter 5, I apply the method to the gravity data that I recorded at Askja.

4.1 Introduction

As summarized in Chapter 1, monitoring temporal gravity changes can be useful to detect mass movements related to magma processes, and can therefore contribute to characterizing volcanic unrest (e.g. Crossley et al., 2013, Carbone et al., 2017, Van Camp et al., 2017). However, the signal of interest, or residual gravity change (Section 2.2), is emphasized only once all the undesirable signals have been reduced as much as possible (Section 2.2.2). To be able to detect any magma-related residual gravity changes, which are typically on the order of tens to hundreds of microgals (Figure 4.1 and Table 4.1), and which therefore represent variations of only ∼0.1-0.01 ppm around the standard gravity on Earth, high-precision gravimeters have been designed and thorough surveying procedures have been implemented (e.g. Rymer, 1996, Battaglia et al., 2008, Carbone et al., 2017, Van Camp et al., 2017). But, even though equally important, there seem to be a lack of guidance in the estimation of the errors associated to the reduction of

unwanted effects.

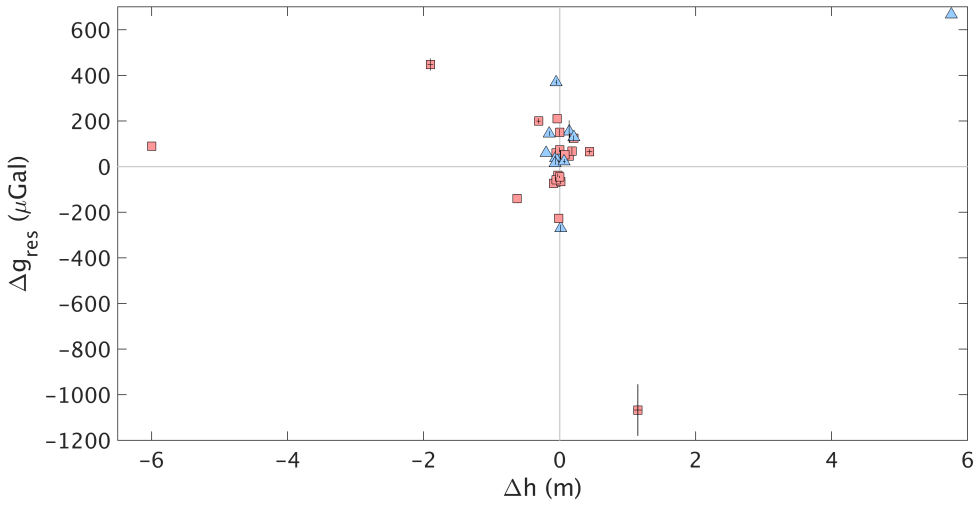

Figure 4.1: Maximum estimated residual gravity changes at volcanoes versus the vertical displacement measured at the same stations. The gravity data were acquired either with LaCoste & Romberg G and/or D meters (red squares), or with Scintrex CG-3M or CG-5 meters (blue triangles). The 1σ error bars are displayed when given. Table 4.1 summarizes the data used in the figure with corresponding references.

Rymer (1989) presented an overview of all possible error sources involved when using LaCoste & Romberg (LCR, LaCoste & Romberg (2004)) gravimeters during a single survey. They came to the conclusion that the error standard deviation of any drift-corrected gravity signal ($\hat{g}_{\mathrm{DC}}$ in Section 2.2.3) should be $\leq$10 μGal at best, and $\sim$33 μGal, at worst. Even though this analysis provides some information on where to focus effort to reduce errors when using LCR gravimeters, it does not provide any method to quantify errors on a case-by-case basis. Moreover, worst-case errors seem to have been underestimated, such as, for example, the one associated with the leveling of the instrument, and this study does not cover errors associated to temporal gravity changes.

Twenty years later, Lederer (2009) provided an overview of error sources likely to affect temporal gravity changes, and they highlighted that error standard deviations of $\sim$6 and $\sim$11 μGal can possibly be achieved, in optimal field conditions, when respectively using SCG gravimeters (type CG-5) and LCR gravimeters (type G). Even though this study provides an exhaustive list of error sources, it lacks information to precisely quantify errors, especially for groundwater-mass changes and calibration ef-

Table 4.1: List of data used in Figure 4.1 and corresponding references. Temporal gravity has been applied to more volcanoes (Carbone et al., 2017) but the maximum residual gravity changes were not always provided, neither the associated error standard deviation.

ID	Volcano	Station	Period	Δg_{res}(μGal)	σ_{res}(μGal)	Δh (m)	$\sigma_{\Delta h}$(m)	Gravimeter	References
1	Askja	*Caldera centre*	Mid. 1988 - Mid. 2007	-140		-0.625		LCR-G	Rymer et al., 2010 and ref. therein
2	Askja	*Caldera centre*	Mid. 2007 - Mid. 2008	60		-0.05		LCR-G	Rymer et al., 2010 and ref. therein
3	Etna	TG	Late. 1995 - Mid. 1998	50		0.03		SCG CG3M	Del Negro et al., 2013 and ref. therein
4	Etna	TG	Mid. 1999 - Mid. 2002	30		0.03		SCG CG3M	Del Negro et al., 2013 and ref. therein
5	Etna	TG	2010 – Late 2011	60		-0.2		SCG CG3M	Del Negro et al., 2013 and ref. therein
6	Izu-Oshima	MK	Dec. 1986 - Aug. 1987	-68	3.3	-0.05		LCR-G	Wanatabe et al, 1998
7	Izu-Oshima	MK	Aug. 1987 - Oct. 1987	26	5.3	-0.01		LCR-G	Wanatabe et al, 1998
8	Izu-Oshima	MK	Nov. 1987 - Mar 1988	-38	7.2	-0.027		LCR-G	Wanatabe et al, 1998
9	Izu-Oshima	MK	Mar. 1988 – Mar. 1991	47	9.2	0.14		LCR-G	Wanatabe et al, 1998
10	Kilauea	HVO41	Dec. 1975 - Jan. 2008	448	27	-1.9	0.041	LCR-G	Johnson et al., 2010
11	Kilauea	HVO44	Dec. 2008 - Jul. 2010	53	20	0.006		SCG CG-5	Bagnardi et al., 2014
12	Kilauea	HVOLG	Jul. 2010 - Mar. 2011	37	15	-0.06		SCG CG-5	Bagnardi et al., 2014
13	Kilauea	HVOLG	Mar. 2011 - Nov. 2012	154	49	0.14		SCG CG-5	Bagnardi et al., 2014
14	Komagatake	BM 1310	Nov. 1996 - May 1998	15	6	-0.065		SCG CG-3M	Jousset et al., 2000b
15	Krafla	A004	Mid. 1990 - Mid. 1995	-73		-0.09		LCR-G	De Zeeuw Van Dalfsen et al., 2006 and ref. therein
16	Krafla	OS5684	Mid. 1996 - Mid. 2003	-65		0.018		LCR-G	De Zeeuw Van Dalfsen et al., 2006 and ref. therein
17	Laguna del Maule	GLM06	Apr. 2013 - Jan. 2014	124	12	0.208		LCR-G	Miller et al., 2017
18	Laguna del Maule	GLM07	Mar. 2015 - Feb. 2016	68	16	0.182		LCR-G	Miller et al., 2017
19	Long Valley	17JCM82	1982 - 1999	66	11	0.44	0.04	LCR-G and -D	Tizzani et al., 2009 and ref. therein
20	Mauna Loa	C1	Feb. 1984 - May 1984	-57	11	-0.052		LCR-G	Johnson, 1995
21	Mayon	TLC1	Dec. 1992 - Dec. 1996	150	15	0		LCR-G and -D	Vajda et al., 2012 and ref. therein
22	Merapi	DOZ	1993 - 1994	370	11	-0.05	0.01	SCG CG-3M	Jousset et al., 2000a
23	Merapi	DOZ	1994 - 1995	-270	15	0.015	0.003	SCG CG-3M	Jousset et al., 2000a
24	Mount St Helens	SLOB	Mid. 2010 – Mid. 2016	145	10	-0.153	0.003	2 SCG CG-5	Battaglia et al., 2018
25	Pacaya	*E of crater*	Jun. 1979 - Jan. 1980	210		-0.036		LCR-G	Eggers, 1983
26	Pacaya	*NW of crater*	Jan. 1980 - Jun. 1980	-227		-0.013		LCR-G	Eggers, 1983
27	Piton de la Fournaise	610	Nov. 1997 - Mar. 1998	129		0.21		SCG CG-3M	Bonalvot et al., 2008
28	Poas	G1	1985 - 1989	200	11	-0.31	0.03	LCR-G	Rymer and Brown, 1989
29	Sakurajima	BM.SVO	1975 - Nov. 1982	89		-6		LCR-G	Yokoyama, 1989 and ref. therein
30	Sierra Negra	SN09	Jun. 2002 - Jun. 2005	-1067	113	1.15	0.06	LCR-G	Vigouroux et al., 2008 and ref. therein
31	Soufriere Hills	STPT	Jun. 2006 - Jan. 2007	-45	5.5	0		LCR-G	Hautmann et al., 2010
32	Soufriere Hills	MVO2	Jan. 2007 - Aug. 2008	74	10	0		LCR-G	Hautmann et al., 2010
33	Three Sisters	CENTER	Aug. 2002 – Sept. 2009	52		0.078		LCR-G and -D	Zurek et al., 2012
34	Usu	UST	Oct. 1996 - Aug. 1997	23	10	0.067	0.02	SCG CG-3M	Jousset and Okada, 1999
35	Usu	BM 8002	Jul. 1998 - Nov. 2000	667		5.76		SCG CG-3M	Jousset et al., 2003

fects ($\Delta\hat{g}_{\text{wtr}}$ and $\Delta\hat{g}_{\Delta\text{cal}}$ in Section 2.2.3). Moreover, it wrongly assumes that the use of the local gravity gradient is the most appropriate to estimate the component due to surface deformation ($\Delta\hat{g}_{\text{elev}}$ in Section 2.2.3).

In this chapter, I go one step further in the analysis of errors associated to temporal gravity changes, by presenting a statistical approach providing key information for users to quantify the full error budget of residual gravity changes, when using SCG (types CG-3/CG-3M and CG-5) and LCR (types G and D) gravimeters (Section 2.2). In addition to providing equations for case-by-case calculations, I provide ranges of expected error standard deviations for each gravity reduction, from best-to-worst case scenarios, to allow users to decide on where to focus their efforts to minimizing errors, according to the magnitude of the signal of interest.

I especially shed light on how to precisely estimate (1) the error associated with the levelling of the instrument, as it can be significant when using standard LCR instruments and has rarely been reported in the past, (2) the error in the drift function, as I reveal that it can also reflect unexplained "environmental" errors, such as due to air pressure, air temperature, rainfall and soil moisture, which are usually neglected when unknown, and (3) the error due to temporal changes in calibration, which has never been fully estimated in the past, and depends on whether the same gravimeter was used for all surveys and whether any recalibration was performed. Although I focus on volcanic applications, this method is equally applicable to other applications, using relative spring gravimeters.

4.2 Problem Setup

The residual error ξ_{res}, which reflects the deviation of the estimated residual gravity change, $\Delta\hat{g}_{\text{res}}$, from the true Δg_{res} (Section 2.2.3), can be expressed from the residual errors of each component on the left-hand side of Equation 2.11:

$$\xi_{\text{res}} = \Big[\xi_{\text{DC}}\Big]_{t_2-t_1} + \xi_{\Delta\text{cal}} + \xi_{\text{elev}} + \xi_{\text{wtr}} \tag{4.1}$$

$$\therefore \xi_{\text{res}} = \Big[\varepsilon_{\text{DC}}\Big]_{t_1} - \Big[\varepsilon_{\text{DC}}\Big]_{t_2} + \xi_{\Delta\text{cal}} + \xi_{\text{elev}} + \xi_{\text{wtr}} \tag{4.2}$$

where the residual errors, $\left[\varepsilon_{\mathrm{DC}}\right]_{t_1}$ and $\left[\varepsilon_{\mathrm{DC}}\right]_{t_2}$, correspond to the deviations of the estimated drift-corrected gravity signal, $\hat{g}_{\mathrm{DC}}$, from the true g_{DC}, in the first and second survey, respectively (Section 2.2.3).

Each of these two residual errors is therefore the sum of the residual errors of each parameter on the left-hand side of Equation 2.8, and because it is reasonable to assume that, for a single measurement, the calibration factor $k(t)$ equals 1 with negligible associated error (e.g. Battaglia et al. (2018) and Appendix B.2), any $\varepsilon_{\mathrm{DC}}$ can be expressed as follows:

$$\varepsilon_{\mathrm{DC}} = \varepsilon_{\mathrm{meas}} + \varepsilon_{\mathrm{ET}} + \varepsilon_{\mathrm{OL}} + \varepsilon_{\mathrm{P}} + \varepsilon_{\mathrm{T}} + \varepsilon_{\mathrm{base}} \tag{4.3}$$

Moreover, because $\varepsilon_{\mathrm{meas}}$ can be separated into a vibration noise component, $\varepsilon_{\mathrm{vib}}$, and a component due to the levelling of the gravimeter, or instrumental tilt, $\varepsilon_{\mathrm{tilt}}$, the above equation can be re-written as follows:

$$\varepsilon_{\mathrm{DC}} = \varepsilon_{\mathrm{vib}} + \varepsilon_{\Delta\mathrm{tilt}} + \varepsilon_{\mathrm{ET}} + \varepsilon_{\mathrm{OL}} + \varepsilon_{\mathrm{P}} + \varepsilon_{\mathrm{T}} + \varepsilon_{\mathrm{base}} \tag{4.4}$$

where $\varepsilon_{\Delta\mathrm{tilt}}$ is the differential error due to tilt at the site of interest, relative to the base (i.e. equivalent to the error of the drift-corrected tilt component), and $\varepsilon_{\mathrm{vib}}$ only relates to the measurement at the site, as vibration noise at the base are included in $\varepsilon_{\mathrm{base}}$, which is derived from the drift function (Section 2.2.3).

I go on to show that all the residual errors of Equations 4.2 and 4.4 are independent and approximately Gaussian. Consequently, each $\varepsilon_{\mathrm{DC}}$ and ξ_{res} equal zero on average, and their respective standard deviations, σ_{DC} and σ_{res}, can be estimated as the square roots of the sum of the variances of all of their residual error components, addressed in turn in this paper:

$$\sigma_{\mathrm{DC}} = \sqrt{\sigma^2_{\mathrm{vib}} + \sigma^2_{\Delta\mathrm{tilt}} + \sigma^2_{\mathrm{ET}} + \sigma^2_{\mathrm{OL}} + \sigma^2_{\mathrm{P}} + \sigma^2_{\mathrm{T}} + \sigma^2_{\mathrm{base}}} \tag{4.5}$$

$$\sigma_{\mathrm{res}} = \sqrt{\left[\sigma^2_{\mathrm{DC}}\right]_{t_1} + \left[\sigma^2_{\mathrm{DC}}\right]_{t_2} + \sigma^2_{\Delta\mathrm{cal}} + \sigma^2_{\mathrm{elev}} + \sigma^2_{\mathrm{wtr}}} \tag{4.6}$$

It is worth noting that when the site of interest has been occupied several times during the same survey, such as when doing double-daily loopings (e.g. Bagnardi et al.,

2014), the final σ_{DC} can be determined using the covariance formula from weighted least-squares:

$$\sigma_{\mathrm{DC}}^2 = \left[\mathbf{G}^{\mathrm{T}}{\mathbf{Q_{dd}}}^{-1}\mathbf{G}\right]^{-1} \tag{4.7}$$

where $\mathbf{Q_{dd}}$ is the variance-covariance matrix listing, in the diagonal, the variances, $\left[\sigma_{\mathrm{DC}}^2\right]_{j=1}$ to $\left[\sigma_{\mathrm{DC}}^2\right]_{j=M}$, corresponding to the M occupations at the given site, and $\mathbf{G}$ is the forward matrix operator, which is a vector of ones in this case.

4.3 Vibration noise

Vibration noise results from a combination of noise sources, which, in addition to the unavoidable internal error caused by imperfect sensors, may be anthrogpogenic (e.g. due to traffic, pedestrians and unstable ground), natural (e.g. due to wind, heavy rain, earthquake and microseismic noise resulting from the action of waves in the open-ocean), and/or caused by the user, when handling and transporting the gravimeter (e.g. Goncharenko et al., 2018, Boddice et al., 2018; and references therein). This latter error component makes vibration noise approximately Gaussian, in field conditions.

The magnitude of the internal error depends on the type of spring gravimeter used, such as the error due to transportation, which can be reduced by allowing recovery time for the levelled instrument before starting a measurement (e.g. Seigel, 1995, Scintrex, 2009, Van Camp et al., 2017). The anthropogenic errors and most of the natural errors can be reduced by setting up stations on stable ground, sheltering the gravimeter from wind and rain and filtering the raw data out for high-frequency noise (e.g. Jacob et al., 2010, Van Camp et al., 2017, Boddice et al., 2018). Finally, the microseismic noise is hard to reduce without affecting the signal of interest, but, when necessary, it can be predicted from e.g. ambient seismic noise (e.g. Goncharenko et al., 2018).

Because temporal gravity signals are often at the micro-scale, it is likely that some remaining non-negligible vibration noise, σ_{vib}, remains despite a careful acquisition. To lower this σ_{vib} to a suitable level with respect to the magnitude of the signal of interest, it is common practice to successively record N gravity samples, $(g_s)_{i=1}$ to $(g_s)_{i=N}$, during any given site occupation and to compute the least-squares mean of these N

samples. Even though N should be large enough to minimize σ_{vib} as much as possible, it should also be small enough to avoid detecting low-frequency signals such as tidal effects (e.g. Boddice et al., 2018).

When assuming that the N repeated samples, recorded during a single site occupation, are independent and randomly drawn from an approximately Gaussian distribution, the standard error, σ_{vib}, of the least-squares gravity measurement, g_{meas}, equals the error standard deviation, σ_p, of the population represented by the N samples, divided by the square root of N (e.g. Bonvalot et al., 1998, Scintrex, 2009, Debeglia and Dupont, 2002, Boddice et al., 2018):

$$\sigma_{\text{vib}} = \frac{\sigma_p}{\sqrt{N}} \tag{4.8}$$

where σ_{p} (i.e. SD in the Scintrex user's manuals, Scintrex (1995, 2009)) can be estimated using the common formula for variance with a normalization factor of N-1.

When the N gravity samples are acquired with a high-frequency, Z sets of acquisition can be successively recorded during the same site occupation, providing Z least-squares gravity measurements, $(g_{\text{meas}})_{k=1}$ to $(g_{\text{meas}})_{k=Z}$, each with an associated $(\sigma_{\text{vib}})_k$, determined using Equation 4.8 (Figure 4.2). An overall gravity measurement, $(g_{\text{meas}})_j \pm (\sigma_{\text{vib}})_j$ can then be computed, for this j^{th} site occupation, using weighted least-squares, where the variances, $(\sigma^2_{\text{vib}})_{k=1}$ to $(\sigma^2_{\text{vib}})_{k=Z}$ are listed in the diagonal of the variance-covariance matrix (blue highlight in Figure 4.2). On the other hand, when the N gravity samples are acquired with a low frequency, only one set of samples can usually be acquired (Z=1). In this case, the unique least-squares gravity average of the N samples, $(g_{\text{meas}})_{k=1}$, and its associated vibration noise, $(\sigma_{\text{vib}})_{k=1}$, determined using Equation 4.8, directly equal $(g_{\text{meas}})_j \pm (\sigma_{\text{vib}})_j$ (i.e. when Z=1, the green highlight in Figure 4.2 equals the blue highlight).

When the site has been reoccupied M times during the survey, the M reproduced gravity measurements, $(g_{\text{meas}})_{j=1}$ to $(g_{\text{meas}})_{j=M}$, determined either using least-squares or weighted least-squares, depending on the recording frequency of the samples, can be averaged using weighted-least squares, where the variances, $(\sigma^2_{\text{vib}})_{j=1}$ to $(\sigma^2_{\text{vib}})_{j=M}$,

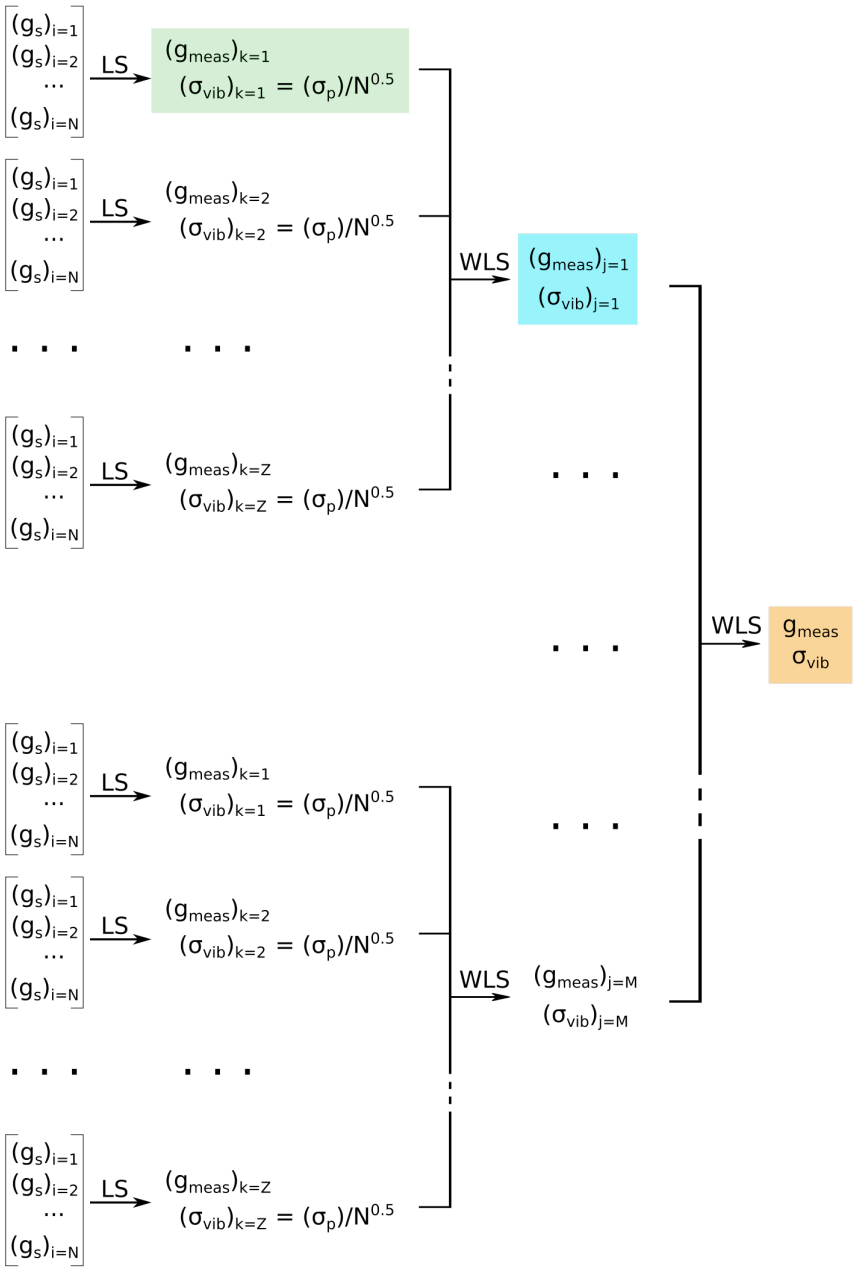

Figure 4.2: Flow diagram illustrating the procedure usually undertaken to obtain a gravity measurement per survey, at any given station. Depending on the samples recording frequency per site occupation, either a single (Z=1) or several (Z >1) set(s) of N gravity samples are recorded successively (Figure 4.3); and, depending on the type of gravimeter used and time constraints, the given station can be either re-occupied once (M=1) or several times (M >1) during the same survey. Based on the strategy chosen, the gravity measurement of any site, per survey, can either be the one highlighted in green (Z=1 and M=1), in blue ($Z \geq$1 and M=1) or in orange ($Z \geq$1 and M >1). The larger Z and M, the more minimized the vibration noise. See Section 4.3 for more details.

are listed in the diagonal of the variance-covariance matrix. This final weighted least-squares average provides the gravity measurement, $g_{\mathrm{meas}} \pm \sigma_{\mathrm{vib}}$, at the given site, for a

given survey (Figure 4.2). If the site was occupied only once during the survey (M=1), $g_{\text{meas}} \pm \sigma_{\text{vib}}$ either equals the least-squares average of the N samples when Z=1, or it equals the weighted-least average of Z successive sets of acquisition, when Z >1, (Figure 4.2).

Each time a weighted average is calculated, a χ^2 test can be undertaken to ensure that the mean is representative of the data (Section 3.4.4), and the probability can be lowered to 50% to be more selective. In the presence of any anomalously high $(\sigma_{\text{vib}})_k$ or $(\sigma_{\text{vib}})_j$, which could be explained by e.g. an earthquake, the site should ideally be reoccupied. Alternatively, the corresponding gravity measurement, i.e. $(g_{\text{meas}})_k$ or $(g_{\text{meas}})_j$, could be dropped by outlier detection, for Z and M large enough, respectively.

4.3.1 σ_{vib} for SCG gravimeters

SCG gravimeters directly output gravity measurements as the least-squares averages of N 1-second samples, along with their associated σ_p (Equation 4.8). The samples are automatically recorded for a time duration chosen by the operator and filtered for high-frequency noise (N = DUR - #Rej in the Scintrex user's manuals). Due to both the automated system and the high-frequency samples recording, these instruments offer the possibility of successively recording Z least-squares gravity measurements, with Z chosen by the operator. The gravity measurement of any j^{th} site occupation is therefore commonly determined as the weighted least-squares average of Z successive measurements (blue highlight in Figure 4.2), and when the site has been reoccupied M times, a further weighted-least-squares can be performed (orange highlight in Figure 4.2). Even though additional filtering approaches are available to reduce the high-frequency noise (e.g. Scintrex, 2009, Boddice et al., 2018), repeating (Z >1) and reproducing (M >1) the acquisitions can already be an efficient approach to minimize the vibration noise associated to an SCG measurement.

Even though the SCG sensor imperfections are expected to have a negligible contribution to the final σ_{vib} (Goncharenko et al., 2018), handling and transportation can induce some spring relaxation, so-called hysteresis effect, causing high gravity variations at the beginning of the gravity acquisition (e.g. Flury et al., 2007, Reudink et al.,

2014, Champollion et al., 2018). Consequently, when fewer than a few tens of minutes have been given to a levelled SCG gravimeter, to recover from handling and transportation, a systematic drift can be observed over the Z repeated gravity measurements (e.g. Champollion et al. (2018) and Figure 4.3). In this case, only the measurements after convergence to a plateau, if any, should be retained. If the convergence never happens while the tilt offsets and sensitivities have recently been checked (e.g. Bonvalot et al., 1998, Scintrex, 2009, Van Camp et al., 2017), the instrument is in need of repair (Personal communication, M. Poland, 2016). Alternatively, when Z is too small to have the chance to reach the convergence, a χ^2 test (Section 3.4.4) could help discarding any unrealistic weighted average, $(g_{\text{meas}})_j$, relative to a given site occupation (Figure 4.3). Thanks to the high frequency of samples recording and because Z repeated measurements are often recorded successively, reproducing M gravity measurements at each site does not seem essential when carefully handling SCG gravimeters, but it can still be a way to check that the instrument is behaving as expected.

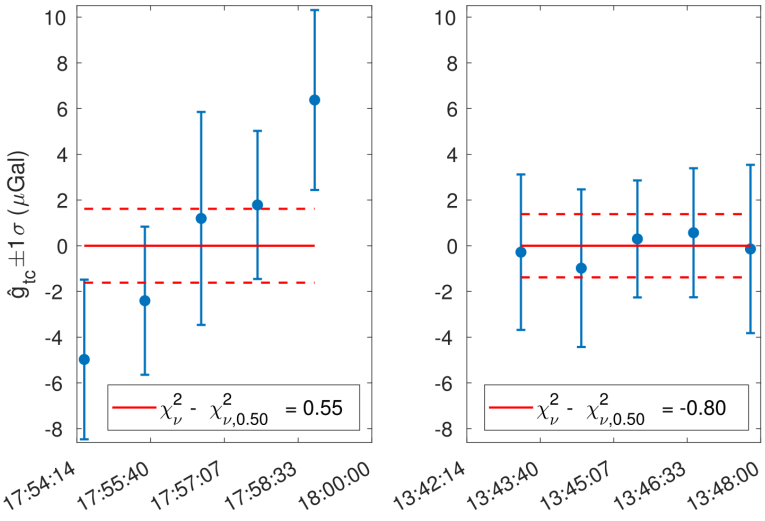

Figure 4.3: Examples of systematic drift trend observed from Z=5 consecutive 1-minute tidally-corrected gravity measurements ($\hat{g}_{\text{TC}} = g_{\text{meas}}$ - $\hat{g}_{\text{ET}}$ - $\hat{g}_{\text{OL}}$, Equation 2.7), recorded at station VIKR (Askja volcano, Iceland, Chapter 5), on the 17$^{\text{th}}$ (left) and 18$^{\text{th}}$ (right) of August 2015, using the Scintrex CG-5 No. 968. In each case, the weighted average gravity measurement is highlighted ($(g_{\text{meas}})_j$, solid red line), with associated error standard deviation (dashed red line). The χ^2 tests with 50% probability emphasize that $(g_{\text{meas}})_j$ is not representative of the data on the left graph (χ^2_ν-$\chi^2_{\nu,0.50}$>0, Section 3.4.4), but it is acceptable on the right graph.

It has already been demonstrated that repeating Z measurements with an SCG gravimeter, can provide a minimized $(\sigma_{\text{vib}})_j$ (Figure 4.2) of $\leq$10 μGal, in low vibration

conditions (e.g. Lederer, 2009, Budetta and Carbone, 1997, Bonvalot et al., 1998, Flury et al., 2007). Even though this low magnitude can still be achieved on volcanoes, such as at Askja, (Iceland), where, in both 2015 and 2016, I improved $(\sigma_{\text{vib}})_j$ from ∼2-12 to ∼<1-4 μGal, by repeating Z=5 records per site occupation, this low level of noise in not always guaranteed (Figure 4.4). Indeed, in 2017, the level of noise was higher at Askja, and using the same procedure as in 2015 and 2016, I minimized $(\sigma_{\text{vib}})_j$ from ∼5-38 to ∼2-17 μGal. Moreover, during the 2012 gravity survey carried out by Marco Bagnardi (Jet Propulsion Laboratory, NASA) at Kilauea (Hawaii), the Z=5 recording procedure lowered $(\sigma_{\text{vib}})_j$ from ∼9-151 to ∼5-54 μGal (Figure 4.4). These observations emphasize that the number Z of repeated records should be planned according to the level of noise, which can vary from one time to another and from one place to another, due to e.g. local seismicity.

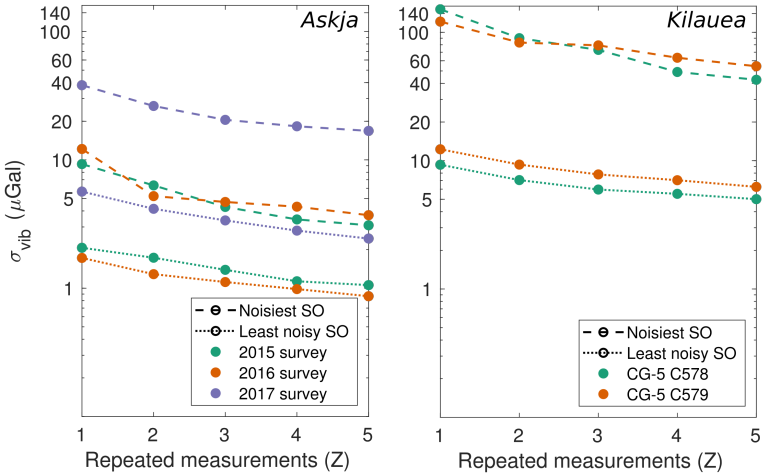

Figure 4.4: Variations in error standard deviation due to vibration noise, σ_{vib}, when varying the number Z, of consecutive gravity measurements, from 1 to 5, at Askja volcano (i.e. during the three surveys that I carried out using the Scintrex gravimeter CG-5 No. 968), versus at Kilauea, during the survey that Marco Bagnardi (Jet Propulsion Laboratory, NASA), carried out with two Scintrex CG-5 gravimeters (No. 578 and No. 579, Bagnardi et al. (2014)). Both graphs show the evolution of σ_{vib} at the noisiest (dashed curves) and least noisy site occupations, SO, recorded during each survey.

4.3.2 σ_{vib} for LCR gravimeters

"Standard" LCR gravimeters are LCR instruments with initial devices, i.e. not upgraded with any more precise components. Because these standard models are not able to automatically measure gravity, the N consecutive samples need to be recorded manually

by the user. Thanks to the analogue system, any single LCR measurement is a low-pass reading, i.e. with vibration noise filtered out to some degree (e.g. LaCoste & Romberg, 2004). Even though it is likely that readings recorded with standard LCR instruments are within two standard deviations of SCG measurements, the amount of vibration noise can hardly been quantified. Indeed, the low frequency of samples recording implies that the least-squares average (green highlight in Figure 4.2) is directly the gravity measurement, $(g_{\text{meas}})_j$, of that j$^{\text{th}}$ site occupation (i.e. Z=1), and the typically small N, means that (1) the associated vibration noise error, $(\sigma_{\text{vib}})_j$, is reduced by less than an order of magnitude (Equation 4.8), and (2) there is no guarantee that $(g_{\text{meas}})_j$ is representative of the population, neither that the samples distribution can be approximated as Gaussian. Moreover, the common practice of manually rejecting outlier samples, using an arbitrary threshold, biased the sampling, just as σ_p (Equation 4.8). Additionally, if more than one user made the measurements, different perceptions of the reading line can induce several tens of microgals of error, and the reading line should always be approached from the same side, as errors due to backlash can be of a few tens of microgals (e.g. Rymer, 1989, LaCoste & Romberg, 2004). For all these reasons, caution is therefore required when interpreting results from standard LCR gravimeters used for temporal gravity studies, and because any anomalous $(g_s)_i$ or $(g_{\text{meas}})_j$ are unlikely to be detected, nor filtered out, reoccupying stations during the survey to reproduce measurements is essential.

When upgraded with an Aliod electronic feedback system, LCR gravimeters, are able to continuously record N samples for a duration set by the user (e.g. LaCoste & Romberg, 2004, Vigouroux et al., 2008, Zurek et al., 2012, Carbone et al., 2017). This upgrade is necessary to record a sufficiently large amount of samples to be representative of the population and to better estimate vibration as there is then a higher chance that the sampling will be Gaussian (Equation 4.8). Moreover, it provides a sufficiently high samples recording frequency to offer the possibility to record Z sets of acquisitions (Figure 4.2). I could not determine whether each $(\sigma_{\text{vib}})_{k=1}$ to $(\sigma_{\text{vib}})_{k=Z}$ are provided by the instrument, such as when using SCG gravimeters (section 4.3.1). If not, the final σ_{vib} can hardly be quantified, but if possible to retrieve each sample, then the

record can be filtered out for high-frequency noise (e.g. Boddice et al., 2018), and each $(\sigma_{\text{vib}})_k$ can be estimated, to then determine $(\sigma_{\text{vib}})_j$ for the given j^{th} site occupation. This parameter corresponds to the final σ_{vib} when M=1, or, alternatively, σ_{vib} can be determined from the $(\sigma_{\text{vib}})_{j=1}$ to $(\sigma_{\text{vib}})_{j=M}$, when M >1 (Figure 4.2).

4.4 Error in differential tilt with respect to the base station

Any tilt of the instrument with respect to the vertical causes a decrease of g_{tilt} in measured gravity that can be computed using the small angle approximation:

$$g_{\text{tilt}} = g_0(\cos\theta_x \cdot \cos\theta_y) = g_0 \cos\theta \approx \frac{g_0}{2}\theta^2 \tag{4.9}$$

where θ_x and θ_y are the tilt angles in radians, in two orthogonal directions, θ is the overall magnitude of tilt, also in radians, and g_0 is the absolute gravity value at the site of interest, usually approximated to the average gravity value at sea level or Standard gravity, i.e. 9.806×10^8 μGal (e.g. Scintrex, 2009, Crossley et al., 2013, Van Camp et al., 2017).

The small angle approximation induces an error of <1 μGal compared with using the non-approximated equation, as long as $\theta \leq$1800 arcsec (Niebauer et al., 2016), and because the largest possible residual from the Standard gravity is 4.2×10^6 μGal (Hirt et al., 2013), the approximation of any local g_0 to the Standard gravity leads to an error of <2 μGal when $\theta \leq$200 arcsec (Equation 4.9). Because such tilt angles are not expected to be reached in gravity surveying, the uncertainty of g_{tilt} mainly depends on the uncertainty of θ, which depends on the uncertainties of θ_x and θ_y.

The residual error, $\varepsilon_{\text{tilt}}$, is always negative, but when considering measurements relative to the base station, and assuming that θ_x and θ_y are equal and drawn from Gaussian distributions, the residual error, $\varepsilon_{\Delta\text{tilt}}$ (Equation 4.4), can be approximated as Gaussian, with a mean of zero and an error standard deviation, $\sigma_{\Delta\text{tilt}}$ (Appendix B.1).

$\sigma_{\Delta\text{tilt}}$ depends on the number, M, of base occupations, but converges to $\sim 0.024\sigma^2_{\theta_{\text{x}}}$ when the base has been occupied at least 8 times during the survey and $\sigma^2_{\theta_{\text{x}}}$ is in arcsec^2 (Figure 4.5). The convergence to a plateau after a sufficiently large M is due to the

probability density function formula of $P(\varepsilon_{\Delta tilt})$ (Appendix B.1), involving a division by the gamma function of n: for given tilt error standard deviations in orthogonal directions, a large n leads to approximately constant $P(\varepsilon_{\Delta tilt})$ and the associated error standard deviations are then also approximately constant. Before computing these error standard deviations for SCG and LCR gravimeters, I define ranges of most probable orthogonal tilt errors, which depend on the type of tilt sensors used.

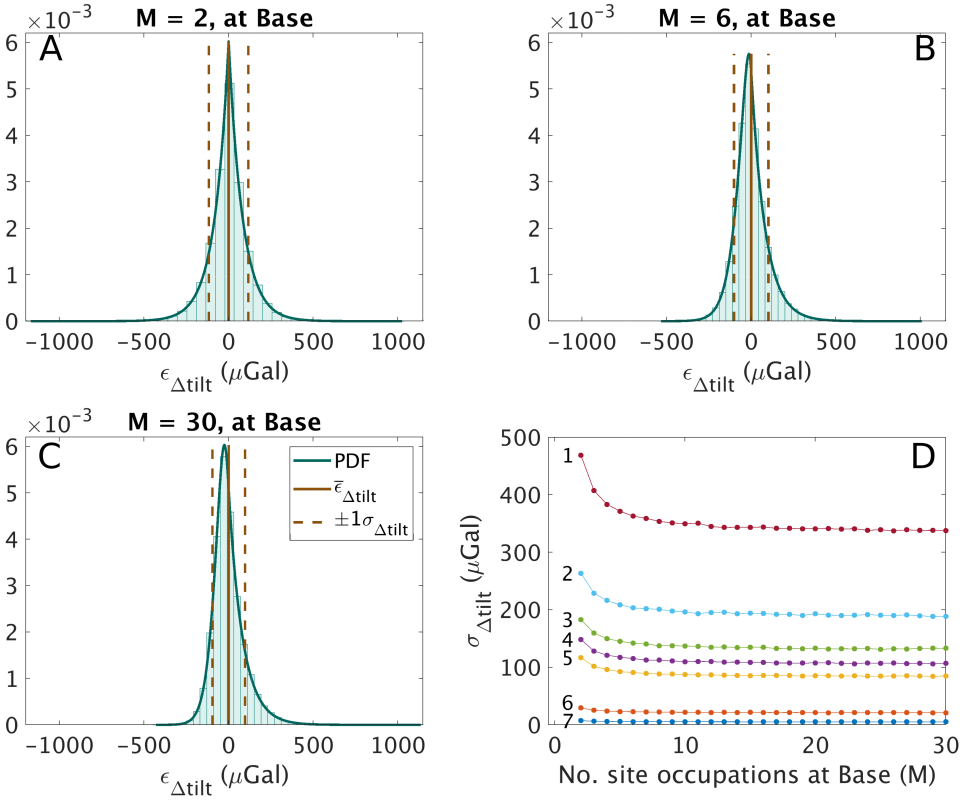

Figure 4.5: A-C: Probability density functions (dark green curves) of the spatial difference in error due to tilt, $\varepsilon_{\Delta tilt}$, between a station of interest and the base station (Equations B.7 and B.8, in Appendix B.1), and for different numbers of base occupations (M). As a check on these theoretical distributions, I simulated 100,000 realisations of the errors for each case and potted the corresponding histograms (light green). The mean and standard deviations, $\bar{\varepsilon}_{\Delta tilt} \pm \sigma_{\Delta tilt}$, are highlighted in solid and dashed vertical brown lines, respectively. In these examples, both 1-D standard deviations of tilt angle errors equal 60 arcsec, which is that expected for a standard LCR G gravimeter, when the bubbles are centered within one division (Section 4.4). D: Dependence of $\sigma_{\Delta tilt}$ with M at the base station. Each curve corresponds to a specific type of tilt sensors (Refer to Table 4.2 for the curve indices).

Gravimeter, tilt sensors	$\varepsilon_{\theta_x} = \varepsilon_{\theta_y}$	$\sigma_{\theta_x} = \sigma_{\theta_y}$ (arcsec)	$\sigma_{\Delta\text{tilt}}$ (μGal)	Curve indices in Figure 4.5D
SCG meters	0	1-5	0.02-0.6	X-X
LCR D Electronic sensors	0.5-2 mm	1.9-7.5	0.1-1.4	X-X
LCR G-meters Electronic sensors	0.5-2 mm	3.6-15	0.3-5	X-X
Shaded default LCR D-meters	0.5-2 mm	7.5-30	∼1.5-21	X-6
Shaded default LCR G-meters	0.5-2 mm	15-60	∼5-85	7-5
Unshaded default LCR D-meters	0.5-2 mm	67.5-90	∼110-195	4-2
Unshaded default LCR G-meters	0.5-2 mm	75-120	∼135-345	3-1

Table 4.2: Range of error standard deviations, $\sigma_{\Delta\text{tilt}}$, when the base is occupied at least 8 times. The indices for each sensor/scenario are mentioned when plotted in Figure 4.5D, otherwise 'X' means that the curve was not plotted. For each LCR tilt sensor/scenario, I have estimated a reasonable range of error standard deviations for the orthogonal tilt angle components, which I assume to be equal and equivalent to levelling within 0.5-2 mm (see Section 4.4.1 for more details).

4.4.1 Reasonable ranges for σ_{θ_x} and σ_{θ_y}

SCG gravimeters are able to automatically correct for tilt angles up to ±200 arcsec in both orthogonal directions, with σ_{θ_x} and σ_{θ_y} being equal to 1-5 arcsec depending on the reading duration (e.g. Scintrex, 2009, Bonvalot et al., 1998). Because SCG gravimeters provide real-time magnitudes of tilt angles, I assume that, even though the SCG tripod is sensitive to the sun's heat (e.g. Jacob et al., 2010), users are meticulous enough to keep tilt angles much below the threshold for automatic correction, and I also assume that tilt offsets and sensitivities are regularly checked (e.g. Bonvalot et al., 1998, Lederer, 2009, Van Camp et al., 2017). Based on these assumptions, σ_{θ_x} and σ_{θ_y} should not exceed 1-5 arcsec, when using SCG gravimeters (Table 4.2).

Standard LCR gravimeters are equipped with two thermally-sensitive orthogonal spirit bubble levels (LaCoste & Romberg, 2004) and, because these instruments do not measure the tilt, tilt errors cannot be corrected on a case-by-case basis, and any undetected tilt angle becomes part of the tilt error. Assuming that the bubbles can be centred using the naked eye within 0.5-2 mm, depending on local vibration noise conditions and surveyor's meticulousness, σ_{θ_x} and σ_{θ_y} range within 7.5-30 arcsec, when

using an LCR D meter, and 15-60 arcsec, when using an LCR G meter, as the respective tilt sensitivities are 30 and 60 arcsec/division (LaCoste & Romberg (2004), Table 4.2). Note that these tilt sensitivities should regularly be checked to avoid additional error of a few tens of microgals (e.g. Rymer, 1989, Lederer, 2009). The sun's heat can further shift the bubbles by up to 60 arcsec/division in both x and y directions, and σ_{θ_x} and σ_{θ_y} can therefore be raised up to ∼67.5-90 arcsec, when using a D meter, and ∼75-120 arcsec, when using a G meter (Table 4.2). Even though the tilt error of standard LCR gravimeters is an unavoidable error, it is clear that the careful operation can minimize it.

Default LCR gravimeters can be upgraded with pendulum-like electronic tilt sensors, which are not thermally sensitive and have better tilt sensitivities than the standard instruments, equivalent to 7.5 and 15 arcsec/division on a spirit level, for D and G meters, respectively (LaCoste & Romberg, 2004). Assuming a human error of 0.5-2 mm (as above), the use of such electronic tilt sensors reduces σ_{θ_x} and σ_{θ_y} to ∼1.9-7.5 arcsec, when using D meters and ∼3.6-15 arcsec, when using G meters (Table 4.2).

Aliod LCR gravimeters (Section 4.3.2) are equipped with digital electronic tilt sensors, which need to be manually adjusted to the maximum gravity before every survey (LaCoste & Romberg, 2003). These devices record the magnitude of tilt angles in orthogonal directions, but I was not able to find any information on their precision.

4.4.2 $\sigma_{\Delta\text{tilt}}$ for SCG and LCR gravimeters

From the reasonable possible ranges of σ_{θ_x} and σ_{θ_y}, detailed in Section 4.4.1, I have applied my new method, presented at the beginning of this section 4.4, to estimate the error contribution due to tilt effects relative to the base station: when the base station has been occupied at least 8 times during the survey, $\sigma_{\Delta\text{tilt}}$ is systematically $\leq$0.6, 1.4 and 5 μGal when using SCG, LCR D and LCR G gravimeters, respectively (Figure 4.5 and Table 4.2), and when the latter two have been upgraded with pendulum-like electronic sensors (Section 4.4.1). On the other hand, using standard LCR D or G gravimeters could introduce errors of a few tens to up to a few hundreds of microgals. This clearly justifies the need to have a precise tilt sensor when performing gravity

surveying, to secure low magnitudes of $\sigma_{\Delta\text{tilt}}$.

4.5 Errors due to solid Earth tides and ocean loading

Solid Earth tides are a response to the interaction between gravitational and centrifugal forces in the Sun-Moon-Earth system, causing periodical internal mass redistribution of an ocean-less Earth and consequent gravity site displacement. The gravity signal, g_{ET}, induced by these solid Earth tides during a measurement also includes some direct gravitational effect on the proof mass of the gravimeter (e.g. Van Camp et al., 2017). Unlike LCR gravimeters, SCG gravimeters have the capability to automatically reduce for the estimated $\hat{g}_{\text{ET}}$ (Equation 2.6), at the time and location of the gravity measurement. However, because this estimation is solely based on the Longman formula (Longman, 1959), which assumes an elastic and ocean-less Earth, this approach is not precise enough, when studying gravity changes at the microscale (e.g. Bonvalot et al., 1998, Van Camp et al., 2017, Boddice et al., 2018).

The anelasticity of the Earth can be accounted for by scaling the Longman calculation using the appropriate gravimetric factor (e.g. Agnew, 2007, Battaglia et al., 2012, USNO, 2016), which enables estimating $\hat{g}_{\text{ET}}$ with a residual error, $\varepsilon_{\text{ET,model}}$, not exceeding 3 μGal (Personal communication, M. Battaglia, 2018). Assuming that $\varepsilon_{\text{ET,model}}$ is drawn from a Gaussian distribution with mean zero, 3 μGal has $\sim$5% chance of occurring when $\sigma_{\text{ET,model}}$ $\sim$1.5 μGal. Alternatively, harmonic methods can also be used to provide $\hat{g}_{\text{ET}}$ with $\varepsilon_{\text{ET,model}}$ of 0.1 μGal or even to the nanogal scale (e.g. Wenzel, 1996, Van Camp and Vauterin, 2005), leading to negligible $\sigma_{\text{ET,model}}$ when the signal of interest is at the microgal scale.

The response of the ocean tides causes periodical redistribution of the ocean loads, which produces additional internal mass redistribution and a resulting additional gravity site displacement. The gravity signal, g_{OL}, induced by such ocean loading effect, during a measurement, is commonly estimated ($\hat{g}_{\text{OL}}$ in Equation 2.6) using ocean tide models, OTMs, and ocean tide programs, OTPs (e.g. Scherneck and Bos, 2011, Battaglia et al., 2012). Depending on (1) the type of OTM chosen, (2) the method used to extrapolate

coastlines, (3) the type of Earth model used, (4) the OTP chosen and (4) the site location, a residual error, $\varepsilon_{\mathrm{OL,model}}$, of between <1 and 5% usually arises (e.g. Boy et al., 2003, Bos and Baker, 2005, Petit and Luzum, 2010, Stammer et al., 2014). This translates to $\varepsilon_{\mathrm{OL,model}}$ ranging from ∼1.2 to 6 μGal, in an extreme case, i.e. when considering a maximum peak-to-peak ocean loading amplitude of ∼120 μGal. When assuming that $\varepsilon_{\mathrm{OL,model}}$ is drawn from a Gaussian distribution, with the highest 5% residual error having ∼5% chance of occurring, this extreme case would lead to $\sigma_{\mathrm{OL,model}}$ ∼3 μGal. For lower ocean loading variations, $\sigma_{\mathrm{OL,model}}$ could be $\ll$1 μGal. When necessary, the use of more recent OTMs and OTPs tends to reduce $\sigma_{\mathrm{OL,model}}$ as well as when using additional tide gauges data or estimating the overall tidal variations (solid Earth tides and ocean loading) directly from continuous gravity records, especially along the coast or on small islands (e.g. Hautmann et al., 2010, Stammer et al., 2014).

In addition to these uncertainties induced by the model chosen to estimate $\hat{g}_{\mathrm{ET}}$ and $\hat{g}_{\mathrm{OL}}$, some other errors may arise from the survey procedure. Indeed, the corresponding error standard deviations, $\sigma_{\mathrm{ET,survey}}$ and $\sigma_{\mathrm{OL,survey}}$, linearly vary by up to ∼0.6 and ∼0.06 μGal, respectively, per minute of timing residual error (ε_t), up to ∼1×10^{-5} and ∼2×10^{-5} μGal, respectively, per meter of latitude error ($\varepsilon_{\mathrm{lat}}$), and up to ∼2×10^{-5} and ∼3×10^{-5} μGal, respectively, per meter of longitude error ($\varepsilon_{\mathrm{lon}}$). Based on these variations, $\sigma_{\mathrm{ET,survey}}$ and $\sigma_{\mathrm{OL,survey}}$ are mostly dependent on timing errors, and ε_t needs to be within 1.5-30 min, depending on the location of the area of study, to minimize $\sigma_{\mathrm{ET,survey}}$ and $\sigma_{\mathrm{OL,survey}}$ to ≤1 μGal (Figure 4.6). In the worst case, recording the time, 10 min before an LCR measurement is carried out, could induce a $\sigma_{\mathrm{ET,survey}}$ of up to ∼6 μGal, while $\sigma_{\mathrm{OL,survey}}$ would still be ≤1 μGal. Making a timing mistake of 1h, for example due to confusion between UTM (Coordinated Universal Time) and local time, could introduce in the worst case $\sigma_{\mathrm{ET,survey}}$ and $\sigma_{\mathrm{OL,survey}}$ of ∼36 and ∼3.9 μGal, respectively.

In summary, when being meticulous with respect to time in the field and when choosing appropriate models to estimate $\hat{g}_{\mathrm{ET}}$ and $\hat{g}_{\mathrm{OL}}$, the resulting overall error standard deviations, $\sigma_{\mathrm{ET}} = \sqrt{\sigma^2_{\mathrm{ET,model}} + \sigma^2_{\mathrm{ET,survey}}}$, and $\sigma_{\mathrm{OL}} = \sqrt{\sigma^2_{\mathrm{OL,model}} + \sigma^2_{\mathrm{OL,survey}}}$ (Equation 4.5) could be less that one microgal, but the use of inaccurate models and/or

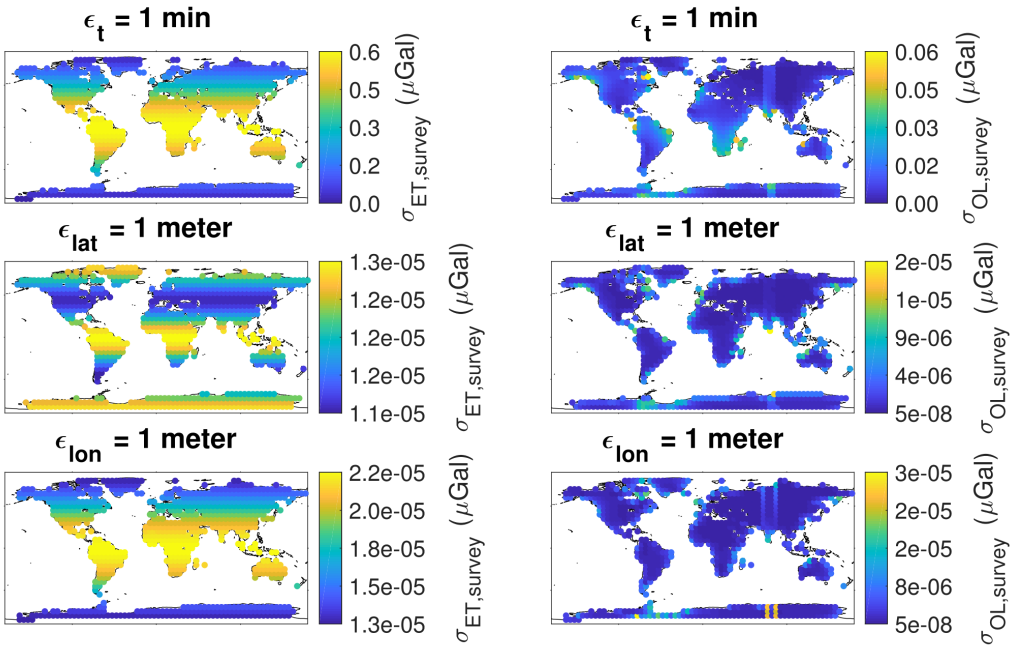

Figure 4.6: Spatial variations in the error standard deviations, $\sigma_{\mathrm{ET,survey}}$ and $\sigma_{\mathrm{OL,survey}}$, corresponding to the survey error component of the respective gravity signals due to solid Earth tides (left column) and ocean loading (right column), calculated, per node, over a 5-by-5 degree grid globe, from the approximately Gaussian distributions of the respective residual errors, $\varepsilon_{\mathrm{ET,survey}}$ and $\varepsilon_{\mathrm{OL,survey}}$, which were interpolated for a timing residual error of 1 min (ε_t, top row), a latitude residual error of 1 meter ($\varepsilon_{\mathrm{lat}}$, middle row) and a longitude residual error of 1 meter ($\varepsilon_{\mathrm{lon}}$, bottom row), over a year of tidal variations (5-min spacing), against time, latitude and longitude, respectively. These tidal variations were estimated using the GTOOLS package, in which I incorporated the ocean harmonics from the FES2012 model (Lyard et al., 2006; updated), to estimate ocean tides (Petit and Luzum, 2010, Scherneck and Bos, 2011, Battaglia et al., 2012). Repeating this procedure while varying the magnitudes of ε_t, $\varepsilon_{\mathrm{lat}}$ and $\varepsilon_{\mathrm{lon}}$ highlighted linear relationships with $\sigma_{\mathrm{ET,survey}}$ and $\sigma_{\mathrm{OL,survey}}$ (See Section 4.5).

the presence of timing errors, could raise σ_{ET} and σ_{OL} to a few tens of microgals.

4.6 Error related to atmospheric pressure and temperature

During a survey, the gravitational attraction of the atmospheric mass as well as the consequent deforming Earth's surface, together induce an overall gravity signal, g_{P}, affecting any gravity measurement. Even though g_{P} usually remains spatially constant over areas of ∼50 km-radius around the occupied site, it can vary temporally due to air pressure changes, with an amplitude of a few millibars for periods of months or years, up to a few tens of millibars per day (e.g. Merriam, 1992, Bonvalot et al., 1998, Jousset et al., 2000a, Cigolini et al., 2009). Merriam (1992) demonstrated that $\hat{g}_{\mathrm{P}}$

(Equation 2.6) can be estimated using a precise admittance value of -0.356±0.1 μGal mbar^{-1}. Continuously or hourly measuring air pressure at, at least, one station (e.g. Jacob et al., 2010), provides precise time-series of $\hat{g}_{\mathrm{P}}$, and $\hat{g}_{\mathrm{P}} \pm \sigma_{\mathrm{P}}$ can then be derived at any time t, using the weighted least-squares, where the variances of the air pressure measurements are listed on the diagonal of the variance-covariance matrix. When air pressure variations have not been monitored, I demonstrate in Section 4.7 that the unknown variations in $\hat{g}_{\mathrm{P}}$ can be captured as an error, at the base station, from the time-series of tidally-corrected base measurements, and due to the wide spatial stability of air pressure, this error can be constant at all stations.

Even though sealed, spring gravimeters can be affected by atmospheric temperature (e.g. Bonvalot et al., 1998, Fores et al., 2017). Because it is likely that the air temperature varies spatially and temporally, by at least a few degrees during a survey, variations in the resulting gravity effect, g_{T}, can be of a few tens of microgals (e.g. El Wahabi et al., 2001). Because g_{T} is usually instrument-dependent, no precise admittance value can be derived for spring gravimeters in general. To overcome this problem, an admittance value (TEMPCO) is determined for every manufactured SCG gravimeter, which can then automatically correct for internal temperature variations within ±2 mK, but despite this improvement, this automatic correction might not always be reliable, neither correlated with air temperature effects (e.g. Fores et al., 2017). Similarly as for air pressure changes, I demonstrate in Section 4.7 that any possible unknown variation in $\hat{g}_{\mathrm{T}}$ can be captured as an error, at the base station, from the time-series of tidally-corrected base measurements, and this error might be approximately constant over the whole area of study if similar temperature variations are observed at different sites. As good practice, large effects to due thermal shocks can be minimized when keeping resting gravimeters at a similar temperature to field conditions, and when ensuring that batteries are always properly charged (e.g. Seigel, 1995, Rymer, 1996, LaCoste & Romberg, 2004, Scintrex, 2009). Thermal shocks can be detected by, for example, comparing the drift curve in the field with the drift curve at rest (Personal communication, T. Jacob, 2018).

4.7 Instrumental drift and base component

Spring creep leads to drift of the gravity reference of spring gravimeters with time. How it drifts depends on the instrument and age of the sensors, but is usually approximately linear for periods of up to about a week, and quadratic or even cubic for longer periods (e.g. Budetta and Carbone, 1997, Bonvalot et al., 1998, Debeglia and Dupont, 2002, Lederer, 2009, Jacob et al., 2009, Battaglia et al., 2018). This instrumental drift needs to be characterized to be able to predict the gravity value, $\hat{g}_{\text{base}}$, at the base station, at the time of any gravity measurement, and reduce this effect to determine the drift-corrected gravity signal at a given site ($\hat{g}_{\text{DC}}$ in Equation 2.8).

The instrumental drift is commonly modelled from the daily time-series of reproduced base measurements, after they have been corrected for tidal effects, and possibly for known atmospheric pressure and temperature changes (Sections 4.5 and 4.6). This approach implies that the drift offsets and sensitivity are regularly checked (e.g. Van Camp et al., 2017), and that the user is always consistent in the measuring procedure at each site, without changing the clock, to keep any possible timing error constant throughout the survey. In addition, it assumes that no temporal gravity changes that could have occurred during the survey, other than due to the instrumental drift, remains at that stage. But this hypothesis might not always be true when, for example, large unknown variations in air pressure or air temperature have occurred, or when, for example, heavy precipitations have increased the groundwater-mass content of the unsaturated zone during the survey (Sections 4.6 and 4.10). Other effects, such as inappropriate tidal corrections or technical issues, can also induce extra variations to the drift, but assuming that users are careful when handling their instrument and performing the gravity reductions, these effects are likely to have a much smaller impact that the effects due to pressure, temperature and groundwater-mass changes, identified here as the meteorological effects.

I go on to show that it is best to estimate the instrumental drift over at least a few days rather than a single day, in order to take into account these possible non-negligible meteorological effects in the variances of the drift parameters, and propagate them into the variance, σ^2_{base}, of $\hat{g}_{\text{base}}$ (Equation 4.5). This procedure includes the meteorological

effects at the base station only, but the results can be generalised to the entire survey area when the effects uniformly affect the zone of interest (Sections 4.6 and 4.10). Alternatively, when meteorological effects are not uniformly distributed, several base stations can be set up.

4.7.1 Theory

Over up to a week, the reference of the spring gravimeter is likely to vary at a linear rate (see beginning of Section 4.7), $\hat{\dot{g}}_{\text{ref}} \pm \sigma_{\text{ref}}$, which can be estimated along with the y-intercept, $\hat{c}_0 \pm \sigma_{c_0}$, using a weighted least-squares approach, from the time-series of all the M reproduced tidally-corrected base measurements, g_{TC}, recorded at the times $t = t_{\text{B}_\text{i}}$, and possibly corrected for atmospheric pressure and temperature effects. The variances, σ^2_{TC}, characterizing the vibration noise, tidal errors, and possibly the pressure and temperature errors (Sections 4.3, 4.5 and 4.6), are listed in the diagonal of the variance-covariance matrix.

As highlighted by Battaglia et al. (2018), several stations can be used to estimate the drift. But, rather than estimating $\hat{\dot{g}}_{\text{ref}}$ and $\hat{c}_0$ from an arbitrary superposition of the data, considering the first base measurement as the reference, I suggest to instead estimate a single drift rate, along with as many y-intercepts as the base stations used. In this case, the forward matrix operator has one column listing the times, and each other column relative to each y-intercept, are a list of ones and zeros, depending on what station was measured at what time. For example, if the stations P and Q are taken into account to estimate the drift parameters, the algebraic system is:

$$\begin{bmatrix} \left[(g_{\text{TC}})_{\text{B}_{j=1}}\right]_{\text{P}} \\ \left[(g_{\text{TC}})_{\text{B}_2}\right]_{\text{Q}} \\ \left[(g_{\text{TC}})_{\text{B}_3}\right]_{\text{P}} \\ \left[(g_{\text{TC}})_{\text{B}_4}\right]_{\text{P}} \\ \left[(g_{\text{TC}})_{\text{B}_5}\right]_{\text{Q}} \\ \cdots \\ \left[(g_{\text{TC}})_{\text{B}_{j=M}}\right]_{\text{Q}} \end{bmatrix} = \begin{bmatrix} t_{\text{B}_{j=1}} & 1 & 0 \\ t_{\text{B}_2} & 0 & 1 \\ t_{\text{B}_3} & 1 & 0 \\ t_{\text{B}_4} & 1 & 0 \\ t_{\text{B}_5} & 0 & 1 \\ \cdots & \cdots & \cdots \\ t_{\text{B}_{j=M}} & 0 & 1 \end{bmatrix} \begin{bmatrix} \hat{\dot{g}}_{\text{ref}} \\ (\hat{c}_0)_{\text{P}} \\ (\hat{c}_0)_{\text{Q}} \end{bmatrix} \tag{4.10}$$

In case of sudden drift offset(s) (or tares), which can easily happen when using LCR and Scintrex CG-3/CG-3M gravimeters, but are unlikely to occur when using Scintrex CG-5 instruments (e.g. Rymer, 1989, Seigel, 1995, Scintrex, 2009), the model should be adapted to estimate these offsets (e.g. Equation 3.3).

The possible error impact of a non-negligible meteorological effect can be detected by testing the goodness-of-fit of the model, using a χ^2 test, with ν equalling M-2 (Section 3.4.4). When the χ^2_ν related to any given drift function is smaller or equal to the expected $\chi^2_{\nu,0.95}$, the assumed linear model fits the data within 95% confidence. In this case, the meteorological errors are either negligible and/or their gravity effects have been estimated well, and the standard deviation, σ_{base}, associated with any predicted $\hat{g}_{\text{base}} = \hat{\dot{g}}_{\text{ref}} t + \hat{c}_0$, can then be determined by propagation of errors:

$$\sigma_{\text{base}} = \sqrt{(t\sigma_{\text{ref}})^2 + \sigma^2_{c_0} + 2t\ cov(\hat{\dot{g}}_{\text{ref}}, \hat{c}_0)} \tag{4.11}$$

On the other hand, when the obtained χ^2_ν exceeds the expected $\chi^2_{\nu,0.95}$, either the linear assumption is wrong or the errors are underestimated. When the linear model looks appropriate with all $(g_{\text{TC}})_{\text{B}_i}$ and all $(\sigma^2_{\text{TC}})_{\text{B}_i}$ precisely estimated, such situation probably indicates non-negligible meteorological errors. In this case, the residual error, $(\varepsilon_{\text{base}})_{\text{B}_i}$, between any observed $(g_{\text{TC}})_{\text{B}_i}$ and its prediction $(\hat{g}_{\text{TC}})_{\text{B}_i}$, equals the data error, $(\varepsilon_{\text{TC}})_{\text{B}_i}$ plus some possible meteorological error, $(\varepsilon_{\text{met}})_{\text{B}_i}$:

$$(\varepsilon_{\text{base}})_{\text{B}_i} = (\varepsilon_{\text{TC}})_{\text{B}_i} + (\varepsilon_{\text{met}})_{\text{B}_i} \tag{4.12}$$

and, the same relationship applies to variances:

$$(\sigma^2_{\text{met}})_{\text{B}_i} = (\sigma^2_{\text{base}})_{\text{B}_i} - (\sigma^2_{\text{TC}})_{\text{B}_i} \tag{4.13}$$

Deriving $(\sigma^2_{\text{base}})_{\text{B}_i}$ at any time $t = t_{\text{B}_i}$ using the drift rate estimated using weighted least-squares (Equation 4.10) would not provide an appropriate estimate is this situation of $\chi^2_\nu > \chi^2_{\nu,0.95}$. However, re-estimating the drift parameters using the least-squares percentile bootstrap approach (Section 3.4.4) would be appropriate as the uncertainty of

the linear model, likely due to unknown meteorological effects (Equations 4.12 and 4.13), would be taken into account. These re-estimated errors, resulting from thousands of iterations, can then be propagated into $(\sigma_{\text{base}})_{\text{B}_i}$ using Equation 4.11. It is worth noting that when several base stations are considered, all the data should be combined by superimposing the linear functions, previously estimated from Equation 4.10, to estimate only one average intercept via the percentile bootstrap approach, and then use Equation 4.11.

At this stage, the unknown meteorological effects have been included in our estimate of $(\sigma^2_{\text{base}})_{\text{B}_i}$, i.e. for any base station measurement. Even though meteorological effects can be spatially-constant over the area of study (Sections 4.6 and 4.10), it is wrong to estimate $(\sigma^2_{\text{met}})_{t_i}$ any time $t = t_i$ and relative to any given station, using Equation 4.13, where $(\sigma^2_{\text{TC}})_{t_i}$ would be associated with the tidally-corrected measurement recorded at the given station, and $(\sigma^2_{\text{base}})_{t_i}$ would have been derived from the drift function. Indeed, these two error parameters have been estimated by propagation of errors, and differentiating them will provide a $(\sigma^2_{\text{met}})_{t_i}$, which will be generally smaller than the original variance that we are trying to determine.

Nevertheless, because Equation 4.13 also applies to the variances of drift rates, it is possible to estimate a spatially and temporally constant σ^2_{met} per drift function:

$$\left[\sigma^2_{\text{ref}}\right]_{\text{met}} = \left[\sigma^2_{\text{ref}}\right]_{\text{LS,boot}} - \left[\sigma^2_{\text{ref}}\right]_{\text{WLS}} \tag{4.14}$$

where $\left[\sigma^2_{\text{ref}}\right]_{\text{met}}$ is the drift rate variance that would be expected using weighted least-squares, with constant weights, equaling the inverse of the σ^2_{met} that we are looking for, $\left[\sigma^2_{\text{ref}}\right]_{\text{LS,boot}}$ is the average drift rate variance obtained from the least-squares percentile bootstrap approach described above, and $\left[\sigma^2_{\text{ref}}\right]_{\text{WLS}}$ is the drift rate variance obtained using weighted least-squares on the original tidally-corrected original base measurements, i.e. from Equation 4.10. Using trial and error, it is possible to search for the smallest constant σ^2_{met} that would provide the expected $\left[\sigma^2_{\text{ref}}\right]_{\text{met}}$, while satisfying a χ^2 test with 95% probability.

To verify that this approach is reliable, a simulation scenario can be tested, where the

above method is applied using the original errors of the tidally-corrected base measurements, to which random errors, generated from a Gaussian distribution with variance equaling σ^2_{met}, are added. As mentioned in the next section, the original variance σ^2_{met} can be retrieved within a few microgals.

When the area of study is too large to reasonably assume spatially-constant meteorological effects, having several scattered base stations, and performing this procedure per cluster of sites around each base station, could contribute to estimating a temporally constant σ_{met} per station cluster. Moreover, weekly variations of σ_{met} could be monitored for long surveys, from weekly drift function estimations.

4.7.2 Applications to Askja

I have applied the overall method described above to the gravity data that I recorded at the Askja caldera (Iceland), during the summers 2015, 2016 and 2017 (see Chapter 5 for more information on the surveys). In each case, non-negligible unknown temporal changes, which could possibly be due to meteorological effects, were detected by the χ^2 test (Section 4.7.1). To take these effects into account in the drift model, I used the least-squares percentile bootstrap approach, which increased the drift rate variances by an order of magnitude compare to when using the usual weighted least-squares approach (Table 4.3).

Survey	$\left[\hat{\dot{g}}_{\text{ref}} \pm \sigma_{\text{ref}}\right]_{\text{WLS}}$	$\left[\hat{\dot{g}}_{\text{ref}} \pm \sigma_{\text{ref}}\right]_{\text{LS,boot}}$
2015	-18.56±0.03 μGal	-18.70±0.33 μGal
2016	-18.90±0.01 μGal	-18.73±0.23 μGal
2017	-24.31±0.08 μGal	-24.43±0.61 μGal

Table 4.3: Drift rates and associated error standard deviations ($\hat{\dot{g}}_{\text{ref}} \pm \sigma_{\text{ref}}$), estimated, at Askja volcano, from the tidally-corrected reproduced base station measurements that I recorded during the summer surveys in 2015, 2016 and 2017 (see Chapter 5 for more information on the surveys). I compare here the linear regression estimations obtained either using weighted least-squares and the original errors (WLS), or using the least-squares percentile bootstrap approach (LS,boot). See Section 4.7.1 for more details on the method.

This increase propagated into the estimation of σ_{base}, associated with any predicted $\hat{g}_{\text{base}}$ at any time t of a site occupation (Figure 4.7 and 4.8). It is worth noting that one way to minimize σ_{base} is to increase the number of base measurements, and that

σ_{base} is always smaller in the middle of the time-series when performing the percentile bootstrap method (Figure 4.8). Taking additional base measurements a few days before and after the survey could therefore also contribute to minimizing σ_{base}.

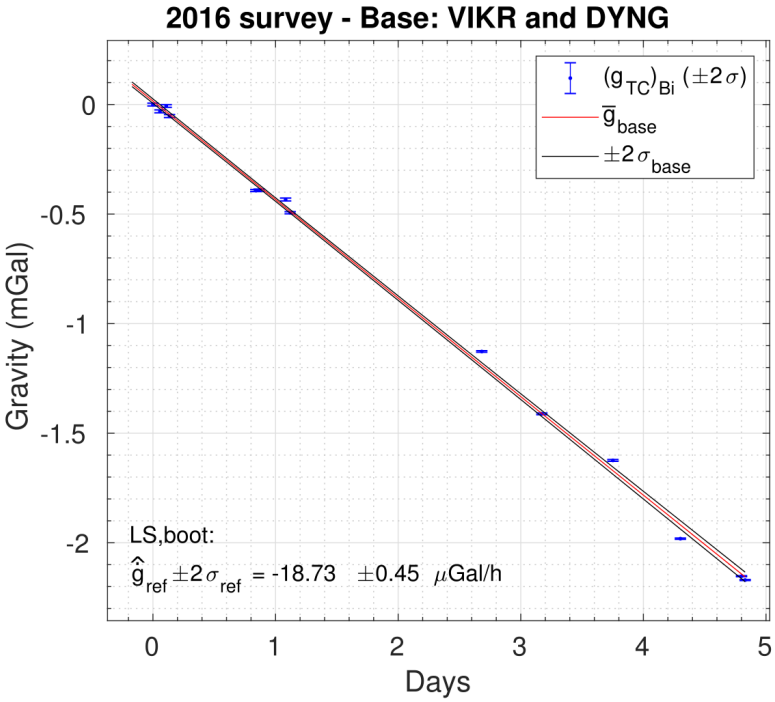

Figure 4.7: Drift function estimation combining base measurements recorded at two base stations, using the Scintrex gravimeter CG-5 No. 968 (Chapter 5). The blue data points are the tidally-corrected base measurements (TC), with error bars taking into account vibration noise and tidal errors (Section 4.3 and 4.5), the red line highlights the best fit linear drift rate, which is very similar when using WLS or LS,boot (Table 4.3), and the black lines highlight the $\pm 2\sigma$ bounds for σ_{base} at any time during the survey, when estimated using LS,boot. This therefore takes into account the uncertainty of the model, which is assumed to be caused by unknown meteorological effects (Section 4.7.1).

Because pressure and temperature variations recorded at three weather stations in the vicinity of Askja showed similar temporal changes (Figure 4.9), I assumed that the meteorological effects due to pressure and temperature changes are spatially constant at any time t, over the Askja caldera. In addition, I assumed that the groundwater mass variations in the unsaturated zone are also spatially constant over the caldera, which measures ~8 km across. Even though this assumption might not be true, it might be a reasonable approximation as precipitations and humidity often vary along with pressure and temperature. Based on these assumptions, I translated these unknown meteorological effects into a spatially and temporally constant error standard deviation, σ_{met}, of

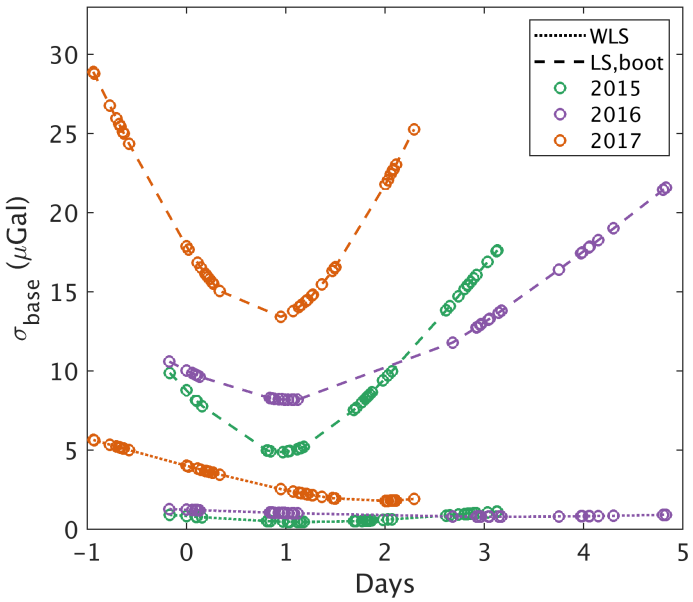

Figure 4.8: Graph showing the difference in magnitudes of σ_{base}, for the three surveys that I carried out at Askja volcano (colors), using either the usual weighted least-squares (WLS) approach or the least-squares percentile bootstrap (LS,boot), which is the right approach to take into account unknown meteorological effects (Section 4.7.1).

$\sim$22, $\sim$34 and $\sim$42 μGal in 2015, 2016 and 2017, respectively (Equation 4.14). To verify whether these original σ_{met} were reasonably estimated, I performed the simulation test introduced at the end of Section 4.7.1, and I could retrieve the σ_{met} with less than 2 microgal difference. Because the magnitudes of pressure and temperature changes (Figure 4.9) should translate into relatively small temporal gravity changes (Section 4.6), the meteorological effects characterized by σ_{met} at Askja were most likely mainly due to groundwater-mass variations in the unsaturated zone (Sections 4.7.1 and 4.10).

This overall drift analysis demonstrates the benefits of estimating the drift function over at least a few days, and even though regularly taking measurements at the base station is essential to reduce errors and detect any possible jump, the common practice of systematically taking a base measurement at the beginning and end of each day does not seem to be strictly necessary anymore.

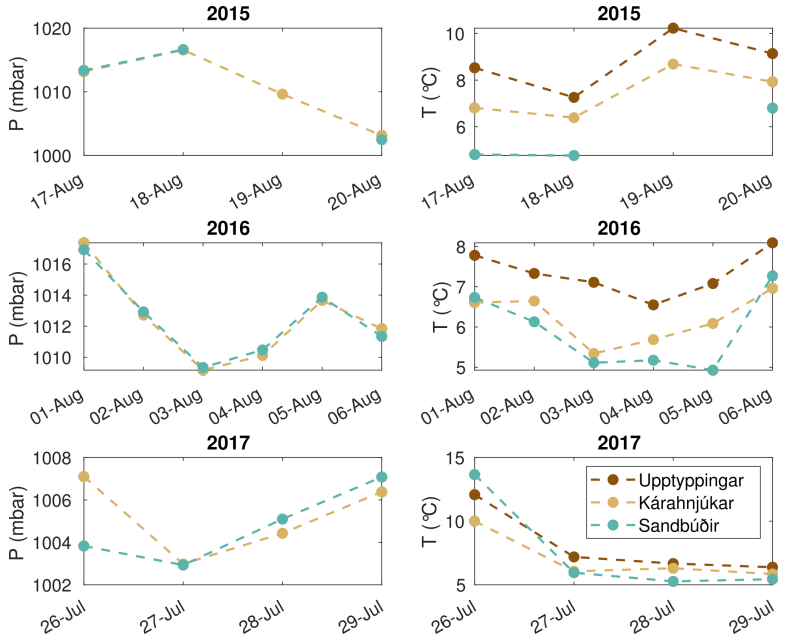

Figure 4.9: Variations of atmospheric pressure and temperature recorded at three weather stations around Askja (colors) during each survey that I carried out in the summers 2015, 2016 and 2017 (Icelandic MET office, 2019).

4.8 Error due to temporal variations in calibration factor

Spring gravimeters require a calibration factor to convert any gravity sample, from counter units (LCR meters) or volts (SCG meters) to gravity values in milligals (g_s in Section 4.3) (Scintrex, 1995, Valliant, 1991, Scintrex, 2009):

$$g_s(t) = \hat{k}_0 \varrho \tag{4.15}$$

where ϱ is the reading before conversion and $\hat{k}_0$, is the calibration factor initially determined at the manufacture (so-called GCAL1 in the Scintrex user's manual). SCG gravimeters automatically perform this conversion, but it has to be manually performed when using LCR gravimeters, with a calibration table provided by the manufacturer, listing a value of $\hat{k}_0$ for different ranges of milligals (LaCoste & Romberg, 2004).

First of all, the manufacture calibration itself induces some error in $\hat{k}_0$, specific to each type of gravimeter, and equalling $\sim 10^{-4}$, $\sim 5\times10^{-4}$ and $\sim 5\times10^{-5}$ μGal when using SCG, LCR D and LCR G gravimeters (e.g. Valliant, 1991, Scintrex, 2009). Then, it is common that $\hat{k}_0$ varies with time due to small instabilities in the reading sensors,

such as stress relaxation, which induces additional error if not estimated (e.g. Valliant, 1991, Budetta and Carbone, 1997, Scintrex, 2009). Here, I present a new approach to estimate the calibration error of any temporal gravity change.

In theory, any calibration factor $k(t)$ (Equation 2.6), and so-called GCAL2 in the Scintrex user's manual, can be computed by multiplying $\hat{k}_0$ by a scale factor $f(t)$, which describes the variations from $\hat{k}_0$ between the time of manufacture and t:

$$k(t) = \hat{k}_0 f(t) \tag{4.16}$$

Consequently, the residual error, $\varepsilon_{k(t)}$, of the estimated $\hat{k}(t)$, depends on $\hat{k}_0$ and on the error, $\varepsilon_{f(t)}$, of the estimated $\hat{f}(t)$, which can be determined using different methods described later, in Section 4.8.1:

$$\varepsilon_{k(t)} = \hat{k}_0 \varepsilon_{f(t)} \tag{4.17}$$

As demonstrated in Appendix B.2, the calibration residual error, $\xi_{\Delta\text{cal}}$ (Equation 4.1), of the temporal calibration component relative to the base ($\Delta\hat{g}_{\Delta\text{cal}}$ in Equation 2.11), can be derived from the above equation, as follows:

$$\xi_{\Delta\text{cal}} = \varepsilon_{f(t_2)} \Big[\hat{g}_{\text{DC}}\Big]_{t_2} - \varepsilon_{f(t_1)} \Big[\hat{g}_{\text{DC}}\Big]_{t_1} \tag{4.18}$$

where $\varepsilon_{f(t_1)}$ and $\varepsilon_{f(t_2)}$ are the residual errors of the scale factors, estimated for the respective survey at t_1 and t_2. These scale factor residual errors lead $\xi_{\Delta cal}$ to depend on whether the same or different gravimeters are used between surveys, and on whether variations in the calibration factor have been monitored (by user recalibrations). It is worth noting that because $\xi_{\Delta\text{cal}}$ depends on the observed gravity signals, it correlates somewhat with topography.

4.8.1 Dependence on the number of gravimeters used

When two different instruments are used ($\text{I}_1 \neq \text{I}_2$), $\varepsilon_{f(t_1)}$ and $\varepsilon_{f(t_2)}$ are independent, and the standard deviation, $\sigma_{\Delta\text{cal}}$ (Equation 4.6), of the residual error, $\xi_{\Delta\text{cal}}$, is then

determined by propagating the errors from Equation 4.18:

$$\left[\sigma_{\Delta\text{cal}}\right]_{\text{I}_1\neq\text{I}_2} = \sqrt{\sigma^2_{f(t_2)}\left[\hat{g}^2_{\text{DC}}\right]_{t_2} + \sigma^2_{f(t_1)}\left[\hat{g}^2_{\text{DC}}\right]_{t_1}} \tag{4.19}$$

On the other hand, when the same instrument is used for the two surveys ($\text{I}_1 = \text{I}_2$), a potential calibration change implies that $\varepsilon_{f(t_1)}$ and $\varepsilon_{f(t_2)}$ covary:

$$\varepsilon_{f(t_2)} = \varepsilon_{f(t_1)} + \varepsilon_{\delta f} \tag{4.20}$$

where $\varepsilon_{\delta f}$ describes the change in the scale factor between the two surveys. Because of the correlation between $\varepsilon_{f(t_1)}$ and $\varepsilon_{f(t_2)}$, it is not straightforward to compute $\sigma_{\Delta\text{cal}}$ from Equation 4.18. However, by substituting Equation 4.20 into Equation 4.18, $\xi_{\Delta\text{cal}}$ can be expressed with parameters that do not covary:

$$\left[\xi_{\Delta\text{cal}}\right]_{\text{I}_1=\text{I}_2} = \varepsilon_{f(t_1)}\Delta\hat{g}_{\text{DC}} - \varepsilon_{\delta f}\left[\hat{g}_{\text{DC}}\right]_{t_2} \tag{4.21}$$

and, by propagation of errors, $\sigma_{\Delta\text{cal}}$, can be computed as:

$$\left[\sigma_{\Delta\text{cal}}\right]_{\text{I}_1=\text{I}_2} = \sqrt{\sigma^2_{f(t_1)}\Delta\hat{g}^2_{\text{DC}} + \sigma^2_{\delta f}\left[\hat{g}^2_{\text{DC}}\right]_{t_2}} \tag{4.22}$$

Because the temporal change in gravity signature relative to the base, $\Delta\hat{g}_{\text{DC}}$, is usually much smaller than the relative gravity of a single survey, $\hat{g}_{\text{DC}}$, the above equation can be approximated as follows:

$$\left[\sigma_{\Delta\text{cal}}\right]_{\text{I}_1=\text{I}_2} \approx \sqrt{\sigma^2_{\delta f}\left[\hat{g}^2_{\text{DC}}\right]_{t_2}} \tag{4.23}$$

4.8.2 $\sigma_{\Delta\text{cal}}$ when gravimeters have been recalibrated by users

The most common method to recalibrate spring gravimeters consists of repeating measurements along a calibration line, where the absolute gravity values are well-known: the ratio of absolute gravity ties to the corresponding observed gravity ties, i.e. obtained from spring gravimeter measurements, provides an estimation, $\hat{f}_{\text{cal}} \pm \sigma_{f_{\text{cal}}}$, of the scale factor at the time t_{cal} of recalibration (e.g. Debeglia and Dupont, 2002). The overall

calibration line should cover, at least, a similar gravity range as the maximum $\hat{g}_{\mathrm{DC}}$ value at the study of interest (e.g. Flury et al., 2007, Jacob et al., 2010, Meurers, 2012), and therefore, it is better if the calibration line is located within the study area.

Such recalibration procedures can be performed either during or outside the survey period. In the former case, simultaneously recording absolute or alternatively super-conducting measurements (Section 2.2.1), with relative measurements (i.e. hybrid gravimetry, e.g. Francis and Hendrickx (2001), Bonvalot et al. (2008), Carbone et al. (2017)) implies that the estimated $\hat{f}_{\mathrm{cal}}$ directly equals $\hat{f}(t)$, and the error standard deviation of the scale factor for this given survey (i.e. $\sigma_{\mathrm{f(t_1)}}$ or $\sigma_{\mathrm{f(t_2)}}$, Section 4.8.1) equals $\sigma_{f_{\mathrm{cal}}}$. Consequently, $\sigma_{\Delta\mathrm{cal}}$ is calculated using Equation 4.19, no matter whether the same or different gravimeters have been used between surveys. Based on published time-series of recalibrations, we can expect $\sigma_{f(t_1)}$ or $\sigma_{f(t_2)}$ to range within ∼30-300 ppm if directly derived from recalibration procedures (Table 4.4), and as an example, $\sigma_{\Delta\mathrm{cal}}$ should therefore be ∼4.2-45 μGal when $\left[\hat{g}_{\mathrm{DC}}\right]_{t_1} \approx \left[\hat{g}_{\mathrm{DC}}\right]_{t_2} = 100$ μGal.

Gravimeter	Method of recalibration	Ranges of recalibration errors (σ_{cal})	Scale factor rates: $\hat{\dot{f}} \pm \sigma_{\hat{\dot{f}}}$ (Weighted least-squares)	Ref.
CG-3M No.9310234	-The residual gravity changes reflect variations in the calibration scale factor. -Calibration line near the area of study, with unknown absolute gravity values.		1. ∼5 ppm/d (∼0-7 mth) 2. ∼2 ppm/d (∼7-12 mth) 3. ∼0.05 ppm/d (≥∼12 mth)	[1],[2]
CG-5 No.40236	-Calibration line, with known absolute gravity values, ∼150 km away from the study area.	∼50-65 ppm	∼0.39±0.04 ppm/d (≥∼6-48 mth)	[3]
CG-5 No.167	-2 calibration lines with known absolute gravity values, one at the area of study and the other ∼50-100 km away.	∼120-350 ppm	1. ∼1.8±0.3 ppm/d (∼0-14 mth) 2. ∼1.8±0.3 ppm/d (∼0*-9 mth) 3. ∼0.07±0.96 ppm/d (≥∼9 mth)	[4],[5]
CG-5 No.578	-3 calibration lines with known absolute gravity values, at ∼400 km, ∼150 km and ∼1200 km away from the area of study.	∼30-80 ppm	∼0.06±0.03 ppm/d (≥∼16 mth)	[6]**
CG-5 No.579	Same as for the CG-5 No.578	∼30-80 ppm	1. ∼0.01±0.03 ppm/d (≥∼16 mth) 2. ∼-7.6±1.14 ppm/d (∼0*-3 mth)	[6]**

Table 4.4: Summary of error parameters relating to user recalibrations that have been reported in previous studies, with associated error standard deviations mentioned when provided. (*) A new $\hat{k}_0$ had been estimated during a new servicing at the manufacture. (**) The rates from this paper should be treated cautiously as they rely on relatively low numbers of recalibrations. [1] Budetta and Carbone (1997); [2] Carbone and Rymer (1999); [3] Meurers (2012); [4] Jacob et al. (2009); [5] Jacob et al. (2010); [6] Battaglia et al. (2018).

When recalibrations are performed outside the survey period, $\hat{f}(t)$ can be interpolated from a linear or linear segmented model, based on subsequent recalibration measurements:

$$\hat{f}(t) = \hat{\dot{f}}t + \hat{f}_0 \tag{4.24}$$

where $\hat{\dot{f}}$ is the scale factor rate of the weighted least-squares regression line, fitting the recalibration time-series, $\hat{f}_0$ is the y-intercept and, by propagating the errors,

$$\sigma_{f(t)} = \sqrt{(t\sigma_{\hat{\dot{f}}})^2 + \sigma^2_{\hat{f}_0} + 2t\ cov(\hat{\dot{f}}, \hat{f}_0)} \tag{4.25}$$

where $\sigma_{\hat{\dot{f}}}$ and $\sigma_{\hat{f}_0}$ are the respective error standard deviations of $\hat{\dot{f}}$ and $\hat{f}_0$, estimated by the weighted least-squares approach. Assuming reasonable values for $\sigma_{f(t_{\text{cal}})}$ of between 30 and 300 ppm (Table 4.4), $\sigma_{f(t)}$ ranges between ~21 and ~300 ppm, when recalibrations are performed only at the beginning and end of a 10-year period (Figure 4.10A). On the other hand, $\sigma_{f(t)}$ is lowered between ~9 and ~170 ppm when recalibrations are performed every year over 10 years (Figure 4.10B). In each case, the smallest errors are obtained when the survey occurs in the middle of the recalibration time-series, and the longer the time-series, the more minimized $\sigma_{f(t)}$, for any given survey at t. It is worth noting that $\sigma_{f(t_1)}$ or $\sigma_{f(t_2)}$ might be better minimized when interpolated from a user recalibration time-series, even when these user-recalibrations are performed during the surveys (see beginning of Section 4.8.2).

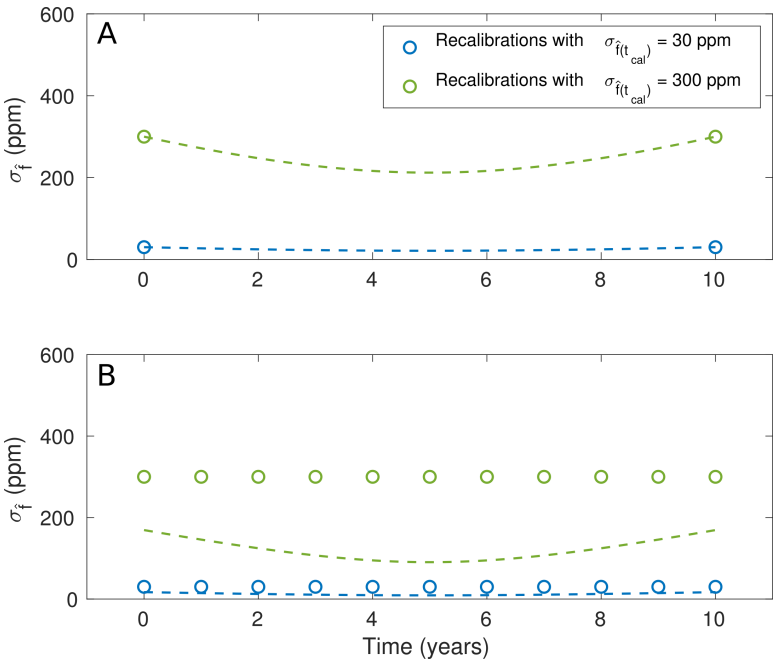

Figure 4.10: Error standard deviations of the scale factor at any time (dashed lines), over 10 years, estimated based on the number of user recalibrations (circles) and precisions of these recalibrations (colors, 30 versus 300 ppm).

By substituting these ranges of values into Equation 4.19, where $\sigma_{f(t1)} = \sigma_{f(t2)} = \sigma_{f(t)}$, and into Equation 4.23, where $\sigma_{\delta f} = \sigma_{\hat{f}}\,\delta t$, $\left[\sigma_{\Delta\text{cal}}\right]_{I_1 \neq I_2}$ is a few tens of microgals when assuming a recalibration time-series of 10 years, and, for the same 10-year period of recalibrations, $\left[\sigma_{\Delta\text{cal}}\right]_{I_1 = I_2}$ is <5 μGal when $\delta t = 1$ year, i.e. per year between surveys (Figure 4.11). Using the same regularly recalibrated gravimeter is therefore usually the best option for minimizing calibration errors, especially when looking at temporal gravity changes over just a few years.

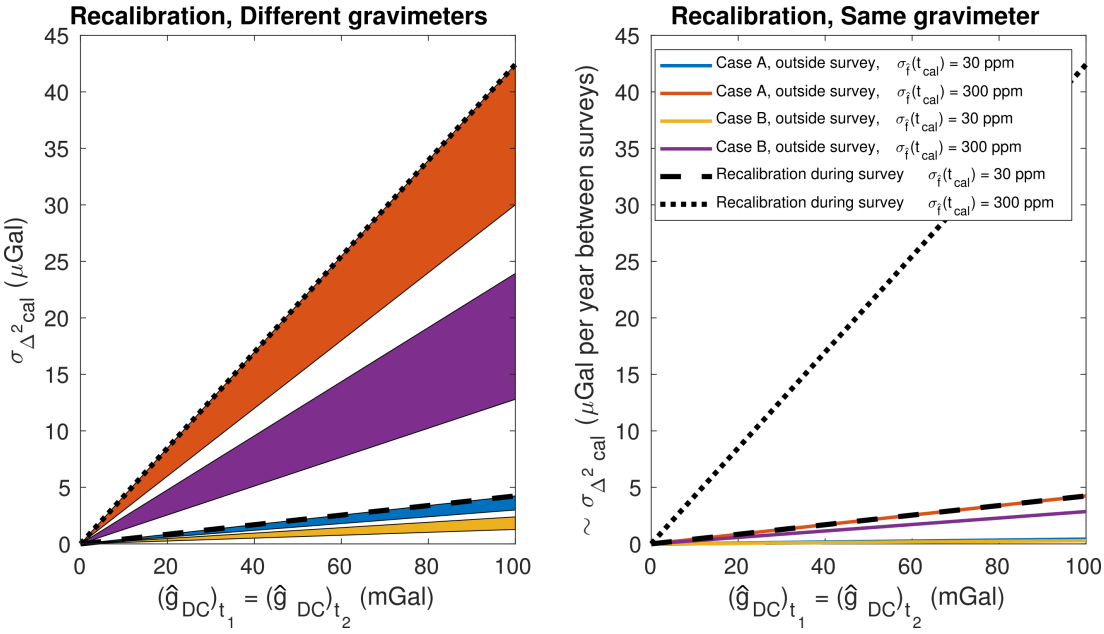

Figure 4.11: Standard deviation of the calibration error in the temporal change of drift-corrected gravity signal against the magnitude of drift-corrected gravity in the area of study, when same (right) or different (left) gravimeters are used for the two surveys. Both cases cover 10 years, during which 2 recalibrations (Case A) versus 11 (Case B) have been carried out. Precision of 30 or 300 ppm are tested in each case.

It is worth noting that recalibration along calibration lines might not be required when the residual gravity changes (Section 4.1) directly reflect temporal changes in calibration factor (e.g. Budetta and Carbone, 1997). In this case, the error of the residual gravity changes represents the calibration error.

4.8.3 $\sigma_{\Delta\text{cal}}$ when gravimeters have not been recalibrated by users

When no recalibration has been performed, the samples g_s are calibrated using only the initial (or re-initiated, Table 4.4) calibration factor, $\hat{k}_0$, i.e. $f(t) = 1$ in Equation 4.16.

Consequently, the error standard deviation, $\sigma_{f(t)}$, of this arbitrary scale factor of 1, takes into account the unmonitored temporal variations in the scale factor rate, for the time duration Δt, between manufacture and t, in addition to the initial error standard deviation of $\hat{k}_0$ (values provided per gravimeter at the beginning of Section 4.8).

Although it is hard to predict unmonitored variations in the scale factor, I assume here some rates of change based on studies where gravimeters have been regularly recalibrated, to get a feeling of magnitudes of calibration error to be expected. From Table 4.4, I assume an SCG scale factor rate with a mean of zero and error standard deviation of 3 ppm per day, if the manufacturer calibration occurred less than a year ago, and 0.5 ppm per day if it was carried out more than a year ago. This illustrates the usual tendency of SCG scale factor rates to reach a plateau about one year after manufacture or servicing (Table 4.4). Based on a recorded LCR scale factor rate change of ∼67 ppm/year (e.g. Budetta and Carbone, 1997; and references therein), I assume an LCR scale factor rate with mean zero and error standard deviation that increases by 0.1 ppm per day (an error of ±67 ppm has therefore a ∼5% chance of occurring after one year). This LCR rate should be treated cautiously as discrete jumps of ∼1000 ppm in the scale factor rate of LCR gravimeters have been observed over a few months (e.g. Budetta and Carbone, 1997; and references therein).

If the unmonitored temporal change in scale factor always have the same sign (A. Hugill, personal communication, 2017), $\sigma_{f(t)}$, for each instrument, can be expressed as follows:

$$\left[\sigma_{f(t)}\right]_{\mathrm{SCG}} = \sqrt{(10^{-4})^2 + [(3\times10^{-6})\Delta t]^2} \text{ for } \Delta\mathrm{t} \leq 365 \text{ days} \quad (4.26)$$

$$\left[\sigma_{f(t)}\right]_{\mathrm{SCG}} = \sqrt{(10^{-4})^2 + [(3\times10^{-6})\times365]^2 + [(5\times10^{-7})(\Delta t - 365)]^2}$$
$$\text{for } \Delta\mathrm{t} > 365 \text{ days} \quad (4.27)$$

$$\left[\sigma_{f(t)}\right]_{\mathrm{LCRD}} = \sqrt{(5\times10^{-4})^2 + [10^{-7}\Delta t]^2} \quad (4.28)$$

$$\left[\sigma_{f(t)}\right]_{\mathrm{LCRG}} = \sqrt{(5\times10^{-5})^2 + [10^{-7}\Delta t]^2} \quad (4.29)$$

By substituting these equations into Equation 4.19, the use of two different unrecalibrated gravimeters, leads to $\left[\sigma_{\Delta\mathrm{cal}}\right]_{\mathrm{I_1}\neq\mathrm{I_2}}$ <3 μGal for Δt ≤10 years and per mGal

of $\left[\Delta\hat{g}_{\mathrm{DC}}\right]_{t_1} = \left[\Delta\hat{g}_{\mathrm{DC}}\right]_{t_2}$, i.e. for example $\left[\sigma_{\Delta\mathrm{cal}}\right]_{\mathrm{I}_1\neq\mathrm{I}_2}$ <300 μGal when $\left[\Delta\hat{g}_{\mathrm{DC}}\right]_{t_1} = \left[\Delta\hat{g}_{\mathrm{DC}}\right]_{t_2}$ = 100 mGal (Figure 4.12). Moreover, $\left[\sigma_{\Delta\mathrm{cal}}\right]_{\mathrm{I}_1\neq\mathrm{I}_2}$ increases with Δt.

If however, the same unrecalibrated gravimeter is used for the two surveys, $\sigma_{\delta f} = \sigma_{f(t)}\ \delta f$ in Equation 4.23. Assuming $\left[\Delta\hat{g}_{\mathrm{DC}}\right]_{t_2}$ ≤100 mGal and $\sigma_{f(t)}$ = 3, 0.5 and 0.1 ppm per day and per year between surveys (Equations 4.26-4.29), $\left[\sigma_{\Delta\mathrm{cal}}\right]_{\mathrm{I}_1=\mathrm{I}_2}$ is up to ∼110 μGal and <20 μGal when using an SCG meter during the first year and more than one year after manufacturer calibration, respectively, and it is <5 μGal when using an LCR gravimeter (Figure 4.12). Consequently, for a same magnitude of $\left[\Delta\hat{g}_{\mathrm{DC}}\right]_{t_1} \approx \left[\Delta\hat{g}_{\mathrm{DC}}\right]_{t_2}$, it is better to use the same rather than different unrecalibrated gravimeters, as the calibration error then depends mostly on the time between surveys (δt) rather than on the time since manufacturer calibration (Δt). But, as mentioned previously, these results are based on assumed scale factor rates, which might not always be appropriate, especially when using LCR gravimeters, as scale factor rate jumps can occur.

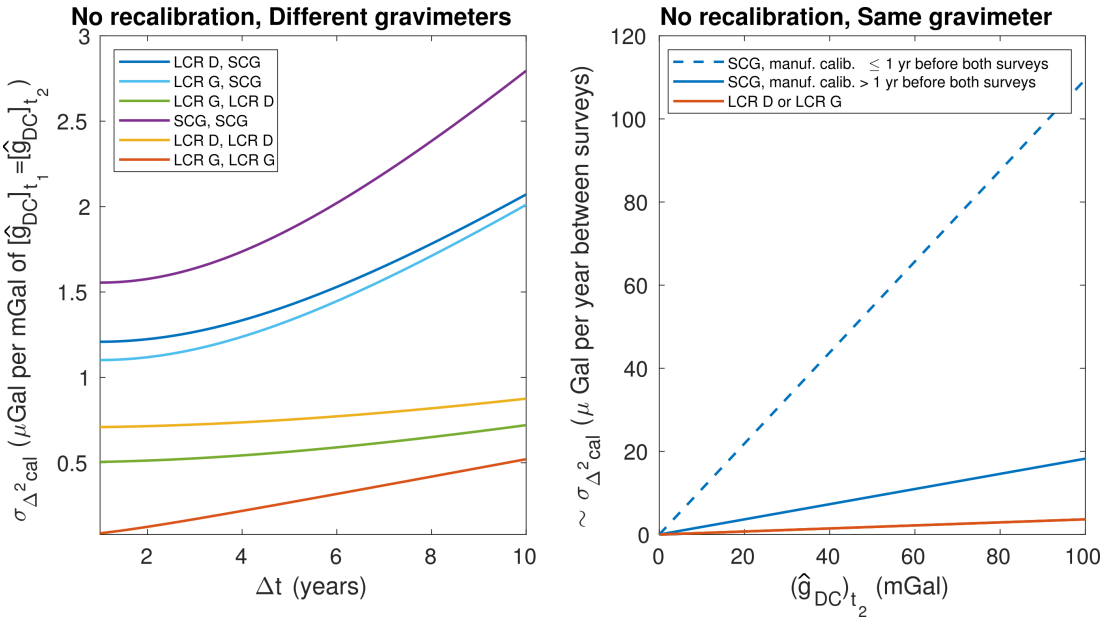

Figure 4.12: Same as Figure 4.11, but here, no recalibrations have been performed during the 10-year period, and the variations in scale factor depend on the gravimeter used and either the time since manufacture, Δt, when different gravimeters are used, or the time between surveys, δt, when the same instrument is used (Section 4.8.3).

In conclusion, calibration errors are kept to a minimum when always using the same regularly recalibrated gravimeter, and, in this case, errors of <5 μGal can be achieved

with any spring gravimeter, especially when the surveys are $\leq$1 year apart. However, using unrecalibrated gravimeters can easily lead to tens or hundreds of microgals of error.

4.9 Error associated with temporal gravity change due to elevation change

Any change in surface elevation, Δh, between two surveys, causes a gravity change with two components: Δg_{elev}, due to the change in elevation itself and usually related to subsurface volumetric strain at the deforming reservoir (Section 1.4), and a possible Δg_{def}, due to subsurface displacements of density gradients, from crustal compressibility around the deforming body (e.g. Walsh and Rice, 1979, Rundle, 1982, Rymer, 1994, Battaglia et al., 2008, Segall, 2010a, Vajda et al., 2015). Even though the aim is to isolate residual gravity changes relative to mass changes, other than due to elevation or groundwater bodies (Section 4.2), the possible Δg_{def} signal should, in theory, be corrected. However, because its estimation implies assuming geometries for the deforming source, this should be part of the modelling and interpretation. Consequently, $\Delta \hat{g}_{\text{DC}}$ can only be reduced by an estimate of Δg_{elev} (Equation 2.10), at this stage (I treat temporal gravity changes due to groundwater-table fluctuations in Section 4.10).

Any $\Delta \hat{g}_{\text{elev}}$ is commonly quantified by multiplying the estimated $\Delta \hat{h}$ by a gravity gradient. In the literature, either a locally measured vertical gravity gradient, VGG, or the theoretical free-air gravity gradient, FAG_{theo}, are used (VGG, e.g. Williams-Jones and Rymer, 2002, Williams-Jones et al., 2003, de Zeeuw-van Dalfsen et al., 2005, Bonaccorso et al., 2011, Greco et al., 2012) (FAG_{theo}, e.g. Jousset et al., 2000b, Battaglia et al., 2003, Johnson et al., 2010, Del Negro et al., 2013, Bagnardi et al., 2014). Before estimating a reasonable range of error for any $\Delta \hat{g}_{\text{elev}}$, I demonstrate that FAG_{theo} is the most appropriate and most precise to use, and I provide ranges of expected errors when using any of these two gravity gradients.

4.9.1 Most appropriate gravity gradient to estimate $\Delta\hat{g}_{\text{elev}}$

By definition, any variations in the VGG depend on the surrounding topography, the non-uniform static density distribution below the surface, the elevation change Δh producing Δg_{elev}, and the subsurface variations in density, producing Δg_{def} (e.g. LaFehr, 1991, Vajda et al., 2015). Because the VGG not only depends on elevation, it is inappropriate to call it a free-air gradient (LaFehr, 1991). On the other hand, the FAG_{theo}, equalling -308.3 μGal m^{-1}, is only elevation-dependent, as it describes the gravitational attraction of the Earth with respect to the distance to its centre of mass, assuming a spherical Earth, with a radius of 6,371 m, consisting of layers of uniform density, and having a mass of 5.9722×10^{24} kg (e.g. Chambat and Valette, 2001, Kearey et al., 2002, USNO, 2016). From these two definitions, the VGG may seem like a better gravity gradient to use than the FAG_{theo}, as it captures local effects, but actually, the vast majority of these local effects usually cancel, depending on the source causing deformation (e.g. LaFehr, 1991, Rymer, 1994, Segall, 2010a).

When the source causing Δh is at least a few kilometers depth, which is usually the case for active magma reservoirs (Section 1.2.1), the surrounding topography as well as the shallower static density contrasts move together with the gravity station undergoing the elevation change (e.g. LaFehr, 1991, Rymer, 1994, Segall, 2010a). Consequently, after the elevation change has occurred, the gravity effects of these density contrasts remain unchanged at the surface, and they therefore do not produce any temporal gravity change between the two surveys spanning Δh (Figure 4.13). Using the VGG to estimate the gravity change due to Δh, would, in this case, capture the signatures of the two remaining temporal gravity signals, Δg_{elev} and Δg_{def}; whereas, using the FAG_{theo}, would only capture Δg_{elev}, as intended (see beginning of Section 4.9).

Unlike the surrounding topography and the shallow static density contrasts, most of the heterogeneous bodies that are deeper than the active source are not expected to move with the gravity station (e.g. Rymer, 1994). After the elevation change has occurred, even though they are static bodies, their depths with respect to the surface are modified, and taking the difference in $\Delta\hat{g}_{\text{DC}}$ between the two surveys, captures the residual gravity signals due to these depth changes, in addition to Δg_{elev} and Δg_{def}

(Figure 4.13). In theory, this additional unwanted residual effect could be estimated using the VGG, but, as explained above, this gravity gradient would also capture Δg_{elev} and Δg_{def}. Even though the FAG_{theo} would not capture these residual effects, it still seems more appropriate to use it, to avoid capturing Δg_{def}. The residual gravity effects of the deep static anomalous bodies would then be taken into account in the error of the FAG_{theo} (Figure 4.13).

4.9.2 Error of the gravity gradients when estimating $\Delta\hat{g}_{\text{elev}}$

As argued in Section 4.9.1, estimating $\Delta\hat{g}_{\text{elev}}$ by multiplying $\Delta\hat{h}$ by the FAG_{theo} is generally more appropriate than using the VGG. Here, I demonstrate that the quantification of the errors associated with the use each of these gravity gradients confirms this information.

The use of the FAG_{theo} introduces an error, $\varepsilon_{FAG_{\text{theo}}}$, which has three components: $\varepsilon_{R_{\text{lat}}}$, reflecting the change in the $\varepsilon_{FAG_{\text{theo}}}$ with latitude as the Earth's radius varies (and local altitude above sea level); $(\varepsilon_{\Delta\rho})_{\text{crust}}$, reflecting residual gravity signatures of deep static density contrasts induced by Δh (Section 4.9.1); and $(\varepsilon_{\Delta\rho})_{\text{mantle}}$, reflecting gravity signatures due to any dynamic topography caused by mantle convection:

$$\varepsilon_{FAG_{\text{theo}}} = \varepsilon_{R_{\text{lat}}} + (\varepsilon_{\Delta\rho})_{\text{crust}} + (\varepsilon_{\Delta\rho})_{\text{mantle}} \tag{4.30}$$

$\varepsilon_{R_{\text{lat}}}$ can reasonably be neglected as the maximum difference of ∼14 km between the average Earth radius, considered in the FAG_{theo} calculation (Section 4.9.1), and the radius at the Poles, induces a variation, $\varepsilon_{R_{\text{lat}}}$, of only ∼2.1 μGal m^{-1}. $(\varepsilon_{\Delta\rho})_{\text{mantle}}$ can also be reasonably neglected anywhere at the Earth's surface, as any long-wavelength density contrasts (>50 km) produce maximum absolute variations in the FAG_{theo} of ∼0.1 μGal m^{-1} at 225 km above the Earth's surface (e.g. Bouman et al., 2016). Finally, batholiths, lacoliths and other plutons are among the largest anomalous bodies that can be observed in the deep crust, but, because their density contrasts do not usually exceed 200 kg m^{-3}, their residual gravity signature after Δh has occurred, should be $(\varepsilon_{\Delta\rho})_{\text{crust}}$ ≤5 μGal per meter of elevation change, as this value is for an extreme case

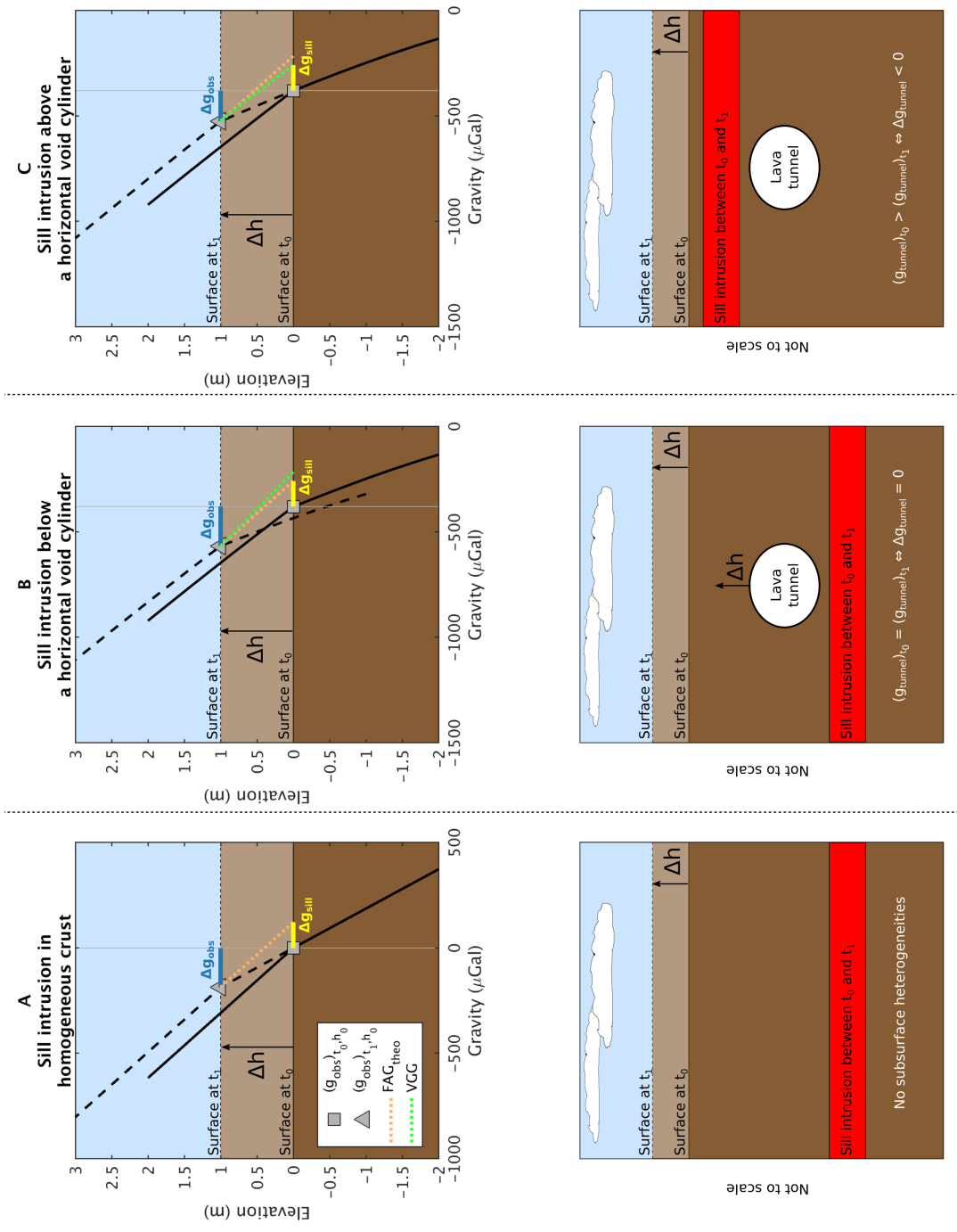

Figure 4.13: Analysis of the best approximation to the gravity gradient to compute the gravity change caused by a surface elevation of Δh, produced by a sill intrusion in a homogeneous crust (A), below a horizontal void cylinder - or lava tunnel (B), and above the lava tunnel (C). The top three panels display the variations in gravity with elevation at the times $t = t_0$ (solid black line) and $t = t_1$ (dashed black line). In each scenario, the temporal change in drift-corrected gravity signal (blue horizontal line), the correction due to elevation change depending on the type of gradient used (orange and green dotted lines), and the residual gravity change due to the sill intrusion (yellow horizontal line) are highlighted. The bottom three panels are sketches to illustrate each scenario. All assumptions for the simulation are stated in the text (e.g. LaFehr, 1991, Rymer, 1994, Segall, 2010a).

of a spherical body, with a radius of 10 km and an initial depth to centre of 13 km (Figure 4.14). Even if a void sphere of same radius and same depth would produce a residual gravity signature of $(\varepsilon_{\Delta\rho})_{\text{crust}}$ ~70 μGal per meter of elevation change, such large void spaces are unlikely to be present at such depths, and because void spaces usually lie within the first few hundreds of meters of crust, they are usually shallow enough to undergo the deformation and to therefore not produce any temporal signal (Section 4.9.1). It is worth noting that infinite horizontal cylinders have negligible residual gravity signatures, as only the 2-D section of the cylinder produces some gravity signal (Figure 4.14), and because horizontal infinite sheets produce gravity signals that are independent of depth, their temporal signature is null for the same reason as shallow density contrasts (Section 4.9.1). From this analysis, it seems reasonable to assume that $\varepsilon_{FAG_{\text{theo}}}$ is always $\leq$5 μGal m^{-1}.

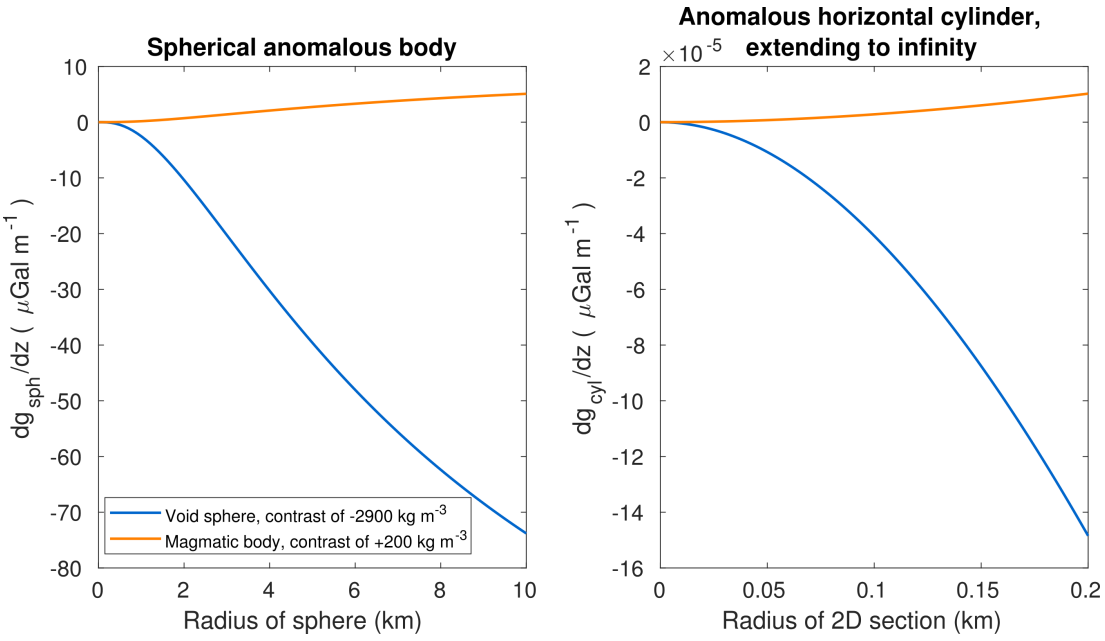

Figure 4.14: Gravity anomaly per meter of change in depth (dg/dz). I have simulated such gravity effect considering spheres (left) and infinite horizontal cylinders (right), having approximate density contrasts for void cavities and plutons. In each case, I computed the derivative dg/dz based on the Newton's law, and to test a worst-case scenario, I assumed that we are right above the static anomalous body, of which the top lies at 3 km depth only (deforming magma chambers can then still lie above these bodies). I have not simulated the case of an infinite slab, because its gravity signature is independent from depth and therefore cancels out when computing the temporal gravity change between two surveys (See Section 4.9.2 for more details.

.

On the other hand, using the VGG to estimate $\Delta\hat{g}_{\text{elev}}$, introduces a different error,

ε_{VGG}, composed of the error, ε_m, due to the measurement procedure, which usually consists of taking several gravity measurements at different heights along the vertical (e.g. Rymer, 1996); and ε_{dev}, describing the deviation of the VGG from the true gravity gradient, which can be well-approximated by the FAG_{theo} when elevation changes are involved:

$$\varepsilon_{VGG} = \varepsilon_m + \varepsilon_{\text{dev}} \tag{4.31}$$

Assuming that (1) the VGG is determined from two gravity measurements, separated by a vertical length, ΔL, of 1±0.05 m, (2) the gravity difference $\left[\hat{g}_{\text{DC}}\right]_{\Delta L} = \left[\hat{g}_{\text{DC}}\right]_{\text{ground}} - \left[\hat{g}_{\text{DC}}\right]_{\text{tripod}}$, is -330.0 μGal m^{-1}, which is the average expected at most volcanic sites (see below), and (3) both $\left[\hat{g}_{\text{DC}}\right]_{\text{ground}}$ and $\left[\hat{g}_{\text{DC}}\right]_{\text{tripod}}$ are determined within ±5-100 μGal (Sections 4.3-4.7), the standard deviation, σ_m, of ε_m, ranges within ∼18-142 μGal m^{-1}, from propagation of errors:

$$\sigma_m = \sqrt{\left[\frac{\left[\sigma_{\text{DC}}\right]_{\Delta L}}{\Delta L}\right]^2 + \left[\frac{-\left[\hat{g}_{\text{DC}}\right]_{\Delta L}}{\Delta L^2}\sigma_{\Delta L}\right]^2} \tag{4.32}$$

This range assumes that the tilt and drift errors can be neglected, which is not always the case (Sections 4.4 and 4.7).

Based on a meta-analysis of 105 measurements of VGG, recorded at various volcanic sites (Figure 4.15), VGG equals ∼-330.0±38.5 μGal m^{-1}, on average at volcanic sites, except at stratovolcano summits, such as at the top of Merapi, where it is ∼-508.6±20.0 μGal m^{-1} on average. It is worth noting that the standard deviations of these approximately Gaussian distributions take into account variations in topography and heterogeneous crust at volcanic sites, but also σ_m. When assuming that these standard deviations correspond to ε_m, ε_{VGG} equals ∼60 μGal m^{-1}, at most volcanic sites, and ∼220 μGal m^{-1}, at the top of Merapi. This is because ε_{dev}, describing the absolute deviations of the means from the precise FAG_{theo} respectively equal ∼21.7 and ∼200.3 μGal m^{-1} (Equation 4.31).

In conclusion, it is very likely that using the FAG_{theo} to estimate $\Delta\hat{g}_{\text{elev}}$ would induce an error standard deviation, $\sigma_{FAG_{\text{theo}}}$, of ≤1 μGal m^{-1} (as $\varepsilon_{FAG_{\text{theo}}} = 5$ μGal m^{-1}

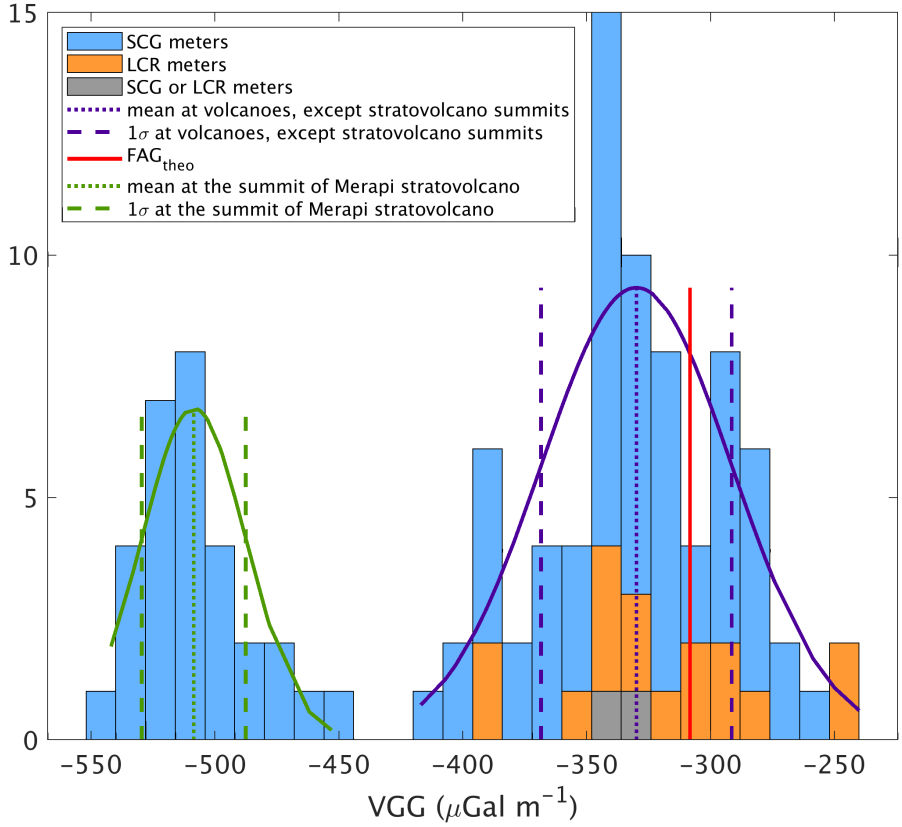

Figure 4.15: Distribution of the local vertical gravity gradients (FAG_{local} or VGG) measured at volcanic sites with Scintrex CG-3M and CG-5 gravimeters (SCG) and with LaCoste & Romberg G and D instruments (LCR). The largest Gaussian distribution (purple PDF) includes 75 values measured at Askja, Krafla, Masaya, Etna (foot to flank), Kilauea, Mauna Loa, Laguna Del Maule and Merapi (foot to flank); whereas the other Gaussian distribution (green PDF) includes 30 values measured at the summit of the Merapi stratovolcano (Berrino et al., 1984, Johnson, 1992, Rymer and Tryggvason, 1993, Johnson, 1995, Jousset, 1996, Williams-Jones et al., 2003, Kauahikaua and Miklius, 2003, de Zeeuw-van Dalfsen et al., 2006, Greco et al., 2012, 2015, Bonforte et al., 2017, Miller et al., 2017). For comparison, the theoretical free-air gradient is highlighted in red.

in extreme cases). On the other hand, using the VGG would induce an error standard deviation, σ_{VGG}, unlikely to be smaller than a few tens of microgals. Consequently, in addition to being more appropriate (Section 4.9.1), the use of the FAG_{theo}, is also more precise.

4.9.3 Error of the gravity change due to elevation change

Because I have demonstrated in Section 4.9.2 that in most cases, the error standard deviation, $\sigma_{FAG_{\text{theo}}}$, of the FAG_{theo} is negligible, the standard deviation, σ_{elev}, char-

acterizing the error of any estimated $\Delta\hat{g}_{\text{elev}}$, then depends on the magnitude of the FAG_{theo} and on the uncertainty, $\sigma_{\Delta\text{h}}$, of the estimated elevation change $\Delta\hat{h}$:

$$\Delta\hat{g}_{\text{elev}} = FAG_{\text{theo}}\Delta\hat{h} \tag{4.33}$$

$$\therefore \sigma_{\text{elev}} = \sqrt{(FAG_{\text{theo}}\sigma_{\Delta h})^2} \tag{4.34}$$

Assuming that the error standard deviation of any single elevation, h, measured using precise geodetic techniques, ranges between 3-12 mm (e.g. Wright et al., 2004, Lagios et al., 2005, Dzurisin, 2007b, Battaglia et al., 2018), $\sigma_{\Delta h}$, then ranges within 4.2-21.2 mm ($\sigma^2_{\Delta h} = \sigma^2_h + \sigma^2_h$), and consequently, σ_{elev} should usually range within $\sim$1.3-6.5 μGal. When one leg of the instrument has not been locked for performing the survey, with e.g. a brass ring (e.g. Jacob et al., 2010), an additional height error standard deviation of $\leq$ 15 mm may arise, which would raise $\sigma_{\Delta h}$ to $\sim$21-34 mm and σ_{elev} to $\sim$4.6-7.4 μGal, at worst.

On the other hand, the inappropriate use of the VGG to estimate $\Delta\hat{g}_{\text{elev}}$, implies that ε_{VGG} (Section 4.9.2) contributes to the error budget of σ_{elev}, which would then range within $\sim$10-60 μGal, on average at volcanic sites, except at stratovolano summits, where it could rise to a hundred of microgals:

$$\varepsilon_{\text{elev}} = \varepsilon_{VGG}\Delta\hat{h} \tag{4.35}$$

$$\therefore \sigma_{\text{elev}} = \sqrt{\varepsilon_{VGG}\sigma^2_{\Delta h}} \tag{4.36}$$

4.10 Error of the gravity change due to groundwater-mass fluctuations

The gravity change induced by groundwater-mass variations between two surveys, Δg_{wtr} (Equation 2.10), can be expressed as follows:

$$\Delta g_{\text{wtr}} = \Big[\Delta g_{\text{wtr}}\Big]_{\text{sat}} + \Big[\Delta g_{\text{wtr}}\Big]_{\text{unsat}} \tag{4.37}$$

where $\left[\Delta g_{\text{wtr}}\right]_{\text{sat}}$ and $\left[\Delta g_{\text{wtr}}\right]_{\text{unsat}}$ are the gravity changes due to groundwater-mass variations, between the two surveys, in the saturated and unsaturated/vadose zones, respectively.

$\left[\Delta g_{\text{wtr}}\right]_{\text{sat}}$ is usually estimated using the infinite slab sheet approximation, with the water density, ρ_{wtr}, scaled to an estimation of the effective/open porosity, ϕ, for the aquifer slab, to consider only the circulating groundwater (e.g. Battaglia et al., 2008):

$$\left[\Delta \hat{g}_{\text{wtr}}\right]_{\text{sat}} = 2\pi G \rho_{\text{wtr}} \hat{\phi} \Delta \hat{z} \approx 41.91 \hat{\phi} \Delta \hat{z} \;\; \mu\text{Gal} \tag{4.38}$$

where G is the gravitational constant and $\Delta\hat{z}$ is the change in groundwater-table level, estimated in meters. The error standard deviation of the estimated $\left[\Delta \hat{g}_{\text{wtr}}\right]_{\text{sat}}$, can be computed by propagating the errors and it therefore depends on $\hat{\phi}$ and $\Delta\hat{z}$, and their associated error standard deviations, σ_{ϕ} and $\sigma_{\Delta z}$:

$$\left[\sigma_{\text{wtr}}\right]_{\text{sat}} = \sqrt{\left[\Delta \hat{z} 41.94 \sigma_{\phi}\right]^2 + \left[41.94 \hat{\phi} \sigma_{\Delta z}\right]^2} \tag{4.39}$$

The open porosity of volcanic rocks, such as lava, pyroclastic deposits, obsidians, hyaloclastites and fractured basalts, ranges widely within $\hat{\phi}$ = 2-40% (e.g. Freeze and Cherry, 1979, Sruoga and Rubinstein, 2006, Pola et al., 2012, 2014, Schaefer et al., 2015). Because it is hard to determine the precise bulk porosity of the crust, I assume a wide range of 5-30%, to characterise volcanic areas in general.

Jin and Feng (2013) demonstrated that the maximum amplitude of groundwater-table variations over the entire globe was 80 mm yr^{-1} for the period 2002-2012. However, because local peaks can be much higher (e.g. Harnisch and Harnisch, 2002), I assume that $\Delta\hat{z}$ can easily range between a few cm up to 4 meters during a gravity survey. And, even though groundwater-table changes can be determined within a few centimeters from wells or satellite altimetry on lakes (Nielsen et al., 2015), it is often very challenging to reach this precision in remote volcanic areas. As a reasonable example, I assume that $\sigma_{\Delta z}$ can reach up to one meter.

Based on these values, I tested the impact of each parameter on the estimation of $\left[\sigma_{\text{wtr}}\right]_{\text{sat}}$ (Equation 4.39). As illustrated by Figure 4.16, for a given $\sigma_{\Delta z}$, $\left[\sigma_{\text{wtr}}\right]_{\text{sat}}$ is

more dependent on $\Delta\hat{z}$ when σ_ϕ is large; whereas the smaller σ_ϕ, the more $\left[\sigma_{\text{wtr}}\right]_{\text{sat}}$ is dependent on $\hat{\phi}$. In summary, $\left[\sigma_{\text{wtr}}\right]_{\text{sat}}$ can be up to ∼20 μGal, in volcanic areas, when $\Delta\hat{z}$ ∼1 m, but it can be up to ∼50 μGal, when Δz ∼4 m.

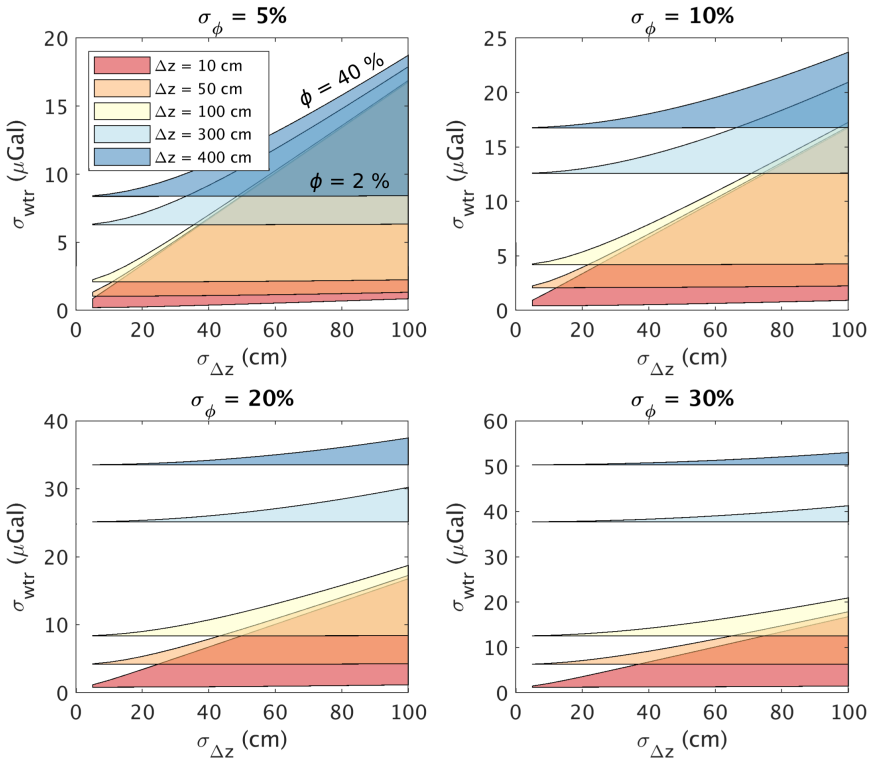

Figure 4.16: Variations in error standard deviations of the gravity changes due to groundwater-table fluctuations, depending on the magnitudes (colors) and errors (x-axis) of groundwater-table changes. Each panel is for a certain error in porosity, but the porosity itself always ranges between 2% (bottom of each triangle) to 40% (top of each triangle).

Unlike $\left[\Delta g_{\text{wtr}}\right]_{\text{sat}}$, no general model can approximate the temporal gravity change, $\left[\Delta g_{\text{wtr}}\right]_{\text{unsat}}$, as it depends on the local geology, hydrology, climatic conditions (e.g. Jacob et al., 2010, Champollion et al., 2018). Moreover, the possible presence of a hydrothermal system can induce complex scenarios of water-mass changes. Ideally, soil moisture measurements, e.g. using frequency domain capacitance probes or lysimeters (e.g. Longuevergne et al., 2009, Creutzfeldt et al., 2010), should be performed during each gravity survey, in addition to supplementary measurements, such as precipitation and glacier ice melting, in order to estimate $\left[\Delta g_{\text{wtr}}\right]_{\text{unsat}}$ from hydrological models (Battaglia et al., 2018). Alternatively, when no measurements are available, the estimation of $\left[\Delta g_{\text{wtr}}\right]_{\text{unsat}}$ is usually part of the interpretation, and performing surveys during

the same season each year should help to minimize $\left[\Delta g_{\text{wtr}}\right]_{\text{unsat}}$ if the groundwater-table variations are seasonal (e.g. Harnisch and Harnisch, 2002).

It is worth noting that groundwater mass variations in the unsaturated zone, may also occur during a single survey. When in-situ measurements of hydrological parameters are available, the resulting short-term gravity change can be modeled, and reduced before estimating the drift. But when unknown, I demonstrated in Section 4.7 that it is possible to include these short-term gravity variations into the drift error.

4.11 Total error budget

Once all the errors presented in this chapter have been quantified, the error standard deviation, σ_{res}, associated to the parameter of interest, $\Delta\hat{g}_{\text{res}}$, can be determined using propagation of errors, as demonstrated in Section 4.2.

Table 4.5 summarizes the best-to-worst ranges of error standard deviation, expected for each parameter, and which I have detailed in each of the above sections. My analysis shows that, in field conditions, σ_{res} is likely to range between $\sim$10 to 100s of microgals, and that the errors especially due to vibration noise, tilt, drift, calibration and water-masses in the unsaturated zone, can have a high impact on the total error budget. It is worth reminding that LCR gravimeters need to be always orientated in the same direction during a survey, to minimize the impact of variations in the Earth's magnetic field on their metal spring (e.g. Rymer, 1996).

By looking back to Figure 4.1, 60% of the maximum recorded residual gravity changes have magnitudes ranging within $\pm$100 μGal, and among the 40% which have an error standard deviation provided, 43% of these provided errors are $\leq$10 μGal. Even though there are chances that these errors have been well-estimated, it is also possible that they have been underestimated.

4.12 Conclusion

In this Chapter, I have presented a detailed statistical approach providing equations for users to precisely estimate the error budget associated to residual gravity changes,

Error parameter	Expected range (μGal)	Influencing factors	Section
σ_{vib}	~1 to a few 100s	vibrations, automatic/manual recording, N, Z, M	4.3
$\sigma_{\Delta\text{tilt}}$	<1 to a few 100s	level sensitivities, electronic/bubble sensors, sunheat	4.4
$\sigma_{\text{ET,survey}}$	Up to 0.6 per ε_t in min	clock residual error (ε_t)	4.5
$\sigma_{\text{ET,model}}$	$\ll$1 to a few	Model uncertainty	4.5
$\sigma_{\text{OL,survey}}$	up to 0.06 per ε_t in min	clock residual error (ε_t)	4.5
$\sigma_{\text{OL,model}}$	$\ll$1 to a few	Model uncertainty	4.5
σ_{P}	<1 to a few 10s	Magnitude of variations in air pressure, and measurement uncertainty, if recorded	4.6
σ_{T}	<1 to a few 10s	Sealing quality, magnitude of variations in air temperature, and measurement uncertainty, if recorded	4.6
σ_{base}	a few to several 10s	M at the base, σ_{vib}, σ_{ET}, σ_{OL}, presence/absence of temporal effects external to the drift	4.7
$\sigma_{\Delta^2\text{cal}}$	a few to a few 100s	Same/different gravimeters are used, regular/no recalibrations	4.8
σ_{elev}	a few to several 10s	Elevation measurement uncertainties, type of free-air gradient used	4.9
$\left[\sigma_{\text{wtr}}\right]_{\text{sat}}$	a few to a few 10s	Water-table level, porosity and uncertainties	4.10
$\left[\sigma_{\text{wtr}}\right]_{\text{unsat}}$	a few to several 10s (at least)	Variations in soil moisture and groundwater infiltration during the survey, can be derived from the drift curve	4.10
$\boldsymbol{\sigma_{\text{res}}}$	**~10 to several 100s**		

Table 4.5: Summary of best-to-worst ranges of error standard deviations to expect when performing temporal gravity surveys. The green, yellow and red highlights show the error parameters that respectively need low, medium and high attention to minimize the total error budget. These colors are just indications as the impact depends on the magnitude of the parameter of interest.

using spring gravimeters. Even though I focused on volcanic applications, the method is equally applicable to other applications, in which case some gravity components, presented here as unwanted signals, could be the parameter of interest.

Additionally, I provided ranges of errors that should be expected in any field conditions. Based on this overall analysis, I suggest three key pieces of advice, which seem to often left out, but are fundamental to help users to obtain precise results.

1. The choice of the type of spring gravimeter is essential to precisely constrain the vibration noise component and reduce the error impact due to an imprecise levelling of the instrument. A gravimeter equipped with an automatic recording system and precise levelling sensors, such as Scintrex gravimeters (SCG) or alternatively, LaCoste & Romberg (LRC) gravimeters, upgraded with the appropriate devices, should therefore be preferred compare to standard LCR gravimeters. In volcanic studies, LCR gravimeters are widely used (Figure 4.1), but it is rarely reported whether the instruments have been properly upgraded.

2. Using always the same suitable gravimeter and regularly monitoring the temporal variations of its calibration factor from recalibrations, is the most suitable ap-

proach to minimize calibration errors, especially when studying long-term gravity changes. Over short-term periods (up to a few years) and when the magnitude of drift-corrected gravity change does not vary much over the area of study, recalibrations might not be necessary when using a Scintrex instrument that is at least a few years old.

3. I propose to abandon the traditional method of estimating the drift function per day, and to rather prefer an estimation over at least a few days. In addition to minimizing the error of the drift parameters, by providing more data points, this approach provides a chance to estimate unknown meteorological effects as part of the drift error. This can provide a first order approximation of, for example, groundwater-mass variations in the unsaturated zone, which are challenging to precisely estimate, and which can have a high impact on the error budget.

As suggested in previous studies, I also encourage users to measure air pressure, air temperature and groundwater-table variations, during each gravity survey, when possible. Finally, users should always keep in mind that the level of tolerated final error depends on the magnitude of gravity change to be detected, and surveying strategies should be planned accordingly.

Chapter 5

Temporal Gravity at The Askja Central Volcano

This chapter addresses the fourth and fifth objectives of my thesis, which aim to record gravity across the Askja caldera using precise methodologies and constrain the related mass changes. In this chapter, I also investigate the causes of subsidence, by comparing my gravity results with deformation results from Chapter 3.

5.1 Introduction

Temporal variations in gravity were monitored within the Askja caldera from 1988 to 2010, by Hazel Rymer (Open University, UK), who was successively accompanied by Geoff Brown (1988-1992), Corinne Locke (1994-1997) and Elske De Zeeuw Van Dalfsen (2002-2003) (de Zeeuw-van Dalfsen, 2004). As presented in Section 1.5.2, a continuous decrease of $\sim$140 μGal was revealed in the centre of the Askja caldera from 1988 to 2007, followed by an increase of $\sim$60 μGal from 2007 to 2009 (Figure 1.8). The hypothesis of magma drainage from the "geodetic reservoir" (Section 1.5.1) down to deeper levels, to explain the Askja subsidence, originated from the correlation between the gravity decrease time-series and the centre of subsidence, while no sign of surface deformation, typical for lateral magma movements, could be observed (e.g. de Zeeuw-van Dalfsen et al. (2005)). Hypotheses of magma crystallization and plate spreading effects were

also suggested (Section 1.5.3). Although the observed gravity increase could be within the noise level (Figure 1.8), it was assumed to be due to a magma inflow at the geodetic reservoir and/or some mass increase in the hydrothermal system of Askja (Rymer et al., 2010, de Zeeuw-van Dalfsen et al., 2013).

The main limitation of these previous studies was the lack of spatial coverage, which prevented the extraction of the spatial gravity signature of the caldera and to use inversion modelling techniques to constrain the location, depth and magnitude of the mass changes related to the observed gravity changes (e.g. Equation 1.20). I sought to improve this limitation in order to test whether the current subsidence and gravity changes are related, as this information could help understanding the causes of subsidence, which are still unclear.

I initially wanted to extend the existing gravity time-series, in collaboration with Hazel Rymer. Unfortunately, it was not possible to link my measurements to earlier data, due to insufficient details on calibration and on how corrections had been made in the past, and I was therefore restricted to my 3-year dataset (2015-2017). Nevertheless, I took the initiative of starting a new time-series, to adapt the surveying and data processing methods with the aim of precisely estimating and minimizing the error budget. In addition to studying the gravity changes at Askja between 2015 and 2017, this case study is therefore also a first application of my error analysis approach, presented in Chapter 4.

5.2 A new gravimeter

Before my PhD, gravity surveys were carried out at Askja, using "standard" LaCoste & Romberg gravimeters (LCR, Section 4.3.2), and the residual gravity changes were averaged over three groups of stations (Figure 1.8), after reductions for tides, drift and elevation changes, from the initial least-squares average of 2-3 gravity samples per site occupation (Section 1.5.2 and e.g. de Zeeuw-van Dalfsen et al. (2005)). Final uncertainties only considered the vibration noise at each site occupation, and the dispersion of the data around the final residual gravity average per group of stations.

Even though recording 2-3 samples per site occupation is the usual methodology when using standard LCR instruments, the small number of observations does not guarantee that the least-squares average is representative of the population, neither that the sampling distribution can be approximated as Gaussian. This can be critical when studying gravity signals at the microscale (Section 4.3). Carrying out further successive averages to determine a residual gravity change per group of stations could be a way of reducing the impact of possible biased least-squares measurements. But it could also bias the final results even more, and due to the lack of statistical control on the averages, it is difficult to know which of these two scenarios has been implemented at Askja.

To better control uncertainties, standard LCR gravimeters need to be upgraded with an electronic feedback system (Section 4.3). When possible, it is even preferable to use Scintrex gravimeters, as these models are specifically designed to automatically compute least-squares gravity measurements from the automatic record of a series of gravity samples (Section 4.3.1). In collaboration with the University of Iceland, I was able to use a Scintrex CG-5 (No. 968) for each of my three gravity surveys. In addition to precisely constrain measurement errors, the use of this particular gravimeter was ideal because it is stored in the premises of the University of Iceland, in Reykjavik, and this could facilitate the reproduction of campaigns in the future.

5.3 Data acquisition

I carried out each of the three gravity surveys, over 4-5 days, and during the summer period, as it is the optimal season to get easy access to Askja and to maximise the chances of having a suitable weather for measuring gravity.

My collaboration with the University of Iceland, as well as the financial support from FUTREVOLC, GRSG, COMET and RAS, enabled the realisation of these three surveys, with the spatial extension of the gravity network and simultaneous elevation measurements at almost all gravity stations, from GPS. Indeed, Freysteinn Sigmundsson and Sveinbjörn Steinþórsson (University of Iceland) installed four new benchmarks

during the 2015 gravity survey, and each year we jointly planned the gravity and GPS surveys to be simultaneous, with Vincent Drouin and Freysteinn Sigmundsson (University of Iceland). This latter point was also a significant improvement from previous studies, when elevation changes were estimated using the two-Mogi-source deformation model from Sturkell et al. (2006) (Table 1.2), due to the lack of elevation data available (de Zeeuw-van Dalfsen et al., 2005).

Among the four new benchmarks installed, three contributed to the extension of the network in the south west and central parts of the caldera (MYV1, MYV2 and CASK) and one was the redefinition of DYNG as a gravity station: a new benchmark was installed near the continuous GPS structure, to facilitate the precise reproduction of gravity measurements at this station in the future (Figure 5.1). In addition, I added to the gravity network, STAM and VATN, which were set up as GPS stations in 2009, to extend the profile up to the south-west caldera edge. For consistency and to facilitate communication, I renamed the old gravity stations that are part of the GPS network, using their GPS station names, and I also simplified other names when needed (Appendix C.1).

During each gravity survey, I strictly followed the same approach for the sake of consistency:

1. The parameters of the CG-5 gravimeter (No. 968) were configured in the same way each time (Appendix C.1).

2. I was always accompanied by a co-worker to help handling the gravimeter smoothly (Stephanie Dumont in 2015 and 2016, and Andy Hooper, in 2017).

3. When driving, the gravimeter was safely attached in a specific wooden case, padded with foam. When walking, the instrument was carried in a rucksack, and we used walking poles to reduce as much as possible the impact of sudden shaking due to the uneven ground of the Askja caldera floor.

4. We systematically used an umbrella to shelter the gravimeter from wind and raindrops, and no one was moving during any gravity acquisition, to reduce vibration noise.

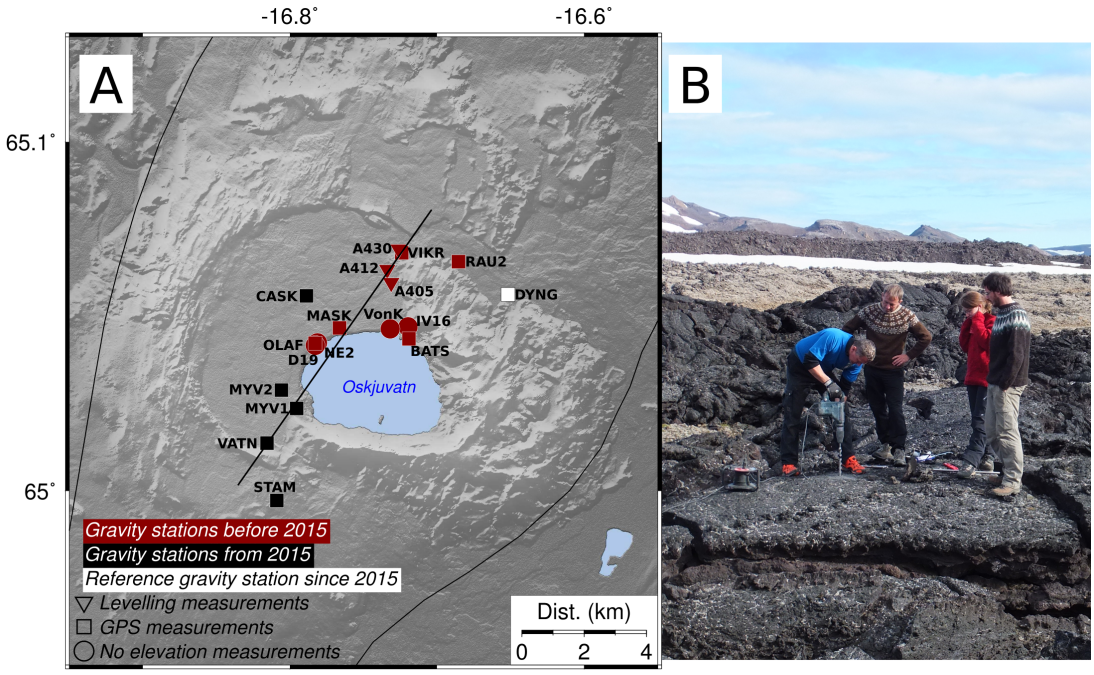

Figure 5.1: A: Gravity network at Askja, since 2015, specifying the method of elevation measurement at each station, if any. The black line highlights the profile onto which results have been projected (Section 5.5) and the new station names are mentioned on the map. Refer to Appendix C.1 to see the old names and location descriptions. B: Photo of the installation of the new benchmark at DYNG, in 2015.

5. Each site occupation consisted of an automatic succession of Z=5 gravity measurements, each resulting from a 1-minute-long continuous record of 1-second gravity samples (Section 4.3). Due to an automatic despiking filter (Scintrex, 2009), the number of observations per measurement was therefore $N \leq$60.

6. The gravity stations were usually re-occupied twice during the same day, ideally when looping through a group of stations, but, because the Askja caldera is ∼8 km across and walking is the only way to get around, the two occupations were sometimes successive. In this situation, I would usually wait ∼10-15 minutes, before re-doing the overall measuring procedure again. When time permitted, I sometimes re-occupied a station on a different day, to ensure continuity in measurements.

7. To estimate the drift function (Section 4.7), I used VIKR (2015-2017) and DYNG (2016-2017) as base stations (Figure 5.1), and we usually re-occupied them twice per day, once in the morning and once in the evening. However, a single mea-

surement was sometimes recorded at either one or both base stations, because it was the easiest way to proceed, and as discussed in Section 4.7, this approach is unlikely to impact the drift estimation. DYNG could not be re-occupied several times in 2015, because the new benchmark was installed during this survey (see above).

8. Finally, I chose station DYNG as the reference for temporal gravity changes, because it not affected by the Askja subsidence (Chapter 3), and it might therefore not be affected by the gravity changes of Askja. In the past, the station VIKR was used (Figure 5.1).

5.4 Data processing

To determine the residual gravity change, $\hat{g}_{\text{res}} \pm \sigma_{\text{res}}$, at each station, between any pair of surveys (2015-2016, 2015-2017 and 2016-2017), I followed the general approach illustrated by Figure 2.7. Because I could not record air pressure nor temperature variations, the first stage was to estimate the tidally- and drift-corrected gravity signature, $\hat{g}_{\text{DC}}$, per station and per survey (Equations 2.10 and 4.5), and the second stage was to reduce all unwanted temporal contributions from the temporal change $\Delta\hat{g}_{\text{DC}}$, between any two surveys (Equations 2.11 and 4.6). For the first stage, I employed the GTOOLS software (Battaglia et al., 2012), which I improved to better constrain uncertainties (Chapter 4), and for the second stage, I wrote my own package, according to the same approach.

5.4.1 First stage: Drift-corrected gravity signal per station and per survey

My improved version of GTOOLS (Figure 5.2) reduces the tidal effects, before computing the weighted least-squares time, t_j, and weighted least-squares tidally-corrected gravity, $(\hat{g}_{\text{TC}})_j$, for each j^{th} site occupation (figure 4.2), taking into account uncertainties due to vibration noise, earth tides, ocean loading and the possible use of an imprecise clock. It then estimates the drift parameters, from a linear function over the whole survey, using given base stations, to predict the tidally-corrected base gravity

signal, $(\hat{g}_{\text{base}} \pm \sigma_{\text{base}})_j$, at each time t_j. A single $\hat{g}_{\text{DC}} \pm \sigma_{\text{DC}}$ is then determined at each station, per survey, from the $(\hat{g}_{\text{DC}})_{j=1}$ to $(\hat{g}_{\text{DC}})_{j=M}$, of the M occupations per station, using weighted least-squares (Section 4.3). χ^2 tests are inserted when necessary, to verify the robustness of the models, and improve them as appropriate.

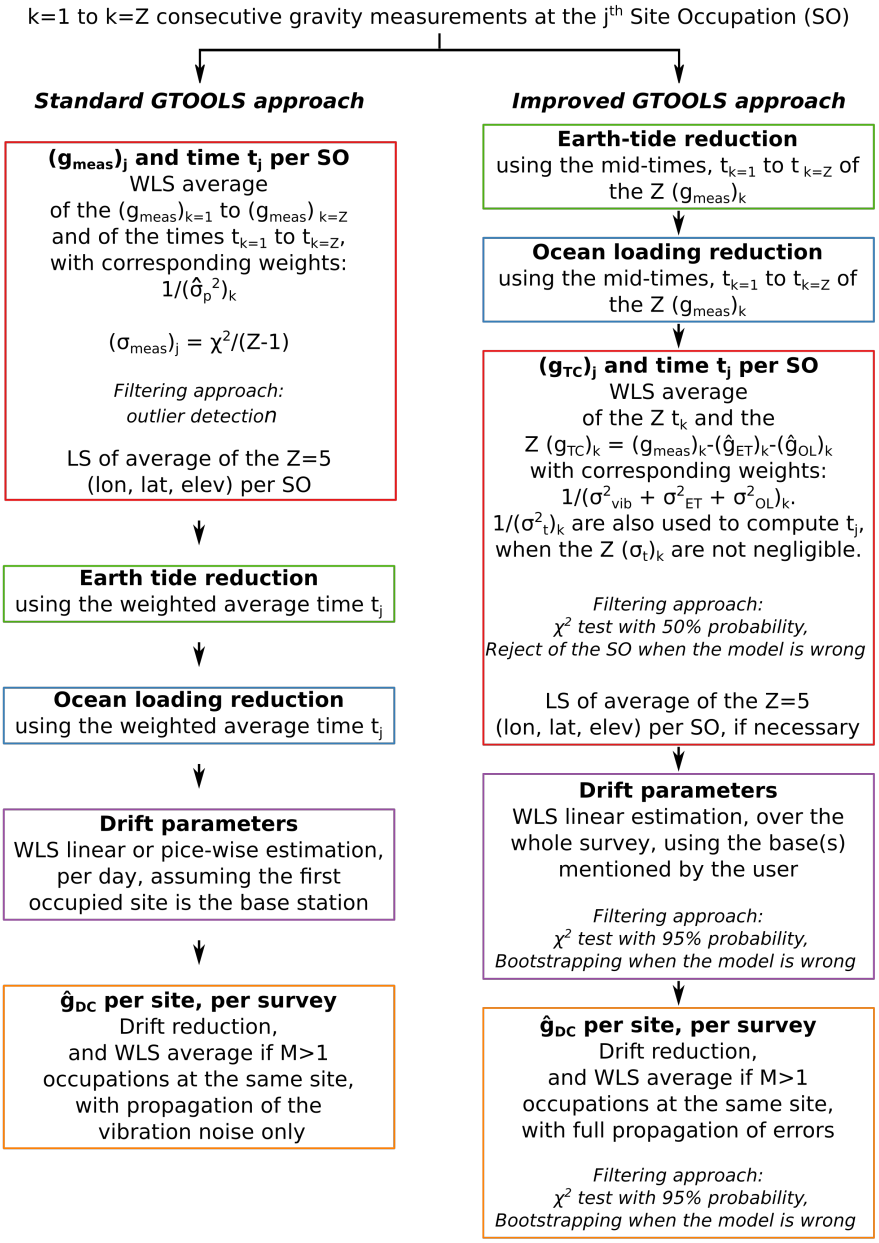

Figure 5.2: Comparison of the standard GTOOLS software, which estimates a single drift-corrected gravity signal, $\hat{g}_{\text{DC}}$, per station and per survey, with the version I have improved. SO: site occupation, Z: number of repeated measurements, M: number of reproduced measurements, WLS: weighted least-squares, LS: least-squares. Refer to Section 5.4, Figures 2.7 and 4.2 for more details on symbols and procedures, and to Sections 3.4.4 and 4.3 for more details on the χ^2 tests and bootstrapping approaches.

GTOOLS currently does not enable to reduce for the gravity effects of measured air pressure and air temperature changes (Section 4.6). However, when estimating the drift function, the new version enables to estimate these effects, as part of σ_{base}, along with any other possible unknown temporal changes affecting the instrumental drift (Section 4.7). If assumed to affect the area of study homogeneously, a constant meteorological error, σ_{met}, can be derived for the entire survey, from the uncertainty of the linear model.

Following the improved version of GTOOLS and based on the application at Askja, Equations 2.8 and 4.5 can be re-written as follows, for any j^{th} site occupation:

$$(\hat{g}_{\text{DC}})_j = (\hat{g}_{\text{TC}})_j - (\hat{g}_{\text{base}})_j \tag{5.1}$$

$$(\sigma_{\text{DC}})_j = \sqrt{(\sigma^2_{\text{TC}})_j + \sigma^2_{\text{met}} + (\sigma^2_{\text{base}})_j} \tag{5.2}$$

where $(\hat{g}_{\text{TC}})_j$ is the tidally-corrected signal, equalling $(\hat{g}_{\text{meas}})_j$ - $(\hat{g}_{\text{ET}})_j$ - $(\hat{g}_{\text{OL}})_j$; the error contribution due to instrumental tilt is neglected due to the use of a Scintrex gravimeter model (Table 4.2); and the calibration factor at the time t_j is, at this stage of processing, assumed to equal one. The uncertainty of such assumption is taken into account later, in the error budget of the residual gravity change (Section 5.4.2).

Here, I summarize the parameters that I have used to estimate each reduction necessary to determine a $\hat{g}_{\text{DC}}$ per station and per survey. Overall, the magnitudes gradually decrease from 0 mGal at the reference station DYNG, in the north-east, to -55 mGal at STAM in the south-west (Figures 5.1 and 5.3), and, despite the low level of vibration noise, the fully integrated error standard deviations, σ_{DC}, range within ∼20-30 μGal in 2015, ∼16-29 μGal in 2016, and ∼18-43 μGal in 2017 (Table 5.1). These large ranges illustrate how meteorological effects, which are often ignored, can impact the error budget.

5.4.1.1 Reduction for tidal effects

In the improved version of GTOOLS, the gravity signals due to solid Earth tides, $\hat{g}_{\text{ET}}$, and ocean loading, $\hat{g}_{\text{OL}}$, are successively estimated just as in the standard version, but

the mid-times of each of the Z=5 successive 1-minute gravity measurements are considered, rather than using the weighted averaged time of each site occupation (Figure 5.2).

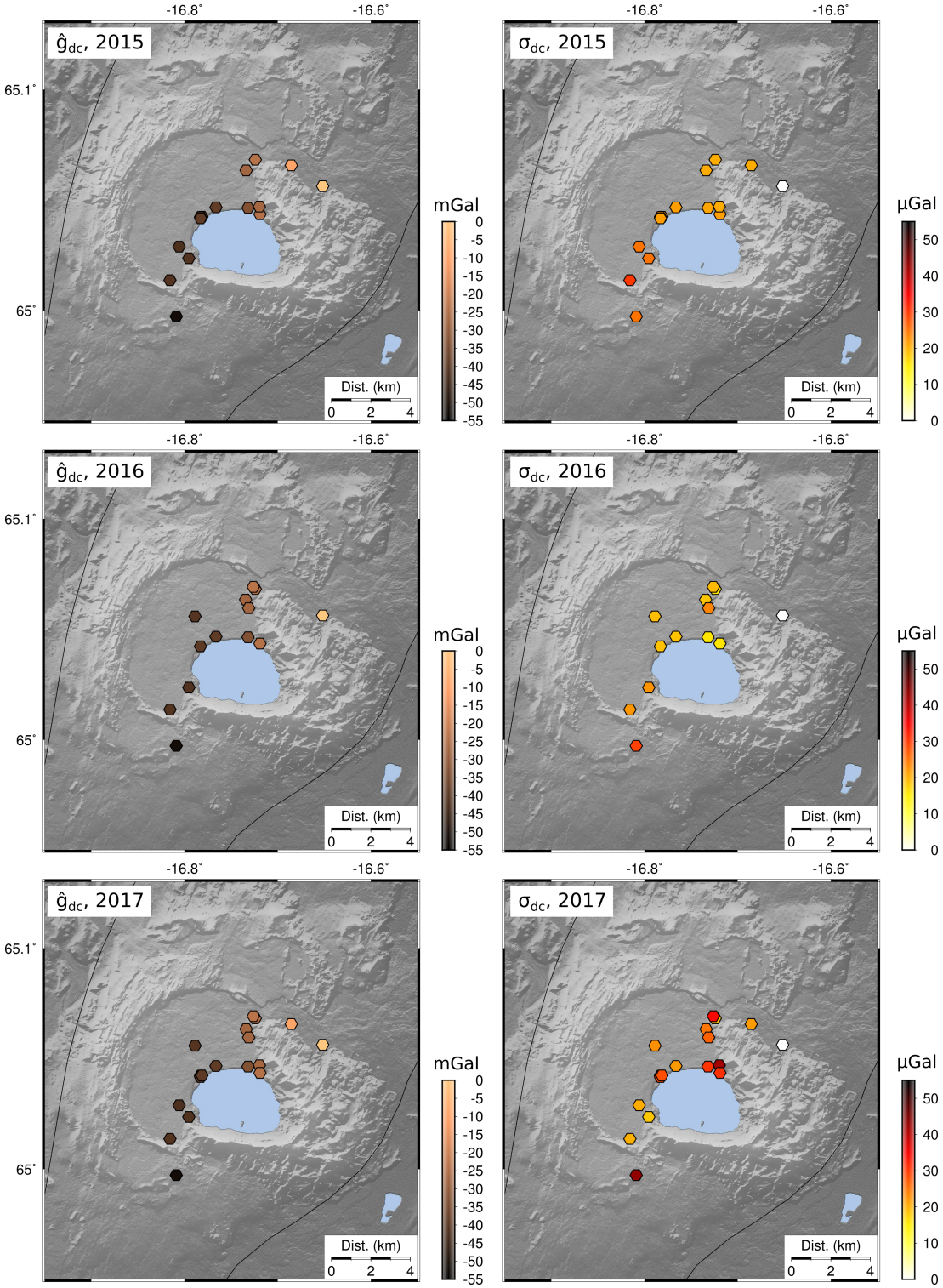

Figure 5.3: Drift-corrected gravity signals (left) and associated fully integrated error standard deviations (right), determined within the Askja caldera, in 2015 (top), 2016 (middle) and 2017 (bottom). See Section 5.4.1 for more details and Figure 5.1 for station names.

	2015 (μ**Gal**)	**2016** (μ**Gal**)	**2017** (μ**Gal**)	**Sections**
σ_{ET}	0.7	0.7	0.7	5.4.1.1
σ_{OL}	0.01-0.25	0.04-0.25	0.01-0.23	5.4.1.1
σ_{vib}	1-2	1-4	2-17	5.4.1.2
$\sigma_{\Delta\mathrm{tilt}}$	*neglected*	*neglected*	*neglected*	5.4.1
σ_{P}	$\in \sigma_{\mathrm{base}}$ & σ_{met}	$\in \sigma_{\mathrm{base}}$ & σ_{met}	$\in \sigma_{\mathrm{base}}$ & σ_{met}	5.4.1.3
σ_{T}	$\in \sigma_{\mathrm{base}}$ & σ_{met}	$\in \sigma_{\mathrm{base}}$ & σ_{met}	$\in \sigma_{\mathrm{base}}$ & σ_{met}	5.4.1.3
σ_{base}	5-17	8-22	13-29	5.4.1.3
σ_{met}	22	34	42	5.4.1.3
σ_{DC} per SO	23-28	35-41	45-50	5.4.1
$\boldsymbol{\sigma_{\mathrm{DC}}}$ per survey	**20-30**	**16-29**	**18-43**	5.4.1

Table 5.1: Summary of the error standard deviations contributing to the tidally- and drift-corrected gravity signal, $\hat{g}_{\mathrm{DC}}$, taken relative to DYNG (Equation 5.2). All error components are provided per site occupation (SO), except σ_{met} which is a constant estimate per survey, and in reality, σ_{ET} and σ_{OL} are estimated a step ahead, for each of the Z=5 gravity measurements (Figure 5.2). The final error $\boldsymbol{\sigma_{\mathrm{DC}}}$ is given a each station, per survey, i.e. by averaging the M site occupations, taken relative to DYNG. See Section 5.4.1 for more details.

In GTOOLS, the Earth tides are estimated using an improved version of the Longman formula, taking into account the anelasticity of the Earth, and the ocean tide estimation requires the use of an ocean tide model to extract the ocean loading constituents at each station location (Section 4.5). Among the various models available, I used the DTU10 ocean tide model (developed at the Technical University of Denmark), as it is the most appropriate model for regions outside ±60° latitude (Cheng and Andersen, 2011, Stammer et al., 2014).

The error standard deviations, σ_{ET} and σ_{OL}, of $\hat{g}_{\mathrm{ET}}$ and $\hat{g}_{\mathrm{OL}}$, are estimated depending on timing and model errors, but neglecting latitude and longitude errors (Figure 5.2). This approach was reasonable in my case because I used latitude and longitude coordinates with a precision of few tens of meters maximum (Section 4.5). Indeed, I considered the unique official GPS coordinates of each GPS-gravity station (Drouin and Sigmundsson, 2013), Erik Sturkell provided the coordinates of the levelling-gravity stations derived from UTM (Coordinated Universal Time), and I recorded the coordinates of the remaining four stations (Section 5.3), using a hand-held GPS, with uncertainty of ±10 meters. Additionally, I could reasonably neglect timing errors, as I made sure that, for each survey, the clock of the gravimeter was correct within a few seconds. Based on Section 4.5, I therefore assumed that $(\sigma_{\mathrm{ET}})_k$ and $(\sigma_{\mathrm{OL}})_k$ respectively equal 1.5 and

$0.05 \times (\hat{g}_{\mathrm{OL}})_k$ μGal, for each k=1 to k=Z=5 gravity measurement.

5.4.1.2 Tidally-corrected gravity average per site occupation

After reducing each the Z=5 gravity measurements for tidal effects, the improved version of GTOOLS, computes a single $(\hat{g}_{\mathrm{TC}})_j$ at any j^{th} site occupation using weighted least-squares, with the sum of the variances due to vibration noise, $(\sigma^2_{\mathrm{vib}})_k$, Earth tides, $(\sigma^2_{\mathrm{ET}})_k$, and ocean loading, $(\sigma^2_{\mathrm{OL}})_k$, of each of the k=1 to k=Z=5 successive acquisitions, listed in the diagonal of the variance-covariance matrix (Figure 5.2). Each $(\sigma^2_{\mathrm{ET}})_k$ and $(\sigma^2_{\mathrm{OL}})_k$ are estimated as explained in Section 5.4.1.1, and each $(\sigma^2_{\mathrm{vib}})_k$ is computed using Equation 4.8, with σ_p and $N \leq$60 provided by the instrument.

I set up the χ^2 test, conducted to verify whether $(\hat{g}_{\mathrm{TC}})_j$ is representative of the Z=5 tidally-corrected gravity measurements, using 50% probability rather than 95%, to make sure that any possible unreliable measurements were discarded (Figure 4.3).

Because I neglected timing errors (Section 5.4.1.1), the averaged time, t_j, of each j^{th} retained site occupation was determined using exactly the same weighting as for the tidally-corrected gravity average (Figure 5.2).

Finally, rather than estimating the least-squares coordinates of each j^{th} retained site occupation, such as possible in any of the two versions of GTOOLS, when the GPS of the gravimeter is used, I considered unique latitude and longitude coordinates per station, as explained in Section 5.4.1.1.

5.4.1.3 Drift parameters and predicted signal at the base station

The case study application presented in Section 4.7.2, presents the procedure that I followed to estimate the drift parameters for each of my three surveys, and that I implemented in the improved version of GTOOLS.

Even though the weighted least-squares drift rates of -18.56 ± 0.03 μGal h^{-1} in 2015, -18.90 ± 0.01 μGal h^{-1} in 2016, and -24.31 ± 0.08 μGal h^{-1} in 2017, are all in accordance with the theoretical drift of a quartz spring (Scintrex, 2009), none of these linear models passed the χ^2 test with 95% probability. Because the data errors were precisely estimated, this suggests the presence of unknown gravity variations in addition to the

instrumental drift. I therefore re-evaluated the parameters using the least-squares percentile bootstrap approach, which changed the drift rates to -18.70 ± 0.33, -18.73 ± 0.23 and -24.43 ± 0.61 μGal h^{-1}, respectively (Section 4.7). These re-evaluations raised the standard deviations $(\sigma_{\text{base}})_j$, of the predicted base station signals, $(\hat{g}_{\text{base}})_j$, at any time t_j, from about 0.5-1.1 to 5-17 μGal in 2015, 1-1.3 to 8-22 μGal in 2016, and 1.8-5.5 to 13-29 μGal in 2017 (Figure 4.8 and Table 5.1).

At Askja, these estimates of $(\sigma_{\text{base}})_j$ probably include the unknown gravity variations of meteorological effects, with a likely high contribution of groundwater-mass changes in the unsaturated zone, and a likely minor contribution from changes in air pressure and air temperature. As described in Section 4.7.2, I assumed that these meteorological effects impacted all stations homogeneously during each survey, and I therefore derived a constant error standard deviation, σ_{met}, equalling 22 μGal in 2015, 34 μGal in 2016 and 42 μGal in 2017 (Table 5.1). If I had had appropriate devices to measure meteorological parameters, the uncertainties would have likely been smaller as most of the effects would have be reduced.

5.4.2 Second stage: Reduction of unwanted temporal gravity changes

Reducing the temporal drift-corrected gravity change, $\Delta\hat{g}_{\text{DC}}$ for the effects due to surface deformation and groundwater-mass changes, while considering calibration variations, provides a temporal gravity signature, which could be explained by any other mass change, such as magma movements and/or mass fluctuations in the hydrothermal system of Askja (Section 2.2.3). Because snow falls occurred at Askja during the week before the 2015 gravity survey, another unwanted temporal effect, due to the removal of snow mass loads, over 2015-2016 and 2015-2017, also needed to be taken into account.

Consequently and based on Equations 2.11 and 4.6, the residual temporal gravity change, $\Delta\hat{g}_{\text{res}} \pm \sigma_{\text{res}}$, at a given station within the Askja caldera, and between any two surveys, can be expressed as follows:

$$\Delta\hat{g}_{\text{res}} = \Delta\hat{g}_{\text{DC}} - \Delta\hat{g}_{\text{elev}} - \left[\Delta\hat{g}_{\text{wtr}}\right]_{\text{sat}} - \Delta\hat{g}_{\text{snow}} \tag{5.3}$$

$$\sigma_{\text{res}} = \sqrt{(\sigma^2_{\text{DC}})_{t_1} + (\sigma^2_{\text{DC}})_{t_2} + \sigma^2_{\text{elev}} + \sigma^2_{\Delta\text{cal}} + \left[\sigma^2_{\text{wtr}}\right]_{\text{sat}} - \sigma^2_{\text{snow}}} \tag{5.4}$$

where $\sigma^2_{\Delta\text{cal}}$ is the variance of the neglected gravity change due to variations in calibration factor (Equation 5.1), and only the gravity component due to groundwater-mass changes in the saturated zone, $\left[\Delta\hat{g}_{\text{wtr}}\right]_{\text{sat}}$ (Section 4.10), is estimated here, as that due to groundwater-mass variations in the unsaturated zone has already been taken into account as part of the meteorological effects, in $(\sigma_{\text{base}})_j$ and σ_{met} (Section 5.4.1).

Below, I summarize the parameters that I have used to estimate each unwanted temporal gravity contribution and determine $\Delta\hat{g}_{\text{res}} \pm \sigma_{\text{res}}$ at each station, for the periods 2015-2016, 2016-2017 and 2015-2017. As illustrated by Figure 5.4, an expected approximate bowl shape gravity signature was observed across Askja, between 2015 and 2016, with maximum decrease of about 98±29 μGal at MASK, i.e. in the centre of the caldera, and minimum decrease of about 34±40 at STAM and 22±31 μGal at A412, i.e. towards the caldera edges. However, the bowl-shape signature was not clearly observed over 2016-2017. Indeed, the maximum decrease of 68±40 μGal was recorded at station A430, whereas negligible variations of about +7±30 and −21±30 μGal were recorded at MASK and OLAF, respectively. Over the full period 2015-2017, the bowl shape signature still dominates with about −120±38 μGal at D19, and −90±35 at MASK. Table 5.2 summarizes the error budget of these results, which are analysed in Section 5.5, i.e. after explaining how I estimated each unwanted parameter (Equations 5.3 and 5.4).

5.4.2.1 Reduction for elevation changes effects

To estimate $\Delta\hat{g}_{\text{elev}} \pm \sigma_{\text{elev}}$ (Equations 5.3 and 5.4), the elevation change, $\Delta\hat{h} \pm \sigma_{\Delta h}$, needs to be determined at each station between each pair of surveys (Section 4.9). At Askja, eleven gravity stations are now part of the GPS network, three belong to the levelling network, and four do not have any elevation records (Figure 5.1).

I estimated the time-series of annual elevation changes, $\hat{h}(t)$, at each GPS-gravity station taken relative to DYNG, from the vertical GPS time-series, which Vincent Drouin provided, and I removed deformation signals external to the Askja volcanic system, as already explained in Section 3.4.1.

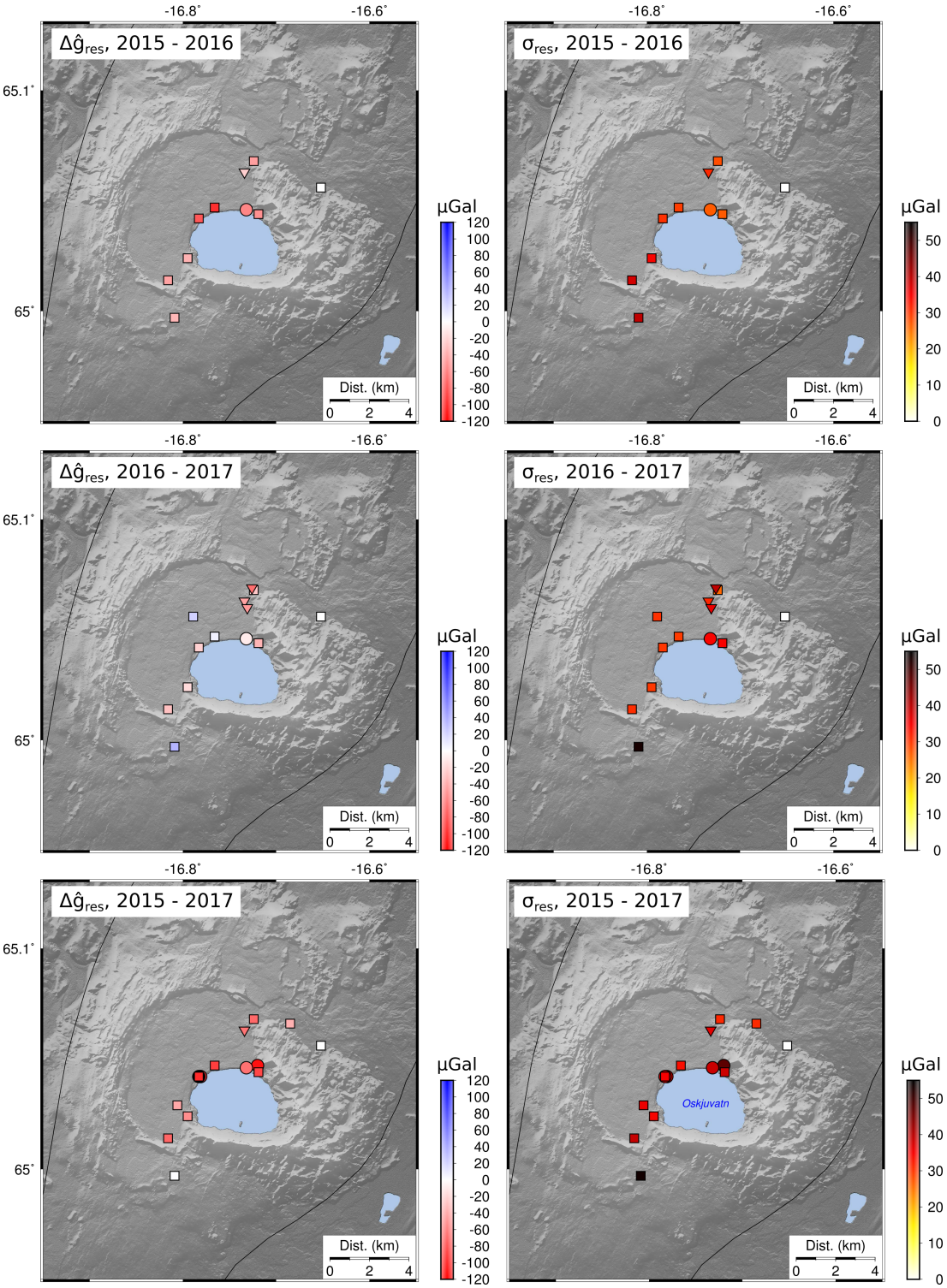

Figure 5.4: Residual gravity changes (left) and associated fully integrated error standard deviations (right), determined within the Askja caldera, from 2015 to 2016 (top), 2016 to 2017, (middle) and 2015 to 2017 (bottom). There is no error at DYNG because it is the reference station: its uncertainty is propagated at all the other stations. See Section 5.4 for more details on the calculation process, and Section 5.5 for the analysis and Figure 5.1 for station names.

	2015-2016 (μGal)	**2016-2017 (μGal)**	**2015-2017 (μGal)**	**Sections**
$\sigma_{\Delta DC}$	26-38	25-52	28-50	5.4.2
σ_{elev}	1-3	1-5	1-7	5.4.2.1
$\sigma_{\Delta^2 cal}$	4-9	4-9	3-19	5.4.2.2
$\left[\sigma_{wtr}\right]_{sat}$	*neglected*	*neglected*	*neglected*	5.4.2.3
$\left[\sigma_{wtr}\right]_{unsat}$	$\in \sigma_{base}$ & σ_{met}	$\in \sigma_{base}$ & σ_{met}	$\in \sigma_{base}$ & σ_{met}	5.4.1.3
σ_{snow}	0.5-14	-	0.5-14	5.4.2.4
$\boldsymbol{\sigma_{res}}$	**27-40**	**26-53**	**31-54**	5.4.2

Table 5.2: Summary of the error standard deviations contributing to the residual gravity change, $\hat{g}_{res}$, between any two surveys, and taken relative to DYNG. See Section 5.4.2 for more details.

Because station A404 is common to the levelling and GPS networks (Figure 3.7), I used this station to calibrate the levelling measurements, which Erik Sturkell provided, into time-series of $\hat{h}(t)$, at each levelling-gravity station. However, no levelling measurements had been carried out at these stations in 2015, and I therefore extracted the displacements for this survey, using linear interpolation over 2014-2016, with weighted least-squares, before doing the calibration.

Finally, I extracted the time-series of $\hat{h}(t)$ at the remaining gravity stations from the line-of-sight displacements of the Sentinel-1 ascending and descending InSAR datasets (Table 3.1), which I had independently decomposed over a 100-by-100 meter grid, as explained in Section 3.5. I determined a $\hat{h}$ per satellite sensor, at each required station and per survey, by estimating a spatial average around each given station and a temporal average per summer (Section 3.4.4). When pixels were available in both datasets, I estimated the time-series of $\hat{h}(t)$ by averaging data from both datasets, which always agreed well within errors. Otherwise, i.e. for station IV16, which did not have any information from the ascending dataset, the time-series of $\hat{h}(t)$ directly equalled the one extracted from the descending dataset.

As illustrated by Figure 5.5, the expected bowl-shape signature of the subsidence was observed over 2015-2016, with maximum decreases of about 2.8±0.7 and 2.9±0.7 cm, respectively at OLAF and MASK, while a negligible deformation of +0.2±0.6 cm was observed at STAM. The decrease of about 2.9 cm observed at RAU2 is likely to be anomalous due to its large GPS uncertainty of 1.7 cm. Over 2016-2017, even though

the expected subsidence signature was also observed, magnitudes were smaller than over 2015-2016, with -1.3 ± 0.7 cm at MASK, -0.4 ± 0.7 cm and -1.5 ± 0.1 cm at D19, while the deformation was still near to negligible on the caldera edges, with $+1.2\pm0.9$ cm at VATN, $+1.1\pm1.6$ cm at STAM, and $+1.6\pm0.6$ cm at RAU2. Over 2015-2017, these changes generated maximum decreases in the centre of the caldera, with about -4.1 ± 0.6, -3.4 ± 0.7 and -3.1 ± 0.1 cm, at MASK, OLAF and D19, respectively, and minimum variations at the caldera edges, with $+1.3\pm1.6$, -1.0 ± 0.9 and -1.2 ± 2.2 cm, at STAM, VATN and RAU2, respectively.

All these magnitudes of elevation change, which are compared with the residual gravity changes in Section 5.5.2, produced some $\Delta\hat{g}_{\text{elev}}$ ranging between about -1 and $+9$ μGal over 2015-2016, -10 and $+9$ μGal over 2016-2017, and -4 and $+12$ μGal over 2015-2017. The associated σ_{elev} never exceeded 10 μGal (Section 4.9.3 and Table 5.2).

5.4.2.2 Uncertainty due to unknown calibration effect

The calibration factor of Scintrex gravimeters, initially determined at manufacture, is expected to vary at a rate, $\dot{f}$, of a few ppm per day during the first year after purchase, but it usually then reaches a plateau with error standard deviation, $\sigma_{\dot{f}}$, of ∼0.01-0.5 ppm per day (Section 4.8). Because the Scintrex CG-5 No. 968 (Section 5.3), was bought in 2012 and had never been recalibrated since purchase (Personal communication, M.T. Gudmundsson, 2018), it is very likely that the variations in calibration factor had reached the plateau, and I therefore assumed a $\sigma_{\dot{f}}$ of 0.5 ppm per day between 2015 and 2017.

Based on Equation 4.23 and Section 4.8.3, the resulting error standard deviation, $\sigma_{\Delta\text{cal}}$, caused by such $\sigma_{\dot{f}}$, can be approximated, at each station, using the time duration between any pair of surveys and the magnitude of $\hat{g}_{\text{DC}}$ of the second survey. Consequently, based on Figure 5.3, a resulting $\sigma_{\Delta\text{cal}}$ of about 4-9 μGal needed to be considered for the 1-year periods of 2015-2016 and 2016-2017, and of about 3-19 μGal over 2015-2017 (Table 5.2).

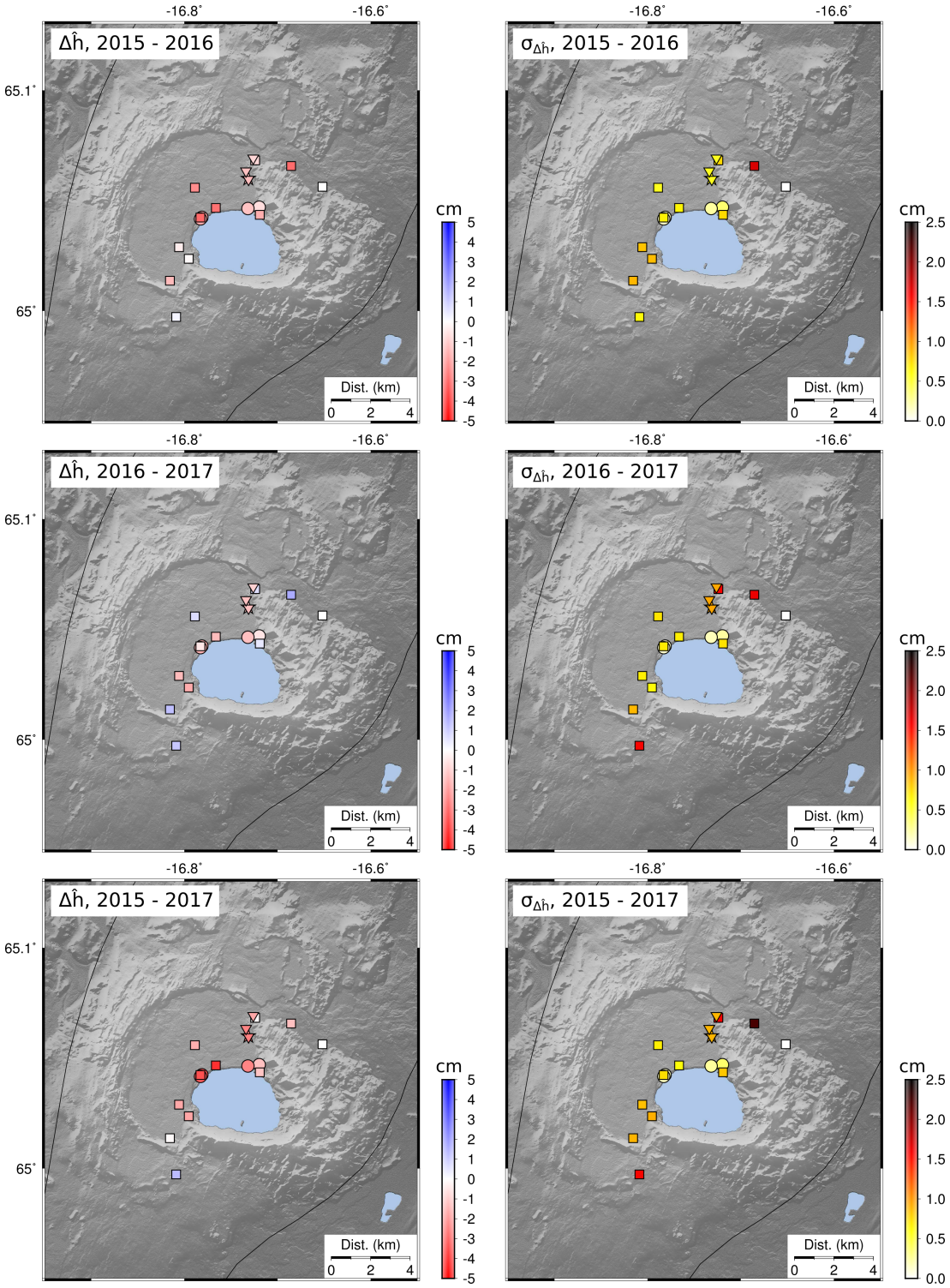

Figure 5.5: Elevation changes (left) and associated error standard deviations (right), determined within the Askja caldera, from 2015 to 2016 (top), 2016 to 2017, (middle) and 2015 to 2017 (bottom). The symbols refer to the elevation measurement method (Figure 5.1), and the star is station A404, which is not part of the microgravity network, but was used to calibrate the levelling measurements in deformation relative to DYNG. See Section 5.4.2.1 for more details.

5.4.2.3 Effects due to groundwater-mass variations

The temporal gravity change due to groundwater-mass variations has two components: $\left[\Delta\hat{g}_{\mathrm{wtr}}\right]_{\mathrm{sat}}$ reflecting changes in the saturated zone, i.e. caused by fluctuations in the water-table level, and $\left[\Delta\hat{g}_{\mathrm{wtr}}\right]_{\mathrm{unsat}}$ reflecting changes in the unsaturated zone, such as due to influx of rainwater or soil moisture variations (Section 4.10). I used a new approach to take into account this latter component, which is challenging to precisely estimate, into the error budget of each drift-corrected gravity signature (Section 5.4.1.3). To estimate the remaining $\left[\Delta\hat{g}_{\mathrm{wtr}}\right]_{\mathrm{sat}}$, I used the usual infinite slab sheet approximation (Equation 4.38), assuming an open porosity, $\phi \pm \sigma_{\phi}$, of 20±15%, i.e. with a large-enough uncertainty to characterize the heterogeneity of the volcanic and pumice fillings of the Askja caldera (Section 4.10). Moreover, I assumed that the water-table changes, $\Delta\hat{z} \pm \sigma_{\Delta z}$, vary similarly as the Öskjuvatn lake level, over the entire area of study.

Using a time-series of these lake level variations (Figure 5.6), which Karina Nielsen (National Space Institute of Denmark) derived from CryoSat-2 satellite altimetry (Nielsen et al., 2015), I estimated water-level changes as the difference in the weighted least-squares averages of lake level per summer, between each pair of surveys (Figure 5.6). From this lake-level time-series, $\Delta\hat{z}\pm\sigma_{\Delta z}$ equalled about +0.98±0.14 m over 2015-2016, −0.67±0.13 m over 2016-2017, and +0.32±0.10 m over 2015-2017. A resulting gravity change, $\left[\Delta\hat{g}_{\mathrm{wtr}}\right]_{\mathrm{sat}}$, of about +8±6, −6±4 and +3±2 μGal, is likely to have affected the area of study during 2015-2016, 2016-2017 and 2015-2017, respectively (Equation 4.38).

If the water-mass variations at Öskjuvatn reflect the variations of groundwater-masses beneath Askja, this analysis implies that the temporal gravity changes, $\left[\Delta\hat{g}_{\mathrm{DC}} - \Delta\hat{g}_{\mathrm{elev}}\right]$, should all be shifted by a constant of less than ±10 μGal, even at the reference station DYNG. Because this shifting would not affect the overall residual gravity anomaly, I decided to neglect $\left[\Delta\hat{g}_{\mathrm{wtr}}\right]_{\mathrm{sat}}$. Even though groundwater-masses might not vary homogeneously over the area of study, this discarding should not affect final results as the lake level variations should still indicate the order of magnitude for $\left[\Delta\hat{g}_{\mathrm{wtr}}\right]_{\mathrm{sat}}$, which is very small compare to the error budget of the residual gravity changes (Table 5.2).

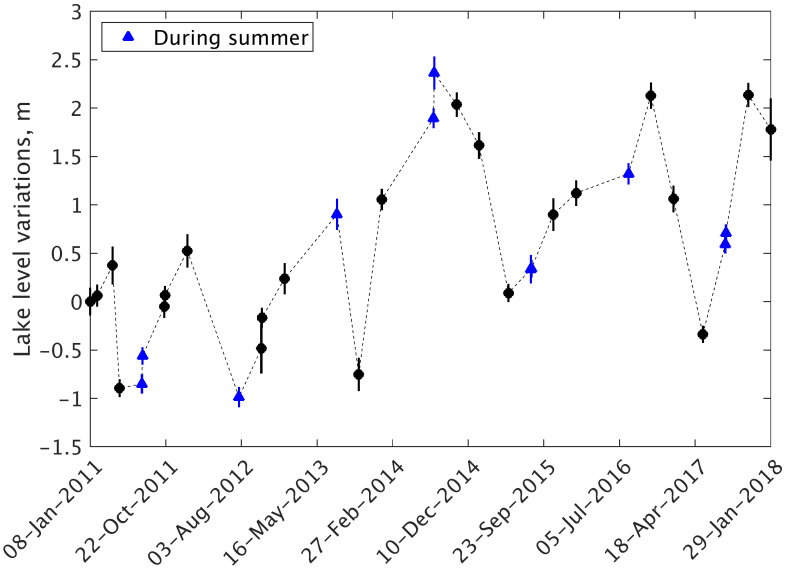

Figure 5.6: Time-series of the lake level variations at Öskjuvatn, determined by Karina Nielsen, using CryoSat-2 satellite altimetry (Nielsen et al., 2015). I am interested in the lake level variations in summer (blue), between 2015, 2016 and 2017.

5.4.2.4 Effects due to snow-mass variations

The last unwanted temporal component to estimate was the one due snow mass variations over 2015-2016 and 2015-2017 ($\Delta\hat{g}_{\text{snow}} \pm \sigma_{\text{snow}}$ in Equations 5.3 and 5.4).

From field observations, the levelling-gravity stations as well as CASK were surrounded by about 1.5 to 2 meters of snow in 2015, while, in the centre of the caldera, I only noticed snow patches of a few centimeters thick, and there was no snow around VonK, DYNG and MYV2. The site occupations performed at CASK in 2015 could not be used because they had been discarded from the statistical test, when averaging the Z=5 gravity measurements (Figure 5.2), and station A412 was the only levelling-gravity station that could be measured during this survey, because uncovered by snow.

To get an estimation of $\Delta\hat{g}_{\text{snow}} \pm \sigma_{\text{snow}}$, at each required station, I used the infinite slab approximation, similarly as in Equation 4.38, but assuming a bulk snow density of 400 kg m^{-3}, and providing snow thicknesses from 0.05 to 2 meters, with negative signs, because mass had been removed. Considering standard deviations equalling 50% of these approximate thicknesses, a maximum $\Delta\hat{g}_{\text{snow}} \pm \sigma_{\text{snow}}$ of about -25 ± 14 μGal is likely to have affected station A412, a snow effect of about -3 ± 2 μGal is likely to have

occurred at MASK, and the effect should be less than one microgal at OLAF, NE2 and D19 (Table 5.2).

5.5 Analysis of residual gravity changes at Askja

As previously highlighted by Figure 5.4, the spatial pattern of the residual gravity changes at Askja (Equations 5.3 and 5.4) has a negative bowl-shape signature over 2015-2017, with maximum decrease of about 120±38 μGal, observed at station D19 (Section 5.4.2). This gravity signature mainly occurred between 2015 and 2016, when the maximum decrease of about 98±29 μGal was observed at MASK (i.e. <1 km away from D19, Figure 5.1), whereas negligible variations of +7±30 and −21±30 μGal were recorded at MASK and OLAF, respectively, over 2016-2017.

The negative bowl-shape signature, centered on the Askja caldera, can be more clearly highlighted for the periods 2015-2016 and 2015-2017, when fitting second degree polynomial functions to the results, projected along a south-west to north-east profile (Figure 5.7). The estimated extrema of about −70±16 μGal over 2015-2016 and about −91±13 μGal over 2015-2017 are respectively near the cluster containing OLAF, NE2, and D19 and near MASK. On the other hand, the second degree polynomial function for the period 2016-2017 highlights a negligible decrease at the caldera centre, and an estimated maximum low of about −41±18 μGal, near A430, i.e. towards the north-east caldera edge (Figure 5.7). When comparing the polynomial models for the three periods, variations in residual gravity are irregular from one year to another, but the signals seem to be confined within the caldera, with negligible (or near-negligible) variations constantly observed at the caldera edges.

5.5.1 Comparison with previous gravity studies

Due to the use of standard LaCoste & Romberg gravimeters, previous measurements might have been biased (Section 5.2), but assuming that these measurements were acquired with extreme caution, the order of magnitude of temporal changes should still be similar between the two distinct time-series.

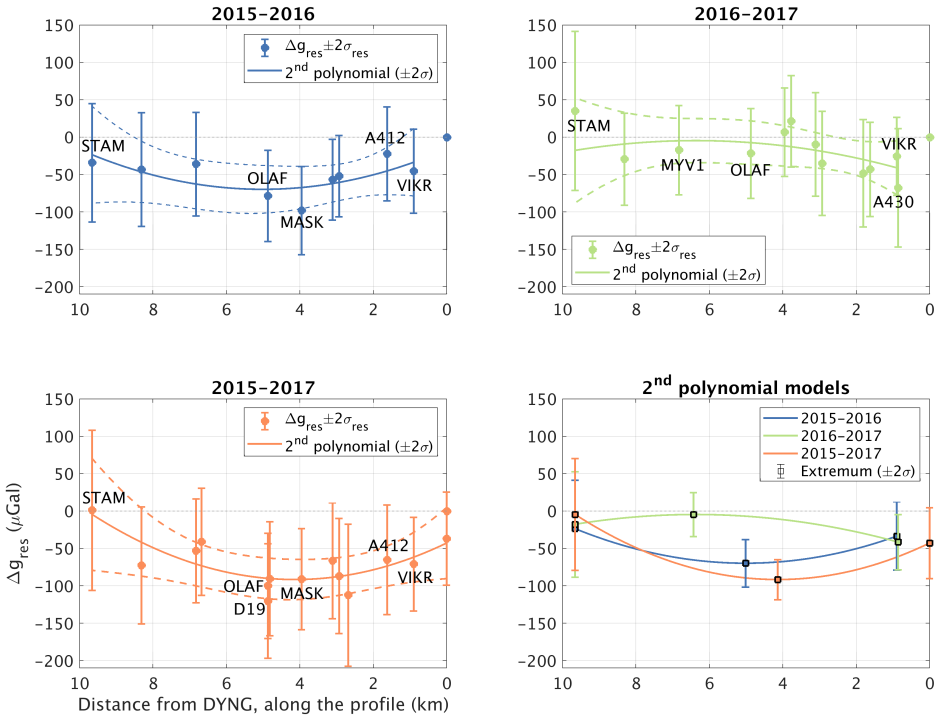

Figure 5.7: A-C: Residual gravity changes relative to DYNG, across Askja, where the station locations have been projected along a SW-NE profile, passing by VATN and VIKR (Figure 5.1). D: Superimposition of the second degree polynomial models of each time period, with extreme estimated values highlighted by the squares.

Based on previous results, I expected to observe a bowl-shape residual gravity change signature across Askja, such as detected over 2015-2016, with maximum decrease centered near OLAF, D19, NE2 and MASK; these stations composed the old gravity centre group, where the long-term gravity decrease had previously been observed (Figure 1.8).

In the past, VIKR was used as reference for gravity changes, whereas I used DYNG, which is further away from the caldera (Figure 5.1). This is very likely the reason why I recorded a much larger change over 2015-2016 compared with previous studies: the weighted least-squares average of the residual gravity change, grouping MASK, OLAF, NE2 and D19 (such as done in previous studies) equals about -90 μGal over 2015-2016. Such a variation had previously been recorded over about 12 years (1988-2002), while absolute yearly fluctuations ranged between <5 and 45 μGal (Figure 1.8B). When taken relative to VIKR, the -90 μGal decrease spanning 2015-2016 is lowered to about -40 μGal, which is in agreement with the previous time-series. Similarly, the central

weighted average over 2016-2017 equals about -10 μGal when taken relative to DYNG, and $+20$ μGal when taken relative to VIKR.

This observation emphasizes the importance of choosing an appropriate reference station for temporal gravity changes, and results from previous studies might have been underestimated. Choosing DYNG for reference seems more appropriate, especially because the zero-gravity change level seems to be reached at the caldera edges (Figure 5.7). However, there is still a risk that my results have been underestimated, as I could not demonstrate that DYNG was outside the gravity change zone during my surveys (Section 5.3). We measured the GPS-gravity station GRAF (N65.287°,W16.090°; Drouin and Sigmundsson (2013) and Appendix C.1) at the beginning and end of each survey, i.e. on the way to and back from Askja. As this station is located at ∼40 km to the north-east of Askja, it is obviously outside the gravity change zone of the caldera, and one could therefore think that it would be an appropriate reference station to verify whether DYNG is affected by any mass change. However, GRAF might have been affected by some local residual gravity variations, and additionally, the gravity changes due to meterologial effects and groundwater-mass variations should have been estimated specifically for this area (Sections 5.4.1.3 and 5.4.2.3). Assuming that these effects were the same in both regions, variations of about -57 ± 38 and $+40\pm41$ μGal occurred at GRAF relative to DYNG, over 2015-2016 and 2016-2017, respectively. These results could equally reflect variations at DYNG and/or GRAF. Extra work would have therefore been required to safely use GRAF as the reference station. Although expensive and not so easy in remote areas, a good and reliable alternative for future surveys would be to continuously monitor gravity at DYNG, during each survey, using an absolute gravimeter (e.g. Carbone et al., 2017, Van Camp et al., 2017).

5.5.2 Comparison with simultaneous surface deformation

The spatial signature of surface deformation along the south-west to north-east profile (Figure 5.8) highlights the bowl-shape more clearly than Figure 5.5. Second degree polynomial functions are very similar over 2015-2016 and 2016-2017, with respective estimated lows of about -1.6 ± 0.1 and -1.5 ± 0.1 cm, constantly located near the station

cluster with OLAF, D19 and NE2. Consequently, twice as much deformation occurred over 2015-2017, with a maximum estimated decrease of -3.1 ± 0.1 cm in the same central area. This steady temporal evolution of the subsidence, confined within the caldera, with constant negligible (or near-negligible) deformation at the caldera edges, is in good agreement with InSAR results from Chapter 3 (e.g. 3.15).

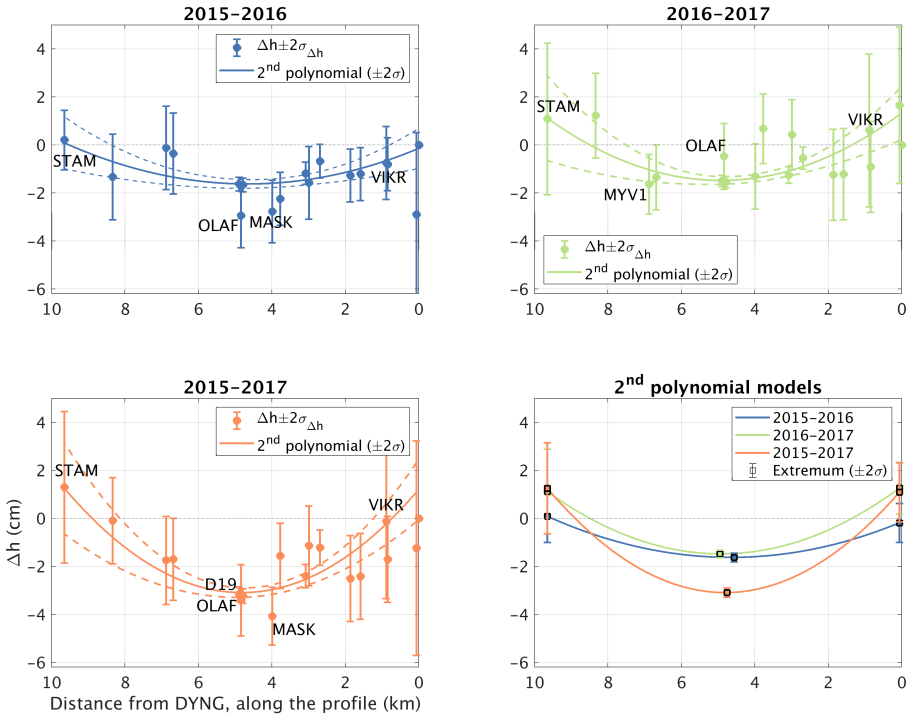

Figure 5.8: A-C: Elevation changes relative to DYNG, projected along the same SW-NE gravity profile as the residual gravity changes in Figure 5.7 (as explained in Section 5.4.2.1, the smallest error bars are underestimated). D: Superimposition of the second degree polynomial models of each time period, with estimated extrema highlighted by the squares.

On the other hand, the irregular variations of annual residual gravity changes are only correlated with the subsidence over 2015-2016 (Figure 5.9), with the magnitudes increasing from maximum lows near MASK and OLAF to approximately negligible variations at the caldera edges. The independent evolution of both signals over 2016-2017 (Figure 5.9) suggests that they are caused by distinct processes, which could be indirectly linked and which induce some temporary similarity in spatial pattern. In the next section, I further investigate the link between surface deformation and temporal gravity using inversion modelling.

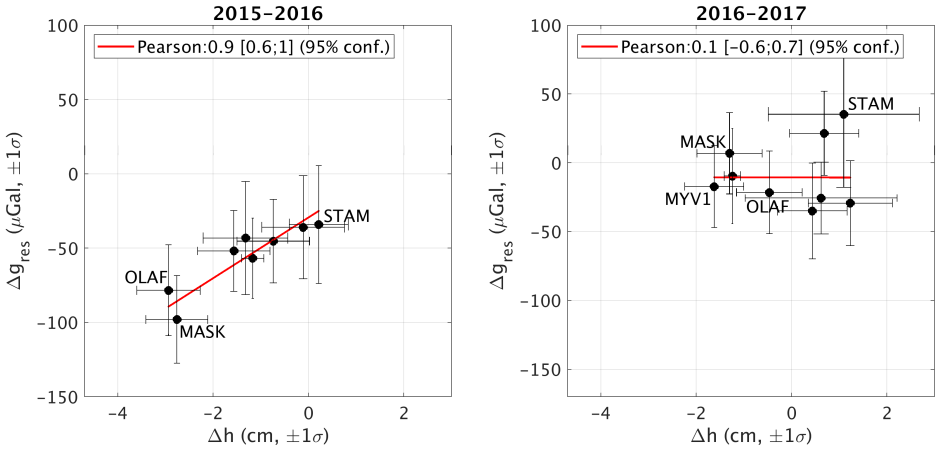

Figure 5.9: Residual gravity changes against elevation changes over 2015-2016 (left) and 2016-2017 (right). The red line highlights the best-fit linear model constrained using Monte Carlo simulation using 10,000 iterations, and taking into account uncertainties in both signals. The Pearson correlation coefficient characterizes the degree of correlation between two variables, with +1 indicating a strong positive correlation and near-zero indicating no linear relationship. Refer to Figure 5.1 for station locations.

5.6 Modelling residual gravity changes at Askja

In Chapter 3, I demonstrated that the Askja subsidence can be explained by an exponentially deflating Mogi reservoir, located at 3 km depth beneath the centre of the main caldera. Using again the MCMC Bayesian modelling approach from GBIS (Section 3.7.1), I solved for the location, depth and magnitude of subsurface mass change that would best predict the non-negligible residual gravity change observed over 2015-2016 (Figure 5.7). Due to the bowl-shape spatial signature of this annual gravity change, I assumed a spherical reservoir geometry and I therefore adapted GBIS to implement Equation 1.20.

5.6.1 Correlated errors of residual gravity changes

Air pressure and air temperature variations as well as water infiltration from rainfall and soil moisture can all be spatially-correlated over periods of hours to days or even months (Sections 4.6, 4.10 and e.g. Jacob et al. (2010)). Consequently, errors due to these "meteorological effects", ε_{met} (Section 5.4.1.3), are likely to covary during any survey, between stations that were occupied over a specific time window. Additionally, the errors, $\varepsilon_{\text{base}}$, of the base measurements, predicted from the drift function should

also covary, because they are estimated from common model parameters: drift rate and y-intercept (Section 4.7.1).

The final errors, ε_{res}, of residual gravity changes between any two stations and any two surveys, therefore covary in agreement with the covariances, C_{base} and C_{met} of the respective $\varepsilon_{\text{base}}$ and ε_{met}, during each survey:

$$C_{\text{res}} = (C_{\text{base}} + C_{\text{met}})_{\text{survey}_1} + (C_{\text{base}} + C_{\text{met}})_{\text{survey}_2} \tag{5.5}$$

where C_{res} is the covariance of ε_{res} at the given station and between the two surveys. This assumes negligible contributions from covariance at other errors.

Assuming low correlation favours fitting the overall magnitude, whereas assuming high correlation favours fitting the shape of the gravity signal. It is therefore important that covariances are included in the variance-covariance matrix in the inversion.

I estimated C_{base} between any pairs of station and per survey, by propagating the errors of the drift function derived using the least-squares percentile bootstrap approach (Section 5.4.1.3):

$$\mathbf{Q_{\hat{d}\hat{d}}} = \mathbf{G Q_{mm} G^T} \tag{5.6}$$

where $\mathbf{G}$ lists the times of base occupations in the first column and ones in the second columns, and $\mathbf{Q_{mm}}$ is the variance-covariance matrix of the drift model parameters, listing the variances of drift rate and y-intercept in the diagonal, and their covariances elsewhere. $\mathbf{Q_{\hat{d}\hat{d}}}$ lists the variances σ^2_{base} in the diagonal and all C_{base} elsewhere.

Because $\varepsilon_{\text{base}}$ are mainly due to meteorological contribution, the covariance of the residuals to the drift function in time reflect the covariance of ε_{met}. Consequently, the covariance function for ε_{met} can be estimated in time using the semi-variogram of the residuals, and assuming that it follows an exponential model (Equation 3.5 with r replaced by separation time, and R being the correlation time for ε_{met}). When assuming that such model is appropriate and combining the two surveys, residuals from the drift can be fitted with a semi-variogram having a range R of 2/3 days, which is equivalent to an effective range of 2 days (e.g. Bagnardi and Hooper (2018) and Figure 5.10). Using this R, individuals variograms can be generated per survey, and although noisy,

I estimated the $(C_s - C_n)$ variance parameter to be 200 μGal for 2015 and 600 μGal for 2016. From all these parameters, I estimated the covariances C_{met} for each survey using Equation 3.5.

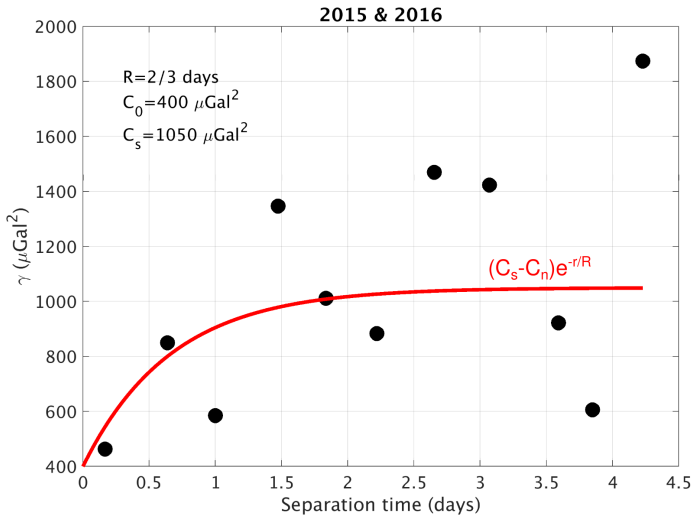

Figure 5.10: Semi-variogram computed using residuals from the drift in both 2015 and 2016. Both surveys were combined to increase the number of datapoints and therefore improve the semi-variogram model. Because residuals from the drift largely comprise unknown meteroro-logical effects, the covariance of these effects between any station measurement should evolve similarly (Section 5.6.1). Refer to Section 3.4.4 and e.g. Bagnardi and Hooper (2018) for more explanations on the semi-variogram approach.

5.6.2 Modelling results

I performed the MCMC Bayesian inversion with one million iterations, taking into account the covariances between errors of residual gravity changes (Section 5.6.1). I refer the reader to Section 3.7.1 for more details on the theory behind the MCMC Bayesian inversion method. Even though the inversion converged well (Appendix C.2), the posterior probability density functions show that the depth could not be well constrained (Figure 5.11), and the upper bound is very dependent on the prior.

When assuming that DYNG is an appropriate reference station for temporal gravity and that the spherical geometry is a suitable model, my inversion suggests that residual gravity changes over 2015-2016 are due to a mass decrease of about 9.5×10^{10} $[-1.5\times10^{12};-7.5\times10^{10}]$ kg located at about 2.8 [2.7;9.9] km beneath MASK (Figure 5.12).

Due to the poorly constrained depth of the gravity source, there is still a probabil-

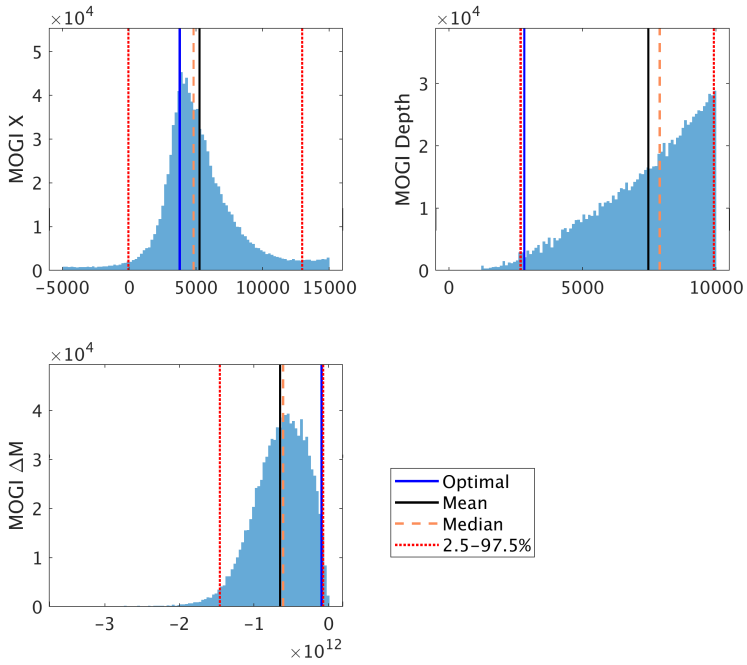

Figure 5.11: 1-D marginal posterior probability density functions for the location, depth and magnitude of mass changes, projected along the profile, with DYNG as reference (Figure 5.7). The most likely solution is highlighted in blue.

ity that mass and volume changes originate from the same depth. Indeed, the range of gravity source position, ranging between 2.7 and 9.9 km overlaps with the position of the deformation source, which ranges within 2.9 to 3.1 km depth (Figure 3.7.3). However, when assuming an incompressible system (Section 1.3.1) with magma density ranging between 2100 and 2800 kg m^{-3} (to account for any possible stage of crystallisation), the volume change of about -6×10^6 m^3, constrained from deformation over 2015-2016 (Figure 3.21), translates into a mass change of between -1.7×10^{10} and -2.3×10^{10} kg. Because this range is outside the 95% confidence interval of $[-1.5\times10^{12};-7.5\times10^{10}]$ kg constrained from gravity, it is likely that both signals are not related. This discrepancy remains if assuming a basaltic magma with compressibility, β_m, of 10^{-10} Pa^{-1}, surrounded by a somewhat fractured crust with a shear modulus, μ, of 10^{10} Pa (Table 1.1) and a compressibility, β_c, of $3/(4\mu)=7.5\times10^{-11}$ Pa^{-1} (e.g. Rivalta and Segall, 2008). Indeed, in such scenario the range of mass change derived from deformation results is between -3.9×10^{10} and -2.9×10^{10} kg (Equation 1.12 and Segall (2010c)).

These results are based on assuming a Mogi source geometry, which is a very simple

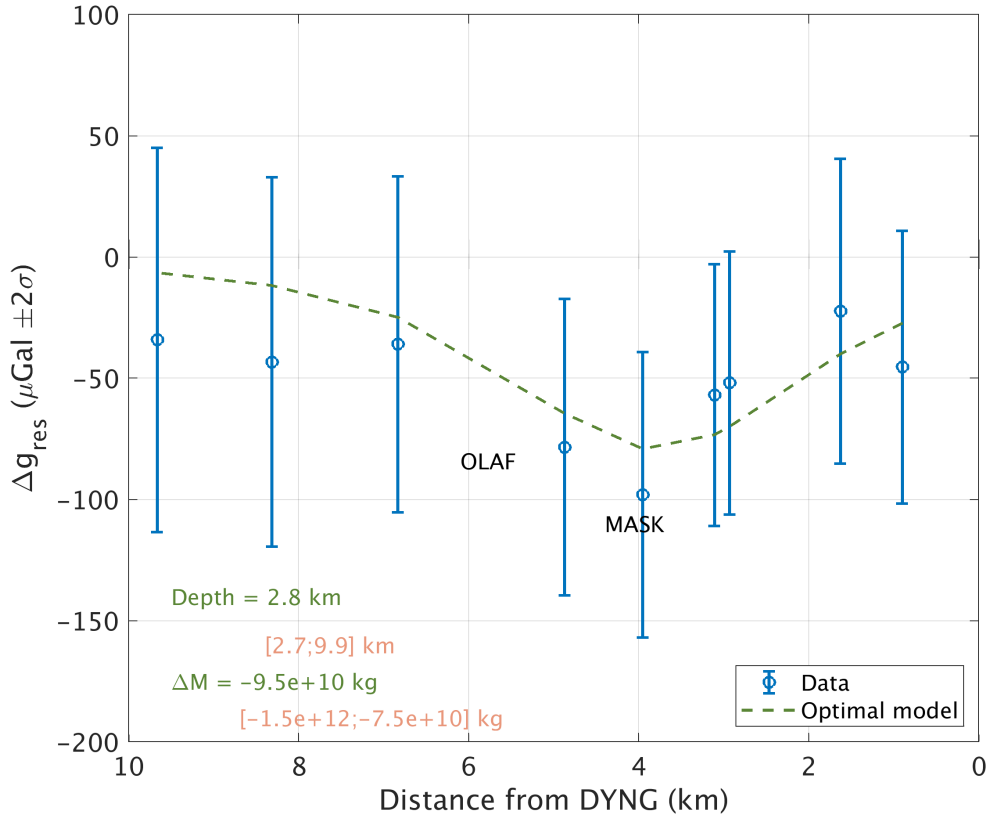

Figure 5.12: Prediction of the 2015-2016 non-negligible residual gravity changes projected along a south-west to north-east profile (Figure 5.1), using an MCMC Bayesian inversion approach with one million iterations, and taking into account the correlation between data errors. See Section 5.6 for more details.

approximation, likely to be far off the reproduction of the real geology but equally likely to reproduce well the physical conditions responsible for the bowl-shape spatial signatures of deformation and gravity change (Section 1.4.2). Moreover, despite the large uncertainties in the gravity changes, the MCMC Bayesian inversion approach provided confidence intervals accounting for the uncertainties. If the Mogi assumption is appropriate, there is therefore 95% confidence that the deformation and gravity models presented here reproduce the mass and volume (or pressure) change conditions beneath Askja.

5.7 Causes of subsidence at Askja

Previous studies assumed that both the subsidence and gravity decrease, centered on the Askja caldera, were due to the same process, located at the "geodetic reservoir" (Section 1.5.3). Based on this assumption, they suggested that magma was continuously draining from the geodetic reservoir down to deeper levels (e.g. Rymer and Tryggvason, 1993, de Zeeuw-van Dalfsen et al., 2005), and even though not expected to generate any gravity change, magma thermal contraction due to cooling and cystallisation, within the reservoir itself, was also proposed to contribute to the subsidence (e.g. Sturkell and Sigmundsson, 2000). In addition, Pedersen et al. (2009) and de Zeeuw-van Dalfsen et al. (2012) highlighted the likely high impact of plate spreading using finite-element modelling.

In this chapter, I have highlighted some discrepancies suggesting that gravity changes are not directly related to the subsidence:

1. Both signals can be uncorrelated in time;

2. When assuming that both signals originate from the same source and are due to magma drainage, the mass change derived from deformation is out of the 95% confidence range of mass change, constrained from gravity.

Moreover, the temporal uncorrelation of both signals was also observed in previous studies, when a gravity increase was recorded over 2007-2009, while the subsidence continued (Section 1.5.2).

Assuming that the Mogi model is appropriate to reproduce the distribution of pressure (volume) and mass changes beneath Askja, my analysis therefore suggests that the hypothesis of magma drainage to explain the subsidence is unlikely. However, the presence of a shallow magma reservoir is not ruled out, and several observations even support its existence: a subsiding caldera implies that there is a shallow magma reservoir, my deformation analysis precisely redefined the depth of this reservoir linked to the subsidence at 3-km beneath the caldera centre, in contrast to previous inversion analyses, which placed it at 3.5 km depth; and Greenfield et al. (2016) observed some seismic velocity attenuation in this area (Section 1.5.4).

Magma crystallisation processes from thermal contraction at the 3-km deep reservoir and extensional stresses induced by plate spreading could both induce the steady and gradually decaying subsidence. The solidification of magma from cooling and crystallisation processes usually induces a volume decrease of 10% from the initial volume of liquid (e.g. Caricchi et al., 2014). If the total decrease of 0.07 km^3 constrained from InSAR (Figure 3.21) would be solely due to this process, the initial volume of magma that would have had solidified over 1983-2017 would be 0.7 km^3. Because the reservoir beneath the caldera should not exceed 15 km^3 (Section 1.5.4), this result does not seem unrealistic, but further investigations should be carried out to estimate whether this process would be occurring. For example, the amount of thermal contraction could be modelled (e.g. Hamlyn et al., 2018), and performing e.g. a magnetotelluric study could help detecting whether magma is present in this reservoir (e.g. Comeau et al., 2015). The extension due to plate spreading could be the main driving force. Indeed, crustal stretching is expected to cause pressure decrease along oceanic ridges. Even though magma flow from high-to-low pressure zones is the common process known to originate from such tectonic destabilisation in volcanic environments (Section 1.3.3), subsidence of weak materials overlying a shallow magma chamber can be another way of accommodating the pressure decrease due to plate spreading or any tectonic event (e.g. Takada and Fukushima, 2013, Pritchard et al., 2013). If this process is happening at Askja, the steady pressure decrease induced by stretching the 3-km deep reservoir could induce similar conditions to the ones that would be generated by a deflating Mogi reservoir, although no magma is flowing out.

The irregular mass changes could be occurring at the top of the magma chamber from e.g. outgassing (Section 1.3.3), but because compositions of the fumaroles at Askja lye within the geothermal range (Personal communication, M. Pfeffer, 2018 - Icelandic Met office), mass changes could instead be occurring in a hydrothermal system overlying the 3-km deep reservoir. Indeed, absolute yearly gravity changes associated with hydrothermal processes can be of about 70-80 μGal (e.g. Saibi et al., 2010). The indirect link between the shallow reservoir and the hydrothermal system could be the reason why temporal variations in deformation and gravity change can be sometimes

correlated, but further investigations would be required to verify whether the source of gravity change is hydrothermal.

5.8 Conclusion

In this chapter I have presented, for the first time, the residual gravity change signature along a south-west to north-east profile, crossing the entire Askja caldera, with full integration of the uncertainties. The use of a new type of gravimeter, equipped with automatic recording and precise electronic sensors facilitated the constraint and minimisation of vibration noise and errors associated with the instrument levelling. Additionally, I used a new reference station, DYNG, which is more appropriate than VIKR, used in previous studies and lying in the gravity change field.

Between 2015 and 2016, there was a bowl-shape gravity signature centered on the Askja caldera, with maximum decrease of about 100 ± 30 μGal at MASK and near-negligible variations at the caldera edges. This signal was spatially correlated with synchronous subsidence measurements, also showing a bowl-shape signature centered on the caldera, with a maximum decrease of -1.6 ± 0.1 cm near OLAF, i.e. at <1 km away from MASK. Between 2016 and 2017, however, a completely different pattern occurred, with near-negligible to negligible gravity variations over the entire caldera, while the subsidence continued to evolve steadily.

I further tested the relationship between both signals by performing the first gravity inversion at Askja: assuming that DYNG is outside the gravity change zone and that a spherical model is appropriate, the 2015-2016 residual gravity changes are best explained by a mass decrease of about 9.5×10^{10} kg located at 2.8 km depth beneath Askja. With respective 95% confidence intervals of $[-1.5\times10^{12};-7.5\times10^{10}]$ kg and [2.7;9.9] km, these optimal values are poorly constrained, but the confidence intervals indicate the range where the depth and mass change sit, with 95% chance. Because the volume change constrained from deformation would imply a mass loss outside the confidence interval to that predicted from gravity, a magma drainage cannot be responsible for the Askja subsidence. This analysis is based on the assumption that the Mogi model is appropriate

to reproduce the physical conditions beneath Askja.

By rejecting the magma drainage hypothesis, this study has reduced the likely causes of subsidence to extensional stress due to plate spreading and magma crystallisation at the shallow reservoir. The source causing the irregular gravity changes could reflect mass fluctuations in a hydrothermal system, situated just above the magma reservoir and possibly being heated up by the cooling magma. In that case, the processes causing deformation and gravity changes would be indirectly linked to some degree, but further investigation are required to verify these remaining hypotheses.

Despite the significant improvements compared with previous gravity studies, more could be learned about the nature of the source of gravity changes by extending the new gravity time-series and quantifying to what extent DYNG is affected by gravity variations. Moreover, measuring air pressure, air temperature and soil moisture variations during each survey should better constrain residual gravity changes, as final errors would be reduced. In that case, several model geometries could be tested, and mass changes could also be simulated using hydrothermal models (e.g. Kipp et al., 2008). In parallel, the presence of magma at 3-km depth could be investigated using other geophysical methods such as, for example, magnetotellurics, and thermal contraction models could be estimated.

Chapter 6

Discussion and Conclusions

6.1 The Askja subsidence in a wider context

From the Smithsonian Institution database (GVP, 2019), 153 episodes of subsidence were measured at volcanoes between 1943 and 2017. In terms of duration, 95 of these episodes lasted <5 years (62.5%) and only 6 episodes lasted ≥20 years (2%), with the Askja subsidence being the longest episode observed at a contemporary active volcano (Table 6.1). Here, I briefly summarize these longest subsidence episodes, and compare them with the Askja subsidence.

Volcano	**Location**	**Landform**	**Last eruption**	**Subsidence duration (yrs)**	**Subsidence location**	**Ref.**
Medicine Lake	Cascades (U.S.)	Caldera	1060 AD*	46**	centered on caldera	[1,2,3]
Askja	Iceland	Caldera	1961	34**	centered on caldera	
Taupo Lake	New-Zealand	Caldera	260 AD	25**	north of caldera	[4,5,6]
Asama	Japan	Complex	2015	24	whole complex	[7]
Mt Vesuvius	Italy	Summit caldera	1944	21**	centered on caldera	[8,9,10]
Kilauea	Hawaii (U.S.)	Summit caldera	2018	20	centered on caldera	[11]

Table 6.1: List of the longest subsidence epsiodes that have been detected at volcanoes. (*) radiocarbon datation; (**) is or might still be on-going. [1]: Dzurisin et al. (2002), [2]: Poland et al. (2006), [3]: Parker et al. (2014), [4] Otway et al. (2002), [5]: Peltier et al. (2009), [6]: Hamling et al. (2015), [7]: Murase et al. (2007), [8]: Tammaro et al. (2013), [9]: Samsonov et al. (2014), [10]: Walter et al. (2014), [11]: Johnson et al. (2010).

The ***Medicine Lake*** caldera (Table 6.1) has been subsiding at a steady rate of about -10 mm yr^{-1} for the entire monitoring time-period (1954-2011), and no update has been provided since then (e.g. Dzurisin et al., 2002, Poland et al., 2006, Parker et al., 2014). The spatial signature of the subsidence was circular, with maximum decrease at

the caldera centre, and mimimum decrease at the edges. Even though this volcano is located along a volcanic arc resulting from subduction, it is subjected to local extensional stresses, and the preferred hypotheses to explain the subsidence are crustal stretching and loading of caldera filling, or magma drainage and/or crystallisation processes (e.g. Dzurisin et al., 2002, Poland et al., 2006, Parker et al., 2014).

At ***Lake Taupo*** (Table 6.1), which is located in a back-arc extensional context, a subsidence of at least 25 years (1984-2009) was locally observed in the northern part of the caldera (e.g. Otway et al., 2002, Peltier et al., 2009). The onset of the subsidence could be an earthquake swarm that occurred in 1983, but, alternatively, the subsidence could have started before this tectonic event (Peltier et al., 2009). The temporal evolution of this localised deformation pattern has been decaying exponentially, with linear rates diminishing from about -11 mm yr^{-1} in 1984 to about -3 mm yr^{-1} in 2009 (e.g. Otway et al., 2002), and no update on the subsidence has been provided since then. Short-term fluctuations, likely due to seismicity and/or geothermal activity, were observed before and after a steady period spanning 1984-1996. The process responsible for the subsidence is still unclear, and could involve crustal stretching, with either fluid loss from a deep hydrothermal system and/or thermal contraction due to magma crystallisation in a deep reservoir (e.g. Otway et al., 2002, Peltier et al., 2009). More recently, Hamling et al. (2015) observed three local subsiding regions (2003-2011) further to the North of the caldera, with rates of about -20 mm yr^{-1}. They suggested that the main process responsible for these discrete subsidence patterns could be thermal contraction of a large magmatic reservoir at about 6 km depth.

Asama (Table 6.1) is a complex of several volcanoes, situated along a volcanic arc with no evidence of extensional regime. A long-term subsidence, affecting the overall complex, occurred between 1943 and 1967, before the deformation reversed to an uplift period up to 2005 (Murase et al., 2007). A correlation between the unsteady deformation and eruption frequency was highlighted, suggesting that magma was the main process controlling deformation at Asama.

The summit caldera of the ***Mt Vesuvius*** stratovolcano (Table 6.1) has been subsiding at a negative rate of <10 mm yr^{-1} since the beginning of monitoring, in 1992,

and at least up to 2013 (e.g. Tammaro et al., 2013, Samsonov et al., 2014, Walter et al., 2014). Discrete short-term uplifts of less than 2 cm were observed as well as seasonal fluctuations. Despite the regional context of subduction, Mt Vesuvius is subjected to some extensional stresses, and its magma plumbing system could be linked to the Campi Flegrei caldera, which is also in this extensional area: Walter et al. (2014) highlighted synchronous episodes of deformation and eruption between both volcanoes. However, the subsidence at Campi Flegrei, monitored since 1992 has reversed to uplift in 2009, whereas the long-term deformation remained undisturbed at Mt Vesuvius (Samsonov et al., 2014). At these two volcanoes, the causes of subsidence, which are still unclear, could be due to crustal stretching, loading of the edifices and/or magma movements (e.g. Tammaro et al., 2013, Walter et al., 2014).

Finally, the summit caldera of ***Kilauea*** (Table 6.1), so-called Halema'uma'u, subsided steadily at a rate of about 75 mm yr^{-1} between 1983 and 2003, when the deformation then reversed to uplift, up to 2007 (Johnson et al., 2010). This long-term subsidence correlated with magma draining from the lava lake and with an eruption that occurred along the so-called East rift zone, on the flank on the shield volcano. More recently, correlations between the Halema'uma'u caldera deformation, its lava lake and eruptions at the East rift zone were again observed (e.g. Baker and Amelung, 2012, Bagnardi et al., 2014). Subsidence at Halema'uma'u is therefore very likely controlled by magma movements.

By comparison, ***Askja*** (Table 6.1) has been gradually subsiding following an exponential decay function over the last 34 years, with maximum rates decreasing from about -25 mm yr^{-1} over 2002-2006 to about -15 mm yr^{-1} over 2015-2017 (Figure 3.15). With a same order of magnitude as observed at the five other volcanoes, the caldera-centered spatial signature of this steady subsidence can be analogous to that observed at Medicine Lake, and an exponential decay was also observed at Lake Taupo. In terms of tectonic context, Askja is subjected to continuous extensional stresses as it lies within a segment of the mid-Atlantic ridge.

Overall, it seems that long-term subsidence episodes at volcanoes are either due to significant magma drainage linked to eruptions, or they occur in extensional contexts. In

the latter case, the end of the subsidence episodes have not yet been detected (Table 6.1), and combinations with subsurface magma movements or crystallisation processes are sometimes proposed, as well as contributions from material loading. Apart from Asama, all other long-term subsidence episodes occurred at calderas, and all but that at Taupo affected the entire calderas. These deformation episodes seem to be the most steady at quiet volcanoes, such as at Medicine Lake and Taupo, but also at Askja, even though its last eruption was relatively recent. Alternatively, when large amounts of magma are clearly linked to the subsidence, such as at Kilauea, the subsidence can also be steady. When put in a wider context, the likely high impact of plate spreading on the Askja subsidence is clearly supported, as well as the unlikely magma drainage.

6.2 Conclusions

The aim of this thesis was to integrate surface deformation with temporal gravity more closely at Askja, to clarify the causes of subsidence. In a wider context, I aimed to contribute to the understanding of physical processes operating at shallow volcanic systems lying along mid-oceanic ridges, by testing the integration of both methods. Here I summarize my key findings per chapter.

6.2.1 Chapter 3: The exponentially decaying Askja subsidence

In Chapter 3, I presented a detailed analysis of the long-term caldera subsidence of Askja, using InSAR datasets from four different satellites, six different tracks and spanning 2002-2017. It is the first time such a 15-year-long time period has been covered using InSAR at Askja. Exploiting the high-spatial resolution of the technique, I analysed the long-term subsidence trend over the entire caldera, and I tested the hypothesis that the deflating magma reservoir, previously constrained at 3-3.5 km depth, could be the combined centre of pressure change of several processes.

My results show that the temporal evolution of the whole Askja subsidence can be approximated by the exponentially decaying model, previously only locally constrained from levelling and which is characterised by a relaxation time of about 42 years over

1983-2017. Assuming a point pressure source, so-called Mogi model, I constrained the volume change that would best explain the bowl-shape subsidence, implementing the exponential decaying model in the inversion. My results show that, if the Mogi model is appropriate, there is 95% chance that the long-term subsidence is explained by a geodetic source located at 3±0.1 km depth, and undergoing an exponentially decaying deflation, with volume change rate likely to have diminished from about 0.0016 km^3 yr^{-1} in 1983 to about 0.0008 km^3 yr^{-1} in 2017. Despite its very simplistic conception, the Mogi model, which likely does not represents well the subsurface geology, is likely to be appropriate to reproduce the pressure conditions causing the bowl-shape subsidence at Askja. This new analysis provides a redefined subsidence model compared with previous studies, with narrower confidence intervals. Even though my results support the presence of a 3-km deep reservoir centred beneath Askja, this does not demonstrate that magma, draining from the shallow source, is causing the subsidence. It rather means that the conditions of pressure decrease related to the subsidence can be approximated by that produced by a continuous magma outflow from a Mogi reservoir.

A localised residual signal could not be predicted by the Mogi model in the north east of the caldera. This emphases the limitations of using inversion modelling approaches that assume very simplistic material properties and reservoir geometries. Strong local variations in pressure field and/or crustal heterogeneities could be the reason why a local subsidence signal has remained. For example, lava overloading from the most recent 1961 eruption could have locally modified material properties in the area where residuals remain.

6.2.2 Chapter 4: Full integration of uncertainties for temporal gravity

In Chapter 4, I presented a statistical analysis that estimates the total error budget associated with residual gravity changes, and I focussed on spring gravimeters as these instruments are mostly used in remote volcanic areas. This work aimed to fill the lack of guidance and help the scientific community to precisely constrain and minimize errors: even though the list of error parameters can be found in the literature, no clear guidance has been provided to quantify case-by-case estimations, and the general

estimations provided have sometimes been underestimated or lacked information. In addition to providing equations to estimate the full error budget associated to residual gravity changes, I also estimated expected ranges of errors, from detailed best-to-worst case scenarios, so that users can anticipate the minimisation of errors.

My results show that (1) error standard deviations associated with vibration noise, imprecise levelling and temporal variations in calibration factor can be up to a few hundreds of microgals; (2) error standard deviations related to air pressure changes, air temperature changes, elevation changes and subsurface water-mass variations can reach at least a few tens of microgals; and (3) error standard deviations of Earth tides and ocean loading effects should not exceed a few microgals.

When using appropriate gravimeters, i.e. equipped with an automatic recording system and precise electronic sensors, errors due to vibration noise and imprecise levelling can be precisely constrained and easily minimized. Despite their similar precision, Scintrex gravimeters are therefore usually more appropriate than LaCoste & Romberg gravimeters for studying temporal gravity. Largest errors due to calibration arise when using different gravimeters and/or when instruments are not recalibrated for long-time periods. To minimize these effects, users should therefore use the same gravimeter and regularly monitor temporal variations in calibration factor.

Precisely measuring air pressure, air temperature and elevation at each gravity station should be usual practice to reduce their respective gravity contributions and easily minimize the error budget. The most challenging parameter to estimate is the gravity effect due to water-mass variations. When wells or lakes are present in the area, the order of magnitude of water-mass variations in the saturated zone can be determined, and measuring the amount of rainfall and soil moisture during gravity surveys could provide an estimate of water-mass variations in the unsaturated zone. Alternatively, when not possible to measure air pressure, air temperature, or water-mass variations, I demonstrated that analysing the drift function over a few days can highlight unknown temporal variations, likely mainly due to these unknown meteorological effects. An estimate of these effects can be derived at any time, at the base station, and assuming that these variations are constant over the area of study, a single bulk estimate can

be derived per survey, for the area of study. Even though not ideal, this estimation provides some constraints on unknown temporal effects, which might mask the signal of interest, and for large areas several base stations can be setup to quantify these effects per zone.

6.2.3 Chapter 5: Different processes causing deformation and gravity changes at Askja

In Chapter 5, I investigated the causes of subsidence by analysing a new temporal gravity time-series I collected, spanning 2015-2017, and comparing results with simultaneous surface deformation. I carried out each survey using a Scintrex gravimeter, rather than a LaCoste & Romberg gravimeter to better constrain and minimize instrumental errors, compared to previous studies. Additionally, the use of this specific instrument should facilitate the reproduction of future gravity campaigns, as it is stored on the premises of the University of Iceland. Compared with previous gravity studies, I enlarged the gravity network to obtain a cross-section across the entire caldera, and I moved the reference station further away from the caldera to minimize underestimation due to unknown gravity variations at the reference station.

My results show irregular annual gravity variations: over 2015-2016, I observed a bowl-shape gravity signal centered on the main caldera, with maximum residual gravity decrease of about 100±30 μGal, whereas negligible variations occurred over 2016-2017. Even though the 2015-2016 signature was spatially correlated with the simultaneous subsidence records (Pearson's coefficent of 0.9 with 95% confidence interval of 0.6-1), the gravity changes and deformation were fully uncorrelated over 2016-2017, suggesting that both signals are not directly linked to the same process.

I confirmed this hypothesis by carrying out the first gravity inversion at Askja. Even though the data errors were too large to precisely constrain the location, depth and magnitude of the mass change that would best reproduce the bowl-shape gravity signal, I could still successfully constrain the most probable solution with reliable confidence intervals. Assuming a spherical source model and assuming that the reference station DYNG is outside the gravity change zone, the 2015-2016 residual gravity changes have

95% chance to be due to a mass decrease of 1.5×10^{12}-7.5×10^{10} kg, located within 2.7-9.9 km depth. Even though there would be a chance that both processes occurred at the same depth, I tested the hypothesis of a magma drainage by comparing the mass decrease derived from the volume change, which I could precisely constrain from deformation over 2015-2016, with the mass change constrained from gravity over the same time period: no matter the magma density assumed, the mass change derived from InSAR is outside the 95% confidence interval constrained from gravity.

Reviewing the hypotheses from previous studies, my analysis shows that it is unlikely that a magma drainage from the 3-km deep reservoir is causing the subsidence and, due to the steadiness of deformation, thermal contraction due magma crystallisation at the shallow reservoir and extension due to plate spreading could both induce the subsidence. This latter possibility is supported by other examples of long-term subsidence episodes at volcanoes (Section 6.1). On the other hand, the irregular and likely shallower gravity changes could be due to mass variations in a hydrothermal system, heated up by the underlying shallow magma reservoir, and in that case, deformation and gravity changes would be indirectly linked. All these remaining hypotheses need further investigations to be verified.

6.3 Recommendations and Future work

Here I provide some recommendations for future work that would contribute to improving my work a step further.

Exploring calibration and meteorological effects

My statistical error analysis has been mainly based on the combination of previously published experimental tests, which provided information on how unwanted gravity contributions usually behave. However, there seems to be a lack of knowledge in temporal variations of calibration factors and meteorological effects. The main reason for this gap is that these parameters are usually specific to instruments and study areas. Even though I provided equations for case-by-case calculations, the best-to-worst range of cal-

ibration errors could be refined by investigating the temporal evolution of calibration factors of many spring gravimeters. Additionally, my bulk error estimation for meteorological effects, derived from the drift function over a few days, could be compared with synchronous measurements of air pressure, air temperature, amount of rainfall and soil moisture. The spatial variations of these effects could also be investigated by performing the comparison at different sites over a large area.

Future gravity surveys at Askja

For future gravity surveys at Askja, I recommend to:

1. Quantify to what extent DYNG is a suitable reference station by continuously recording gravity using an absolute gravimeter.

2. Measure air pressure, air temperature, amount of rainfall and soil moisture at Askja, as constraining these parameters should contribute to minimizing errors and this will consequently enable better constraint of mass changes. Moreover, it will provide an opportunity of testing the robustness the bulk meteorological error derived from the drift function.

3. Start monitoring the variations of the calibration factor of the Scintrex gravimeter from the University of Iceland, to anticipate minimizing calibration errors when the time-series will be spanning several years.

Localised deformation signal

The subsidence signal that could not be predicted by the Mogi model in the north-east part of the caldera could be explored locally by setting up levelling profiles across the fresh lava flows. Currently, the levelling line in this area is located on the lavas. Additionally, source geometries other than the Mogi model could be tested.

The 3-km deep magma reservoir

The 3-km deep reservoir has been largely studied using deformation data. The possible presence of a static cooling and crystallising magma should be investigated using other

geophysical techniques, and magnetotellurics might be the most appropriate as it is a passive technique. Thermal contraction models could also be carried out.

The gravity source at Askja

Extending the new gravity time-series should enable better constraints of gravity changes and mass changes could be simulated testing difference source geometries, but also using hydrothermal models. Additionally, monitoring gravity chqnges at Askja could also be a way to detect any future magma inflow as a drastic gravity increase would then be expected.

6.4 Concluding remarks

In this thesis, I have demonstrated the importance of precisely estimating errors related to temporal gravity, providing equations and detailed methodologies to help the scientific community. I especially highlighted that the type of spring-gravimeter is essential as well as simultaneously measuring meteorological effects and monitoring temporal variations in calibration factor.

Additionally, I have demonstrated that the subsidence and gravity changes are likely unrelated at Askja. This key finding opens up new perspectives to further understand the subsurface processes undergoing at Askja. Extending the new gravity time-series and focusing on imaging the first few kilometers of the crust using alternative techniques should be the next steps to take towards.

Among others, my work has been a great example to highlight that (1) a spatial correlation between two signals does not necessarily imply that they are related, (2) despite its definition, a best-fitting Mogi model does not necessarily imply that magma is involved, and (3) integrating temporal gravity with deformation can help better understanding subsurface processes at volcanoes.

Appendix A

Supplementary material for Chapter 3

A.1 Unwrapping residuals

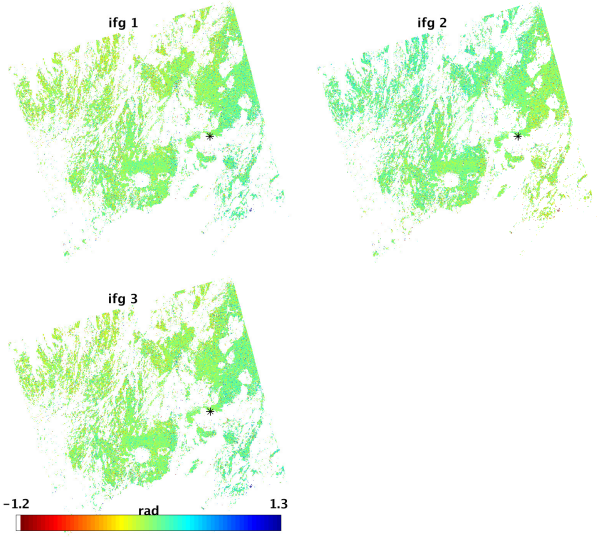

Figure A.1: Unwrapping residuals for the full ERS time-series (2002-2006), given in radians. The star is the reference station DYNG.

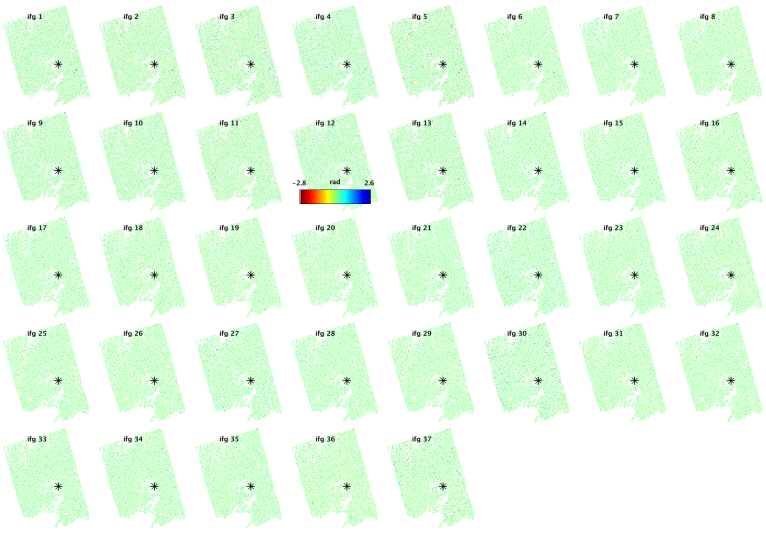

Figure A.2: Unwrapping residuals for the full Envisat time-series (2004-2010), given in radians. The star is the reference station DYNG.

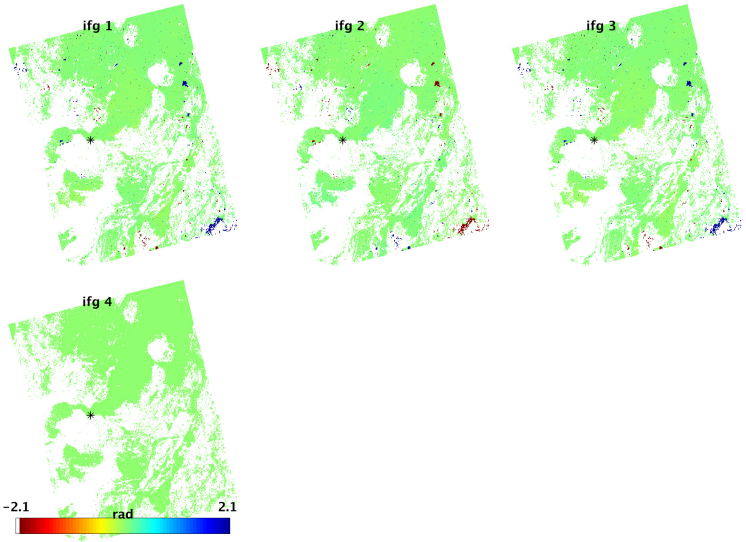

Figure A.3: Unwrapping residuals for the full CSK-A time-series (2010-2012), given in radians. The star is the reference station DYNG.

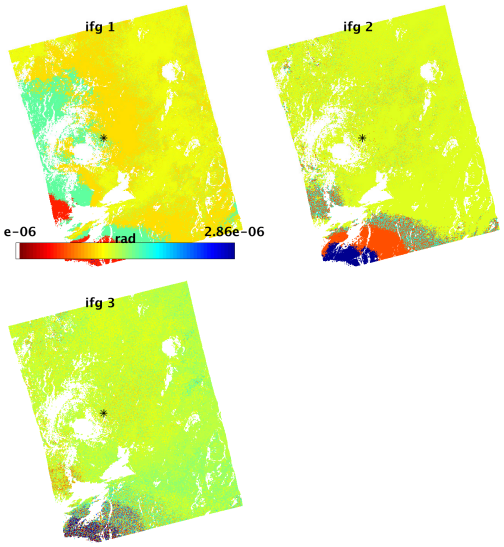

Figure A.4: Unwrapping residuals for the full CSK-A time-series (2014-2015), given in radians. The star is the reference station DYNG.

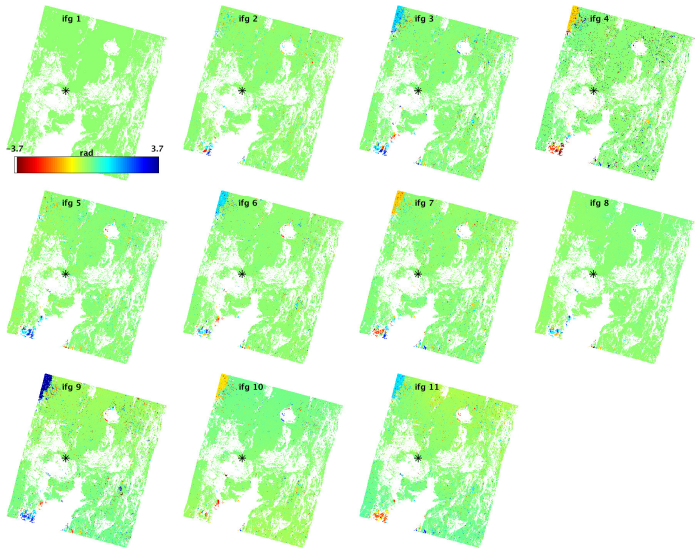

Figure A.5: Unwrapping residuals for the full CSK-D time-series (2012-2015), given in radians. The star is the reference station DYNG.

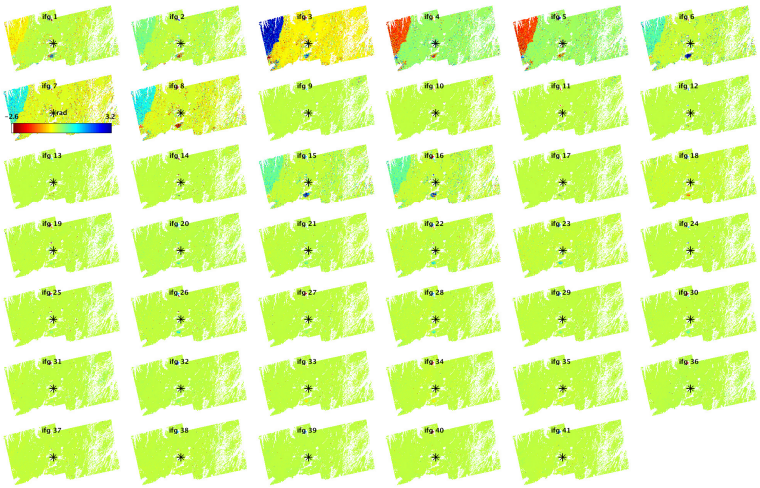

Figure A.6: Unwrapping residuals for the full S1-A time-series (2015-2017), given in radians. The star is the reference station DYNG.

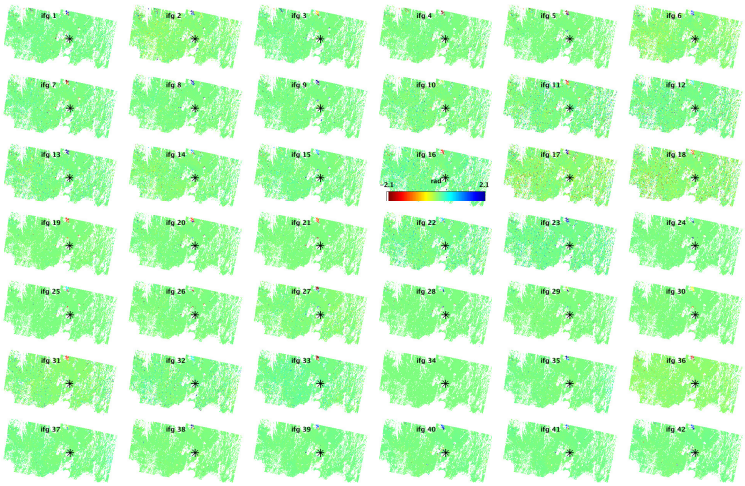

Figure A.7: Unwrapping residuals for the full S1-D time-series (2015-2017), given in radians. The star is the reference station DYNG.

A.2 Fully processed unwrapping InSAR time-series

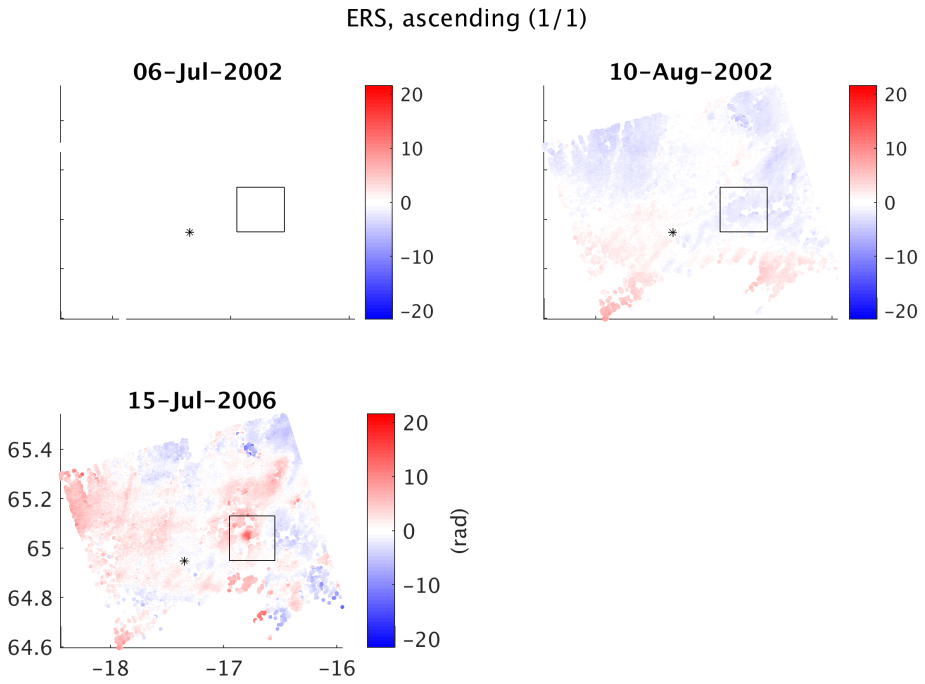

Figure A.8: ERS time-series of unwrapped phase given in radians along LOS, after data-processing and post-processing reductions. Red is deformation away from the satellite, the reference site is highlighted with the star, and the area of study is the black square.

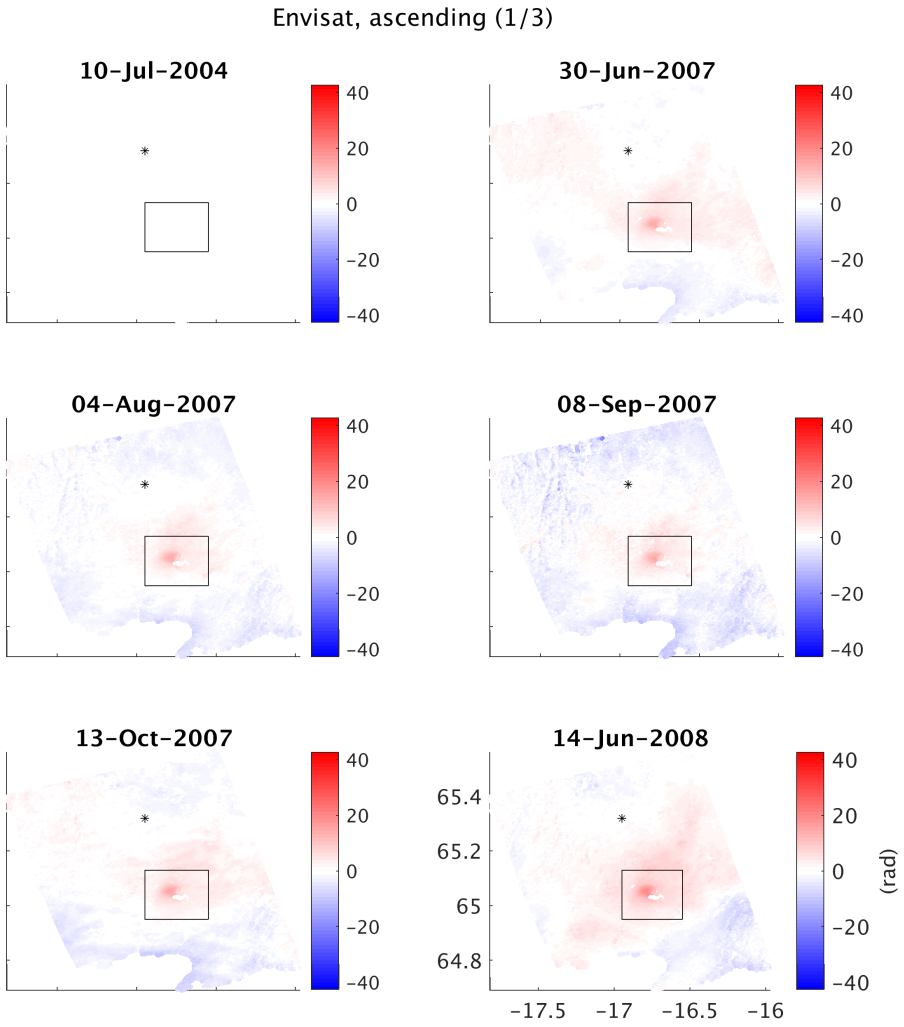

Figure A.9: Envisat time-series of unwrapped phase given in radians along LOS, after data-processing and post-processing reductions. Red is deformation away from the satellite, the reference site is highlighted with the star, and the area of study is the black square.

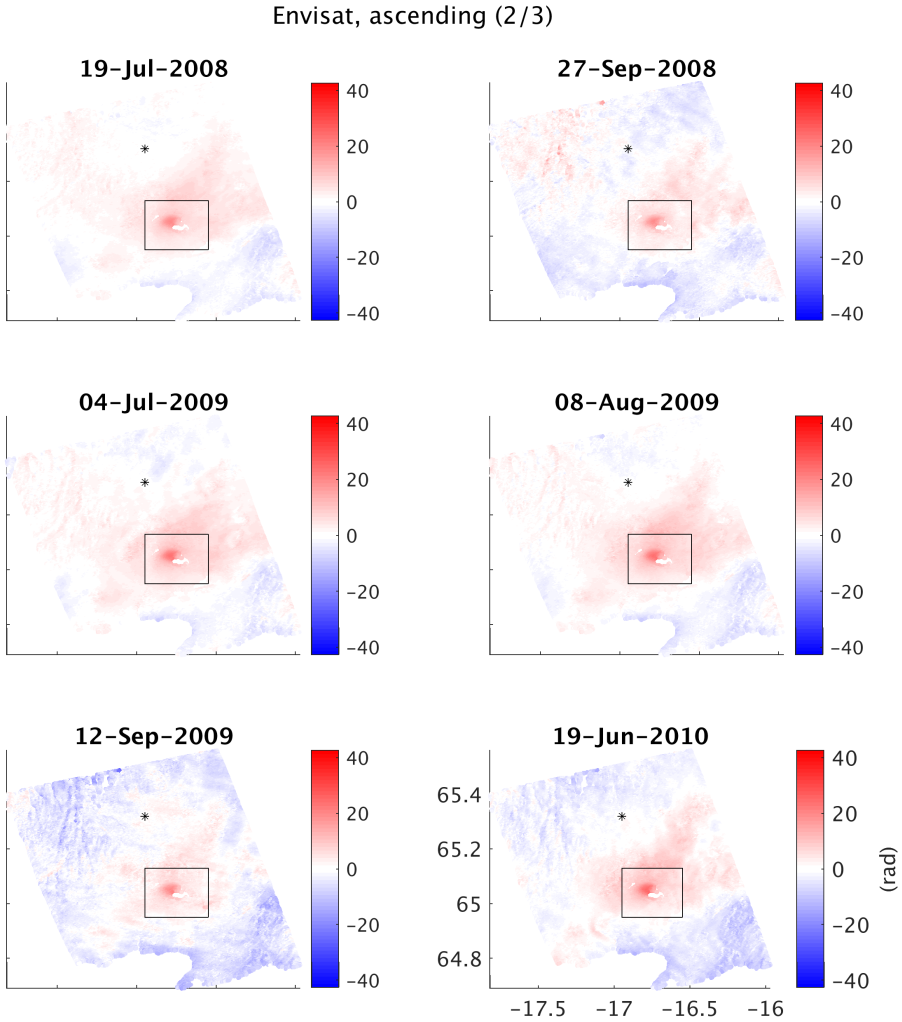

Figure A.10: Continuing of the Envisat time-series.

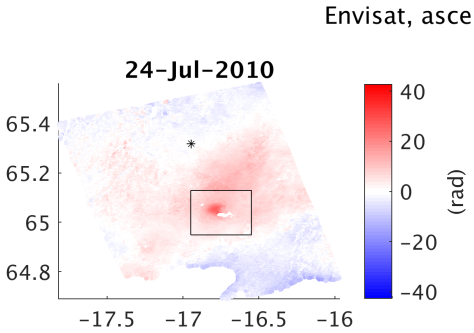

Figure A.11: End of the Envisat time-series.

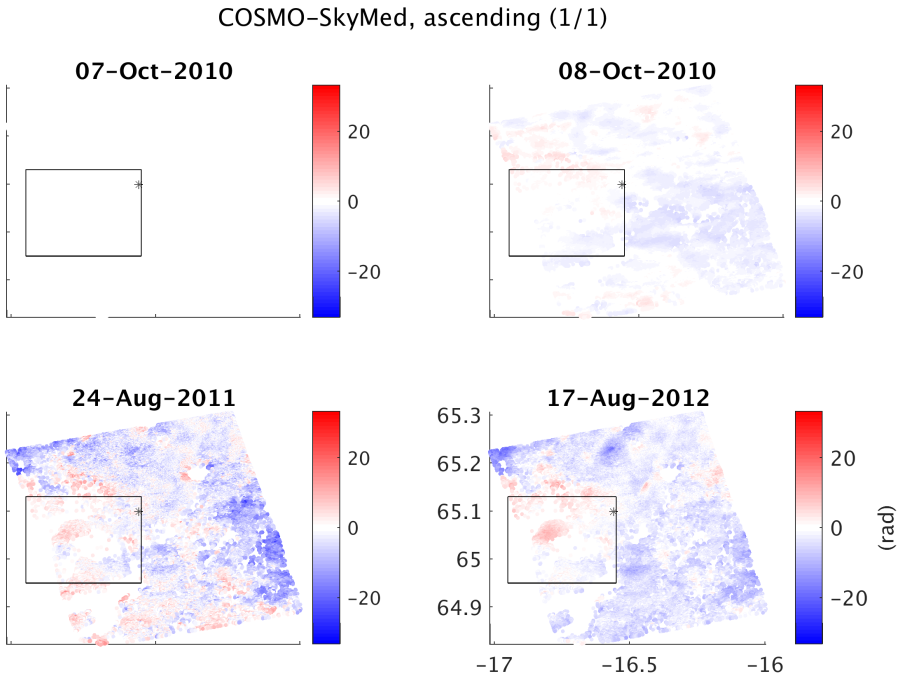

Figure A.12: CSK-A time-series of unwrapped phase spanning 2010-2012, given in radians along LOS, after data-processing and post-processing reductions. Red is deformation away from the satellite, the reference site is highlighted with the star, and the area of study is the black square.

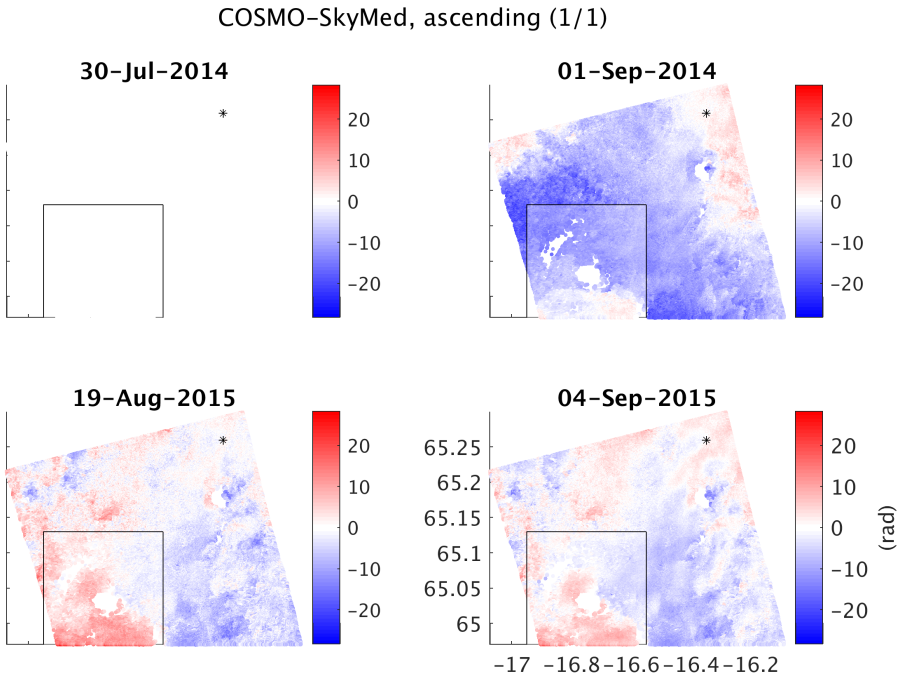

Figure A.13: CSK-A time-series of unwrapped phase spanning 2014-2015, given in radians along LOS, after data-processing and post-processing reductions. Red is deformation away from the satellite, the reference site is highlighted with the star, and the area of study is the black square.

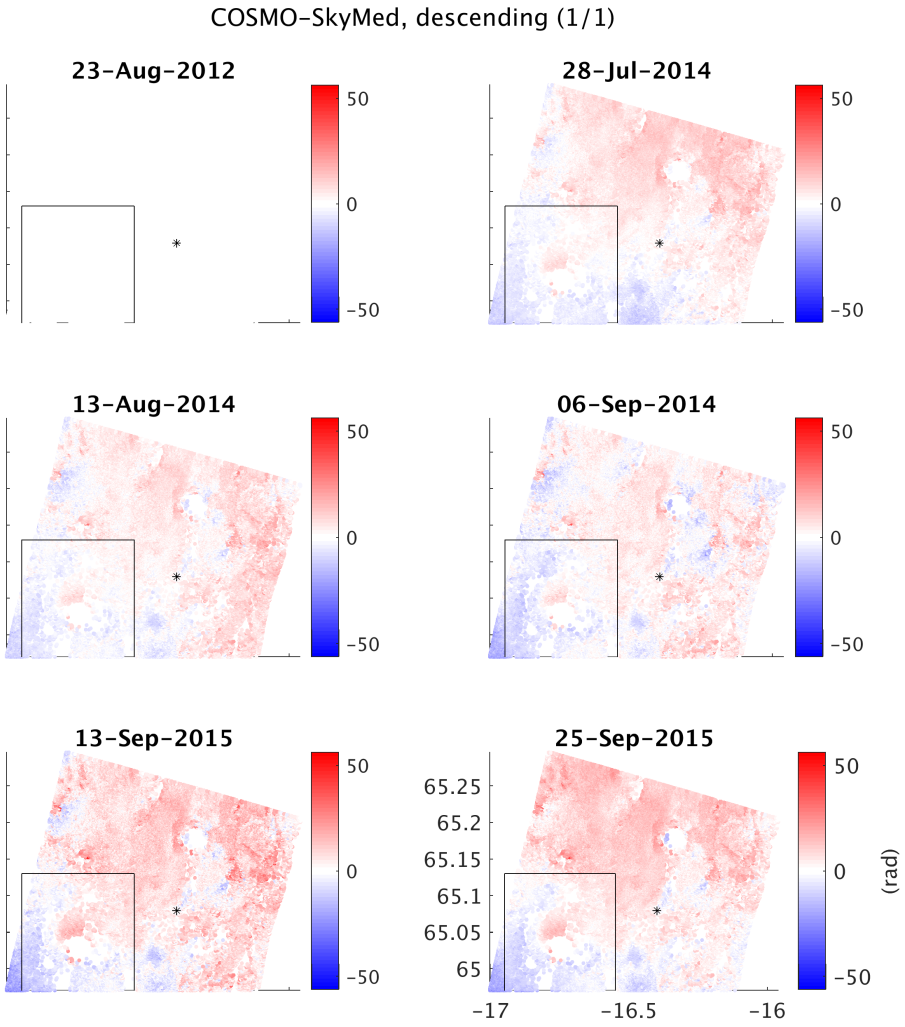

Figure A.14: CSK-D time-series of unwrapped phase, given in radians along LOS, after data-processing and post-processing reductions. Red is deformation away from the satellite, the reference site is highlighted with the star, and the area of study is the black square.

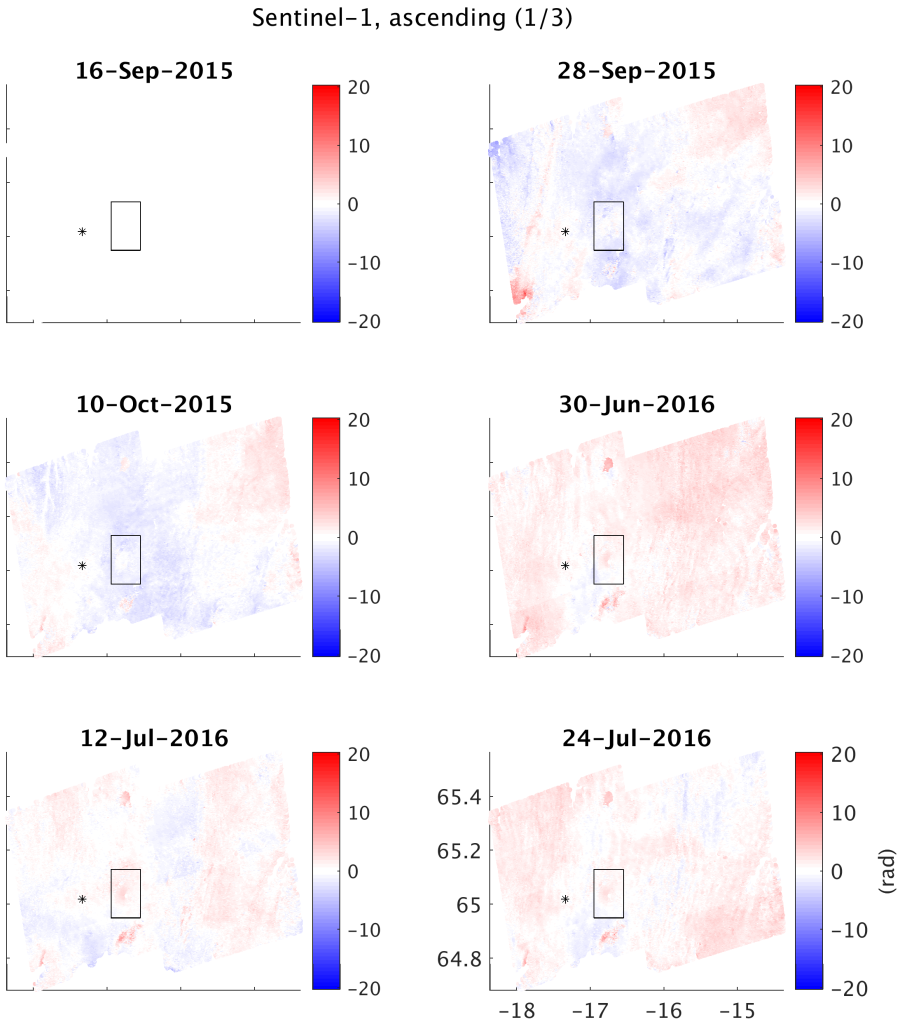

Figure A.15: S1-A time-series of unwrapped phase, given in radians along LOS, after data-processing and post-processing reductions. Red is deformation away from the satellite, the reference site is highlighted with the star, and the area of study is the black square.

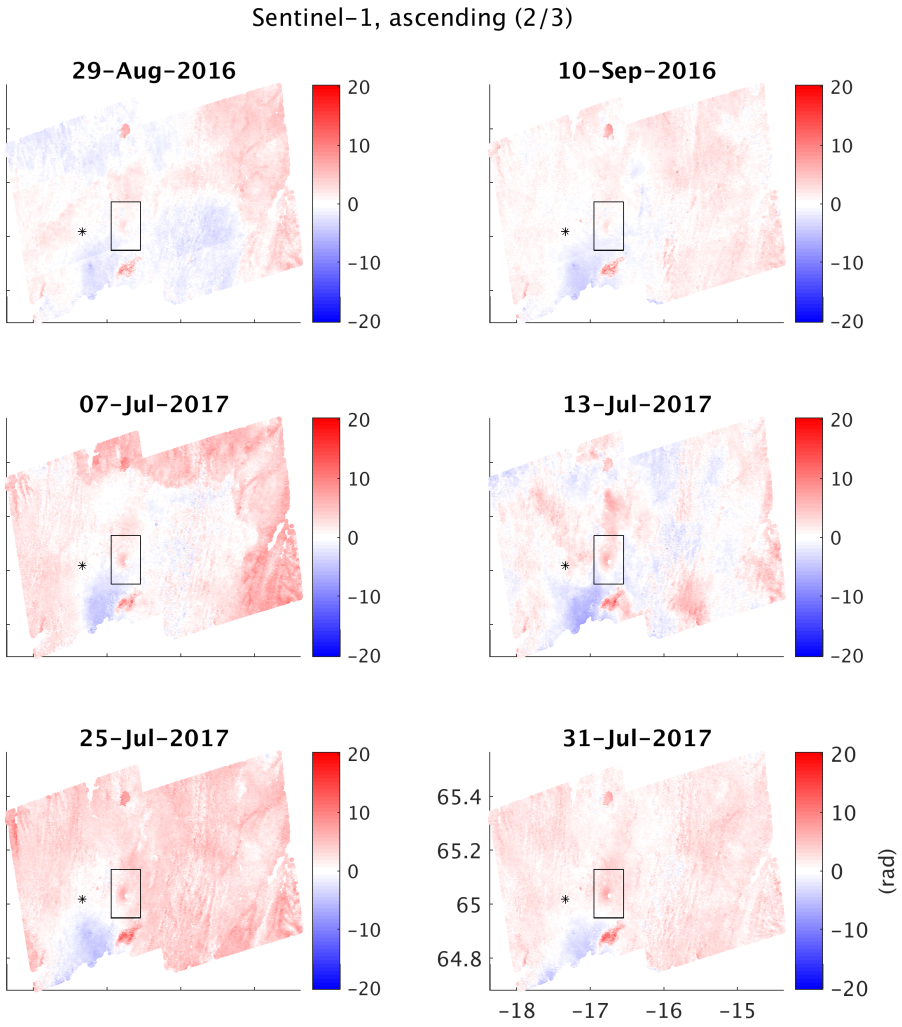

Figure A.16: Continuing of the S1-A time-series.

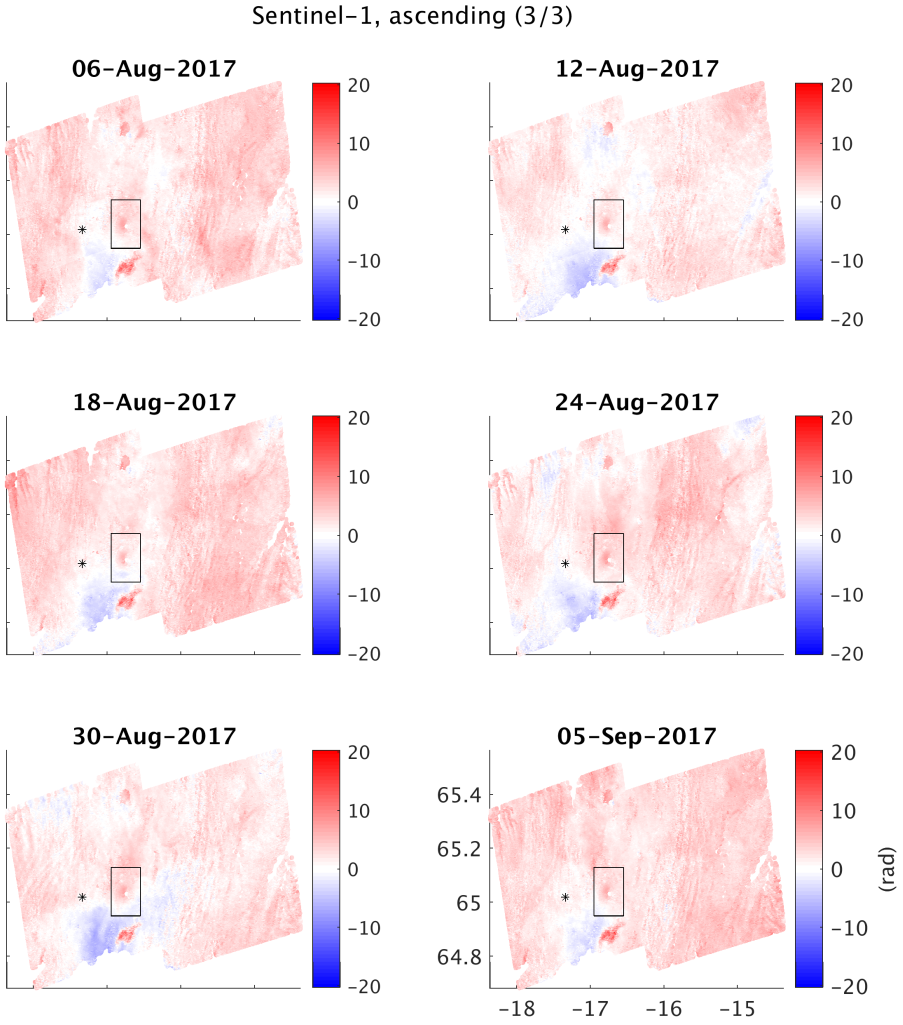

Figure A.17: End of the S1-A time-series.

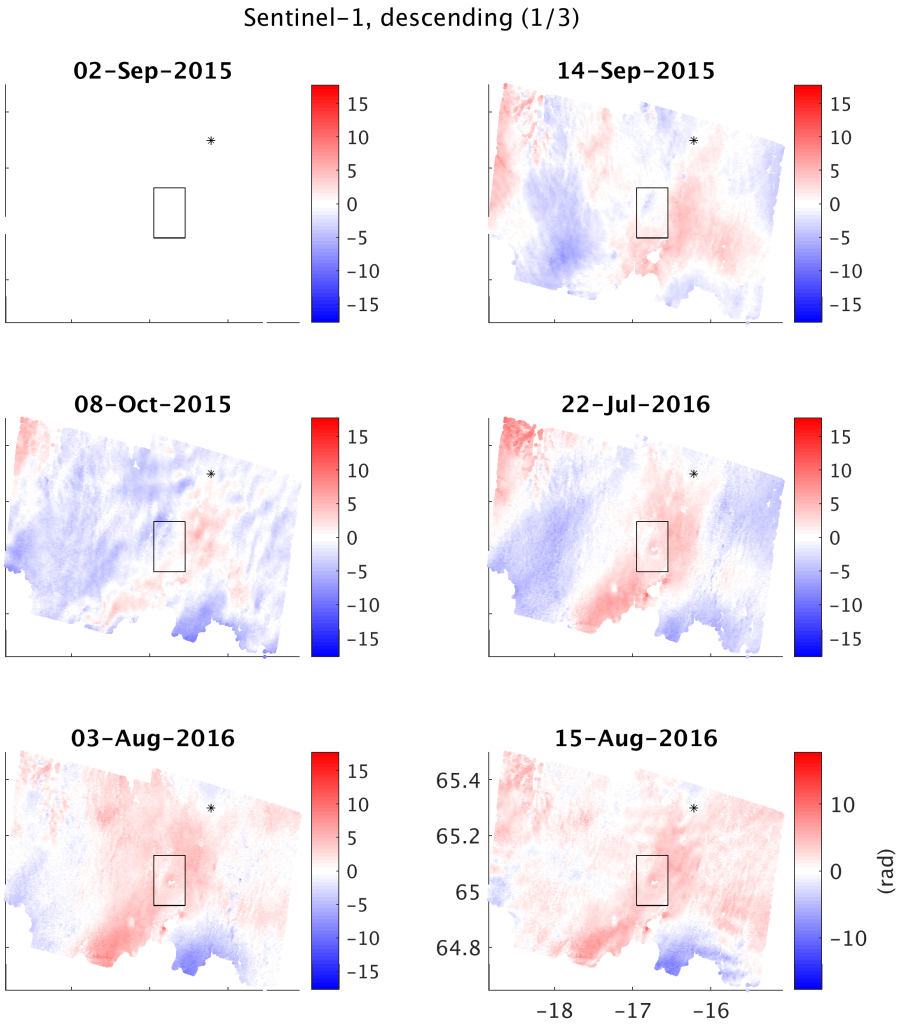

Figure A.18: S1-D time-series of unwrapped phase, given in radians along LOS, after data-processing and post-processing reductions. Red is deformation away from the satellite, the reference site is highlighted with the star, and the area of study is the black square.

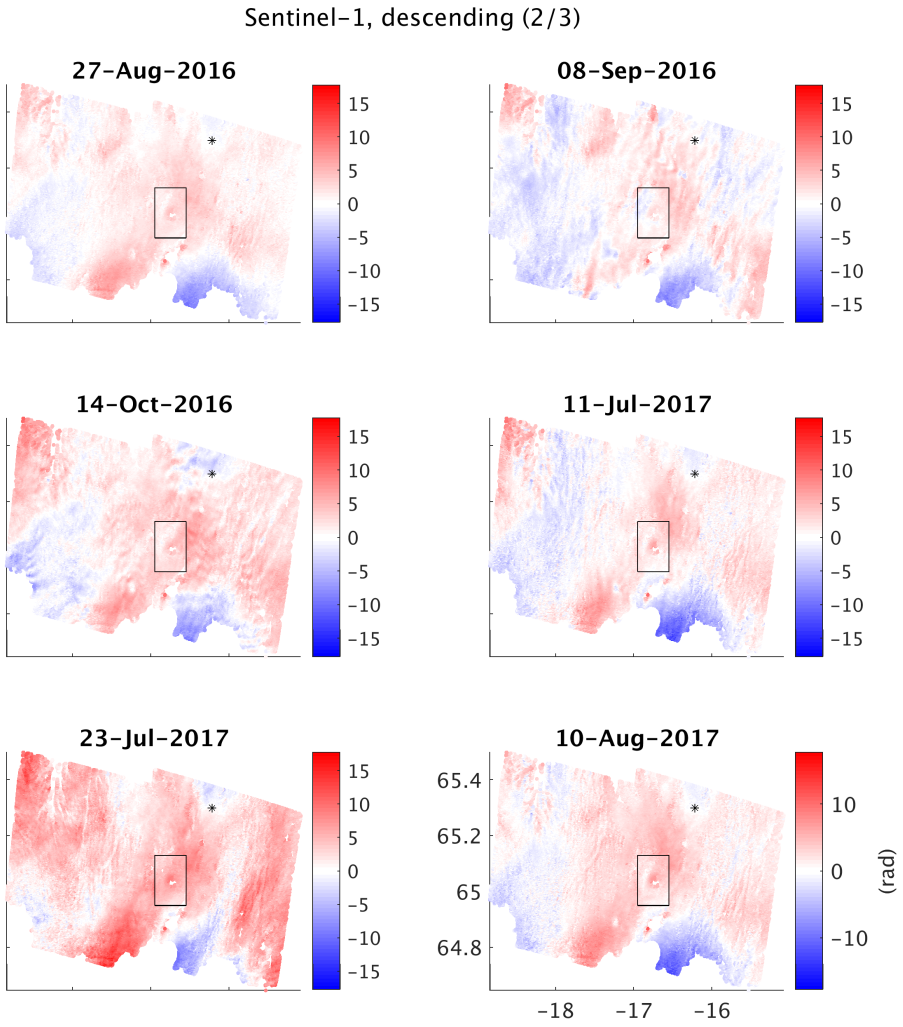

Figure A.19: Continuing of the S1-D time-series.

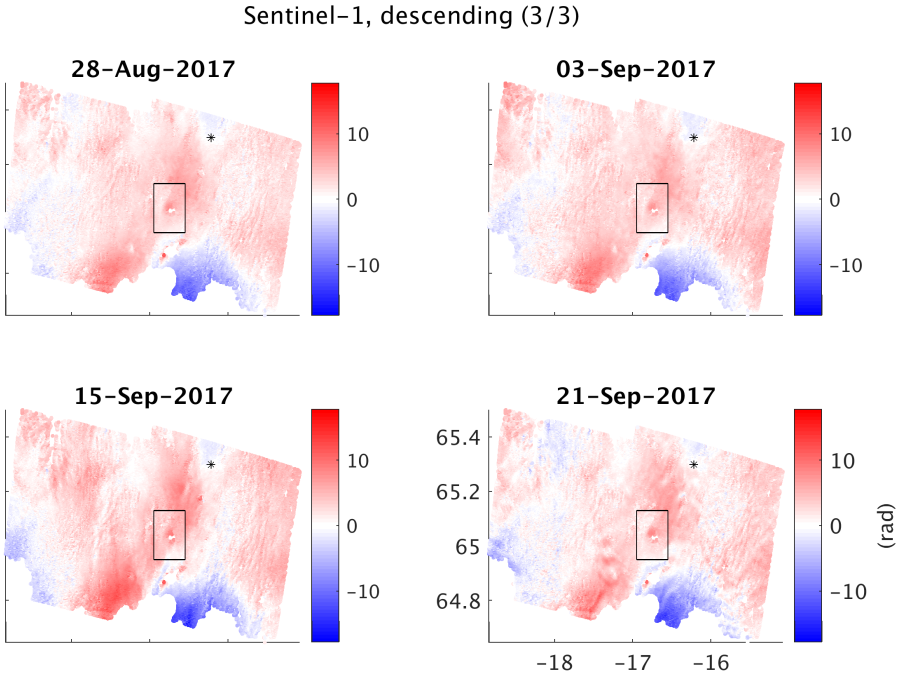

Figure A.20: End of the S1-D time-series.

A.3 Comparison of decomposition approaches

Here, I explain in detail how I decomposed the LOS S1 velocities (2015-2017) into 2-D velocities, assuming (1) negligible north-south motion and (2) constant horizontal pixel directions, contracting towards the caldera centre (Section 3.5.1). I also compare results from both approaches.

To determine $\left[\Delta\dot{\varphi}_{\text{ask}}\right]_{\text{A}}$ and $\left[\Delta\dot{\varphi}_{\text{ask}}\right]_{D}$, I first resampled the S1 ascending and descending LOS displacements, taken relative to DYNG (Section 3.4.2), onto a common grid of 100-by-100 m, by estimating a spatial average value per grid node in each interferogram. To do this, I used weighted least-squares, considering all pixels located within a 200-by-200 meter square box centered on each node, and I set up the variance-

covariance matrix using Equation 3.5 with r=0, due to the negligible distance between the selected pixels. Selecting only the grid nodes where the spatial averages of all interferograms passed the χ^2 test within 95% confidence (Section 3.4.4), I then estimated $\left[\Delta\dot{\varphi}_{\text{ask}}\right]_{\text{A}}$ and $\left[\Delta\dot{\varphi}_{\text{ask}}\right]_{\text{D}}$, using weighted least-squares with the variance-covariance matrix listing the variances obtained from the spatial resampling, in the diagonal. All these estimated velocities passed the χ^2 test within 95% confidence.

I used exactly the same spatial average approach, with the same weights, to resample the incidence angles, Θ_{A} and Θ_{D}, whereas I estimated a single heading angle per viewing geometry, α_{A} and α_{D}, at CASK, i.e. in the middle of the area of interest (Figure 3.7 and Section 3.4.3).

Using all these input values, I could constrain $\hat{\dot{D}}_E$ and $\hat{\dot{D}}_V$, neglecting north-south motions (Equation 3.8). On the other hand, I still needed to determine u_{A} and u_{D}, to carry out the alternative decomposition approach (Equation 3.9), and I used the following dot product formula to estimate them per grid node:

$$u = \boldsymbol{los} \bullet \boldsymbol{d_h} = \begin{bmatrix} \boldsymbol{los_e} & \boldsymbol{los_n} \end{bmatrix} \times \begin{bmatrix} \boldsymbol{d_e} \\ \boldsymbol{d_n} \end{bmatrix} \tag{A.1}$$

where, $\boldsymbol{los_e}$, equalling $sin(\Theta)cos(\alpha)$, and $\boldsymbol{los_n}$, equalling $-sin(\Theta)sin(\alpha)$, are the east-west and north-south components of $\boldsymbol{los}$ in the given satellite viewing geometry (e.g. Wright et al., 2004, Fuhrmann and Garthwaite, 2019), and $\boldsymbol{d_e}$ and $\boldsymbol{d_n}$ are the east-west and north-south components of the fixed horizontal node direction of motion, $\boldsymbol{d_h}$.

I determined $\boldsymbol{d_h}$ at each grid node, assuming a contraction towards the caldera centre, which I constrained using grid search, by comparing the azimuth directions of the observed GPS horizontal displacements taken relative to DYNG (Figure 3.10B), with the predicted directions from the GPS station locations towards any node. For each grid node test, I computed the weighted residual sum of squares (WRSS) between the observed and estimated azimuth directions, with variance-covariance matrix listing the variances associated with the observed azimuth directions. However, rather than calculating each of these variances considering an ellipse with semi-axes corresponding to one error standard deviation along east-west and north-south (Figure 3.10B), I instead assumed a circle with radius equalling the mean error standard deviation of the east-west and north-south components. Even though not exact, this simpler approach still provides a reasonable relative weighting to compute reliable WRSS values. The grid node at which WRSS is the smallest is the approximate centre of deformation (Figure A.21). Knowing the coordinates of this estimated centre of deformation in distance units, I determined $\boldsymbol{d_e}$ and $\boldsymbol{d_n}$, at each grid node, using the usual formulas of unit vector calculations (e.g. Equation 3.12). Finally, after having decomposed $\left[\Delta\dot{\varphi}_{\text{ask}}\right]_{\text{A}}$ and $\left[\Delta\dot{\varphi}_{\text{ask}}\right]_{\text{D}}$ into $\hat{\dot{D}}_H$ and $\hat{\dot{D}}_V$, assuming such constrained horizontal direction of motion (Equation 3.9), I computed $\hat{\dot{D}}_E$ by multiplying $\hat{\dot{D}}_H$ by $\boldsymbol{d_e}$.

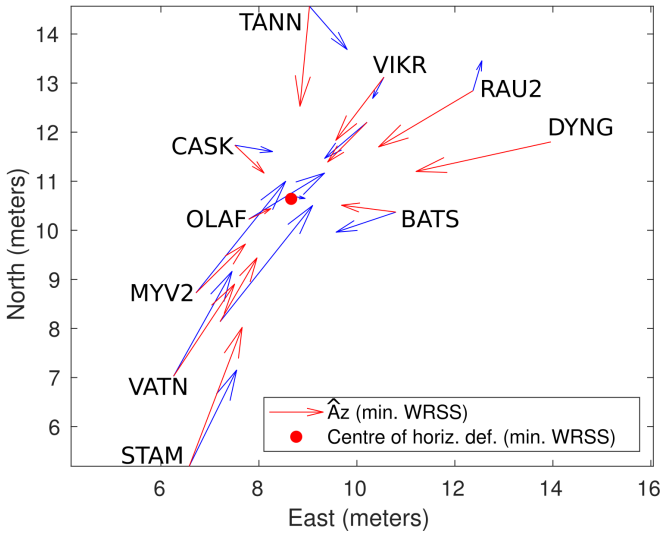

Figure A.21: Plot showing the best centre of horizontal deformation (red dot), determined comparing the observed direction of horizontal motion at the GPS stations, relative to DYNG (blue arrows) with the estimated direction providing a minimum WRSS (red arrows). Most of the GPS station names are mentioned here and the centre of deformation is very close to MASK (Figure 3.7).

When comparing the magnitudes of $\hat{\dot{D}}_E$ and $\hat{\dot{D}}_V$, resulting from the two independent decomposition approaches described above, a large discrepancy along the north-south axis passing through the estimated centre of deformation is clearly noticed (Figure A.22), and this comes from the use of the dot product formula in the approach fixing horizontal directions (Equation A.1). Indeed, near this north-south axis, $\boldsymbol{d_e}$ is minimum, while $\boldsymbol{d_n}$ is close to maximum (i.e. near ± 1), leading to u_{A} and u_{D} being dominated by the north-south component ($\boldsymbol{los_n d_n}$ in Equation A.1). Consequently, in this critical area, the radial signals are dominated by north-south motions, which are very poorly constrained by the LOS signals, and estimates of radial motion are therefore dominated by the error in the InSAR.

Mathematically, this can translate into:

$$\hat{\dot{D}}_V = \frac{\left[\Delta\dot{\varphi}_{\mathrm{ask}}\right]_{\mathrm{A}} u_{\mathrm{A}} - \left[\Delta\dot{\varphi}_{\mathrm{ask}}\right]_{\mathrm{D}} u_{\mathrm{D}}}{\cos(\Theta_{\mathrm{A}})u_{\mathrm{D}} - \cos(\Theta_{\mathrm{D}})u_{\mathrm{A}}} \tag{A.2}$$

$$\hat{\dot{D}}_H = \frac{\left[\Delta\dot{\varphi}_{\mathrm{ask}}\right]_{\mathrm{A}} + \cos(\Theta_{\mathrm{A}})\hat{\dot{D}}_V}{u_{\mathrm{A}}} \tag{A.3}$$

where $\cos(\Theta_{\mathrm{A}})u_{\mathrm{D}}$ and $\cos(\Theta_{\mathrm{D}})u_{\mathrm{A}}$ almost cancel each other, providing an unrealistically large magnitude for $\hat{\dot{D}}_V$, which is then implemented into the estimation of $\hat{\dot{D}}_H$.

When removing pixels located in the critical zone, i.e. where u_{D} and u_{A} have the same signs, both decomposition approaches provides very similar results (Figures A.23 and A.24), and they also compare well with the long-term east-west and vertical bulk linear velocities (Figure A.25).

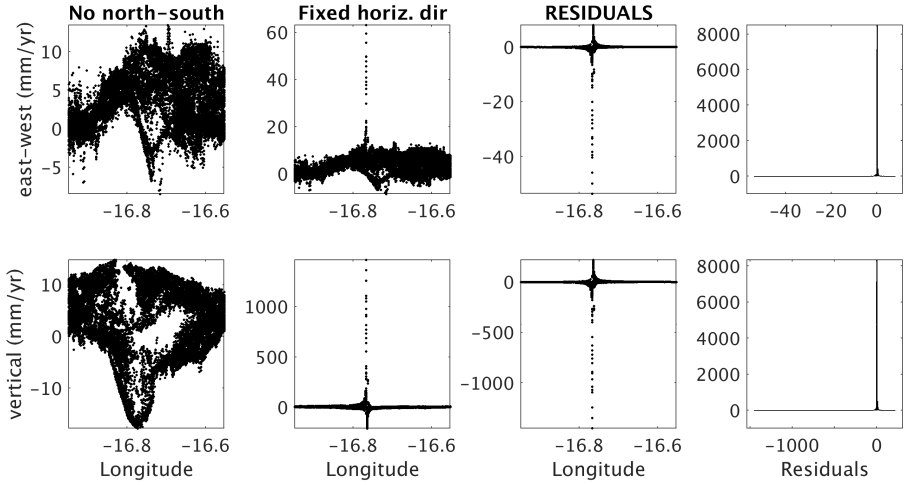

Figure A.22: Decomposition results of the S1 velocities into east-west (top row) and vertical (bottom) velocity components, when either neglecting north-south motions (left) or when assuming horizontal direction of motion towards the caldera centre (middle left). Results are plotted against longitude to highlight the unrealistically large values along the north-south axis passing through the centre of deformation, i.e. along -16.76° longitude, or near MASK (Figures 3.7 and A.21). Residuals are shown against longitude (middle right) and as histograms (right).

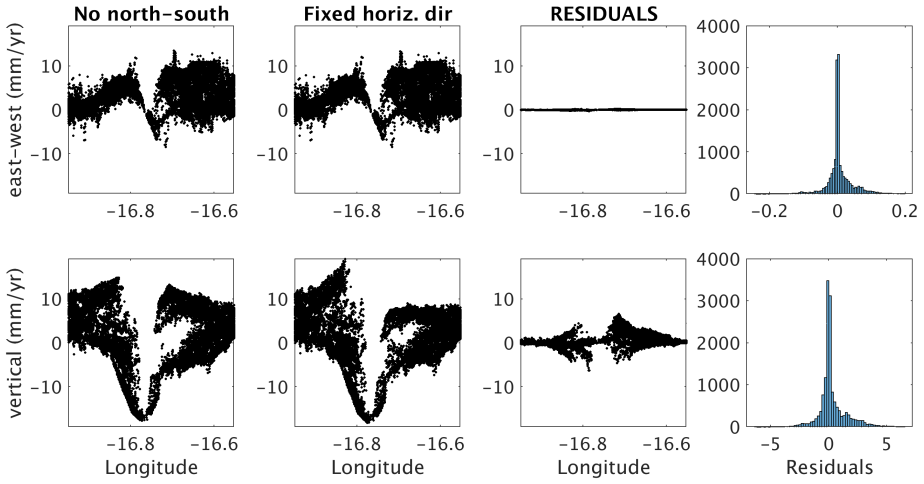

Figure A.23: Same as Figure A.22, but here, results with largest errors have been discarded. See results in map view in Figure A.24.

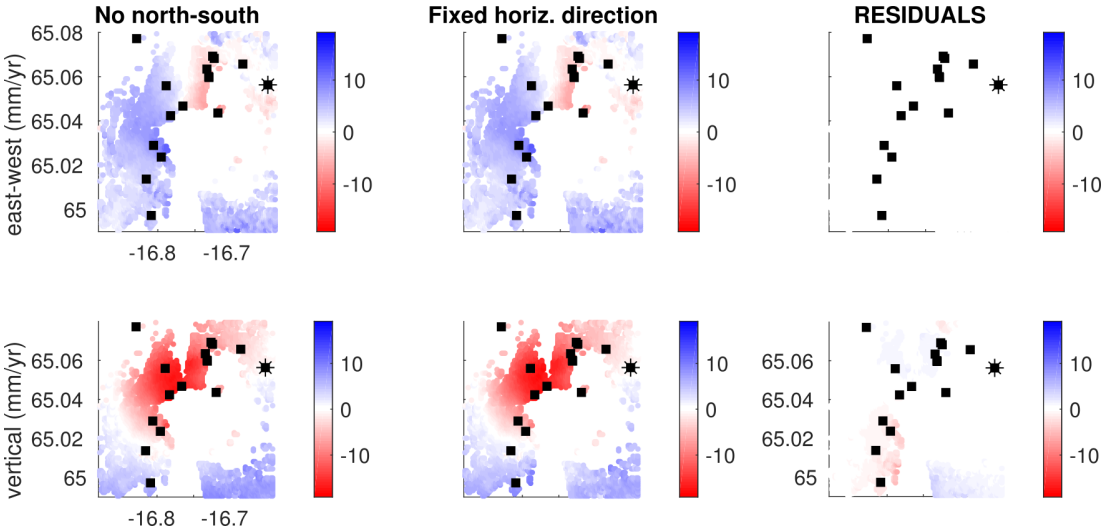

Figure A.24: Same results as in Figure A.23 but displayed in map view. The star is the reference site (DYNG) for deformation, and the squares are the GPS stations (Figure 3.7).

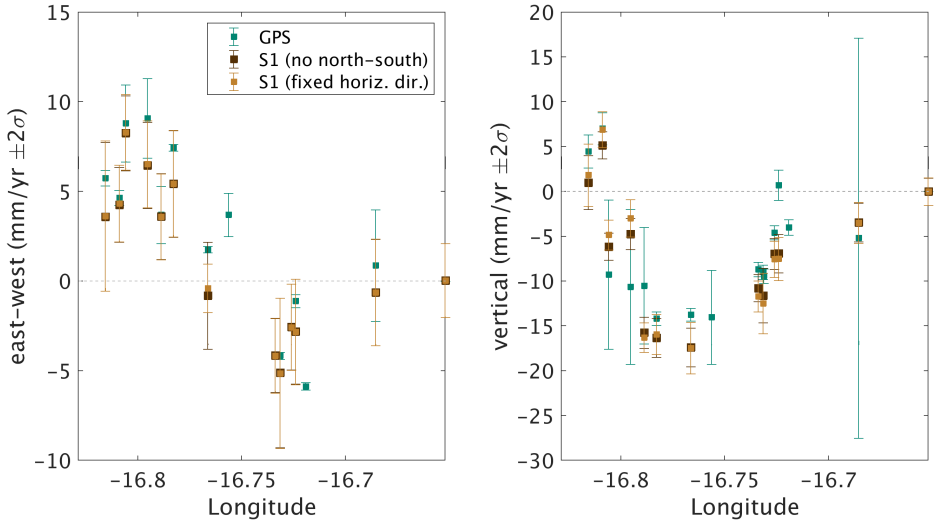

Figure A.25: Comparisons of the decomposed east-west and vertical S1 velocities at each GPS station (Figure A.24), with the observed GPS linear velocities, estimated using weighted least-squares. Each S1 datapoint is the weighted least-squares spatial average of the velocities surrounding each GPS station, when pixels are present.

A.4 Times-series of residuals after removal of the exponential trend

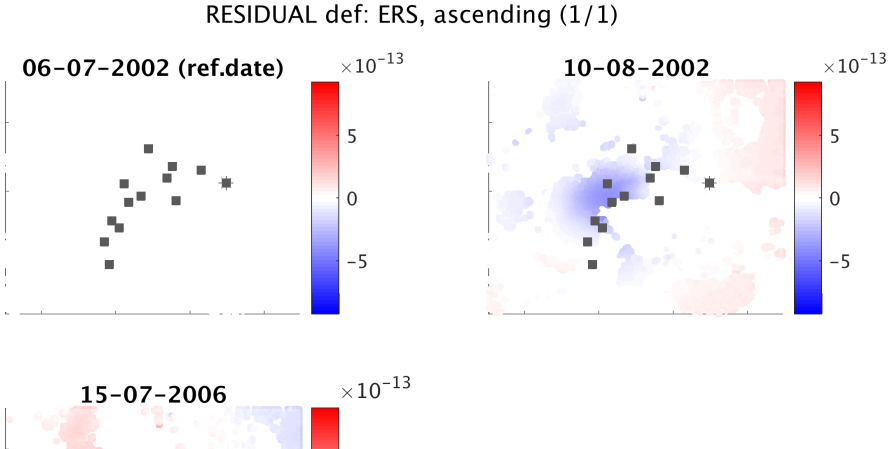

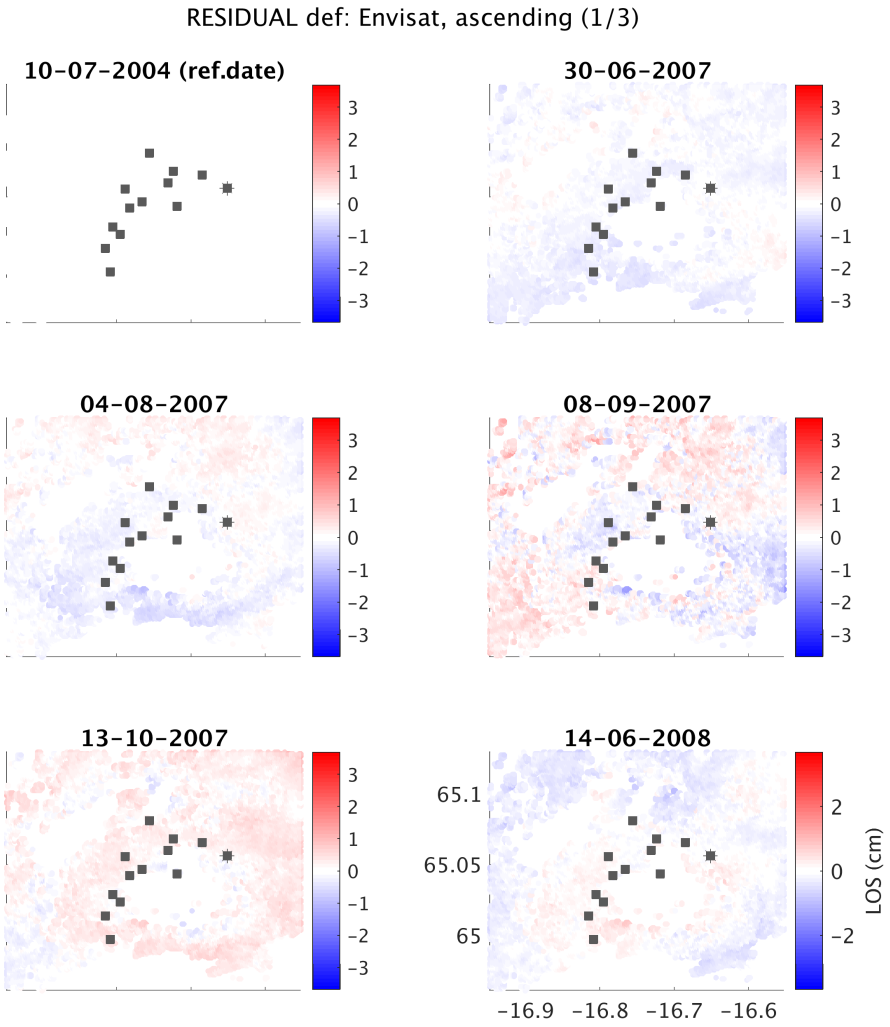

Figure A.27: Envisat time-series showing residual displacements, in cm along LOS, after removal of the exponential subsidence trend. Red is deformation away from the satellite, the reference site is highlighted with the star, and GPS stations are the black squares.

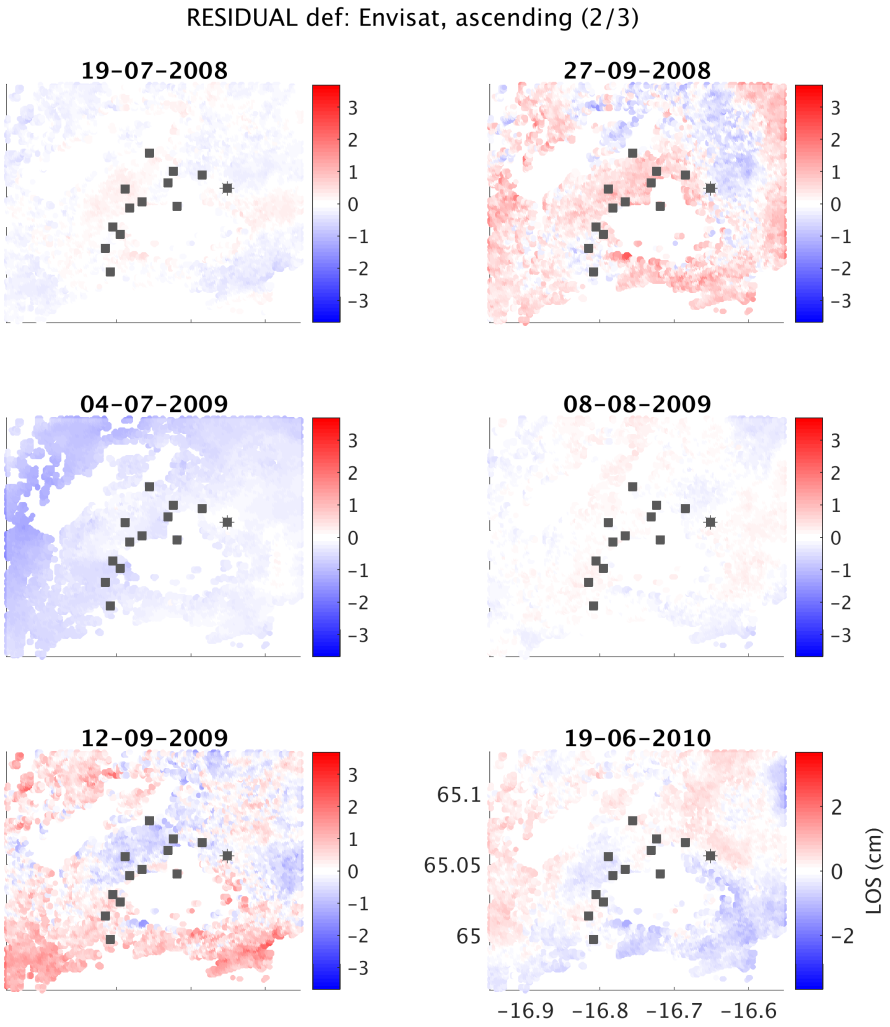

Figure A.28: Continuing of the Envisat time-series.

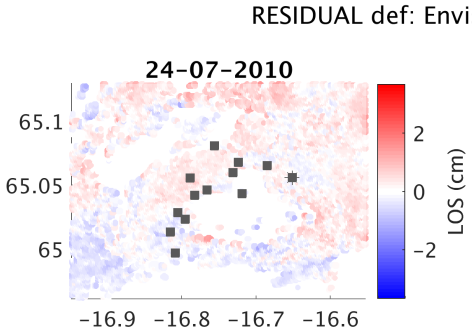

Figure A.29: End of the Envisat time-series.

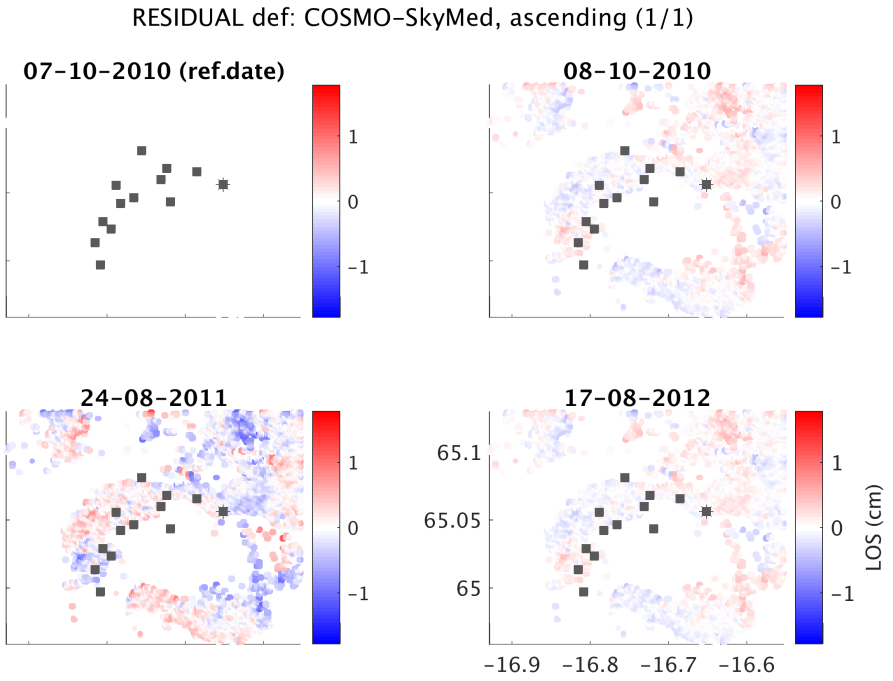

Figure A.30: CSK-A time-series over 2010-2012, showing residual displacements, in cm along LOS, after removal of the exponential subsidence trend. Red is deformation away from the satellite, the reference site is highlighted with the star, and GPS stations are the black squares.

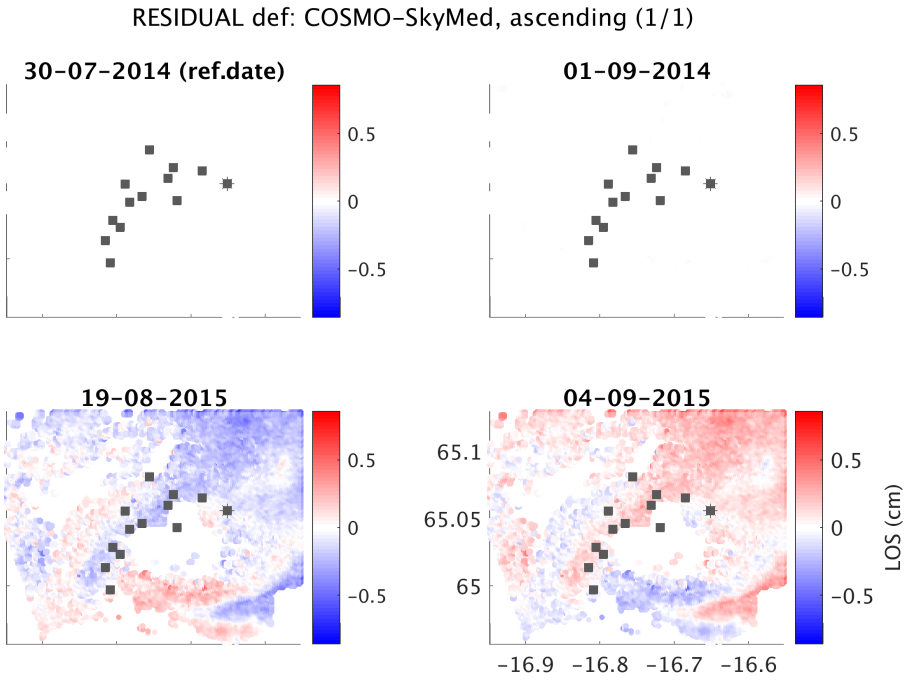

Figure A.31: CSK-A time-series over 2014-2015, showing residual displacements, in cm along LOS, after removal of the exponential subsidence trend. Red is deformation away from the satellite, the reference site is highlighted with the star, and GPS stations are the black squares.

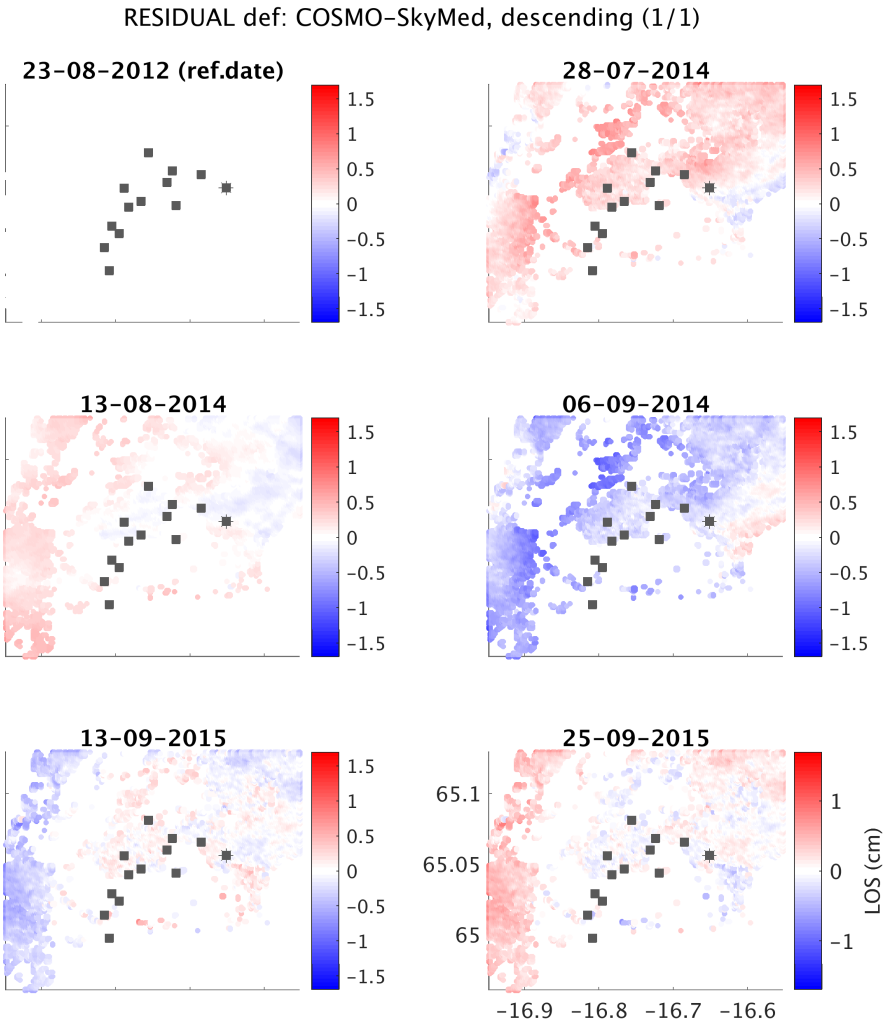

Figure A.32: CSK-D time-series showing residual displacements, in cm along LOS, after removal of the exponential subsidence trend. Red is deformation away from the satellite, the reference site is highlighted with the star, and GPS stations are the black squares.

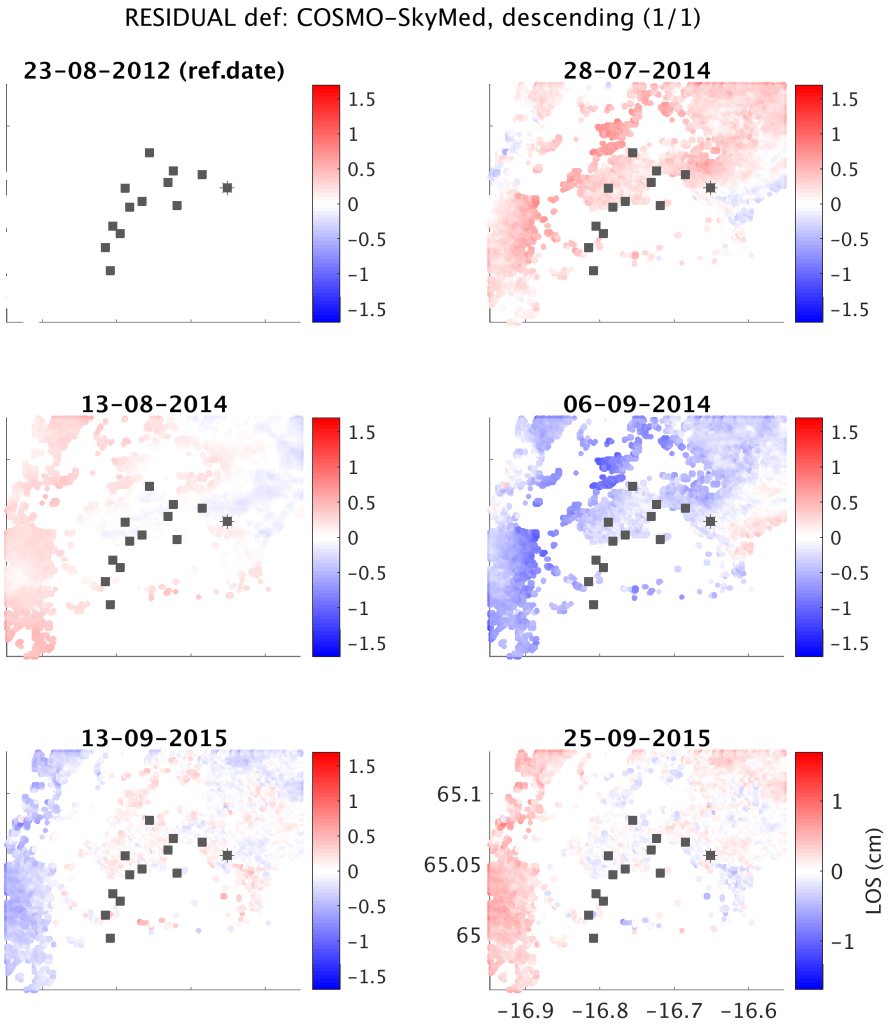

Figure A.33: CSK-D time-series showing residual displacements, in cm along LOS, after removal of the exponential subsidence trend. Red is deformation away from the satellite, the reference site is highlighted with the star, and GPS stations are the black squares.

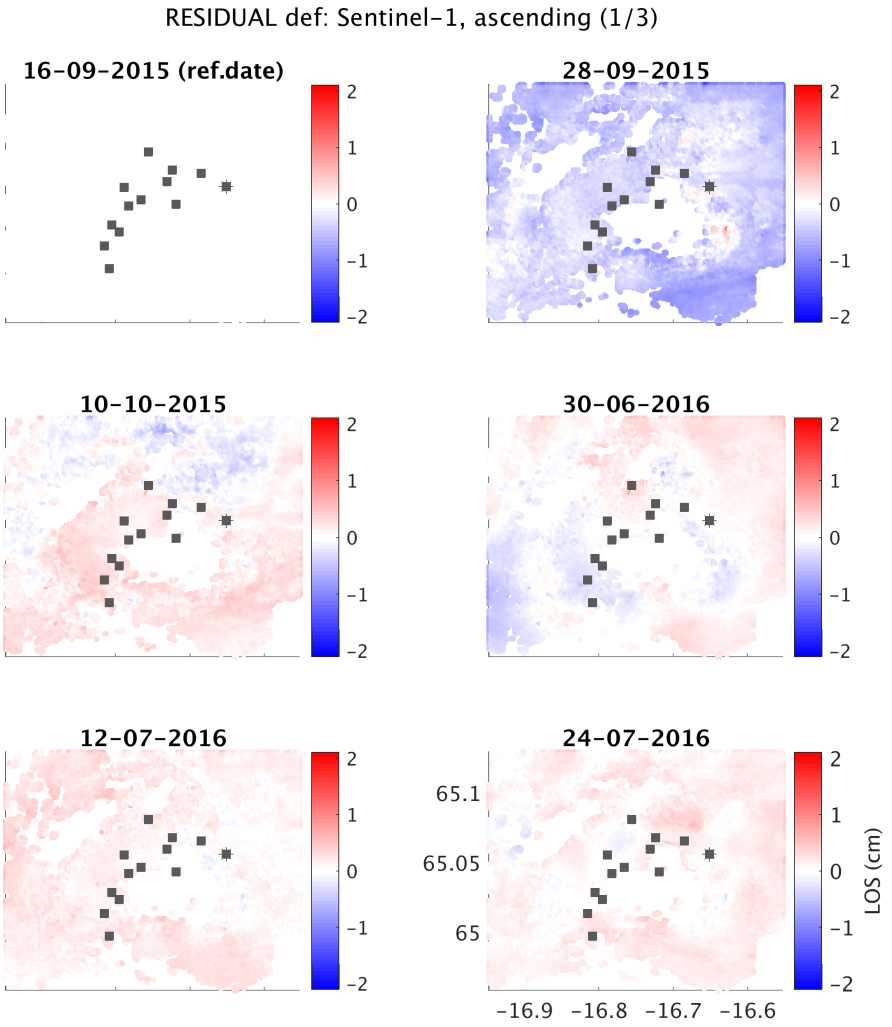

Figure A.34: S1-A time-series showing residual displacements, in cm along LOS, after removal of the exponential subsidence trend. Red is deformation away from the satellite, the reference site is highlighted with the star, and GPS stations are the black squares.

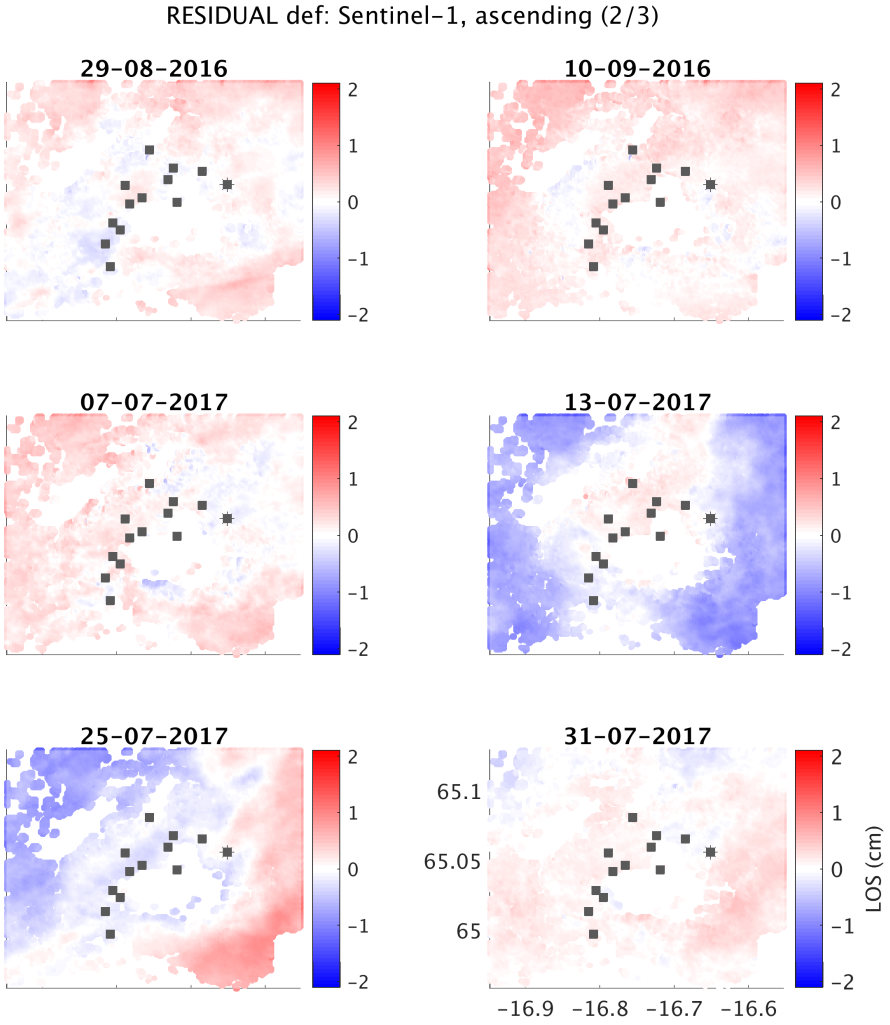

Figure A.35: Continuing of the S1-A time-series.

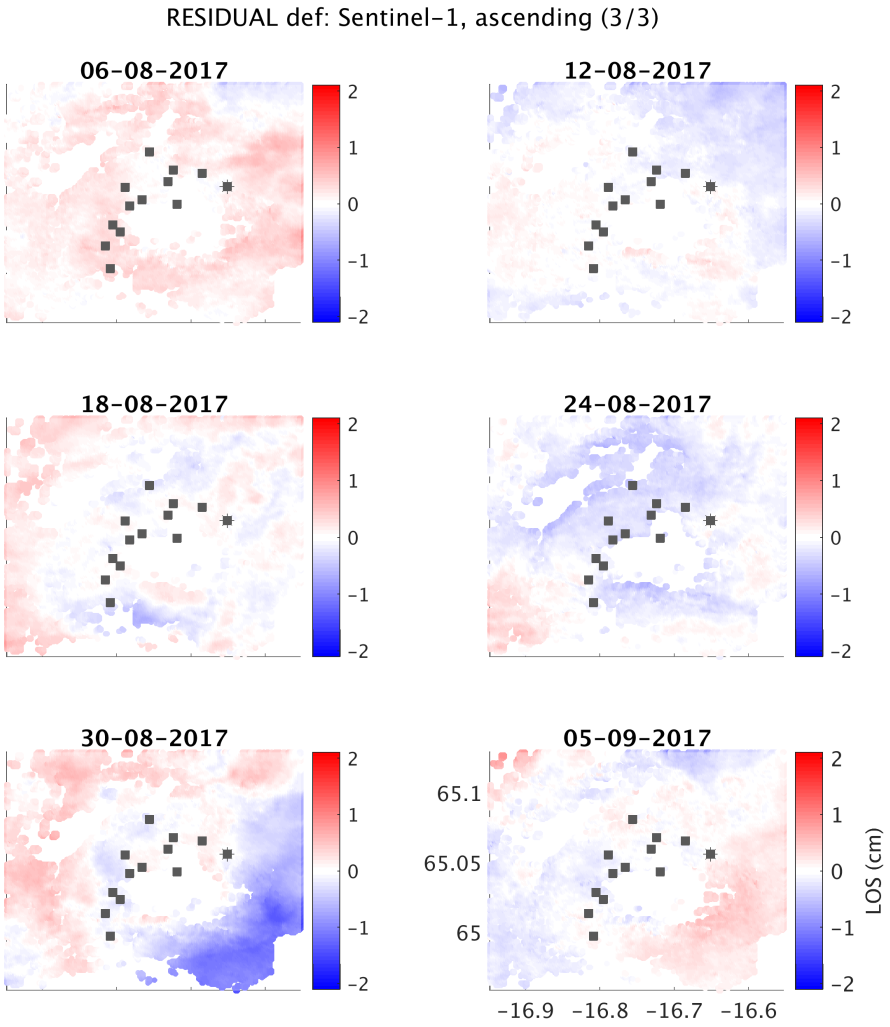

Figure A.36: End of the S1-A time-series.

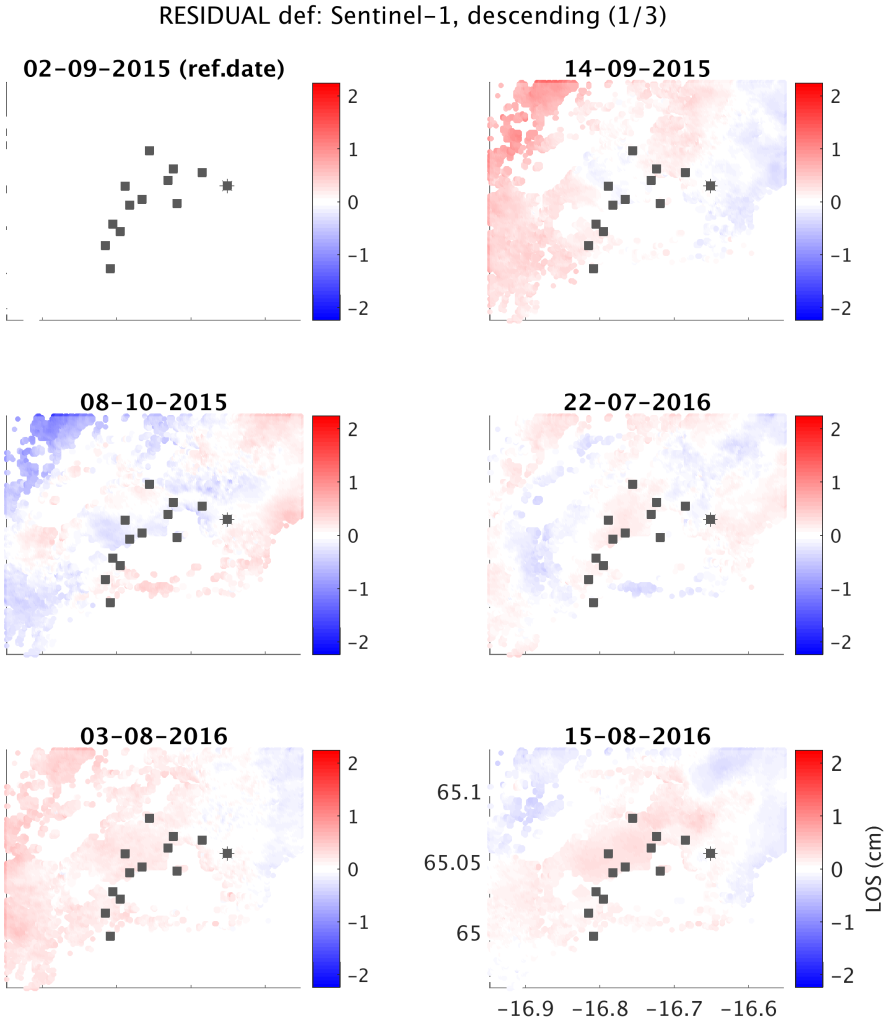

Figure A.37: S1-D time-series showing residual displacements, in cm along LOS, after removal of the exponential subsidence trend. Red is deformation away from the satellite, the reference site is highlighted with the star, and GPS stations are the black squares.

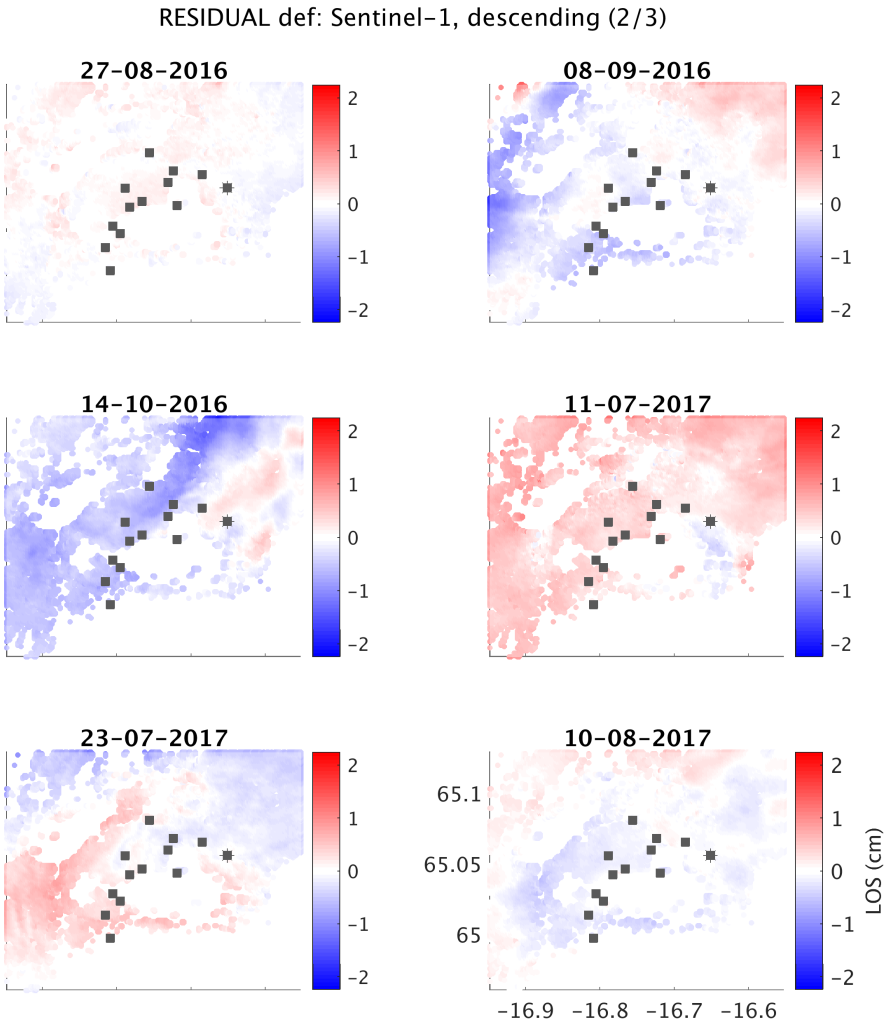

Figure A.38: Continuing of the S1-D time-series.

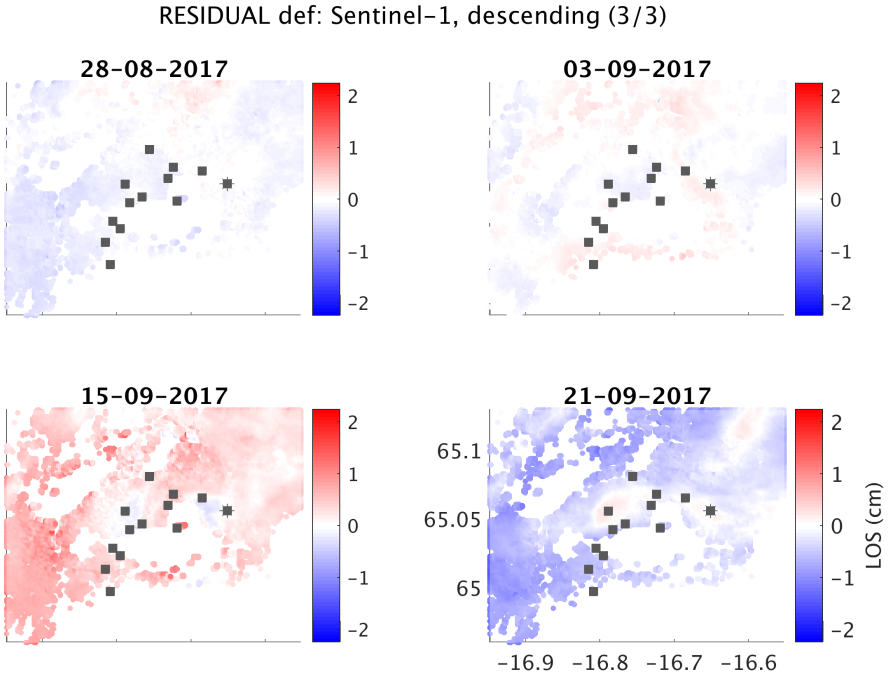

Figure A.39: End of the S1-D time-series.

A.5 Supplementary figures related to the deformation model

Figure A.40: Accepted parameter solution (each plot) against iterations, for the inversion that I carried out using LOS velocities over the 15-year long InSAR time-series, assuming a Mogi source and solving its location (X,Y), depth, volume change (DV), as well as for constants estimating the deformation at the reference, and possible ramps along X and Y.

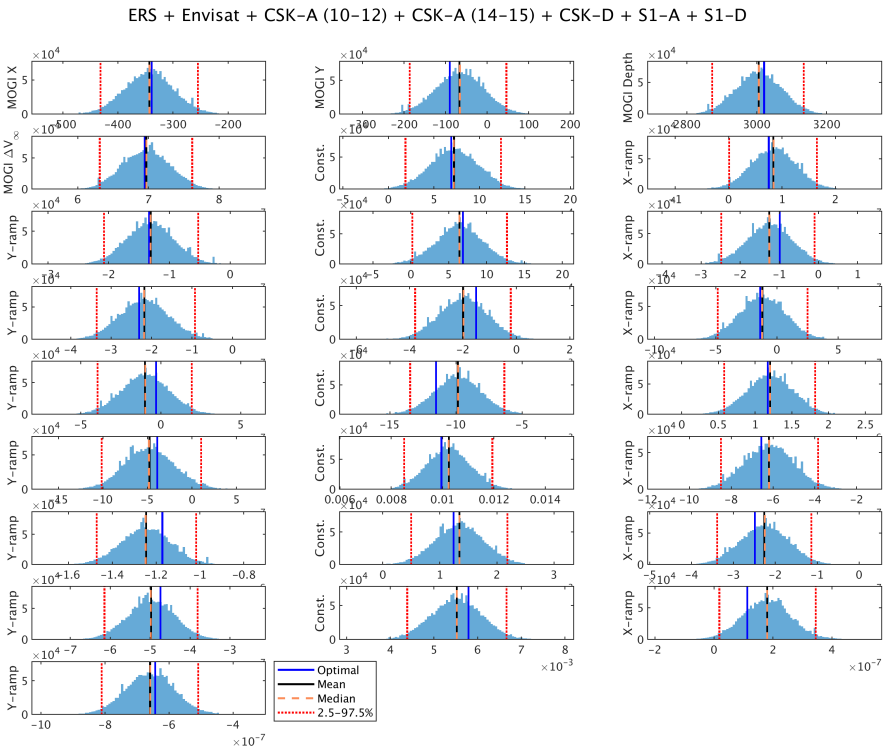

Figure A.41: 1-D marginal posterior probability functions for each parameter constrained in the inversion. The most probable or "optimal" solutions are highlighted in blue, the means are in black, the median are in dashed orange, and the 2.5 and 97.5 percentiles are in dotted red.

Appendix B

Supplementary material for Chapter 4

B.1 Derivation of the approximately Gaussian distribution of $\varepsilon_{\Delta\text{tilt}}$

Based on Equation 4.9, the error, $\varepsilon_{\text{tilt}}$, of the gravity effect due to tilt at any station of interest, depends on the errors, ε_{θ_x} and ε_{θ_y}, of the orthogonal tilt angle components, assumed to be equal and drawn from a Gaussian distribution:

$$\varepsilon_{\text{tilt}} = g_0 \left(\cos\varepsilon_{\theta_x} \cdot \cos\varepsilon_{\theta_y}\right) = g_0 \left(\cos\varepsilon_{\theta}\right) \simeq \frac{g_0}{2}\,\varepsilon_{\theta}^2. \tag{B.1}$$

I explain here how this equation can be derived to demonstrate that the error of the gravity effect due to tilt, between the station of interest and the base station, is drawn from a distribution that can be approximated as Gaussian.

Assuming that ε_θ is drawn from a circular Gaussian distribution with 1-D variance $\sigma_{\theta_x}^2 = \sigma_{\theta_y}^2$ (given in radians), its amplitude is drawn from a Rayleigh distribution, with expected value $(\sqrt{\pi/2})\sigma_{\theta_x}$:

$$\mathrm{P}(\varepsilon_\theta) = \frac{\varepsilon_\theta}{\sigma_{\theta_x}^2} e^{\frac{-\theta^2}{2\sigma_{\theta_x}^2}}. \tag{B.2}$$

The probability distribution function of the square of a Rayleigh-distributed random variable is an exponential, so combining Equations B.1 and B.2 gives:

$$\mathrm{P}(\varepsilon_{tilt}) = \frac{1}{g_0\sigma_{\theta_x}^2} e^{\frac{-\varepsilon_{tilt}}{g_0\sigma_{\theta_x}^2}}, \tag{B.3}$$

with expected value $g_0\sigma_{\theta_x}^2$ and error standard deviation, $\sigma_{\text{tilt}} = g_0\sigma_{\theta_x}^2$.

Assuming that ε_θ has the same distribution at the base than at the station of interest, the corresponding spatial difference in $\varepsilon_{\text{tilt}}$ ($\varepsilon_{\Delta\text{tilt}} = \varepsilon_{\text{tilt}} - \varepsilon_{\text{tilt}}^{\text{B}}$), for a single base occupation, with no contribution from drift, is drawn from a Laplacian distribution

with expected value zero and error standard deviation, $\sigma_{\Delta\text{tilt}} = \sqrt{2} g_0 \sigma^2_{\theta_x}$:

$$\begin{aligned} \mathrm{P}(\varepsilon_{\Delta\text{tilt}}) &= \frac{1}{2 g_0 \sigma^2_{\theta_x}} e^{-\frac{\varepsilon_{\Delta\text{tilt}}}{g_0 \sigma^2_{\theta_x}}} \, for \; \varepsilon_{\Delta\text{tilt}} \geq 0, & \text{(B.4)} \\ &= \frac{1}{2 g_0 \sigma^2_{\theta_x}} e^{\frac{\varepsilon_{\Delta\text{tilt}}}{g_0 \sigma^2_{\theta_x}}} \text{ for } \varepsilon_{\Delta\text{tilt}} < 0. & \text{(B.5)} \end{aligned}$$

To account for the fact that the base component, $\hat{g}_{\text{base}}$ (Equation 2.8), is estimated from multiple base station occupations (Section 4.7), I assume that the distribution of $\varepsilon^{\text{B}}_{\text{tilt}}$ is equal to that of the mean of $n-1$ base occupations (degrees of freedom reduced by one due to simultaneous estimation of drift). The probability density function for the sum of multiple exponentially distributed random variable is a Gamma distribution:

$$\mathrm{P}(\varepsilon^{\text{B}}_{\text{tilt}}) = \frac{\left(\frac{n-1}{g_0 \sigma^2_{\theta_x}}\right)^{(n-1)} {\varepsilon^{\text{B}}_{\text{tilt}}}^{(n-2)} e^{-\left(\frac{n-1}{g_0 \sigma^2_{\theta_x}}\right)\varepsilon^{\text{B}}_{\text{tilt}}}}{\Gamma(n-1)}. \qquad \text{(B.6)}$$

Consequently, based on Equations B.3 and B.6, $\varepsilon_{\Delta\text{tilt}}$ is drawn from the following distribution, with expected value zero:

$$\begin{aligned} \mathrm{P}(\varepsilon_{\Delta\text{tilt}}) &= \frac{(n-1)^n n^{-(n-1)}}{\Gamma(n-1) g_0 \sigma^2_{\theta_x}} e^{-\frac{\varepsilon_{\Delta\text{tilt}}}{g_0 \sigma^2_{\theta_x}}} \text{ for } \varepsilon_{\Delta\text{tilt}} > 0, & \text{(B.7)} \\ &= \frac{(n-1)^n n^{-(n-1)}}{\Gamma(n-1) g_0 \sigma^2_{\theta_x}} e^{-\frac{\varepsilon_{\Delta\text{tilt}}}{g_0 \sigma^2_{\theta_x}}} \Gamma\left(n-1, \frac{-n\varepsilon_{\Delta\text{tilt}}}{g_0 \sigma^2_{\theta_x}}\right) \text{ for } \varepsilon_{\Delta\text{tilt}} < 0. & \text{(B.8)} \end{aligned}$$

B.2 Calibration error, relative to the base station

Any j^{th} average g_{meas} (Section 4.3), relative to the survey carried out at $t = t_i$, is obtained by multiplying the mean, $\bar{\varrho}$, of all ϱ from all gravity samples by the calibration factor, k_i, at that specific time. Because the calibration factors of SCG and LCR gravimeters are not expected to vary by more than a few ppm per day (Section 4.8), they can be considered as constant throughout a survey, and the drift-corrected gravity signal, g_{DC}, can therefore be expressed as follows:

$$g_{\text{DC}} = k_i \, (\bar{\varrho} - \bar{\varrho}_{\text{base}}). \qquad \text{(B.9)}$$

Because k_i is usually given as a proportion of the manufacturer-determined calibration factor, k_0 (Valliant, 1991, Scintrex, 1995, 2009), its error, ε_{k_i}, can also be expressed as a proportion of k_0:

$$\begin{aligned} k_i &= k_0 \, f(t_i), & \text{(B.10)} \\ \varepsilon_{k_i} &= k_0 \, \varepsilon_{f(t_i)}, & \text{(B.11)} \end{aligned}$$

where $f(t_i)$ is the scale factor at $t = t_i$, i.e. characterizing the calibration drift since the k_0 was determined.

Consequently, the calibration error, $\varepsilon_{\Delta\text{cal}}$, of the drift-corrected gravity signal, can be computed by multiplying ε_{k_i} by the estimate of the drift-corrected gravity (Equations B.9-B.11):

$$\varepsilon_{\Delta\text{cal}} = \varepsilon_{k_i} \, (\bar{\varrho} - \bar{\varrho}_{\text{base}}), \tag{B.12}$$

$$\therefore \varepsilon_{\Delta\text{cal}} = \varepsilon_{f(t_i)} \, \hat{g}_{\text{DC}}. \tag{B.13}$$

Following the same reasoning, the calibration error, $\varepsilon_{\Delta^2\text{cal}}$, of the temporal change in drift-corrected gravity, between two surveys carried out at $t = t_1$ and $t = t_2$, is then:

$$\varepsilon_{\Delta^2\text{cal}} = \varepsilon_{f(t_2)} \, (\hat{g}_{\text{DC}})_{t_2} - \varepsilon_{f(t_1)} \, (\hat{g}_{\text{DC}})_{t_1}. \tag{B.14}$$

Appendix C

Supplementary material for Chapter 5

C.1 Information for gravity surveys at Askja

Table C.2: List of survey parameters setup in the Scintrex gravimeter for each surveys.

CG-5 Options	
Tide correction	NO
Cont. tilt	YES
Auto rejection	YES
Terrain corr.	NO
Seismic filter	NO
Raw data	YES
Read time	60 SEC
Factory Flas	80
#of Cycles	5
Start delay	5 SEC
Line separation	0
Station separation	0
Auto station inc.	NO
Chart scale	1
Measurement	GRAPHIC
LCD heater	ON
Record Amb. Temp.	YES

Table C.1: List of gravity stations at Askja, mentioning new names vs. old names, and providing detailed descriptions of locations.

Name	Old name,when Different	Benchmark ID	Coordinates	Description
Grafarlond			N65.27027 - W16.10282	To reach the station you need to take the track F88 to Askja from road 1, which starts about 35 km from Reykjahlid (Myvatn), when driving towards Egilsstadir. F88 is just before the bridge. An old track is still visible to drive to the benchmark, starting at N65.27168 - W16.11274. The pin is located on top of an isolated boulder to the N of the northern end of the landing strip. "FM33" was apparently painted in white on the boulder. This is a national base of which the absolute gravity value was determined in 1968: 982 222.18 Gal
DYNG		No ID, new pin in 2015	N65.05632 W16.65161	DYNG GPS station (N65.05631° - W16.65177°) was first measured in 2002 but has been monumented by a quadripode in the meantime. A new benchmark for gravity has been installed in 2015, at 8.8 m from the continuous GPS site towards N80.
RAU2	83009	NE 83/009	N65.06572 - W16.68547	The benchmark is located on a flat paoheohe lava (1961) on the left (S of road), at 5.5 km from Drekki when driving to Askja (or 2.4 km from the intersection road to Dyngja). The pin is circled with yellow paint.
VIKR	83001	NE 83/001	N65.06827 - W16.72405	The benchmark is located on the left when walking about 100 m along the road from the Askja car park back to Drekki (3rd yellow stick). A cairn on paoheohe lava at around 400 m towards NW indicates the station that is circled with yellow paint.
A430	430	430	N65.06914 - W16.72755	This station is part of the levelling line and circled with yellow paint. Follow the road from the car park until you reach the second yellow stick. Walk through the a'a lavas towards N325 (you should see a yellow stick in that direction). You will need the GPS coordinates to find the benchmark while getting closer and closer to this far yellow stick but you will never reach the yellow stick. A cairn indicates the benchmark.
A412	412	412	N65.06350 - W16.73503	This station is part of the levelling line and is circled with yellow paint. Follow the touristic path from the Askja car park to the caldera for 700 m, i.e. over the spatter cones. Start walking towards NW and look for cairns.
A405	405	405	N65.05989 - W16.73217	This station is part of the levelling line and is circled with yellow paint. Located on a large paoheohe lava, a cairn indicates the benchmark, which is located at few hundred meters away from the path that goes into the caldera, and few hundred meters after you passed the board on eruptions explanations.
IV16		Yellow paint on side of Boulder	N65.04706 - W16.71969	Walk down the touristic path to reach Viti. When looking at the eastern Askja caldera rim (Viti in your back), you will see plenty of boulders and large blocks due to rock slide. One boulder (1.5 m3) has a flat surface slightly tilting towards S. The name "IV-16" was painted in yellow on the NE surface but you can actually now read "I 16" if you look carefully. The measurement is taken on the N side of the boulder (no pin).
BATS	D-18 (old pin)	JH14-04	N65.04360 – W16.71909	There are 4 or 5 benchmarks in this area. The one that was previously measured had the inscription "Darthmouth 18" (GPS) but does not allow to have the tripod horizontal when being right above the benchmark due to the shape of the rock. In 2015,I decided to make the measurement at the benchmark JH14-04 (yellow pin) which is at approx. 10-15 m towards N30 (i.e. closer to the lake). A small cairn indicates the station that is on a a'a lava at around 3-5 m away from the lava flow front that is parallel to the edge of the lake.
VonK	Von Knebel	N/A	N65.04647 - W16.73186	This station does not have any pin. It is located at the bottom of the memorial cairn (Rudloff Von Knebel). The measurement is taken S of the cairn on mud ground.
MASK		NE2002 - 005	N65.04674 - W16.76625	This station is part of the campaign GPS network. In the pumice field, you will notice 4 trolls standing up (blocks of lava of approx. 2 m high). The benchmark has green tape around it.
NE2	NE2002 – 006	NE2002 - 006	N65.04247 - W16.78128	Walk 15 min from MASK towards W. You will notice a small tumuli of approx. 100 m from shoreline with cairn.
OLAF	005	82005	N65.04239 - W16.78288	This station is part of the campaign GPS network. Walk 5 min from NE2 towards NW, close to a cairn.
D-19		Darthmouth 19	N65.04175 - W16.78278	Walk 5 min from OLAF towards S. Look for a cairn on a flat paoheohe..
CASK		No ID	N65.05591 - W16.78880	Located on a 1-m-high rounded block of old a'a lava. It is at 1.6 km from D-19 towards N (40 min) and 2.6 km from 412, towards S. The route from 412 to CASK is only composed of a'a lava, so it is quite a hard hike. Walking poles are mandatory!
STAM		NE90013	N64.99727 - W16.80889	This station is part of the campaign GPS network and is reached by car when driving around the S of Askja from Drekki to the SW external edge of the caldera. Located on a pahoehoe block of lava and indicated by a cairn.
VATN		NE0413	N65.01372 - W16.81559	This station is part of the campaign GPS network. From STAM, drive to the top of the SW caldera rim of Askja and walk downwards within the caldera.
MYV1		No ID	N65.02368 – W16.79538	This benchmark is reached by walk from VATN (around 60 min??). Walk in the ash/pumice around the a'a lavas (i.e. along the lake!). The station is at about 5 m from the edge of the lava flow, approx. aligned with the big cairn standing close to the lake.
MYV2		No ID	N65.028945 – W16.80580	This benchmark is reached from MYV1 (around 60 min??). Walk along the lava up to the coord. N65.02506;W16.79341. Walk across the spatter cones, and try to follow the path that you should catch.

C.2 Supplementary figures related to the deformation model

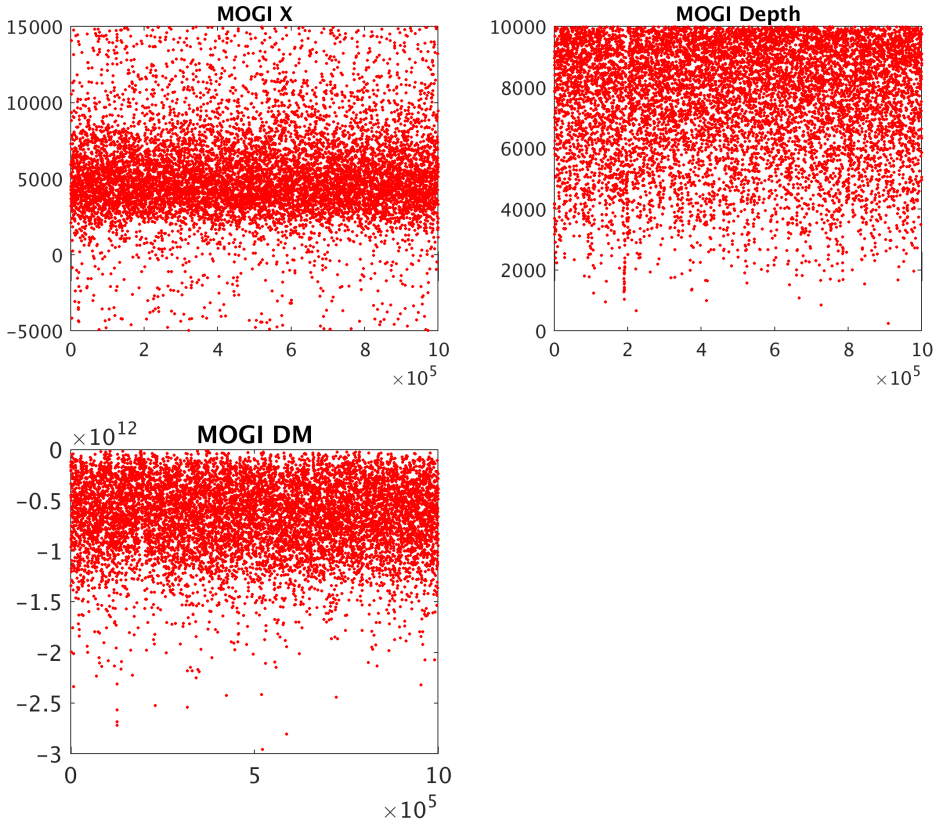

Figure C.1: Accepted parameter solution (each plot) against iterations, for the inversion that I carried out using residual gravity changes over 2015-2016, assuming a spherical source and solving its location (X, along profile, relative to DYNG), depth and mass change (DM).

References

Acocella, V., Di Lorenzo, R., Newhall, C., and Scandone, R. (2015). An overview of recent (1988 to 2014) caldera unrest: Knowledge and perspectives. *Reviews of Geophysics*, 53(3):896–955. 1.1, 3.1

Agnew, D. (2007). 3.06 earth tides. *Treatise on Geophysics, Elsevier, Amsterdam*, pages 163–195. 4.5

Auriac, A. (2014). *Solid Earth response to ice retreat and glacial surges in Iceland inferred from satellite radar interferometry and finite element modelling*. PhD thesis, Faculty of Earth Sciences - University of Iceland. 3.3

Bagnardi, M. and Hooper, A. (2018). Inversion of surface deformation data for rapid estimates of source parameters and uncertainties: A Bayesian approach. *Geochemistry, Geophysics, Geosystems*, 19(7):2194–2211. 3.4.4, 3.4.4, 3.7.1, 5.6.1, 5.10

Bagnardi, M., Poland, M. P., Carbone, D., Baker, . S., Battaglia, M., and Amelung, F. (2014). Gravity changes and deformation at Kīlauea Volcano, Hawai'i, associated with summit eruptive activity, 2009–2012. *Journal of Geophysical Research: Solid Earth*, 119(9):7288–7305. 1.3.3, 1.3.4, 4.2, 4.4, 4.9, 6.1

Baker, S. and Amelung, F. (2012). Top-down inflation and deflation at the summit of Kīlauea Volcano, Hawai âĂŸi observed with InSAR. *Journal of Geophysical Research: Solid Earth*, 117(B12). 6.1

Battaglia, M., Gottsmann, J., Carbone, D., and Fernández, J. (2008). 4D volcano gravimetry. *Geophysics*, 73(6):WA3–WA18. 1.1, 1.3, 1.4, 1.4.1, 1.4.2, 2, 2.2, 2.2.2, 2.2.3, 2.2.3, 4.1, 4.9, 4.10

Battaglia, M., Lisowski, M., Dzurisin, D., Poland, M., Schilling, S., Diefenbach, A., and Wynn, J. (2018). Mass addition at Mount St. Helens, Washington, inferred from repeated gravity surveys. *Journal of Geophysical Research: Solid Earth*, 123. 2.2.3, 2.2.3, 4.2, 4.7, 4.7.1, 4.4, 4.9.3, 4.10

Battaglia, M., Poland, M., and Kauahikaua, J. (2012). GTOOLS: An interactive computer program to process gravity data for high-resolution applications. In *AGU Fall Meeting Abstracts*, volume 1, page 1143. 2.2.3, 4.5, 4.6, 5.4

Battaglia, M., Segall, P., and Roberts, C. (2003). The mechanics of unrest at Long Valley caldera, California. 2. Constraining the nature of the source using geodetic and micro-gravity data. *Journal of Volcanology and Geothermal Research*, 127(3):219–245. 4.9

Bekaert, D., Hooper, A., and Wright, T. (2015a). A spatially variable power law tropospheric correction technique for InSAR data. *Journal of Geophysical Research: Solid Earth*, 120(2):1345–1356. 2.1.3

Bekaert, D., Walters, R., Wright, T., Hooper, A., and Parker, D. (2015b). Statistical comparison of InSAR tropospheric correction techniques. *Remote Sensing of Environment*, 170:40–47. 2.1.3

Berrino, G., Corrado, G., Luongo, G., and Toro, B. (1984). Ground deformation and gravity changes accompanying the 1982 Pozzuoli uplift. *Bulletin of Volcanology*, 47(2):187–200. 4.15

Bevington, P. R. and Robinson, D. K. (1992). Chapter 4: Estimates of means and errors. In *Data Reduction and Error Analysis for the Physical Sciences*, pages 53–74. McGraw-Hill Compagnies. 3.4.4

Biggs, J., Ebmeier, S., Aspinall, W., Lu, Z., Pritchard, M., Sparks, R., and Mather, T. (2014). Global link between deformation and volcanic eruption quantified by satellite imagery. *Nature communications*, 5:3471. 1.1

Björnsson, A., Saemundsson, K., Einarsson, P., Tryggvason, E., and Grönvold, K. (1977). Current rifting episode in north Iceland. *Nature*, 266(5600):318. 1.5.3

Boddice, D., Atkins, P., Rodgers, A., Metje, N., Goncharenko, Y., and Chapman, D. (2018). A novel approach to reduce environmental noise in microgravity measurements using a Scintrex CG5. *Journal of Applied Geophysics*, 152:221–235. 4.3, 4.3.1, 4.3.2, 4.5

Bonaccorso, A., Bonforte, A., Currenti, G., Del Negro, C., Di Stefano, A., and Greco, F. (2011). Magma storage, eruptive activity and flank instability: inferences from ground deformation and gravity changes during the 1993–2000 recharging of Mt. Etna volcano. *Journal of Volcanology and Geothermal Research*, 200(3):245–254. 4.9

Bonforte, A., Fanizza, G., Greco, F., Matera, A., and Sulpizio, R. (2017). Long-term dynamics across a volcanic rift: 21years of microgravity and gps observations on the southern flank of Mt. Etna volcano. *Journal of Volcanology and Geothermal Research*. 4.15

Bonvalot, S., Diament, M., and Gabalda, G. (1998). Continuous gravity recording with Scintrex CG-3M meters: a promising tool for monitoring active zones. *Geophysical Journal International*, 135(2):470–494. 4.3, 4.3.1, 4.3.1, 4.4.1, 4.5, 4.6, 4.7

Bonvalot, S., Remy, D., Deplus, C., Diament, M., and Gabalda, G. (2008). Insights on the March 1998 eruption at Piton de la Fournaise volcano (La Reunion) from microgravity monitoring. *Journal of Geophysical Research: Solid Earth*, 113(B5). 4.8.2

Bos, M. and Baker, T. (2005). An estimate of the errors in gravity ocean tide loading computations. *Journal of geodesy*, 79(1-3):50–63. 4.5

Bouman, J., Ebbing, J., Fuchs, M., Sebera, J., Lieb, V., Szwillus, W., Haagmans, R., and Novak, P. (2016). Satellite gravity gradient grids for geophysics. *Scientific reports*, 6:21050. 4.9.2

Boy, J.-P., Llubes, M., Hinderer, J., and Florsch, N. (2003). A comparison of tidal ocean loading models using superconducting gravimeter data. *Journal of Geophysical Research: Solid Earth*, 108(B4). 4.5

Budetta, G. and Carbone, D. (1997). Potential application of the Scintrex CG-3M gravimeter for monitoring volcanic activity: results of field trials on Mt. Etna, Sicily. *Journal of Volcanology and Geothermal Research*, 76(3-4):199–214. 2.2.2, 4.3.1, 4.7, 4.8, 4.4, 4.8.2, 4.8.3

Burchardt, S. (2018). *Volcanic and igneous plumbing systems*. Elsevier. 1.1

Burgisser, A. and Degruyter, W. (2015). Magma ascent and degassing at shallow levels. In Sigurdsson, H., Houghton, B., McNutt, S., Rymer, H., and Stix, J., editors, *The encyclopedia of volcanoes*, chapter 11, pages 225–236. Elsevier. 1.3.2, 1.3.3

Bürgmann, R., Rosen, P. A., and Fielding, E. J. (2000). Synthetic aperture radar interferometry to measure EarthâĂŹs surface topography and its deformation. *Annual review of earth and planetary sciences*, 28(1):169–209. 2, 2.1

Camitz, J., Sigmundsson, F., Foulger, G., Jahn, C.-H., Völksen, C., and Einarsson, P. (1995). Plate boundary deformation and continuing deflation of the Askja volcano, North Iceland, determined with GPS, 1987–1993. *Bulletin of Volcanology*, 57(2):136–145. 1.2

Carbone, D., Poland, M. P., Diament, M., and Greco, F. (2017). The added value of time-variable microgravimetry to the understanding of how volcanoes work. *Earth-Science Reviews*. 1.1, 2, 2.2.1, 2.2.2, 4.1, 4.1, 4.3.2, 4.8.2, 5.5.1

Carbone, D. and Rymer, H. (1999). Calibration shifts in a LaCoste-and-Romberg gravimeter: comparison with a Scintrex CG-3M. *Geophysical Prospecting*, 47(1):73–83. 4.4

Caricchi, L., Biggs, J., Annen, C., and Ebmeier, S. (2014). The influence of cooling, crystallisation and re-melting on the interpretation of geodetic signals in volcanic systems. *Earth and Planetary Science Letters*, 388:166–174. 5.7

Cashman, K. V., Sparks, R. S. J., and Blundy, J. D. (2017). Vertically extensive and unstable magmatic systems: a unified view of igneous processes. *Science*, 355(6331):eaag3055. 1.2

Chambat, F. and Valette, B. (2001). Mean radius, mass, and inertia for reference Earth models. *Physics of the Earth and Planetary Interiors*, 124(3):237–253. 4.9.1

Champollion, C., Deville, S., Chery, J., Doerflinger, E., Moigne, N. L., Bayer, R., Vernant, P., and Mazzilli, N. (2018). Estimating epikarst water storage by time-lapse surface-to-depth gravity measurements. *Hydrology and Earth System Sciences*, 22(7):3825–3839. 4.3.1, 4.10

Cheng, Y. and Andersen, O. B. (2011). Multimission empirical ocean tide modeling for shallow waters and polar seas. *Journal of Geophysical Research: Oceans*, 116(C11). 5.4.1.1

Cigolini, C., Poggi, P., Ripepe, M., Laiolo, M., Ciamberlini, C., Delle Donne, D., Ulivieri, G., Coppola, D., Lacanna, G., Marchetti, E., et al. (2009). Radon surveys and real-time monitoring at Stromboli volcano: Influence of soil temperature, atmospheric pressure and tidal forces on 222Rn degassing. *Journal of Volcanology and Geothermal Research*, 184(3-4):381–388. 4.6

Comeau, M. J., Unsworth, M. J., Ticona, F., and Sunagua, M. (2015). Magnetotelluric images of magma distribution beneath Volcán Uturuncu, Bolivia: Implications for magma dynamics. *Geology*, 43(3):243–246. 5.7

Corti, G. (2009). Continental rift evolution: from rift initiation to incipient break-up in the Main Ethiopian Rift, East Africa. *Earth-science reviews*, 96(1-2):1–53. 1.2.1

Creutzfeldt, B., Güntner, A., Wziontek, H., and Merz, B. (2010). Reducing local hydrology from high-precision gravity measurements: a lysimeter-based approach. *Geophysical Journal International*, 183(1):178–187. 4.10

Crossley, D., Hinderer, J., and Riccardi, U. (2013). The measurement of surface gravity. *Reports on Progress in physics*, 76(4):046101. 2, 2.2.1, 4.1, 4.4

Curlander, J. C. and McDonough, R. N. (1991). In *Synthetic aperture radar - Systems and signal processing*. New York: John Wiley & sons, Inc. 2.1

Darbyshire, F. A., Bjarnason, I. T., White, R. S., and Flóvenz, Ó. G. (1998). Crustal structure above the Iceland mantle plume imaged by the ICEMELT refraction profile. *Geophysical Journal International*, 135(3):1131–1149. 1.2.1

de Zeeuw-van Dalfsen, E. (2004). *A geophysical study of volcanic processes at a persistently active volcano and at two calderas in a state of unrest.* PhD thesis, The Open University. 1.8, 1.5.2, 5.1

de Zeeuw-van Dalfsen, E., Pedersen, R., Hooper, A., and Sigmundsson, F. (2012). Subsidence of Askja caldera 2000–2009: modelling of deformation processes at an extensional plate boundary, constrained by time series InSAR analysis. *Journal of Volcanology and Geothermal Research*, 213:72–82. 1.1, 1.2, 1.5.3, 3.1, 3.7.3.1, 3.5, 3.7.3.2, 3.7.3.3, 5.7

de Zeeuw-van Dalfsen, E., Rymer, H., Sigmundsson, F., and Sturkell, E. (2005). Net gravity decrease at Askja volcano, Iceland: constraints on processes responsible for continuous caldera deflation, 1988–2003. *Journal of Volcanology and Geothermal Research*, 139(3):227–239. 1.2.2, 1.5.2, 1.5.2, 1.5.3, 4.9, 5.1, 5.2, 5.3, 5.7

de Zeeuw-van Dalfsen, E., Rymer, H., Sturkell, E., Pedersen, R., Hooper, A., Sigmundsson, F., and Ófeigsson, B. (2013). Geodetic data shed light on ongoing caldera subsidence at Askja, Iceland. *Bulletin of Volcanology*, 75(5):1–13. 1.1, 1.2, 1.7, 1.5.2, 1.8, 1.5.2, 1.5.3, 3.1, 5.1

de Zeeuw-van Dalfsen, E., Rymer, H., Williams-Jones, G., Sturkell, E., and Sigmundsson, F. (2006). Integration of micro-gravity and geodetic data to constrain shallow system mass changes at Krafla Volcano, N Iceland. *Bulletin of Volcanology*, 68(5):420–431. 4.15

Debeglia, N. and Dupont, F. (2002). Some critical factors for engineering and environmental microgravity investigations. *Journal of Applied Geophysics*, 50(4):435–454. 4.3, 4.7, 4.8.2

Del Negro, C., Currenti, G., Solaro, G., Greco, F., Pepe, A., Napoli, R., Pepe, S., Casu, F., and Sansosti, E. (2013). Capturing the fingerprint of Etna volcano activity in gravity and satellite radar data. *Scientific Reports*, 3. 4.9

Drouin, V. and Sigmundsson, F. (2013). Search GPS station - CGPS in Iceland. 5.4.1.1, 5.5.1

Drouin, V., Sigmundsson, F., Ófeigsson, B. G., Hreinsdóttir, S., Sturkell, E., and Einarsson, P. (2017). Deformation in the Northern Volcanic Zone of Iceland 2008–2014: An interplay of tectonic, magmatic, and glacial isostatic deformation. *Journal of Geophysical Research: Solid Earth*, 122(4):3158–3178. 1.2, 3.3, 3.4.1, 3.4.2, 3.7.3.2

Dunn, R. A., Toomey, D. R., and Solomon, S. C. (2000). Three-dimensional seismic structure and physical properties of the crust and shallow mantle beneath the East Pacific Rise at 9Âř 30'n. *Journal of Geophysical Research: Solid Earth*, 105(B10):23537–23555. 1.2.1

Dzurisin, D. (2007a). Classical surveying techniques. In Dzurisin, D., editor, *Volcano Deformation: new geodetic monitoring techniques*, chapter 2, pages 33–80. Springer Science & Business Media. 2, 2.2

Dzurisin, D. (2007b). The Global Positioning System: a multipurpose tool. In Dzurisin, D., editor, *Volcano Deformation: new geodetic monitoring techniques*, chapter 4, pages 111–152. Springer Science & Business Media. 4.9.3

Dzurisin, D. (2007c). Lessons from deforming volcanoes. In Dzurisin, D., editor, *Volcano Deformation: new geodetic monitoring techniques*, chapter 7, pages 223–278. Springer Science & Business Media. 1.1

Dzurisin, D. (2007d). *Volcano deformation: new geodetic monitoring techniques.* Springer Science & Business Media. 1.1, 1.3.4

Dzurisin, D. and Lu, Z. (2007). Interferometric synthetic-aperture radar (InSAR). In Dzurisin, D., editor, *Volcano Deformation: new geodetic monitoring techniques*, chapter 5, pages 153–194. Springer Science & Business Media. 2, 2.1, 2.1

Dzurisin, D., Poland, M. P., and Bürgmann, R. (2002). Steady subsidence of Medicine Lake volcano, northern California, revealed by repeated leveling surveys. *Journal of Geophysical Research: Solid Earth*, 107(B12):ECV–8. 6.1

Efron, B. and Tibshirani, R. (1986). Bootstrap methods for standard errors, confidence intervals, and other measures of statistical accuracy. *Statistical science*, pages 54–75. 3.4.4

Eggers, A. (1987). Residual gravity changes and eruption magnitudes. *Journal of Volcanology and Geothermal Research*, 33(1):201–216. 1.3, 1.3.3, 1.3.4, 1.4.2, 2

El Wahabi, A., Ducarme, B., and Van Ruymbeke, M. (2001). Humidity and temperature effects on LaCoste & Romberg gravimeters. *Journal of the Geodetic Society of Japan*, 47(1):10–15. 2.2.2, 4.6

Ferretti, A., Monti-Guarnieri, A., Prati, C., Rocca, F., and Massonet, D. (2007). *InSAR principles-guidelines for SAR interferometry processing and interpretation*, volume 19. 2, 2.1, 2.1.1, 2.2, 2.1.2, 2.4

Ferretti, A., Prati, C., and Rocca, F. (2001). Permanent scatterers in SAR interferometry. *IEEE Transactions on geoscience and remote sensing*, 39(1):8–20. 2.1

Flury, J., Peters, T., Schmeer, M., Timmen, L., Wilmes, H., and Falk, R. (2007). Precision gravimetry in the new Zugspitze gravity meter calibration system. In *Proceedings of the 1st International Symposium of the International Gravity Field Service, Istanbul 2006, Harita Dergisi, Special Issue*. 4.3.1, 4.3.1, 4.8.2

Fores, B., Champollion, C., Le Moigne, N., and Chery, J. (2017). Impact of ambient temperature on spring-based relative gravimeter measurements. *Journal of Geodesy*, 91:269–277. 4.6

Francis, O. and Hendrickx, M. (2001). Calibration of the LaCoste-Romberg 906 by comparison with the superconducting gravimeter C021 in Membach (Belgium). *Journal of the Geodetic Society of Japan*, 47(1):16–21. 4.8.2

Francis, P. and Oppenheimer, C. (2004). *Volcanoes*. Oxford University Press. 1.2, 1.3, 1.3.2, 1.3.3

Freeze, R. A. and Cherry, J. A. (1979). *Groundwater*. Prentice-Hall. 4.10

Fuhrmann, T. and Garthwaite, M. C. (2019). Resolving three-dimensional surface motion with InSAR: Constraints from Multi-Geometry Data Fusion. *Remote Sensing*, 11(3):241. 3.5, 1, A.3

Galland, O., Bertelsen, H., Eide, C., Guldstrand, F., Haug, Ø., Leanza, H. A., Mair, K., Palma, O., Planke, S., Rabbel, O., et al. (2018). Storage and transport of magma in the layered crustâĂŤformation of sills and related flat-lying intrusions. In Burchardt, S., editor, *Volcanic and igneous plumbing systems*, chapter 5, pages 113–138. Elsevier. 1.2, 1.1, 1.2.1

Goncharenko, Y., Boddice, D., Rodgers, A., Atkins, P., Metje, N., and Chapman, D. (2018). Using broadband seismic networks to optimize microgravity survey strategy in the United Kingdom. *Near Surface Geophysics*, 16(4):477–489. 4.3, 4.3.1

González, P. J., , Walters, R. J., Hatton, E. L., Spaans, K., Hooper, A. J., and Wright, T. J. (2016). LiCSAR: Tools for automated generation of Sentinel-1 frame interferograms. In *AGU Fall Meeting Abstracts*. 2.1.2, 2.4, 3.1

Gottsmann, J., Wooller, L., Martí, J., Fernández, J., Camacho, A., Gonzalez, P., Garcia, A., and Rymer, H. (2006). New evidence for the reawakening of Teide volcano. *Geophysical Research Letters*, 33(20). 1.3.4

Grandin, R., Socquet, A., Doin, M.-P., Jacques, E., de Chabalier, J.-B., and King, G. (2010). Transient rift opening in response to multiple dike injections in the Manda Hararo rift (Afar, Ethiopia) imaged by time-dependent elastic inversion of interferometric synthetic aperture radar data. *Journal of Geophysical Research: Solid Earth*, 115(B9). 1.1, 1.2.2, 1.2.2, 1.3.4

Greco, F., Biolcati, E., Pistorio, A., DâĂŹAgostino, G., Germak, A., Origlia, C., and Del Negro, C. (2015). Absolute gravity measurements at three sites characterized by different environmental conditions using two portable ballistic gravimeters. *The European Physical Journal Plus*, 130(3):38. 4.15

Greco, F., Currenti, G., DâĂŹAgostino, G., Germak, A., Napoli, R., Pistorio, A., and Del Negro, C. (2012). Combining relative and absolute gravity measurements to enhance volcano monitoring. *Bulletin of Volcanology*, 74(7):1745–1756. 4.9, 4.15

Greenfield, T. (2016). *The velocity structure and micro-seismicity of the Askja central volcano, Iceland*. PhD thesis, University of Cambridge. 1.5.4, 1.9

Greenfield, T., White, R. S., and Roecker, S. (2016). The magmatic plumbing system of the Askja central volcano, Iceland, as imaged by seismic tomography. *Journal of Geophysical Research: Solid Earth*, 121(10):7211–7229. 1.5.4, 1.9, 3.1, 5.7

GVP (2019). Global Volcanism Program, Volcanoes of the World, v.4.8.2. *Smithsonian Institution*. 6.1

Hamling, I., Hreinsdottir, S., and Fournier, N. (2015). The ups and downs of the TVZ: Geodetic observations of deformation around the Taupo Volcanic Zone, New Zealand. *Journal of Geophysical Research: Solid Earth*, 120(6):4667–4679. 6.1

Hamlyn, J., Wright, T., Walters, R., Pagli, C., Sansosti, E., Casu, F., Pepe, S., Edmonds, M., Kilbride, B. M., Keir, D., et al. (2018). What causes subsidence following the 2011 eruption at Nabro (Eritrea)? *Progress in Earth and Planetary Science*, 5(1):31. 5.7

Hanssen, R. F. (2001). *Radar interferometry: data interpretation and error analysis*, volume 2. Springer Science & Business Media. 2, 2.1, 2.1.1, 2.1.2, 2.4

Harnisch, M. and Harnisch, G. (2002). Seasonal variations of hydrological influences on gravity measurements at Wettzell. *Bull. Inf. Marées Terr*, 137(10):849–10. 4.10, 4.10

Hartley, M. and Thordarson, T. (2012). Formation of öskjuvatn caldera at Askja, North Iceland: mechanism of caldera collapse and implications for the lateral flow hypothesis. *Journal of Volcanology and Geothermal Research*, 227:85–101. 1.5

Hautmann, S., Gottsmann, J., Camacho, A. G., Fournier, N., Sacks, I. S., and Sparks, R. S. J. (2010). Mass variations in response to magmatic stress changes at Soufrière Hills Volcano, Montserrat (WI): Insights from 4-D gravity data. *Earth and Planetary Science Letters*, 290(1):83–89. 1.3.4, 4.5

Hirt, C., Claessens, S., Fecher, T., Kuhn, M., Pail, R., and Rexer, M. (2013). New ultrahigh-resolution picture of Earth's gravity field. *Geophysical research letters*, 40(16):4279–4283. 4.4

Hooper, A. (2008). A multi-temporal InSAR method incorporating both persistent scatterer and small baseline approaches. *Geophysical Research Letters*, 35(16). 2.1.2, 2.1.3, 3.3

Hooper, A., Ófeigsson, B., Sigmundsson, F., Lund, B., Einarsson, P., Geirsson, H., and Sturkell, E. (2011). Increased capture of magma in the crust promoted by ice-cap retreat in Iceland. *Nature Geoscience*, 4(11):783. 3.4.1

Hooper, A., Segall, P., and Zebker, H. (2007). Persistent scatterer interferometric synthetic aperture radar for crustal deformation analysis, with application to Volcán Alcedo, Galápagos. *Journal of Geophysical Research: Solid Earth*, 112(B7). 2, 2.1, 2.1.2, 2.5

Hooper, A., Spaans, K., Bekaert, D., Cuenca, M. C., Arıkan, M., and Oyen, A. (2010). StaMPS/MTI manual. *Delft Institute of Earth Observation and Space Systems Delft University of Technology, Kluyverweg*, 1:2629. 2.4, 2.1.2, 3.1, 3.2

Hooper, A., Zebker, H., Segall, P., and Kampes, B. (2004). A new method for measuring deformation on volcanoes and other natural terrains using InSAR persistent scatterers. *Geophysical research letters*, 31(23). 2.1.2

Hussain, E., Wright, T. J., Walters, R. J., Bekaert, D., Hooper, A., and Houseman, G. A. (2016). Geodetic observations of postseismic creep in the decade after the 1999 Izmit earthquake, Turkey: Implications for a shallow slip deficit. *Journal of Geophysical Research: Solid Earth*, 121(4):2980–3001. 3.4.2

Icelandic MET office (2019). 4.9

Jacob, T., Bayer, R., Chery, J., and Le Moigne, N. (2010). Time-lapse microgravity surveys reveal water storage heterogeneity of a karst aquifer. *Journal of Geophysical Research: Solid Earth*, 115(B6). 4.3, 4.4.1, 4.6, 4.8.2, 4.4, 4.9.3, 4.10, 5.6.1

Jacob, T., Chery, J., Bayer, R., Le Moigne, N., Boy, J.-P., Vernant, P., and Boudin, F. (2009). Time-lapse surface to depth gravity measurements on a karst system reveal the dominant role of the epikarst as a water storage entity. *Geophysical Journal International*, 177(2):347–360. 4.7, 4.4

Jin, S. and Feng, G. (2013). Large-scale variations of global groundwater from satellite gravimetry and hydrological models, 2002–2012. *Global and planetary change*, 106:20–30. 4.10

Johnson, D. J. (1992). Dynamics of magma storage in the summit reservoir of Kīlauea volcano, HawaiâĂŸi. *Journal of Geophysical Research: Solid Earth (1978–2012)*, 97(B2):1807–1820. 4.15

Johnson, D. J. (1995). Gravity changes on Mauna Loa volcano. *Mauna Loa Revealed: Structure, Composition, History, and Hazards*, pages 127–143. 4.15

Johnson, D. J., Eggers, A. A., Bagnardi, M., Battaglia, M., Poland, M. P., and Miklius, A. (2010). Shallow magma accumulation at Kīlauea Volcano, HawaiâĂŸi, revealed by microgravity surveys. *Geology*, 38(12):1139–1142. 1.3.4, 4.9, 6.1

Jousset, P. (1996). *Microgravimétrie et gravimétrie en volcanologie: méthodologie et application au volcan Merapi, Java, Indonésie*. PhD thesis, Université Denis Diderot - Paris VII. 4.15

Jousset, P., Dwipa, S., Beauducel, F., Duquesnoy, T., and Diament, M. (2000a). Temporal gravity at Merapi during the 1993–1995 crisis: an insight into the dynamical behaviour of volcanoes. *Journal of Volcanology and Geothermal Research*, 100(1):289–320. 4.6

Jousset, P., Mori, H., and Okada, H. (2000b). Possible magma intrusion revealed by temporal gravity, ground deformation and ground temperature observations at Mount Komagatake (Hokkaido) during the 1996–1998 crisis. *Geophysical Journal International*, 143(3):557–574. 4.9

Kampes, B. and Usai, S. (1999). Doris: The delft object-oriented radar interferometric software. In *2nd international symposium on operationalization of remote sensing, enschede, the netherlands*, volume 16, page 20. Citeseer. 2.1.2, 2.4, 3.1

Kauahikaua, J. and Miklius, A. (2003). Long-term trends in microgravity at ktiauea's summit during the pu'u'6'6-kupaianaha eruption. *US Geological Survey professional paper*, 1676:165–171. 4.15

Kearey, P., Brooks, M., and Hill, I. (2002). Chapter 6: Gravity surveying. In *An Introduction to Geophysical Exploration*, pages 125–154. Blackwell Science Ltd. 1.3, 2.2.2, 2.6, 2.2.3, 4.9.1

Kipp, K. L., Hsieh, P. A., and Charlton, S. R. (2008). *Guide to the revised ground-water flow and heat transport simulator: HYDROTHERM–Version 3*. US Department of the Interior, US Geological Survey. 5.8

LaCoste & Romberg (2003). *Aliod100 upgrade - User manual v2.1*, LaCoste & Romberg edition. 2.6, 4.4.1

LaCoste & Romberg (2004). *Instruction manual - Model G & D gravity meters*, LaCoste & Romberg edition. 1.5.2, 2.2.2, 2.2.3, 4.1, 4.3.2, 4.4.1, 4.6, 4.8

LaFehr, T. (1991). Standardization in gravity reduction. *Geophysics*, 56(8):1170–1178. 4.9.1, 4.13

Lagios, E., Sakkas, V., Parcharidis, I., and Dietrich, V. (2005). Ground deformation of Nisyros volcano (Greece) for the period 1995–2002: Results from DInSAR and DGPS observations. *Bulletin of volcanology*, 68(2):201–214. 4.9.3

Lederer, M. (2009). Accuracy of the relative gravity measurement. *Acta Geodyn. Geomater*, 6(3):155. 4.1, 4.3.1, 4.4.1, 4.7

Lisowski, M. (2007). Analytical volcano deformation source models. In Dzurisin, D., editor, *Volcano Deformation*, chapter 8, pages 279–304. Springer Science & Business Media. 1.4, 1.4.1, 1.1, 1.4.1, 1.4.2, 1.4.2

Lissenberg, C. J., MacLeod, C. J., and Bennett, E. N. (2019). Consequences of a crystal mush-dominated magma plumbing system: a mid-ocean ridge perspective. *Philosophical Transactions of the Royal Society A*, 377(2139):20180014. 1.2.2, 1.2

Longman, I. M. (1959). Formulas for computing the tidal correction due to the moon and the sun. *Journal of Geophysical Research*, 64:2351–2355. 4.5

Longuevergne, L., Boy, J., Florsch, N., Viville, D., Ferhat, G., Ulrich, P., Luck, B., and Hinderer, J. (2009). Local and global hydrological contributions to gravity variations observed in Strasbourg. *Journal of Geodynamics*, 48(3-5):189–194. 4.10

Lyard, F., Lefevre, F., Letellier, T., and Francis, O. (2006). Modelling the global ocean tides: modern insights from FES2004. *Ocean dynamics*, 56(5-6):394–415. 4.6

Maclennan, J., McKenzie, D., Gronvöld, K., and Slater, L. (2001). Crustal accretion under northern Iceland. *Earth and Planetary Science Letters*, 191(3-4):295–310. 1.2.2

Marjanović, M., Carbotte, S. M., Carton, H., Nedimović, M. R., Mutter, J. C., and Canales, J. P. (2014). A multi-sill magma plumbing system beneath the axis of the East Pacific Rise. *Nature Geoscience*, 7(11):825. 1.2.1, 1.2.2

Marjanović, M., Carbotte, S. M., Carton, H. D., Nedimović, M. R., Canales, J. P., and Mutter, J. C. (2018). Crustal magmatic system beneath the East Pacific Rise (8Âř 20âĂš to 10Âř 10âĂš n): Implications for tectonomagmatic segmentation and crustal melt transport at fast–spreading ridges. *Geochemistry, Geophysics, Geosystems*, 19(11):4584–4611. 1.2.1

Massonnet, D. and Feigl, K. L. (1998). Radar interferometry and its application to changes in the Earth's surface. *Reviews of geophysics*, 36(4):441–500. 2, 2.1.1, 2.1.2, 2.4

McTigue, D. (1987). Elastic stress and deformation near a finite spherical magma body: resolution of the point source paradox. *Journal of Geophysical Research: Solid Earth*, 92(B12):12931–12940. 1.4.2

Merriam, J. (1992). Atmospheric pressure and gravity. *Geophysical Journal International*, 109(3):488–500. 2.2.2, 4.6

Meurers, B. (2012). Superconducting gravimeter calibration by colocated gravity observations: Results from GWR C025. *International Journal of Geophysics*, 2012. 4.8.2, 4.4

Miller, C., Le Mével, H., Currenti, G., Williams-Jones, G., and Tikoff, B. (2017). Microgravity changes at the Laguna del Maule volcanic field: Magma-induced stress changes facilitate mass addition. *Journal of Geophysical Research: Solid Earth*, 122(4):3179–3196. 4.15

Mitchell, M. A., White, R. S., Roecker, S., and Greenfield, T. (2013). Tomographic image of melt storage beneath Askja Volcano, Iceland using local microseismicity. *Geophysical Research Letters*, 40(19):5040–5046. 1.5.4

Mogi, K. (1958). Relation between the eruptions of various volcanoes and the deformations of the ground surface around them. *Bulletin of the Earthquake Research Institute*, 36:99–134. 1.4.2, 3.7.2

Moran, S. C., Newhall, C., and Roman, D. C. (2011). Failed magmatic eruptions: late-stage cessation of magma ascent. *Bulletin of Volcanology*, 73(2):115–122. 1.1

Murase, M., Ono, K., Ito, T., Miyajima, R., Mori, H., Aoyama, H., Oshima, H., Yoshida, Y., Terada, A., Koyama, E., et al. (2007). Time-dependent model for volume changes in pressure sources at Asama volcano, central Japan due to vertical deformations detected by precise leveling during 1902–2005. *Journal of volcanology and geothermal research*, 164(1-2):54–75. 6.1

Niebauer, T., Blitz, T., and Constantino, A. (2016). Off-level corrections for gravity meters. *Metrologia*, 53(2):835. 4.4

Nielsen, K., Villadsen, H., Stenseng, L., Andersen, O. B., and Knudsen, P. (2015). Water levels of lakes and rivers observed from space. In *DTU Sustain Conference 2015*. 4.10, 5.4.2.3, 5.6

Otway, P., Blick, G., and Scott, B. (2002). Vertical deformation at Lake Taupo, New Zealand, from lake levelling surveys, 1979–99. *New Zealand Journal of Geology and Geophysics*, 45(1):121–132. 6.1

Pagli, C., Sigmundsson, F., Arnadóttir, T., Einarsson, P., and Sturkell, E. (2006). Deflation of the Askja volcanic system: constraints on the deformation source from combined inversion of satellite radar interferograms and GPS measurements. *Journal of Volcanology and Geothermal Research*, 152(1):97–108. 1.2, 3.1, 3.7.3.1, 3.21, 3.7.3.2, 3.7.3.3

Parker, A. L., Biggs, J., and Lu, Z. (2014). Investigating long-term subsidence at Medicine Lake Volcano, CA, using multitemporal InSAR. *Geophysical Journal International*, 199(2):844–859. 6.1

Pedersen, R., Sigmundsson, F., and Masterlark, T. (2009). Rheologic controls on interrifting deformation of the Northern Volcanic Zone, Iceland. *Earth and Planetary Science Letters*, 281(1):14–26. 1.1, 1.5.1, 1.5.3, 5.7

Peltier, A., Hurst, T., Scott, B., and Cayol, V. (2009). Structures involved in the vertical deformation at Lake Taupo (New Zealand) between 1979 and 2007: New insights from numerical modelling. *Journal of Volcanology and Geothermal Research*, 181(3-4):173–184. 6.1

Petit, G. and Luzum, B. (eds. 2010). IERS Conventions (2010), IERS Technical Note No. 36, BKG (2010). 4.5, 4.6

Pola, A., Crosta, G., Fusi, N., Barberini, V., and Norini, G. (2012). Influence of alteration on physical properties of volcanic rocks. *Tectonophysics*, 566:67–86. 4.10

Pola, A., Crosta, G. B., Fusi, N., and Castellanza, R. (2014). General characterization of the mechanical behaviour of different volcanic rocks with respect to alteration. *Engineering Geology*, 169:1–13. 4.10

Poland, M., Bürgmann, R., Dzurisin, D., Lisowski, M., Masterlark, T., Owen, S., and Fink, J. (2006). Constraints on the mechanism of long-term, steady subsidence at Medicine Lake volcano, northern California, from GPS, leveling, and InSAR. *Journal of Volcanology and Geothermal Research*, 150(1-3):55–78. 6.1

Pritchard, M., Jay, J., Aron, F., Henderson, S., and Lara, L. (2013). Subsidence at southern Andes volcanoes induced by the 2010 Maule, Chile earthquake. *Nature Geoscience*, 6(8):632. 5.7

Reudink, R., Klees, R., Francis, O., Kusche, J., Schlesinger, R., Shabanloui, A., Sneeuw, N., and Timmen, L. (2014). High tilt susceptibility of the scintrex cg-5 relative gravimeters. *Journal of Geodesy*, 88(6):617–622. 4.3.1

Rivalta, E. and Segall, P. (2008). Magma compressibility and the missing source for some dike intrusions. *Geophysical Research Letters*, 35(4). 1.3.1, 1.3.1, 1.1, 5.6.2

Rosen, P. A., Hensley, S., Peltzer, G., and Simons, M. (2004). Updated repeat orbit interferometry package released. *Eos, Transactions American Geophysical Union*, 85(5):47–47. 2.1.2, 2.4, 3.1

Rundle, J. B. (1982). Deformation, gravity, and potential changes due to volcanic loading of the crust. *Journal of Geophysical Research: Solid Earth*, 87(B13):10729–10744. 4.9

Rymer, H. (1989). A contribution to precision microgravity data analysis using LaCoste and Romberg gravity meters. *Geophysical Journal International*, 97(2):311–322. 4.1, 4.3.2, 4.4.1, 4.7.1

Rymer, H. (1994). Microgravity change as a precursor to volcanic activity. *Journal of Volcanology and Geothermal Research*, 61(3):311–328. 4.9, 4.9.1, 4.13

Rymer, H. (1996). Microgravity monitoring. In *Monitoring and mitigation of volcano hazards*, pages 169–197. Springer. 2, 4.1, 4.6, 4.9.2, 4.11

Rymer, H., Locke, C., Ófeigsson, B. G., Einarsson, P., and Sturkell, E. (2010). New mass increase beneath Askja volcano, Iceland – a precursor to renewed activity? *Terra Nova*, 22(4):309–313. 1.5.2, 1.8, 1.5.3, 5.1

Rymer, H. and Tryggvason, E. (1993). Gravity and elevation changes at Askja, Iceland. *Bulletin of Volcanology*, 55(5):362–371. 1.2, 1.5.2, 1.5.2, 1.5.3, 4.15, 5.7

Saibi, H., Gottsmann, J., and Ehara, S. (2010). Post-eruptive gravity changes from 1999 to 2004 at unzen volcano (japan): A window into shallow aquifer and hydrothermal dynamics. *Journal of Volcanology and Geothermal Research*, 191(1-2):137–147. 5.7

Samsonov, S. V., González, P. J., Tiampo, K. F., Camacho, A. G., and Fernández, J. (2014). Spatiotemporal analysis of ground deformation at Campi Flegrei and Mt Vesuvius, Italy, observed by Envisat and Radarsat-2 InSAR during 2003–2013. In *Mathematics of Planet Earth*, pages 377–382. Springer. 6.1

Schaefer, L. N., Kendrick, J. E., Lavallée, Y., Oommen, T., and Chigna, G. (2015). Geomechanical rock properties of a basaltic volcano. *Frontiers in Earth Science*, 3:29. 4.10

Scherneck, H.-G. and Bos, M. (2011). Ocean tide loading provider. 4.5, 4.6

Scintrex (1995). *CG-3/CG-3M Autograv Automated Gravity Meter - Operation manual*, SCINTREX Limited edition. 2.2.2, 2.2.3, 4.3, 4.8, B.2

Scintrex (2009). *CG-5 Scintrex Autograv System - Operation manual*, SCINTREX Limited edition. 2.2.2, 2.2.3, 4.3, 4.3, 4.3.1, 4.4, 4.4.1, 4.6, 4.7.1, 4.8, 4.8, 5, 5.4.1.3, B.2

Segall, P. (2010a). *Earthquake and volcano deformation*. Princeton University Press. 4.9, 4.9.1, 4.13

Segall, P. (2010b). Graviational effects. In Segall, P., editor, *Earthquake and volcano deformation*, chapter 9, pages 267–296. Princeton University Press. 1.3, 1.3.3, 1.3.4, 1.4.2, 1.4.2

Segall, P. (2010c). Volcano deformation. In Segall, P., editor, *Earthquake and volcano deformation*, chapter 7, pages 200–254. Princeton University Press. 1.3, 1.3, 1.3.1, 1.3.1, 1.4, 1.4.1, 1.4.1, 1.4.2, 1.4.2, 5.6.2

Seigel, H. (1995). A guide to high precision land gravimeter surveys. *Scintrex LTD, Concord, Ontraio*. 4.3, 4.6, 4.7.1

Shinohara, H. (2008). Excess degassing from volcanoes and its role on eruptive and intrusive activity. *Reviews of Geophysics*, 46(4). 1.3.3

Sigmundsson, F. (2006a). *Iceland geodynamics: crustal deformation and divergent plate tectonics*. Springer Science & Business Media. 1.2.1, 1.1, 1.2.1, 1.5, 3.1

Sigmundsson, F. (2006b). Volcano dynamics. In Sigmundsson, F., editor, *Iceland geodynamics*, chapter 5, pages 69–102. Springer Science & Business Media. 1.3, 1.3, 1.4, 1.4.1, 1.5, 1.4.2, 1.4.2

Sigmundsson, F. (2016). New insights into magma plumbing along rift systems from detailed observations of eruptive behavior at Axial volcano. *Geophysical Research Letters*, 43(24):12–423. 1.1, 1.2.1, 1.2.2

Sigmundsson, F., Hooper, A., Hreinsdóttir, S., Vogfjörd, K. S., Ófeigsson, B. G., Heimisson, E. R., Dumont, S., Parks, M., Spaans, K., Gudmundsson, G. B., et al. (2014). Segmented lateral dyke growth in a rifting event at Bárdarbunga volcanic system, Iceland. *Nature*. 1.1, 1.2.2, 1.2.2, 1.3.4, 3.3

Sigmundsson, F., Parks, M., Pedersen, R., Jónsdóttir, K., Ófeigsson, B. G., Grapenthin, R., Dumont, S., Einarsson, P., Drouin, V., Heimisson, E. R., et al. (2018). Magma movements in volcanic plumbing systems and their associated ground deformation and seismic patterns. In Burchardt, S., editor, *Volcanic and igneous plumbing systems*, chapter 11, pages 285–322. Elsevier. 1.2.1

Sigmundsson, F., Pinel, V., Lund, B., Albino, F., Pagli, C., Geirsson, H., and Sturkell, E. (2010). Climate effects on volcanism: influence on magmatic systems of loading and unloading from ice mass variations, with examples from Iceland. *Philosophical Transactions of the Royal Society A: Mathematical, Physical and Engineering Sciences*, 368(1919):2519–2534. 1.2.2

Sigvaldason, G. E. (2002). Volcanic and tectonic processes coinciding with glaciation and crustal rebound: an early Holocene rhyolitic eruption in the Dyngjufjöll volcanic centre and the formation of the Askja caldera, north Iceland. *Bulletin of Volcanology*, 64(3-4):192–205. 1.5

Soriano, C., Beamud, E., and Garcés, M. (2008). Magma flow in dikes from rift zones of the basaltic shield of Tenerife, Canary Islands: implications for the emplacement of buoyant magma. *Journal of Volcanology and Geothermal Research*, 173(1-2):55–68. 1.2.2

Spaans, K. and Hooper, A. (2018). Insights into the stress field around Bárdarbunga volcano from the 2014/2015 Holuhraun rifting event. *Journal of Geophysical Research: Solid Earth*, 123(4):3238–3249. 3.3, 3.4.1

Sparks, R., Biggs, J., and Neuberg, J. (2012). Monitoring volcanoes. *Science*, 335(6074):1310–1311. 1.1

Sparks, R. S. J. and Cashman, K. V. (2017). Dynamic magma systems: implications for forecasting volcanic activity. *Elements*, 13(1):35–40. 1.2, 1.2.2

Sruoga, P. and Rubinstein, N. (2006). Processes controlling porosity and permeability in volcanic reservoirs from the Austral and NeuquÃľn basins, Argentina. *The American Association of Petroleum Geologist Bulletin*, 91(1):115–129. 4.10

Stammer, D., Ray, R., Andersen, O. B., Arbic, B., Bosch, W., Carrère, L., Cheng, Y., Chinn, D., Dushaw, B., Egbert, G., et al. (2014). Accuracy assessment of global barotropic ocean tide models. *Reviews of Geophysics*, 52(3):243–282. 4.5, 5.4.1.1

Sturkell, E. and Sigmundsson, F. (2000). Continuous deflation of the Askja caldera, Iceland, during the 1983–1998 noneruptive period. *Journal of Geophysical Research: Solid Earth*, 105(B11):25671–25684. 1.2, 1.5.3, 3.1, 5.7

Sturkell, E., Sigmundsson, F., and Slunga, R. (2006). 1983–2003 decaying rate of deflation at Askja caldera: pressure decrease in an extensive magma plumbing system at a spreading plate boundary. *Bulletin of Volcanology*, 68(7-8):727–735. 1.5.1, 1.2, 1.7, 1.5.1, 1.5.3, 3.1, 5.3

Takada, Y. and Fukushima, Y. (2013). Volcanic subsidence triggered by the 2011 Tohoku earthquake in Japan. *Nature Geoscience*, 6(8):637. 5.7

Tammaro, U., De Martino, P., Obrizzo, F., Brandi, G., D'Alessandro, A., Dolce, M., Malaspina, S., Serio, C., and Pingue, F. (2013). Somma Vesuvius volcano: ground deformations from CGPS observations (2001-2012). *Annals*. 6.1

Tan, Y. J., Tolstoy, M., Waldhauser, F., and Wilcock, W. S. (2016). Dynamics of a seafloor-spreading episode at the East Pacific Rise. *Nature*, 540(7632):261. 1.2.1

Tarantola, A. (2005). *Inverse problem theory and methods for model parameter estimation*, volume 89. siam. 1.4

Thordarson, T. and Hartley, M. (2016). The askja volcanic system. In Ilyinskaya E, L. G. and Gudmundsson, editors, *Catalogue of Icelandic Volcanoes*. IMO, UI, CPD-NCIP. 1.6, 1.5

Tryggvason, E. (1989). Ground deformation in Askja, Iceland: its source and possible relation to flow of the mantle plume. *Journal of Volcanology and Geothermal Research*, 39(1):61–71. 1.5.1, 1.2, 1.5.3

USNO (2016). The Astronomical Almanac online. 4.5, 4.9.1

Vajda, P., Pavol, P. Z., Papčo, J., and Kubová, A. (2015). Deformation induced topographic effects in inversion of temporal gravity changes: First look at Free Air and Bouguer terms. *Contributions to Geophysics and Geodesy*, 45(2):149–171. 4.9, 4.9.1

Vajda, P., Prutkin, I., Tenzer, R., and Jentzsch, G. (2012). Inversion of temporal gravity changes by the method of local corrections: A case study from Mayon volcano, Philippines. *Journal of Volcanology and Geothermal Research*, 241:13–20. 1.3.4

Valliant, H. D. (1991). Gravity meter calibration at LaCoste and Romberg. *Geophysics*, 56(5):705–711. 2.2.2, 4.8, 4.8, B.2

Van Camp, M. and Vauterin, P. (2005). Tsoft: graphical and interactive software for the analysis of time series and earth tides. *Computers & Geosciences*, 31(5):631–640. 4.5

Van Camp, M., Viron, O., Watlet, A., Meurers, B., Francis, O., and Caudron, C. (2017). Geophysics from terrestrial time-variable gravity measurements. *Reviews of Geophysics*. 2, 2.2, 2.2.1, 4.1, 4.3, 4.3.1, 4.4, 4.4.1, 4.5, 4.7, 5.5.1

van Wyk de Vries, B. and van Wyk de Vries, M. (2018). Tectonics and volcanic and igneous plumbing systems. In Burchardt, S., editor, *Volcanic and igneous plumbing systems*, chapter 7, pages 167–189. Elsevier. 1.2, 1.2.1, 1.2.2

Vigouroux, N., Williams-Jones, G., Chadwick, W., Geist, D., Ruiz, A., and Johnson, D. (2008). 4d gravity changes associated with the 2005 eruption of Sierra Negra volcano, Galápagos. *Geophysics*, 73(6):WA29–WA35. 4.3.2

Wallace, P. J., Plank, T., Edmonds, M., and Hauri, E. H. (2015). Volatiles in magmas. In Sigurdsson, H., Houghton, B., McNutt, S., Rymer, H., and Stix, J., editors, *The encyclopedia of volcanoes*, chapter 7, pages 164–183. Elsevier. 1.3.2, 1.3.3

Walsh, J. and Rice, J. (1979). Local changes in gravity resulting from deformation. *Journal of Geophysical Research: Solid Earth*, 84(B1):165–170. 1.3, 1.3.3, 1.3.4, 1.4.2, 4.9

Walter, T., Shirzaei, M., Manconi, A., Solaro, G., Pepe, A., Manzo, M., and Sansosti, E. (2014). Possible coupling of Campi Flegrei and Vesuvius as revealed by InSAR time series, correlation analysis and time dependent modeling. *Journal of Volcanology and Geothermal Research*, 280:104–110. 6.1

Wenzel, H.-G. (1996). The nanogal software: Earth tide data processing package ETERNA 3.30. *Bull. Inf. Marées Terrestres*, 124:9425–9439. 4.5

Werner, C., Wegmüller, U., Strozzi, T., and Wiesmann, A. (2000). Gamma SAR and interferometric processing software. In *Proceedings of the ers-envisat symposium, gothenburg, sweden*, volume 1620, page 1620. Citeseer. 2.1.2, 2.4, 3.1

Williams-Jones, G. and Rymer, H. (2002). Detecting volcanic eruption precursors: a new method using gravity and deformation measurements. *Journal of Volcanology and Geothermal Research*, 113(3):379–389. 4.9

Williams-Jones, G., Rymer, H., Mauri, G., Gottsmann, J., Poland, M., and Carbone, D. (2008). Toward continuous 4D microgravity monitoring of volcanoes. *Geophysics*, 73(6):WA19–WA28. 2, 2.2

Williams-Jones, G., Rymer, H., and Rothery, D. A. (2003). Gravity changes and passive SO2 degassing at the Masaya caldera complex, Nicaragua. *Journal of Volcanology and Geothermal Research*, 123(1):137–160. 4.9, 4.15

Wright, T. J., Parsons, B. E., and Lu, Z. (2004). Toward mapping surface deformation in three dimensions using InSAR. *Geophysical Research Letters*, 31(1). 3.4.3, 3.5, 1, 4.9.3, A.3

Wright, T. J., Sigmundsson, F., Pagli, C., Belachew, M., Hamling, I. J., Brandsdóttir, B., Keir, D., Pedersen, R., Ayele, A., Ebinger, C., et al. (2012). Geophysical constraints on the dynamics of spreading centres from rifting episodes on land. *Nature Geoscience*, 5(4):242. 1.2.1, 1.2.1, 1.2.2, 1.2

Zurek, J., William-Jones, G., Johnson, D., and Eggers, A. (2012). Constraining volcanic inflation at Three Sisters Volcanic Field in Oregon, USA, through microgravity and deformation modeling. *Geochemistry, Geophysics, Geosystems*, 13(10). 4.3.2